Viscous Compressible Flow Through a Micro-Conduit:

Slip-Like Flow Rate with No-Slip Boundary Condition

by

Di Shen

A Dissertation Presented in Partial Fulfillment
of the Requirements for the Degree
Doctor of Philosophy

Approved May 2019 by the
Graduate Supervisory Committee:

Kangping Chen, Chair
Marcus Herrmann
Huei-Ping Huang
Ronald Calhoun
Juan Lopez

ARIZONA STATE UNIVERSITY

August 2019

ABSTRACT

This dissertation studies two outstanding microscale fluid mechanics problems: 1) mechanisms of gas production from the nanopores of shale; 2) enhanced mass flow rate in steady compressible gas flow through a micro-conduit.

The dissertation starts with a study of a volumetric expansion driven drainage flow of a viscous compressible fluid from a small capillary and channel in the low Mach number limit. An analysis based on the linearized compressible Navier-Stokes equations with no-slip condition shows that fluid drainage is controlled by the slow decay of the acoustic wave inside the capillary and the no-slip flow exhibits a slip-like mass flow rate. Numerical simulations are also carried out for drainage from a small capillary to a reservoir or a contraction of finite size. By allowing the density wave to escape the capillary, two wave leakage mechanisms are identified, which are dependent on the capillary length to radius ratio, reservoir size and acoustic Reynolds number. Empirical functions are generated for an effective diffusive coefficient which allows simple calculations of the drainage rate using a diffusion model without the presence of the reservoir or contraction.

In the second part of the dissertation, steady viscous compressible flow through a micro-conduit is studied using compressible Navier-Stokes equations with no-slip condition. The mathematical theory of Klainerman and Majda for low Mach number flow is employed to derive asymptotic equations in the limit of small Mach number. The overall flow, a combination of the Hagen-Poiseuille flow and a diffusive velocity shows a slip-like mass flow rate even through the overall velocity satisfies the no-slip condition. The result indicates that the classical formulation includes self-diffusion effect and it embeds the Extended Navier-Stokes equation theory (ENSE) without the need of introducing

additional constitutive hypothesis or assuming slip on the boundary. Contrary to most ENSE publications, the predicted mass flow rate is still significantly below the measured data based on an extensive comparison with thirty-five experiments.

ACKNOWLEDGMENTS

First and foremost, I would like to express my sincere and deepest gratitude to my research advisor, Professor Kangping Chen, for the guidance, support and encouragement he gave me throughout the course of my Ph.D. study. Thanks for spending an enormous amount of time with me over the past few years, providing me insights into micro-scale fluid mechanics and supporting me in the pursuit of this challenging low Mach number viscous compressible flow theory with unlimited trust. I am extremely grateful to learn from Professor Kangping Chen and will always cherish the opportunity he gave me to achieve my Ph.D. degree.

I would also like to extend my sincere thanks to my committee: Professor Marcus Herrmann, Professor Huei-Ping Huang, Professor Ronald Calhoun and Professor Juan Lopez, for their insightful comments and invaluable suggestions, which helped me improve this dissertation.

I want to thank all of my former and current colleagues, Wei Huang, Jing Yuan, Kai Zhou, Abhinav Kshitij, Yan Guan, Hechao Li, Xiying Chen, for giving their creative ideas regarding to my work.

I must also thank Professor Valana Wells, who is one of my great motivators and supporters during my Ph.D. study. Thank you for giving me the opportunity to work as a teaching assistant. It gives me the chance to improve my teaching and presentation skills.

Last but not the least, I express my gratitude and love to my parents Jingnan Shen, Hong Chen and my girlfriend Xiaojun Yu, for their unwavering support, encouragement and sacrifices. Your unconditional love and faith in me give me the courage to complete my Ph.D. study.

TABLE OF CONTENTS

Page

CHAPTER Page

CHAPTER Page

CHAPTER Page

CHAPTER Page

LIST OF TABLES

Table Page

LIST OF FIGURES

Figure Page

Figure Page

Figure Page

Figure Page

Figure Page

Figure Page

Figure Page

Figure Page

Chapter 1

Introduction

Low Reynolds number, low Mach number compressible flow of a gas through narrow conduits are encountered in many technological applications such as hydrocarbon recovery, Micro-Electro-Mechanical Systems (MEMS) devices, microfluidics, acoustic wave guide and gas filtration. In this study, we focus on two model problems for applications of such viscous compressible flows to primary hydrocarbon recovery from a petroleum reservoir and microfluidics, respectively. This chapter provides an overview of these two subjects.

1.1. A pore-scale model for hydrocarbon primary recovery from petroleum reservoirs

When a petroleum reservoir is rigid and no fresh fluid is injected into the reservoir to drive the in-situ fluid out of the pore space (figure 1.1), fluid recovery relies entirely on the volumetric expansion of the fluid; and such a process is called *primary recovery* in the petroleum literature (Muskat 1949). Thus, despite of a very low fluid velocity, which would normally justify the incompressible flow approximation from the classical gas dynamics arguments based on a vanishing Mach number, the flow during a primary fluid recovery is physically dominated by the fluid's compressible effect.

A fundamental pore-scale prototype problem for primary recovery is the drainage flow from a long and narrow semi-sealed capillary to a very large reservoir (figure 1.2). The capillary is initially filled with a gas of density ρ_i and the end is opened at $t = 0$ with a fixed exit density ρ_e, which is lower than the initial density ρ_i.

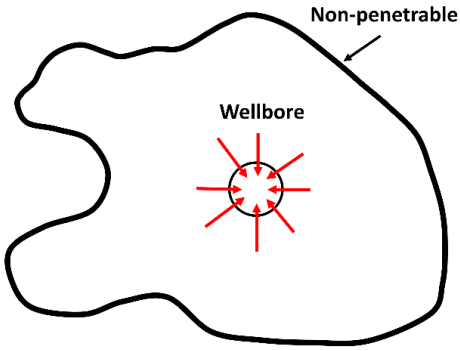

Figure 1.1. Schematic of primary fluid recovery from a porous reservoir. The outer boundary is impenetrable, and the fluid is produced from the inner boundary (e.g. wellbore).

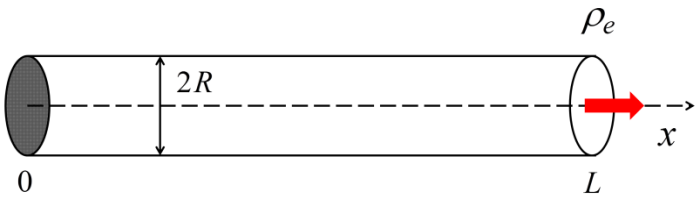

Figure 1.2. Primary recovery: a simple pore-scale model of draining a compressed fluid from a semi-sealed small capillary (from Chen & Shen 2018a). The exit density ρ_e is lower than the initial density ρ_i.

In this dissertation, we study a special kind of low Mach number viscous compressible flow: fluid-expansion induced slow drainage flow from a long narrow capillary tube with a sealed end. Historically, drainage of a compressed gas from a large vessel has been studied in the context of aerodynamics and chemical engineering using inviscid flow theory (Shapiro 1954; Bird et al. 2007). The current work is restricted to the low Mach number limit and it is based entirely on the classical Navier-Stokes equations with no-slip condition. Contrary to the perception that a low Mach number flow can be approximated as an incompressible flow, or at least as a small perturbation to an incompressible flow, compressible effect dominates the drainage process. The lack of a through-flow for this

particular problem allows us to isolate the flow driven by the local fluid volumetric expansion from the Poiseuille-type of flow driven by a pressure-gradient. Unlike the open-tube flow, the current problem is inherently unsteady and there is no corresponding steady-state solution from which a perturbation analysis can be performed even for the low Mach number limit. The density perturbation is assumed to be small in the current work so that consistent linearization can be carried out without any ambiguity and a rigorous analysis can be performed to elucidate the underlying flow and drainage mechanism. The analysis applies equally to a gas as well as a compressible liquid. It will be shown that acoustic wave plays an important role in the drainage process and lubrication-based theory is not suitable for this volume-expansion driven flow. The analysis carried out applies to arbitrarily small capillaries as long as the continuum assumption holds. The current work reveals that this no-slip flow exhibits a slip-like mass flow rate and the period-averaged mass flow rate at the exit (drainage rate) is proportional to the fluid's kinematic viscosity and the average drainage speed is independent of the capillary radius. These intriguing results offer fresh insights to the nature of slow viscous compressible flows in very small capillaries. The analytical result for infinitely large reservoir is further extended to the case of drainage to a finite reservoir as well as a contraction via numerical simulation of the linearized equations.

1.2. Steady compressible flow through a micro-conduit

Rapid growing applications of micro-electro-mechanical systems (MEMS) and microfluidics during the past three decades have stimulated significant research on viscous compressible flow through micron-size conduits (Ho & Tai 1998; Gad-el-Hak 1999; Stone

& Kim 2001; Stone, Stroock & Ajdari 2004; Squires & Quake 2005; Whitesides 2006). Steady compressible flow of a gas through such a micro-conduit can produce a mass flow rate much higher than that predicted by the classical Hagen-Poiseuille solution for macroscale flows (Maxwell, 1879; Knudsen 1909; Arkilic 1994; Harley et al. 1995; Shih et al. 1996; Arkilic et al. 1997a, b; Jang et al. 2002; Maurer et al. 2003; Colin 2005; Ewart et al. 2006, 2007a, b; Cai et al. 2007; Yamaguchi et al. 2011). This departure from the classical result has been attributed to a breakdown of the continuum assumption, which is the basis for the Navier-Stokes equations for macroscale flows. The mean free path in a low-pressure gas flow through a micro-conduit can become comparable to the characteristic length of the confining geometry (Tsien 1946; Karniadakis et al. 2005; Colin 2005) and a large surface-to-volume ratio can make the interaction between the wall and the gas important for the flow. The degree of departure of such a small scale flow from the classical continuum theory is commonly characterized by the Knudsen number, $Kn = \lambda / L_c$, with λ being the mean free path of the gas molecules and L_c the characteristic length of the flow (typically the hydraulic diameter of the conduit). It is widely acknowledged that for Knudsen number $Kn < 0.001$, the classical continuum formulation of the Navier-Stokes equations with no-slip condition holds; and when $Kn > 10$, free molecular flow (Knudsen diffusion) results (Knudsen 1909; Kennard 1938; Malek & Coppens 2003). Thus, as the Knudsen number is increased from a very small value to a large value, the flow changes from a continuum flow to a free molecular flow. The flow regimes between the continuum limit and the free molecular flow limit are commonly classified as the slip-flow regime, the transitional-flow regime etc. in the order of increasing Knudsen number. For example, gas flows through MEMS devices typically

have Knudsen numbers in the range of 0.01 to 1, which fall into the slip and the transitional flow regimes, corresponding to $0.001 < Kn < 0.1$, and $0.1 < Kn < 10$, respectively (Colin 2005). Flow in the slip regime, however, is expected to show only a small to moderate departure from the classical continuum theory, as the Knudsen number is still relatively small. It has been common to assume that in the slip-flow regime, the breakdown of the continuum theory occurs only in the Knudsen layer adjacent to the solid boundary and the Navier-Stokes equations still hold in the bulk of the fluid. Within the Knudsen layer, which has a thickness in the order of the mean free path, gas-wall collision is more frequent than intramolecular collision. This results in a slip-like thin layer, which has been often modeled by a slip boundary condition for the gas motion in the bulk (Maxwell 1879; Beskok & Karniadakis 1999; Zohar et al. 2002; Hadjiconstantinou 2003, 2006; Wu 2008; Zhang et al. 2012). The results from this slip-boundary-condition approach for the slip-flow regime match well with experimentally observed mass flow rate when a slip parameter is tuned to a suitable value. Another popular approach to compressible micro-flow in the slip-flow regime is the Extended Navier-Stokes Equations (ENSE) formulation proposed by Brenner (2005) and Durst et al. (2006). This approach recognizes the importance of self-diffusion (bulk diffusion) caused by a local density gradient in compressible flow through small conduits (Lund & Berman 1966) and it extends the Navier-Stokes equations to include an additional diffusive mass (or volume) flux from self-diffusion (mass or volume) as well as an additional diffusive momentum flux. The overall velocity is assumed to be given by the sum of the convective velocity, as in the Navier-Stokes equations., and a diffusive velocity from the self-diffusion of the fluid mass. Only the convective velocity is made to satisfy the no-slip condition whilst the diffusive velocity is allowed to slip on the wall (Brenner

2005; Durst et al 2006; Chakraborty & Durst 2007; Dongari et al. 2007; Dongari et al. 2009; Dadzie & Brenner 2012; Jaishankar & McKinley 2014). Noticeably, this ENSE approach involves constitutive modifications to both the mass flux and the stress tensor of the classical Newtonian fluid. Many ENSE publications have reported that this approach yields good agreements with experiments without an adjusting parameter, which has been advocated as a major appeal of this approach. The difference between the slip-boundary-condition approach and ENSE is that the former lacks the self-diffusion mechanism in the bulk and it also uses an adjustable slip parameter. It is also noted that Veltzke & Thaming (2012) used a slightly different approach by simply superposing Knudsen diffusion upon the Hagen-Poiseuille flow with a linear pressure profile. The velocity associated with the Knudsen diffusion flux still slips on the wall. They have also produced good agreements with their own experimental measurements. Other approaches that have been successfully applied to the same range as well as higher Knudsen numbers include linearized Boltzmann equations, direct simulation Monte Carlo (DSMC) etc. (Ohwada et al. 1989; Bird 1994; Hadjiconstantinou 2006; Gallis & Torczynski 2012). Together, these studies have significantly advanced our understanding of compressible flow through micro-conduits.

An impetus for the development of the above-mentioned slip-based continuum theories for the slip-flow regime is the failure of the classical continuum formulation of the Navier-Stokes equations with no-slip condition (hereafter referred to as "the classical formulation") to predict the elevated mass flow rate observed in experiments for steady compressible flow through micro-conduits. Here a "slip theory" refers to any theory that either explicitly enforces a slip boundary condition or incorporates a diffusive mass flux that produces a slip velocity on the boundary. As stated in the first section, we have found a surprising no-

slip solution with a slip-like mass flow rate for the volumetric-expansion-driven *transient* drainage flow of a compressible fluid from a semi-sealed micro-capillary (Chen & Shen 2018a, b). We have shown that the mass flow rate for the drainage flow is diffusive and it is proportional to the square of the tube radius, in contrast to the quartic power dependence on the radius from the classical Hagen-Poiseuille theory. Noticeably, the slip-like mass flow rate in the *transient* drainage flow is the result of the longitudinal mass diffusion caused by a local density gradient, consistent with the self-diffusion effect modeled in the ENSE theory for *steady* flows. The result for the drainage flow, however, is strictly derived from the linearized compressible Navier-Stokes equations *without any additional hypothesis*; and the velocity for the drainage flow satisfies the no-slip condition on the capillary wall. This finding naturally raises the following questions:

(a) Is the fluid's self-diffusion effect already embedded in the classical formulation for both transient and steady flows?

(b) Does the classical formulation also admit no-slip solutions with slip-like mass flow rates for *steady* compressible flow through narrow conduits?

(c) If such a steady slip-like solution exists, how does it perform compared to experiments?

To answer these questions, we re-visit the problem of steady compressible gas flow through a long and narrow open micro-conduit (circular tube or 2D channel) within the framework of the classical formulation of the compressible Navier-Stokes equations with no-slip condition. The mathematical theory for low Mach number flows developed by Klainerman & Majda (1982) is employed to expand the governing equations. in terms of the vanishing Mach number and to derive asymptotic equations. for compressible flow

through micro-conduits. It will be shown that for a compressible flow in a long and narrow open conduit, the leading order equations give rise to the Hagen-Poiseuille solution, and the balance between the convective acceleration and an equivalent body force induced by a local density gradient at the next order leads to a steady diffusive field. The cross-sectional averaged mass flux of the diffusive field will be shown to obey the Fick's law of diffusion, which gives rise to the self-diffusion effect. The Helmholtz decomposition theorem is then used to obtain an explicit solution for the diffusive field under the no-slip condition. The mass flow rate of the micro-flow is the sum of the mass flow rate from the Hagen-Poiseuille flow and that due to the diffusive field, which is identical to that from the ENSE theory when adjusted for the contribution of the bulk viscosity. The work will show that the classical formulation already embeds the ENSE theory without the need of introducing additional constitutive hypothesis or assuming slip on the boundary. For a very narrow conduit, the self-diffusion effect dominates, and the mass flow rate is slip-like with a radius-square dependence, even though the velocity satisfies the no-slip condition. These results are then compared to the multiple experiments and other works published in the literature. The pressure profile agrees very well with measured data. Contrary to the claims made in many ENSE publications, the predicted mass flow rate is still significantly below the measured mass flow rate, as the self-diffusion effect is too small to account for the observed mass flow rate deviation from the Hagen-Poiseuille solution in this flow regime.

1.3. Outline of this dissertation

The dissertation is consisted with 6 chapters along with the introduction chapter presented above.

In Chapter 2, a new theory for the fluid-expansion induced, low Mach number drainage flow from a long narrow capillary tube with a sealed end is presented. The present theory is entirely based on the classical Navier-Stokes equations with no-slip boundary condition without any tuning parameter or constitutive modification. The drainage process is dominated by the compressible effect, and density perturbation of the flow is assumed to be small so that consistent linearization can be carried out without any ambiguity and rigorous analysis can be performed to elucidate the underlying flow and drainage mechanism. This micro-scale drainage theory can be applied to the fluid production from massively hydraulically fractured shale formations as it provides a unified physical mechanism on how shale oil and gas are produced from the nanopores of shale.

In Chapter 3, extension of the theory to the microchannel drainage flow with a symmetric end is presented along with detailed analytical derivation process.

In Chapter 4, numerical simulation is performed on the drainage flow from a long narrow conduit into a reservoir or a contraction without using the prescribed exit density boundary condition. Reservoir size effect is analyzed showing that the period-average mass flow rate is affected especially with small size reservoir. An empirical effective diffusive coefficient equation is given for computing the drainage rate from small capillary/channel, applicable from micron size up to millimeter size.

In Chapter 5, the steady compressible gas flow through a long narrow open micro-conduit (circular tube or 2D channel) is being re-visit, within the framework of the classical formulation of the compressible Navier-Stokes equations with no-slip condition. The mathematical theory for low Mach number flows developed by Klainerman & Majda (1982) is employed to expand the governing equations. in terms of the vanishing Mach number

and to derive asymptotic equations. for compressible flow through micro-conduits. Multiple experiments and other published works are being compared with the analytical results.

In Chapter 6, the summary and conclusion will be given for all the problems discussed above.

Chapter 2

Drainage flow of a viscous compressible fluid from a small capillary

2.1. Mathematical formulation

We study the slow viscous drainage flow of a single-phase compressible fluid from a long small capillary with one end sealed by a solid surface (figure 1.2). The capillary has an inner radius R and length L, with $R << L$. The fluid stored in the tube is either a gas or a liquid, and it is initially at rest with a density ρ_i with both ends closed. The capillary tube is embedded in a large bath of the same compressible fluid maintained at a density ρ_e slightly lower than ρ_i. At $t = 0$, the end of the tube at $x = L$ is opened fully, and the density at the exit is maintained at ρ_e all times thereafter. Volumetric expansion causes the fluid to drain from the tube through the opening. The density difference $\rho_i - \rho_e$ is assumed to be small relative to the initial density, $\delta = (\rho_i - \rho_e)/\rho_i << 1$, and temperature variation is negligible. The Mach number defined as the ratio between a characteristic fluid velocity V and the speed of sound c for this drainage flow is assumed to be small, $Ma = V/c << 1$. Thus, the continuity and the compressible Navier-Stokes equations (Chorin & Marsden 1992) can be linearized around the final equilibrium state $(\rho, \mathbf{v}) = (\rho_e, 0)$ so that (Morse & Ingard 1968; Temkin 1981)

$$\frac{\partial \rho'}{\partial t} + \rho_e \nabla \cdot \mathbf{v}' = 0, \tag{2.1}$$

$$\rho_e \frac{\partial \mathbf{v}'}{\partial t} = -\nabla p' + \left(\mu_b + \frac{1}{3}\mu \right) \nabla (\nabla \cdot \mathbf{v}') + \mu \nabla^2 \mathbf{v}', \tag{2.2}$$

where the density perturbation $\rho' = \rho - \rho_e$; p' is the pressure perturbation; $\mathbf{v}'$ is the velocity perturbation which is assumed to be axisymmetric; μ, μ_b are the shear and bulk

viscosities of the fluid, respectively. It can be shown from (2.1) and (2.2) that the density perturbation is governed by a damped wave equation (Morse & Ingard 1968; Temkin 1981)

$$\frac{\partial^2 \rho'}{\partial t^2} = \left(c^2 + D_\rho \frac{\partial}{\partial t} \right) \nabla^2 \rho' , \tag{2.3}$$

where the diffusion coefficient $D_\rho = (\mu_b + 4\mu/3)/\rho_e$ characterizes the diffusion of a small density disturbance. When the sealed end is a rigid sound reflecting surface, the boundary and initial conditions for the density are

$$x = 0 : \frac{\partial \rho'}{\partial x} = 0; \quad x = L : \rho' = 0 ; \tag{2.4}$$

$$t = 0 : \rho' = \rho_i - \rho_e ; \frac{\partial \rho'}{\partial t} = 0 . \tag{2.5}$$

No wall condition for density needs to be specified and the density value on the wall is determined by the solution itself (see section 2.2 below). For the present problem, the mass flow rate at the tube exit $\dot{m}_e(t)$ can be computed once the instantaneous density distribution is obtained from the above initial-boundary-value problem without the need for the explicit knowledge of the corresponding velocity field, as the integral of the continuity equation over the entire tube gives

$$\dot{m}_e(t) = -\int_{Tube} \frac{\partial \rho'}{\partial t} d\mathrm{v} . \tag{2.6}$$

Relation (2.6) is general for a tube with a sealed end, not limited to the linearized problem considered here. It simply states that the mass flow rate from a half-sealed tube equals to the time rate of decrease of the fluid mass inside the tube.

To understand the characteristics of viscous compressible flow in small capillaries, the velocity field will be computed once the density distribution for the linearized flow is

obtained. From the Helmholtz decomposition theorem (Aris 1989; Leal 2010; Panton 2013), the velocity field $\mathbf{v}'$ can be decomposed into the sum of an irrotational part $\mathbf{v}'_{IR}$ and a rotational part $\mathbf{v}'_{RT}$,

$$\mathbf{v}' = \mathbf{v}'_{IR} + \mathbf{v}'_{RT}, \tag{2.7}$$

where the irrotational part is a potential flow and the rotational part is solenoidal (incompressible):

$$\nabla \times \mathbf{v}'_{IR} = 0, \quad \mathbf{v}'_{IR} = \nabla \Phi, \tag{2.8}$$

$$\nabla \cdot \mathbf{v}'_{RT} = 0. \tag{2.9}$$

In the above, Φ is the scalar velocity potential for the irrotational flow. These two parts of the velocity field are called the longitudinal mode and transverse mode respectively in the acoustic literature (Morse & Ingard 1968; Temkin 1981). In the linear theory studied here, the two modes are only coupled through the no-slip condition on the tube wall for the total velocity $\mathbf{v}'$,

$$r = R : \mathbf{v}' = \mathbf{v}'_{IR} + \mathbf{v}'_{RT} = 0. \tag{2.10}$$

The irrotational velocity can be determined from the continuity equation which now takes the form

$$\frac{\partial \rho'}{\partial t} + \rho_e \nabla \cdot \mathbf{v}'_{IR} = 0. \tag{2.11}$$

since $\nabla \cdot \mathbf{v}'_{RT} = 0$. At $x = 0$, $\mathbf{v}'_{IR} = 0$.

The solenoidal velocity $\mathbf{v}'_{RT}$ is governed by the equations for an incompressible flow, which can be expressed in terms of the incompressibility condition and the linearized vorticity diffusion equation

$$\nabla \cdot \mathbf{v}'_{RT} = 0 . \tag{2.12}$$

$$\frac{\partial \boldsymbol{\omega}}{\partial t} = \nu_e \nabla^2 \boldsymbol{\omega} . \tag{2.13}$$

$$\boldsymbol{\omega} = \nabla \times \mathbf{v}' = \nabla \times \mathbf{v}'_{RT} . \tag{2.14}$$

where the kinematic viscosity $\nu_e = \mu / \rho_e$. The solenoidal velocity is solely driven by the no-slip condition imposed on the overall velocity, equation (2.10).

The linearized problem formulated here can be considered as the leading-order solution in an asymptotic expansion in terms of the small density change $\delta = (\rho_i - \rho_e) / \rho_i << 1$. Thus, the neglected terms will be of the order of δ^2. It should be pointed out that the exit boundary condition of a fixed density (or pressure) is frequently used for tube flows and it is an idealization for the interaction between the flow inside the tube and the flow outside of the tube. Imposing an appropriate outlet boundary condition for the unsteady Navier-Stokes equations is generally a non-trivial matter (Gresho 1991; Poinsot & Lele 1992; Sani & Gresho 1994). An exit region of the size of a few tube diameters characterizing the influence on the tube flow from the fluid outside of the tube is expected (Gottlieb & Bird 1979). Since this exit region is small in comparison to the length of the tube, equation (2.6) indicates that the exit effect has a limited influence on the mass flow rate. Numerical solution of the linearized Navier-Stokes equations for drainage flow into a large finite reservoir is carried out in this study to verify whether the fixed density exit boundary condition is an appropriate approximation for drainage flow to a large reservoir. It is also noted that the problem of compressing a prefilled gas during liquid filling of a blind pore is quite different from the flow considered here, as a moving boundary condition must be

imposed at the gas–liquid surface which also involves surface tension effect (Hultmark et al. 2011).

2.2. Density relaxation

It is well known that when solving the Navier-Stokes equations, the only boundary condition required on the solid-fluid surface is the no-slip condition for the velocity and no boundary condition for the pressure or the density is needed (Scarton & Rouleau 1973; Monkewitz 1979). Since the linearized Navier-Stokes equations are being solved here, it is also expected that we only need to impose the no-slip condition for the velocity on the capillary wall without the need to specify a boundary condition for the density. This is confirmed by the solution of the damped wave equation for the density shown in detail below.

It is first noted that, in general, any function $\rho'(r,x,t)$ can be expressed as the sum of a part independent of r and a part that vanishes on the capillary wall,

$$\rho'(r,x,t) = \rho'(R,x,t) + \left[\rho'(r,x,t) - \rho'(R,x,t)\right] = \rho_1'(x,t) + \rho_2'(r,x,t)\,, \qquad (2.15)$$

where the r-dependent part $\rho_2'(r,x,t)$ vanishes on the tube wall, $\rho_2'(R,x,t) = 0$. It turns out that when the method of separation of variables is used to solve the initial-boundary-value problem for the density perturbation (2.3)–(2.5), the r-independent part of the solution $\rho'(R,x,t)$ naturally corresponds to the eigenvalue zero, whilst the r-dependent part $\rho_2'(r,x,t)$ corresponds to the non-zero eigenvalues that are related to the root of the Bessel function J_0. In other words, the boundary value for the density is determined by the eigenvalue problem arising from the separation of variables. Thus, there is no need to

specify the wall condition for the density and the density value on the wall is determined by the solution itself. It is observed that when studying inviscid compressible flows in tubes, it is customary to assume that the density is uniform over the cross-section of the tube. Even with this assumption, density is still part of the solution, and it cannot be prescribed *a priori* (see any textbook on gas dynamics). In the current work, we make no assumption about the uniformness of the density over the tube cross-section or the value of the density on the tube wall. The value of the density on the wall can be obtained from the solution itself, consistent with fluid mechanics theory.

The complete solution for the density perturbation is given by

$$\rho'(r,x,t)=\frac{4(\rho_i-\rho_e)}{\pi}\left[\begin{array}{l}\displaystyle\sum_{n=0}^{N_d}\frac{(-1)^n}{2n+1}e^{-\gamma_n t}\cos\omega_n t\cos\frac{(2n+1)\pi x}{2L}\\ \displaystyle+\sum_{n=N_d+1}^{\infty}\frac{(-1)^n}{2n+1}e^{-\gamma_n t}\cosh\gamma_n\sqrt{1-\varepsilon_n}\,t\cos\frac{(2n+1)\pi x}{2L}\\ \displaystyle+\sum_{m=1}^{\infty}\sum_{n=0}^{\infty}A_{nm}J_0(\alpha_m r)\left[e^{K_{nm}^{+}t}-e^{K_{nm}^{-}t}\right]\cos\frac{(2n+1)\pi x}{2L}\end{array}\right], \quad (2.16)$$

where

$$A_{nm}=\frac{2(-1)^n}{2n+1}\frac{J_1(\beta_m)}{\beta_m\left[J_0'(\beta_m)\right]^2}\frac{\gamma_n}{K_{nm}^{+}-K_{nm}^{-}},\ m=1,2,\ldots;\ n=0,1,2,\ldots$$

$$K_{nm}^{\pm}=-\frac{D_\rho}{2}\left[\frac{(2n+1)^2\pi^2}{4L^2}+\alpha_m{}^2\right]\pm\sqrt{\frac{D_\rho{}^2}{4}\left[\frac{(2n+1)^2\pi^2}{4L^2}+\alpha_m{}^2\right]^2-c^2\left[\frac{(2n+1)^2\pi^2}{4L^2}+\alpha_m{}^2\right]}$$

$$\alpha_m=\frac{\beta_m}{R};\quad J_0(\beta_m)=0,\ m=1,2,\ldots$$

$$\gamma_n=\frac{D_\rho}{2}\frac{(2n+1)^2\pi^2}{4L^2};\ \omega_n=c\frac{(2n+1)\pi}{2L}\sqrt{1-\frac{(2n+1)^2\pi^2 D_\rho{}^2}{16c^2L^2}},$$

$$\varepsilon_n=\frac{16c^2L^2}{(2n+1)^2\pi^2 D_\rho{}^2}<1,\ n>N_d;\ N_d=\mathit{floor}\left[\frac{2cL}{\pi D_\rho}-\frac{1}{2}\right]$$

In the above, J_n is the nth-order Bessel function of the first kind; J_0' is the first derivative of J_0; and β_m are the roots of J_0. The floor function gives the integer less or equal to its argument. The single-sum series in the solution (2.16) is independent of the radial coordinate r, where N_d is an integer such that ω_n becomes imaginary when $n > N_d$. $N_d = O(10^7)$ for meter-length tubes, $L = 1\text{m}$, and typical fluids properties $c = 400\text{m/s}$, $D_\rho = 10^{-5}\text{m}^2/\text{s}$. The part with $n > N_d$ is purely diffusive (non-oscillatory). The decay rate for this diffusive portion of the series is approximately $\exp(-2\gamma_n t)$ or $\exp(-c^2 t / D_\rho)$, whichever is smaller. For $c = 400\text{m/s}$, $D_\rho = 10^{-5}\text{m}^2/\text{s}$, $\exp(-c^2 t / D_\rho) \sim \exp(-10^9 t)$, which is an extremely fast decay; whilst $\exp(-2\gamma_n t)$ always decays faster than the terms with $n \le N_d$. Thus, the purely diffusive part of the series can be neglected in the calculations for large times due to their fast decay.

The double-sum series in the solution (2.16) contains the r-dependence of the density profile which vanishes on the tube wall. The slowest decaying mode in the double-sum series is the $(n, m) = (0,1)$ mode. A Taylor series expansion for small tube radius (more precisely for small ratios of R/L) gives, to the leading order,

$$K_{01}^{+} = -\frac{c^2}{D_\rho{}^2}, \tag{2.17}$$

$$K_{01}^{-} = -\frac{5.81 D_\rho}{R^2}. \tag{2.18}$$

K_{01}^{+} is the aeroacoustic mode, which decays with a rate of $\exp(-c^2 t / D_\rho)$, independent of the length and the radius of the tube; and as shown above, it decays fast as $\exp(-10^9 t)$. K_{01}^{-} is the highly damped viscous mode for very small tubes. For a micron-size tube $R = 10^{-6}\text{m}$ and $D_\rho = 10^{-5}\text{m}^2/\text{s}$, $K_{01}^{-} = -5.81\times 10^7/\text{s}$. Thus, for micron-size tubes, after a

very short time of the order $O(10^{-7}\,\mathrm{s})$, the double-sum series in (2.16) quickly decays to zero and the density relaxes to a profile uniform over the tube cross-section with the density perturbation given by the single-sum series. This density relaxation occurs even faster for nano-size tubes. In other words, the density wave quickly approaches the plane wave solution in a small tube. This fast relaxation of the density in the transverse direction is due to strong transverse viscous diffusion (strong transverse damping effect) in small capillaries. It should be pointed out that the fast density relaxation in the transverse direction is subject to the large length-to-radius ratio constraint for the capillary tube, as (2.17), (2.18) are derived under such conditions. The relaxed density profile has also been confirmed by numerical solution of the linearized Navier-Stokes equations (section 2.6).

The transversely relaxed density perturbation is given by

$$\rho'(r,x,t) = \frac{4(\rho_i - \rho_e)}{\pi} \sum_{n=0}^{N_d} \frac{(-1)^n}{2n+1} e^{-\gamma_n t} \cos\omega_n t \cos\frac{(2n+1)\pi x}{2L}, \qquad (2.19)$$

after neglecting the fast decaying purely diffusive modes. The relaxed density is independent of the radial coordinate r as well as the tube radius R. Equation (2.19) shows that in small capillary tubes, while any density variation in the cross-sectional direction is smoothed out very quickly, viscous damping of the longitudinal variation of density is extremely slow, on the diffusive time scale L^2 / D_ρ (since $\gamma_n \sim D_\rho / L^2$). Equation (2.19) is a damped standing wave solution for the density, with a node at the exit $x = L$ and an antinode at the sealed end $x = 0$.

As shown in figure 2.1a,b, upon the opening of the tube exit, an inward propagating rarefaction wave is initiated and this acoustic wave travels towards the sealed end. Once reflected from the end of the tube, the rarefaction wave travels towards the exit to complete

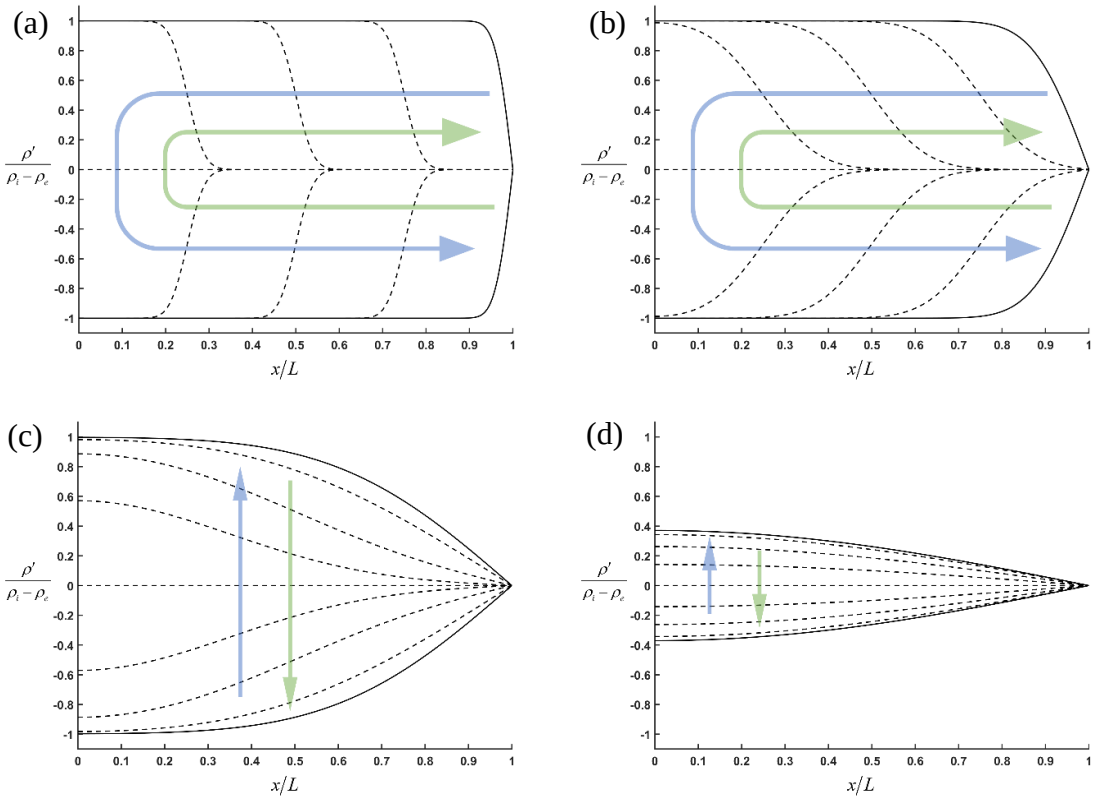

Figure 2.1. Relaxed density perturbation oscillation within 1 period $T = 4L/c$ under different time instance. (a) $t = 10^4 T$, (b) $t = 10^5 T$, (c) $t = 10^6 T$, (d) $t = 10^7 T$. Solid curves represent the initial state of each oscillation, with dashed curves as its transmission states. Blue arrow represents the wave propagating path in the first half period, with the green arrow represents the second half.

the rarefaction phase. The wave then becomes compressive as it travels back towards the sealed end once again, getting reflected from the end, travelling towards the exit and finally completing the compression phase once it reaches the exit.

Notice that throughout the entire wave propagating process, the wave oscillation pattern can be separated into 2 stages. In the early time stage (figure 2.1a,b), the rarefaction and compression density waves propagate along the capillary with a continuously dampened wave front. In the later time stage (figure 2.1c,d), the wave front has been smooth out and

it spreads across the whole capillary. As a result, the maximum amplitude of the density perturbation starts to decay.

Contrary to common belief, the slow damping of the wave amplitude gives the standing acoustic wave a surprisingly long life which is of the diffusive time scale L^2 / D_ρ. This result is consistent with recent findings that an acoustic impulse in a highly confined compressible fluid can create a long-time memory effect for the compressible fluid (Hagen et al 1997; Felderhof 2010; Frydel & Diamant 2012).

2.3. Irrotational velocity field

For the plane wave solution of the density (2.19), the irrotational velocity obtained from the continuity equation becomes $\mathbf{v}'_{IR} = \mathrm{v}'_{x,IR}(x,t)\mathbf{e}_x$, with

$$\mathrm{v}'_{x,IR}(x,t) = \frac{8L}{\pi^2}\frac{\rho_i - \rho_e}{\rho_e}\sum_{n=0}^{N_d}\frac{(-1)^n}{(2n+1)^2}\left(\gamma_n \cos\omega_n t + \omega_n \sin\omega_n t\right)e^{-\gamma_n t}\sin\frac{(2n+1)\pi x}{2L}. \quad (2.20)$$

The solution satisfies the boundary condition at the sealed end, $x = 0$, $\mathbf{v}'_{IR} = 0$. Thus, the irrotational part of the instantaneous velocity is independent of radial coordinate r as well as the tube radius R; and it scales with $c(\rho_i - \rho_e)/\rho_e$, not with the viscous velocity scale from the Poiseuille's law.

As shown in figure 2.2, the irrotational part of the instantaneous velocity also exhibits a similar acoustic wave oscillation pattern. However, determined by different boundary conditions, the irrotational velocity waves always initiate from a steady condition with minimum velocity output (solid curves). Corresponding to the rarefaction phase of the density perturbation, an outflow phase starts with a positive velocity wave propagating inwards and getting reflected at the sealed end boundary $\mathbf{v}'_{x=0,IR} = 0$. A steady outflow

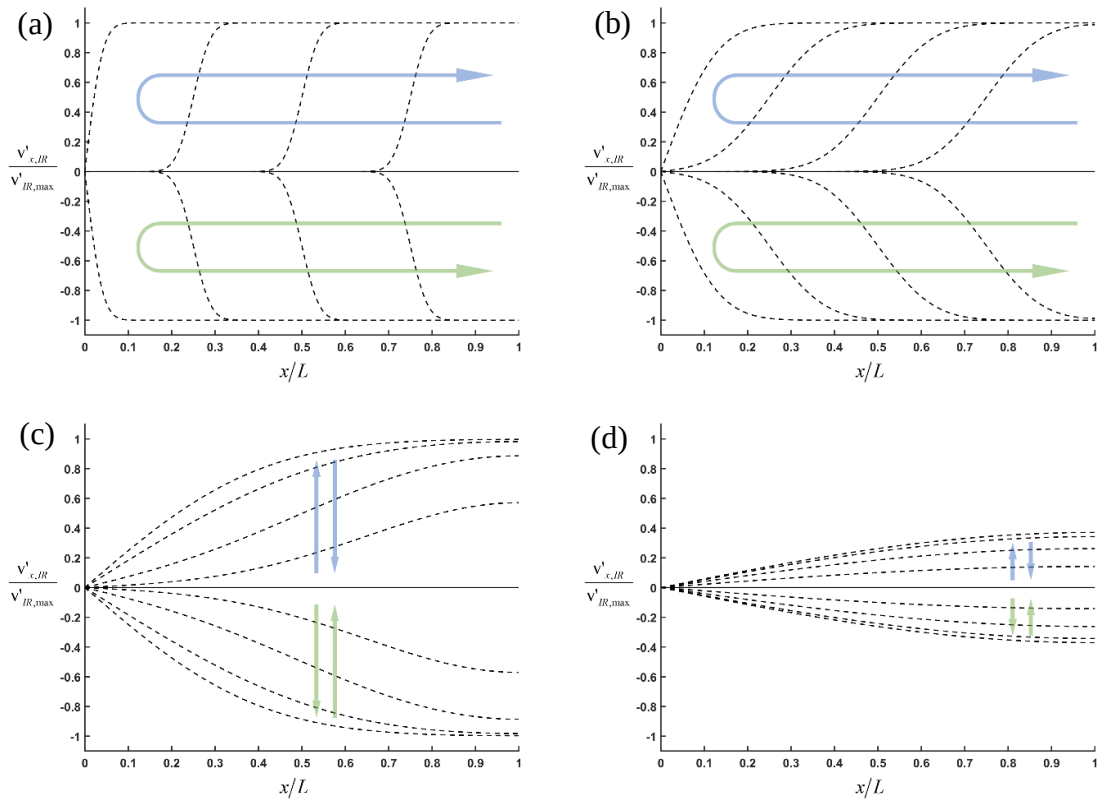

Figure 2.2. Irrotational velocity oscillation within 1 period $T = 4L/c$ under different time instance. (a) $t = 10^4 T$, (b) $t = 10^5 T$, (c) $t = 10^6 T$, (d) $t = 10^7 T$. Solid curves represent the initial state of each oscillation, with dashed curves as its transmission states. Blue arrow represents the wave propagating path in the first half period, with the green arrow represents the second half.

condition maintains at the exit during this first outflow phase. Once the wave reaches to the tube exit, an inflow phase starts as the exit velocity quickly switches from positive to negative. With a steady inflow condition maintains at the exit, this second phase is complete once the negative velocity wave gets reflected at the tube end and travels back to the exit. Noticed, as determined by the density perturbation, the irrotational velocity wave front is also dampened. In later time stage (figure 2.2c,d), maximum outflow and inflow velocity at the exit starts to decay, while the velocity wave front is distributed across the entire capillary.

2.4. Solenoidal velocity field

The solenoidal velocity is axisymmetric and driven by the no-slip condition on tube wall for the overall velocity, equation (2.10). On the sealed end at $x = 0$, the irrotational velocity is zero; thus, the solenoidal velocity satisfies the no-slip condition there. At the exit $x = L$, the perturbation pressure is zero. With these boundary conditions, it is difficult to obtain an analytical solution for the solenoidal velocity even for the plane wave solution of the irrotational velocity. Thus, we choose to find the solenoidal velocity numerically using the software package COMSOL. The linearized unsteady *incompressible* Navier-Stokes equation was solved subject to the above boundary conditions using fully coupled PARDISO direct solver and Jacobian update on every time step. The generalized alpha time stepping method was used with maximum time step set as 1/256 of the period. Quad elements are generated using the mapped mesh tool, dividing the radius of the tube into elements spaced exponentially with finer mesh distributed near the tube wall in order to capture the Stokes boundary layer, and the tube length is divided into linearly spaced elements. Second-order elements for the velocity components and linear elements for the pressure field are used. Mesh refinements are performed to ensure convergence of the numerical results.

It is first noted that for the relaxed density, the irrotational velocity is a plane wave solution. Thus, the radial component of the solenoidal velocity must be zero on the tube wall. The instantaneous volumetric flow rate of the solenoidal velocity over any cross-section of the tube Q_{RT} is identically zero at any time, since $\nabla \cdot \mathbf{v}'_{RT} = 0$ with zero radial velocity on the tube wall implies that $Q_{RT}(x) = Q_{RT}(0) = 0$. This also implies that the solenoidal velocity component $\mathrm{v}'_{x,RT}$ must experience a reversal on any cross-section

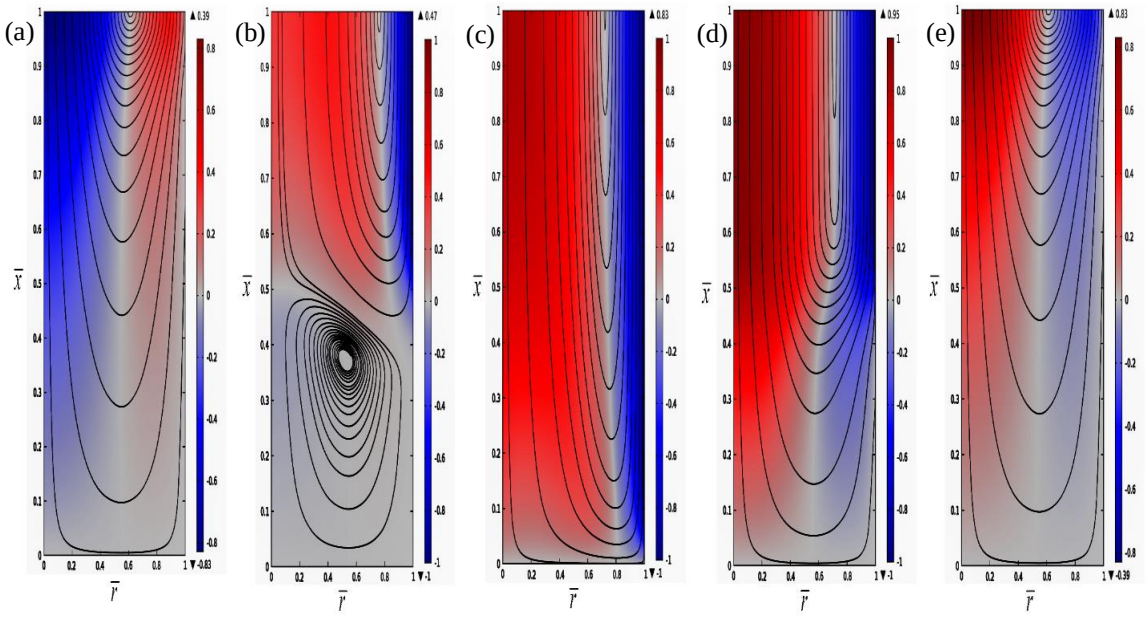

Figure 2.3. Instantaneous streamlines for the solenoidal velocity with $L = 1\text{m}$, $R = 50\mu\text{m}$, for the first half-cycle (rarefaction), starting with $t = 68\text{s}$. $\rho_i = 136.78\text{kg/m}^3$, $\rho_e = 132.68\text{kg/m}^3$, $\mu = 1.99\times10^{-5}\text{Pa}\cdot\text{s}$, $D_\rho = 4.82\times10^{-5}\text{m}^2/\text{s}$. Period $T = 0.0125\text{s}$. Color bars indicate velocity, negative values indicate gas flows into the tube. Flow rate at any cross-section is zero. (a) $t_0 = 68\text{s}$; (b) $t_0 = 68\text{s} + T/8$; (c) $t_0 = 68\text{s} + T/4$; (d) $t_0 = 68\text{s} + 3T/8$; (e) $t_0 = 68\text{s} + T/2$.

Thus, the solenoidal velocity does not contribute to the mass flow rate and the role of the solenoidal velocity is to enforce the no-slip condition on the tube wall for the overall velocity.

Figure 2.3 shows a sequence of the instantaneous streamlines for the solenoidal velocity for a tube with $L = 1\text{m}$, $R = 50\mu\text{m}$ during the first half-cycle of density oscillation (rarefaction) starting at $t = 68\text{s}$. In the figure, $\bar{r} = r/R$; $\bar{x} = x/L$. While the example is specifically for methane at pressure of 25 MPa and temperature at 80°C, the flow

characteristics remain qualitatively the same for common compressible fluids such as air at a lower pressure and temperature. The five instants shown are 1/8 period apart, starting from the beginning of the cycle. Red and blue colors correspond to positive and negative streamwise solenoidal velocities, respectively. At 1/8 period, a weak vortex appears near the end of the tube (figure 2.3b). However, as time increases, this vortex is squeezed towards the end of the tube and it disappeared altogether just before the 1/4 period mark (figure 2.3c). At the end of the half-cycle, the rarefaction wave has travelled back to the tube exit and the solenoidal velocities almost become the mirror images of those at the beginning of the cycle (figure 2.3e), with the fluid at the center portion of the tube moving out of the tube and in the near wall region moving into the tube. The acoustic wave turns around and travels inward as a compressive wave, with the stream-line patterns essentially being the reverse of the sequence shown in figure 2.3. It must be emphasized that these instantaneous streamlines correspond to the solenoidal velocity field, not the total velocity field.

Figure 2.4 shows the effect of tube size on the instantaneous streamlines of the solenoidal velocity field for $R = 100\mu m$, $50\mu m$, $30\mu m$, $10\mu m$ at the instant of 1/8 period. The corresponding instantaneous streamwise velocity profiles at the exit plane are shown in figure 2.5. It is observed that for large tubes ($100\mu m$, $50\mu m$, $30\mu m$), there is a weak vortex near the end of the tube to accommodate the no-slip condition at the end surface (figure 2.4a). This vortex becomes weaker as the tube radius is reduced. The vortex disappears (or is too weak to be plotted) when the radius is reduced to $10\mu m$ (figure 2.4d). For larger tubes, the streamwise solenoidal velocity $v'_{x,RT}$ is the classical Stokes solution driven by an oscillatory boundary ($100\mu m$ tube, figure 2.5). A Stokes boundary layer is formed near

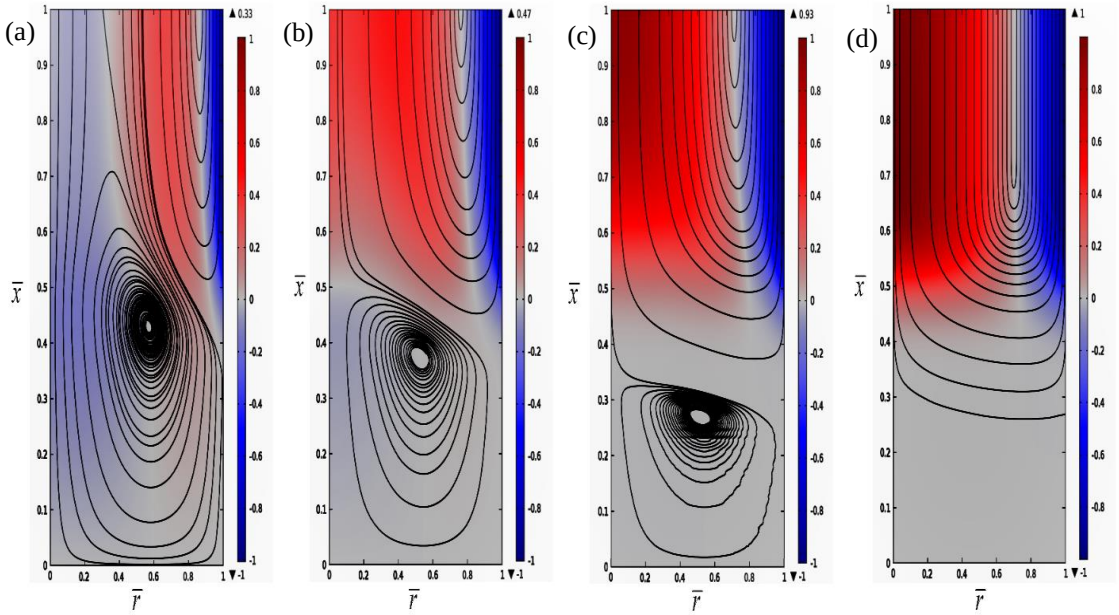

Figure 2.4. Effect of tube size. Streamlines for the solenoidal velocity field with length $L = 1\text{m}$ at time $t = 68\text{s} + T/8$, $T = 0.0125\text{s}$ is the period. (a) $R = 100\mu\text{m}$; (b) $R = 50\mu\text{m}$; (c) $R = 30\mu\text{m}$; (d) $R = 10\mu\text{m}$.

the tube wall, with a thickness of the order of $\delta_{St} \approx \sqrt{2\nu_e/\omega_0} = \sqrt{4L\nu_e/(\pi c)}$, which is independent of the radius and it is approximately $18\mu m$ for the cases shown in figure 2.5. As the tube radius is reduced, the ratio between the Stokes layer thickness and the radius becomes larger ($50\mu\text{m}$ tube, figure 2.5), as the Stokes layer occupies a larger portion of the tube, and the streamwise solenoidal velocity spreads over the entire tube cross-section for very small radii ($10\mu\text{m}$, $30\mu\text{m}$ tube, figure 2.5). Due to the reversal of $\text{v}'_{x,RT}$ discussed earlier, the centerline velocity is always in the opposite direction of the wall velocity. A consequence of the Stokes layer spreading over a larger portion of the tube is that the centerline velocity for the solenoidal velocity $\text{v}'_{x,RT}$ must increase in order to satisfy the condition of zero flux $Q_{RT}(x) = 0$. In the small radius limit, $\text{v}'_{x,RT}$ approaches a parabolic shape, with the centerline and wall velocity having the same magnitude but opposite signs (e.g. $10\mu\text{m}$ tube, figure 2.5).

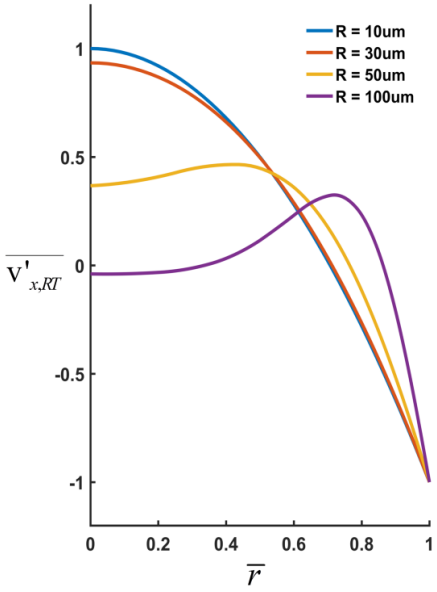

Figure 2.5. Dimensionless streamwise solenoidal velocity profile $\overline{v'_{x,RT}} = v'_{x,RT} / |v'_{x,IR}|$ at the tube exit, $\bar{r} = r / R$, from large tubes to smaller tubes, corresponding to the cases shown in figure 2.4. The Stokes layer occupies a larger portion of the tube as the radius is reduced.

2.5. Drainage rate and the mechanism of fluid production

Draining a compressible fluid from a small capillary with a sealed end is a process of transporting and subsequent extinguishment of the density perturbation initiated at the tube exit. Two transport mechanisms are involved: sonic transport by acoustic wave and diffusive transport by longitudinal density gradient. While the acoustic wave transmits the density perturbation, it also tends to maintain such a disturbance. It is the longitudinal diffusion that damps the acoustic wave and produces fluid drainage.

The instantaneous mass flow rate at the exit can be computed from the density profile by integrating the continuity equation

$$\dot{m}_e(t) = -\int_{Tube} \frac{\partial \rho'}{\partial t} dv = \frac{8R^2 L(\rho_i - \rho_e)}{\pi} \sum_{n=0}^{N_d} \frac{\exp(-\gamma_n t)}{(2n+1)^2} \left(\gamma_n \cos \omega_n t + \omega_n \sin \omega_n t\right) . \quad (2.21)$$

Thus, the mass flow rate oscillates in time and it experiences intervals of positive values (production) followed by negative values (suction) within each period of oscillation. Since the cycle starts from the production phase, a continuous amplitude decay in time ensures that there is a net positive mass production after each oscillation period. The drainage rate $\hat{\dot{m}}_e(t)$ is the period-averaged mass flow rate at the exit and it is given by

$$\hat{\dot{m}}_e(t) = \frac{1}{T}\frac{8(\rho_i - \rho_e)R^2 L}{\pi}\sum_{n=0}^{N_d}\frac{1-\exp(-\gamma_n T)}{(2n+1)^2}\exp(-\gamma_n t)\ . \tag{2.22}$$

When $t >> T$, the higher modes (large n) experience large exponential decays and their contributions to the drainage rate are negligible. The lower modes can be approximated by the leading term in the Taylor series expansion for $1-\exp(-\gamma_n T)$. Thus, the leading-order expression for the drainage rate is given by

$$\hat{\dot{m}}_e(t) = M_L\frac{D_\rho}{L^2}\sum_{n=0}^{N}\exp\left[-\frac{D_\rho(2n+1)^2\pi^2 t}{8L^2}\right], \tag{2.23}$$

where $M_L = \pi R^2 L(\rho_i - \rho_e)$ is the total amount of producible fluid from the capillary for a given density drop $\rho_i - \rho_e$; N is the cutoff integer so that $\gamma_n T = (2n+1)^2\pi^2 D_\rho / 2cL < 1$ for $n < N$ ($N \approx 10^3$ for $D_\rho \approx 10^{-5}\,\mathrm{m^2/s}$, $L = 1\,\mathrm{m}$). Since the period T for a meter-long tube is typically of the order of 0.01 second, the drainage rate expression (2.23) can be used virtually for all times of interest. A period-averaged drainage speed corresponding to the drainage rate can be defined as

$$V_e(t) = \frac{\hat{\dot{m}}_e(t)}{\rho_e \pi R^2} = \frac{\rho_i - \rho_e}{\rho_e}\frac{D_\rho}{L}\sum_{n=0}^{N}\exp\left[-\frac{D_\rho(2n+1)^2\pi^2 t}{8L^2}\right]. \tag{2.24}$$

Thus, fluid is drained from the capillary in an oscillatory huff-n-puff pumping process driven by the decay of the standing acoustic wave. On a time scale much larger than the

period of oscillation, the drainage rate $\hat{\dot{m}}_e(t)$ is determined by the slow diffusive time scale L^2/D_ρ and it is independent of the oscillation frequency. The drainage rate (2.23) is proportional to the diffusion coefficient $D_\rho = (\mu_b + 4\mu/3)/\rho_e$, which is related to the combined bulk and shear viscosities $\mu_b + 4\mu/3$, and the square of the tube radius R^2. If we set the bulk viscosity to zero as in Stokes' hypothesis, then the diffusion coefficient D_ρ is essentially the kinematic viscosity of the fluid. Thus, despite the overall velocity satisfying the no-slip condition on the capillary wall, the flow shows a slip-like mass flow rate which is also proportional to the fluid's kinematic viscosity. This is a fundamental departure from the classical Poiseuille's law which gives a drainage rate inversely proportional to the kinematic viscosity and proportional to the quartic power of the tube radius R^4. The proportionality of the drainage rate to the kinematic viscosity of the fluid is due to the fact that the drainage process is controlled by the diffusion of the density which has a diffusion coefficient proportional to the fluid's kinematic viscosity. The above findings can also be understood in terms of the velocity field: the solenoidal velocity does not contribute to the mass flow rate; and the irrotational velocity is uniform in any cross-section for the relaxed density profile which gives rise to the slip-like mass flow rate, even though the overall velocity does not slip on the tube wall.

The drainage speed $V_e(t)$ scales with the diffusive velocity scale D_ρ/L. This drainage speed is the average Lagrangian velocity for the fluid particles that have exited the tube during one period of oscillation, and it differs significantly from the instantaneous Eulerian velocity at the tube exit. The instantaneous velocity scales with $c(\rho_i - \rho_e)/\rho_e$, much faster than the drainage speed. Despite the high instantaneous velocity, however, the oscillation in the displacement of a fluid particle remains small during the period, in the

centimeter range for $L = 1\,\mathrm{m}$ and $D_\rho = 10^{-5}\,\mathrm{m}^2/\mathrm{s}$. An important property of the drainage speed (2.24) is that it is independent of the capillary radius. In other words, no matter how small a capillary is, a compressible fluid can escape the capillary with a finite speed, even though the mass flow rate might be small due to its R^2-dependence on the capillary radius. Poiseuille's law and the lubrication-type of theory, on the other hand, predict an average exit speed proportional to R^2 and inversely proportional to the shear viscosity, giving rise to an infinitesimally small exit velocity for very small capillaries.

A drain-out time can be defined as the instant when the accumulative produced fluid mass has reached 99% of the producible mass, and it is a measure of how fast a fixed amount of stored fluid is produced. This drain-out time computed from (2.23) is

$$t_d = 3.57 \frac{L^2}{D_\rho}. \tag{2.25}$$

The Poiseuille flow theory, on the other hand, gives a drain-out time proportional to the shear viscosity, $t_d \sim \mu$, instead of the inverse of viscosity as shown by (2.25).

Equations (2.23) and (2.25) show that a large diffusion coefficient D_ρ results in a large drainage rate as well as a small drain-out time. Contrary to intuition, a large drainage rate accompanied by a small drain-out time is actually beneficial for fluid production for drainage flows, as a fixed amount of fluid is produced in a shorter time. This characteristic is quite different from open-end tube flows for which maintaining a high drainage rate produces more fluids due to unlimited supply of fresh fluid from upstream. A conventional approach to slow viscous flow in confined geometries is to invoke the lubrication approximation which results in a Poiseuille-like mass flow rate and average velocity. The lubrication theory ignores all inertia terms and the longitudinal viscous diffusion in the

momentum equation and it ignores the longitudinal mode completely. While this approximation works well for incompressible displacement type of flows, the result above clearly indicates that lubrication theory is not suitable for volume-expansion driven drainage flow of a compressible fluid.

It must be emphasized that the fluid production mechanism revealed above differs significantly from that due to acoustic streaming (Friend & Yeo 2011). Acoustic streaming is a nonlinear inertial phenomenon; and for small density drops, the period-averaged streaming velocity is an order magnitude smaller than that from the current linear theory. In addition, the acoustic streaming velocity is time independent whilst the current theory gives rise to a decaying drainage speed which can be large at early times.

2.6. Numerical solution of the linearized equations and the exit boundary condition

To verify that a prescribed density value at the tube exit is a reasonable approximation to the real situation of a fluid drained into a large reservoir, numerical solutions of the *linearized* Navier-Stokes equations for a larger system consisting of a long narrow semi-sealed tube connected to a large exit reservoir are performed. The drained fluid from the tube enters the cylindrical reservoir at the tube–reservoir junction and exits the system at the far end of the large reservoir with the prescribed density ρ_e ; and the density at the tube-to-reservoir exit has to be found from the numerical solution. The tube has a length-to-radius ratio of $L/R = 1000$, and the reservoir has the same length as the tube but with a radius ranging from $100R$ to $800R$. For a micron-size tube, the reservoir radius will be of the order of $0.1 \sim 0.8mm$. Fluid properties are the same as those used for figure 2.3. The calculations are greatly simplified because of the Helmholtz decomposition, as the density

variation only appears in the longitudinal mode (irrotational field) which can be solved independently in the linearized theory. Specifically, the longitudinal mode equations are (Morse & Ingard 1968; Temkin 1981)

$$\frac{\partial \rho'}{\partial t} + \rho_e \nabla \cdot \mathbf{v}'_{IR} = 0 , \tag{2.26}$$

$$\rho_e \frac{\partial \mathbf{v}'_{IR}}{\partial t} = -c^2 \nabla \rho' + \left(\mu_b + \frac{4}{3}\mu \right) \nabla (\nabla \cdot \mathbf{v}'_{IR}) , \tag{2.27}$$

$$\mathbf{v}'_{IR} = \nabla \Phi . \tag{2.28}$$

For the longitudinal mode, the no-penetration condition is imposed on the solid walls so that the normal component of $\mathbf{v}'_{IR}$ vanishes on the wall. Initially, $\rho' = \mathbf{v}'_{IR} = 0$. The numerical calculations for the longitudinal mode are implemented with the linearized Navier-Stokes solver in COMSOL.

As expected, upstream from the tube exit, density is uniform over the tube cross-section (figure 2.6). As the fluid moves towards the tube exit, the density becomes non-uniform in the cross-section, indicative of the exit effect. At the tube exit, the maximum deviation of the density from ρ_e is defined as $\Delta\rho_{out}$, which changes with time and it can be positive or negative due to oscillation. This maximum density deviation is normalized against $\rho_i - \rho_e$ and plotted against the normalized time t/T for various sizes of the reservoir in figure 2.7. Figure 2.7 shows that the maximum density deviation at the tube exit becomes independent of the reservoir size when the reservoir radius is greater than $100R$. In addition, the maximum density deviation decreases with time. The maximum of the absolute value of $\Delta\rho_{out}$ in each period normalized with $\rho_i - \rho_e$, $\left(\max\left|\Delta\rho_{out}\right|\right)_{Period} / (\rho_i - \rho_e)$, is a measure of the maximum relative error in approximating the tube exit density as ρ_e (or, approximating

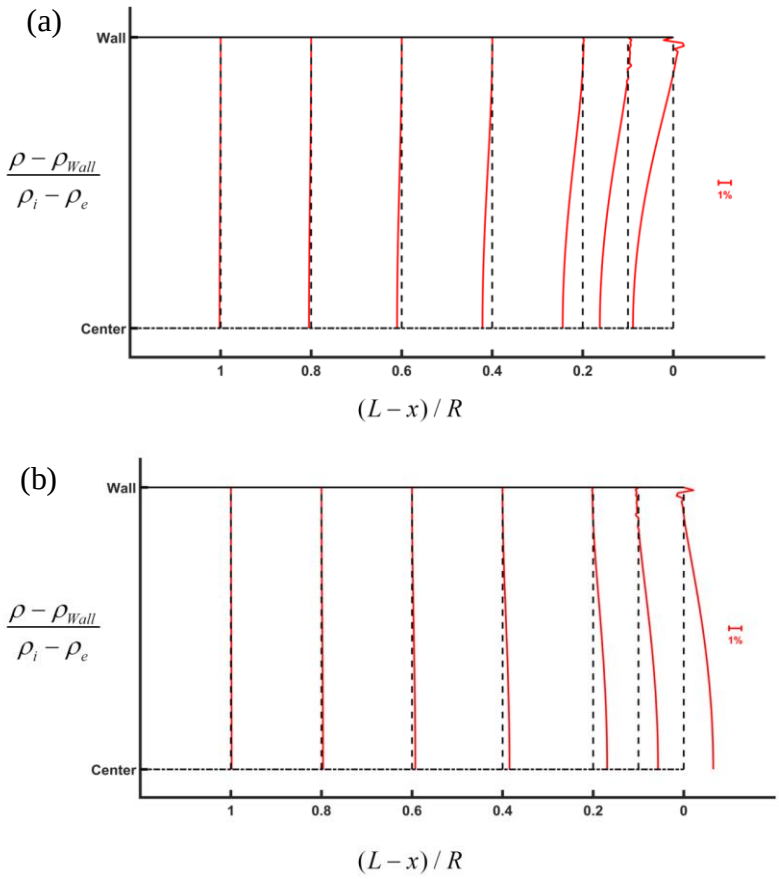

Figure 2.6. Normalized local density difference $(\rho-\rho_{wall})/(\rho_i-\rho_e)$ at various tube cross-sections upstream the tube exit (solid lines). The dashed lines are for $\rho-\rho_{wall}=0$ and the scale bar is the percentage deviation from the dashed lines. "Center" and "Wall" refer to the centerline and the wall of the tube. (a) At one-half period; (b) At one period.

ρ' as zero at the tube exit). This maximum relative error is plotted against t/T for a reservoir with a radius of $300R$ in figure 2.8. Clearly, this maximum error decreases quickly from approximately 3.5% in the early times to just 0.5% after about 25 periods. Since our interest is for large exit reservoir (compared to the narrow tube) and drainage rate at times much larger than the oscillation period, $t \gg T$, ignoring the exit reservoir and approximating the density at the tube exit as ρ_e is justified. Furthermore, figure 2.6 indicates that the exit length is also small, about one tube radius for the case considered.

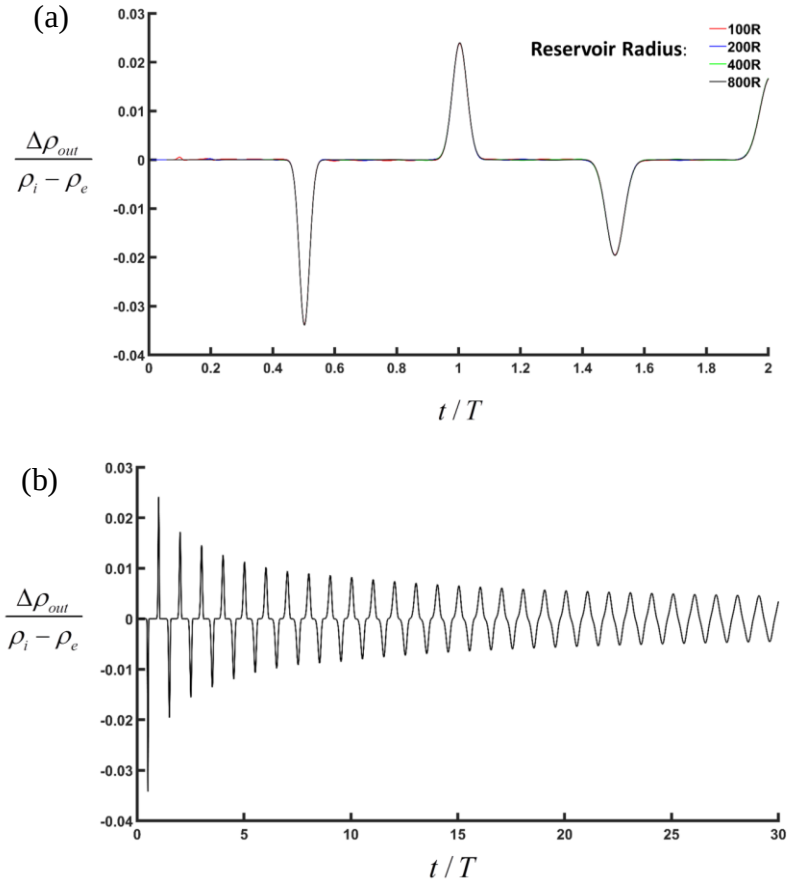

Figure 2.7. (a) Normalized density deviation $\Delta\rho_{out}/(\rho_i - \rho_e)$ at the tube exit as a function of time for various large reservoirs. These curves essentially coincide with each other when the reservoir has a radius greater than $100R$. (b) Normalized density deviation a reservoir with a radius of $300R$ covering a wider range of times.

Numerical solutions are also carried out for a tube with a prescribed density ρ_e at the tube exit in the absence of an exit reservoir. Figure 2.9 compares the numerically computed normalized instantaneous mass flow rate at the exit $\tilde{\dot{m}}_e = \dot{m}_e L^2 / M_L D_\rho$ with that from the analytical solution (2.22) against the dimensionless time on the diffusive time scale, $\bar{t} = D_\rho t / L^2$. Excellent agreements between the analytical solution and the numerical computation are achieved.

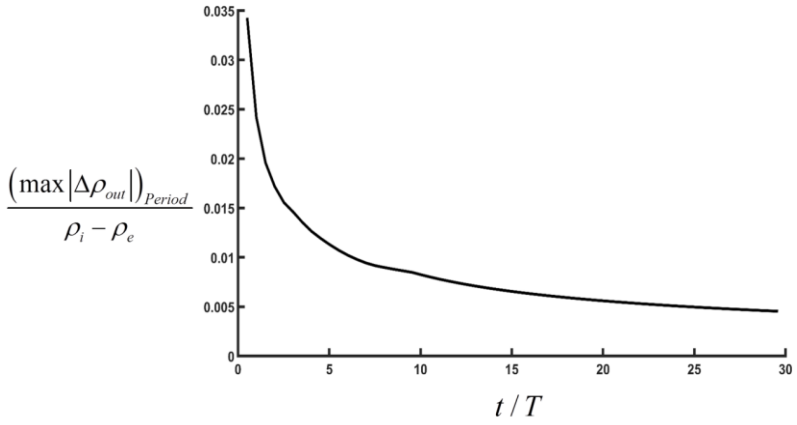

Figure 2.8. Maximum relative error $\left(\max\left|\Delta\rho_{out}\right|\right)_{Period}/(\rho_i-\rho_e)$ in approximating the tube exit density ρ_e as a function of time.

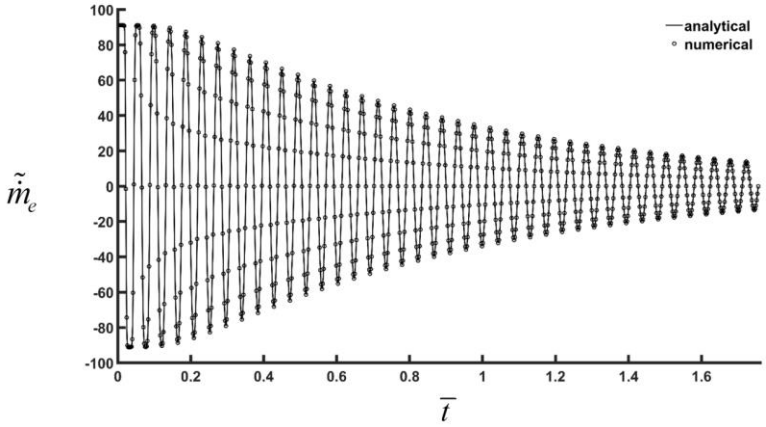

Figure 2.9. Comparison of dimensionless instantaneous mass flow rates between numerical solution and analytical solution. There is no exit reservoir and the exit density is fixed. The dimensionless time $\bar{t}=D_\rho\, t/L^2$ is measured in terms of the long-time diffusive time scale.

2.7. Diffusion equation and capillary with an absorbing end

The envelope of the density oscillation (2.19) is diffusive,

$$\rho_{EVL}(r,x,t)=\rho_e+\frac{4(\rho_i-\rho_e)}{\pi}\sum_{n=0}^{N_d}\frac{(-1)^n}{2n+1}e^{-\gamma_n t}\cos\frac{(2n+1)\pi x}{2L}. \qquad (2.29)$$

The density envelope is plotted in figure 2.10, with the dimensionless time $\bar{t}=D_\rho t/L^2$.

This envelope solution corresponds to the density change on the large diffusive time scale

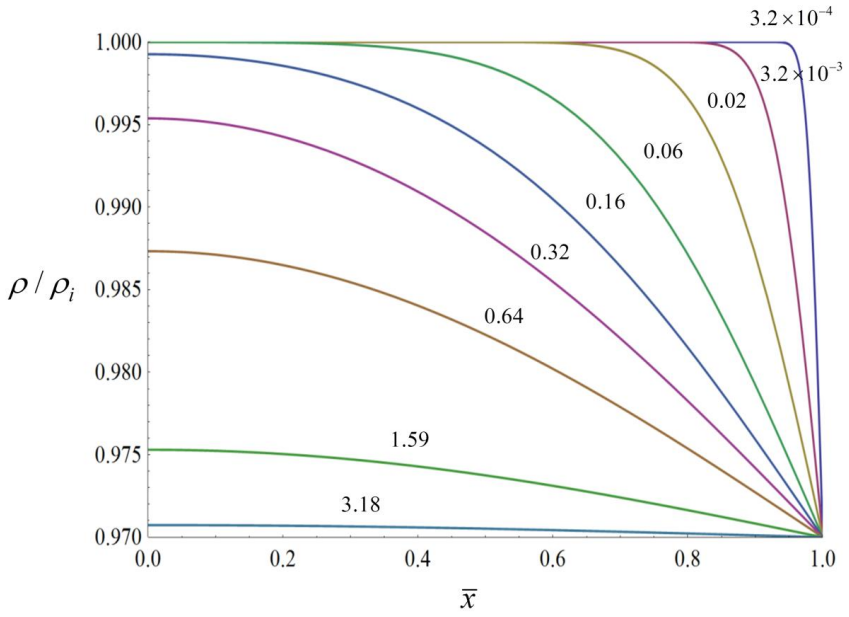

Figure 2.10. Diffusive decay of the density envelope. $D_\rho = 4.82\times10^{-5}\,\mathrm{m}^2/\mathrm{s}$. The numbers above each curve is the dimensionless time $\bar{t}$.

L^2 / D_ρ when the fast oscillation in density has been smoothed out by integrating over the oscillation period.

The solution discussed so far assumes that the surface of the sealed end at $x = 0$ is a perfect reflecting surface for sound waves, with the reflection coefficient $\Re = 1$. If, on the other hand, the surface of the sealed end is non-reflecting, $\Re = 0$, then the rarefaction wave will not be reflected by the sealed end at all. Thus, there will be no standing acoustic wave sloshing around inside the tube. The longitudinal propagation of the density perturbation is then controlled by pure diffusion shortly after the sound wave has reached the end of the tube. In other words, the damped wave equation for the density perturbation degenerates to the corresponding diffusion equation after a very short time,

$$\frac{\partial \rho'}{\partial t} = D_\rho \nabla^2 \rho' . \tag{2.30}$$

The corresponding relaxed density solution is then (Carslaw & Jaeger 1959)

$$\rho(x,t) = \rho_e + \frac{4(\rho_i - \rho_e)}{\pi} \sum_{n=0}^{\infty} \frac{(-1)^n}{2n+1} e^{-\frac{D_\rho (2n+1)^2 \pi^2}{4L^2} t} \cos \frac{(2n+1)\pi x}{2L}. \tag{2.31}$$

The drainage rate becomes

$$\hat{\dot{m}}_{e,diff}(t) = M_L \frac{2D_\rho}{L^2} \sum_{n=0}^{N} e^{-\frac{D_\rho (2n+1)^2 \pi^2 t}{4L^2}}. \tag{2.32}$$

Compared to the case of a reflecting sealed end equation (2.23), the drainage rate is twice as large but the exponents of exponential rate of decay are also twice as large. Thus, fluid is drained from the tube at a faster rate. This is due to the fact that the density in the tube approaches the equilibrium density much faster, as there is no wave motion to help maintaining the density perturbation in the tube. The drainage rates (2.23) and (2.32) both satisfy the condition $\int_0^\infty \hat{\dot{m}}_e(t)dt = M_L$. It is thus observed that even though the drainage rate is controlled by the diffusion of the density perturbation, ignoring the existence of the acoustic wave and using the purely diffusive equation (2.30) from the outset for the case of a perfect reflecting end will lead incorrectly to the drainage rate (2.32) instead of (2.23). When there is a standing acoustic wave inside the capillary, fluid drainage is controlled by the decay of the wave amplitude, or the envelope of the wave. The density envelope equation is not the same as the diffusion equation (2.27); and it can be derived from the damped wave equation (2.3) by the method of multiple scales (Bender & Orszag 1978). The fast time scale is associated with the acoustic wave, $t_F = L/c$, and the slow time scale is associated with diffusion, $t_S = L^2/D_\rho$, with the ratio $\varepsilon = t_F/t_S = D_\rho/cL \ll 1$. Thus, the dimensionless damped wave equation using the fast time scale becomes

$$\frac{\partial^2 \bar{\rho}}{\partial \bar{t}^2} = \left(1 + \varepsilon \frac{\partial}{\partial \bar{t}}\right) \bar{\nabla}^2 \bar{\rho}\,, \tag{2.33}$$

where $\bar{\rho} = \rho' / \rho_e$, $\bar{t} = t / t_F$. Introducing a slow time variable $\bar{\tau} = \varepsilon \bar{t}$ and expanding $\bar{\rho}$,

$$\bar{\rho} = \bar{\rho}_0(\mathbf{x}, \bar{t}, \bar{\tau}) + \varepsilon\, \bar{\rho}_1(\mathbf{x}, \bar{t}, \bar{\tau}) + \ldots \tag{2.34}$$

leads to the equations at the following orders:

$$O(1): \frac{\partial^2 \bar{\rho}_0}{\partial \bar{t}^2} = \bar{\nabla}^2 \bar{\rho}_0\,; \tag{2.35}$$

$$O(\varepsilon): \frac{\partial^2 \bar{\rho}_1}{\partial \bar{t}^2} - \bar{\nabla}^2 \bar{\rho}_1 = \frac{\partial}{\partial \bar{t}} \bar{\nabla}^2 \bar{\rho}_0 - 2 \frac{\partial^2 \bar{\rho}_0}{\partial \bar{t}\, \partial \bar{\tau}}\,; \tag{2.36}$$

The leading-order equation is a wave equation which admits wave solution of the form $\bar{\rho}_0 = \bar{H}(\mathbf{x}, \bar{\tau}) \exp(-i\omega \bar{t})$ with $\bar{H}(\mathbf{x}, \bar{\tau})$ being the envelope. To avoid secular growth for $\bar{\rho}_1$, the forcing term in (2.36) must vanish, leading to the envelope equation

$$\frac{\partial \bar{H}}{\partial \bar{\tau}} = \frac{1}{2} \bar{\nabla}^2 \bar{H}\,, \tag{2.37}$$

which when restored to dimensional form becomes

$$\frac{\partial H}{\partial t} = \frac{D_\rho}{2} \nabla^2 H\,. \tag{2.38}$$

Thus, the density envelope diffuses with a diffusion coefficient $D_\rho / 2$, not D_ρ. This confirms the density envelope solution (2.29) and it explains the origin of the discrepancy between the drainage rates from the damped wave equation $\hat{\dot{m}}_e(t)$ and the purely diffusive equation $\hat{\dot{m}}_{e,diff}(t)$, with the latter being incorrect when the sealed end is sound reflecting. This analysis also shows that the presence of the acoustic wave retards the diffusion of the density disturbance by reducing the diffusion coefficient by one half. The effect of this retardation is the doubling of the drain-out time from that of the purely diffusive process.

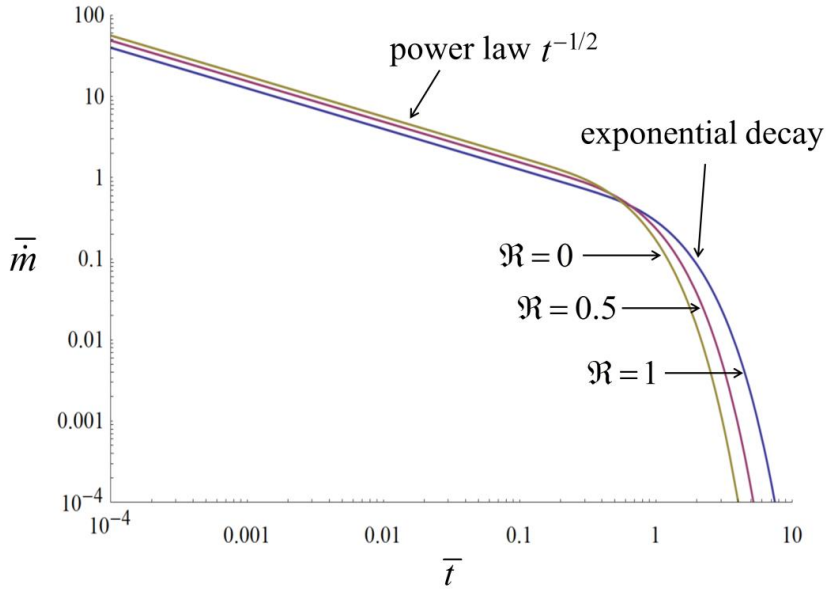

Figure 2.11. Dimensionless drainage rate vs. dimensionless time for various values of the reflection coefficient.

An absorbing surface has a reflection coefficient in the range $0 < \Re < 1$. Thus, the two cases discussed so far can be considered as corresponding to the slowest drainage (perfect reflecting) and the fastest drainage (purely diffusive), respectively. In general, we expect the density perturbation to be similar to (2.19), but with spatially decaying amplitudes. This situation is complicated as the reflection coefficient $\Re$ is generally frequency dependent. However, if the reflection coefficient can be approximated as independent of frequency and we are not interested in the details of the wave motion, we can then simply model the drainage rate for a capillary with an absorbing end as

$$\hat{\dot{m}}_e(t) = M_L \frac{(2-\Re)D_\rho}{L^2} \sum_{n=0}^{N} e^{-\frac{(2-\Re)D_\rho (2n+1)^2 \pi^2 t}{8L^2}} . \tag{2.39}$$

Dimensionless drainage rate $\bar{\dot{m}}_e$ and dimensionless drainage speed $\bar{V}_e(t)$ can be defined as

$$\bar{\dot{m}}_e = \frac{\hat{\dot{m}}_e L^2}{M_L D_\rho} = (2-\Re)\sum_{n=0}^{N} \exp\left[-\frac{(2-\Re)(2n+1)^2 \pi^2 \bar{t}}{8}\right], \tag{2.40}$$

$$\bar{V}_e(t) = \frac{V_e(t) L}{D_\rho} = \frac{\rho_i - \rho_e}{\rho_e}(2-\Re)\sum_{n=0}^{N} \exp\left[-\frac{(2-\Re)(2n+1)^2 \pi^2 \bar{t}}{8}\right], \tag{2.41}$$

where the dimensionless time $\bar{t} = D_\rho\, t / L^2$. Figure 2.11 shows the dimensionless drainage rate $\bar{\dot{m}}_e$ (which is independent of radius) vs. the dimensionless time $\bar{t}$ for various values of $\Re$. The areas underneath these curves are all unity, reflecting the fact that the same amount of fluid is drained. The non-reflecting end ($\Re = 0$) has the highest drainage rate and the shortest drain-out time.

2.8. Mechanism of fluid production from the nanopores of shale

In recent years, oil and gas production from shale has dramatically changed the energy landscape of the world. Compared to conventional sandstone and limestone reservoirs, a large percentage of the pores in shale are very small, with diameters in the 10-100 nm range (Hill et al. 2000; Nelson 2009; Hughes 2013). These nano-size pores result in extremely low permeability for the shale matrix, typically in the range of 0.1 microdarcy to a few nanodarcy ($1\,nd \approx 10^{-21} m^2$) versus the minidarcy ($1\,md \approx 10^{-15} m^2$) range for conventional reservoirs. Recent success in commercial shale production is driven by the technological advances in horizontal well drilling and multistage hydraulic fracturing. A horizontal well exposes the wellbore to a large formation volume while multistage hydraulic fracturing creates a highly interconnected fracture network that breaks the shale formation into small blocks of meter size. Such a small block size significantly reduces the distance fluid has to

travel from the matrix block where it is stored to the high conductivity fracture network where it can move with a much greater speed to the wellbore.

Even after hydraulic fracturing, fluid still has to first travel from the ultra-tight nanopores of a matrix block to the surrounding fractures before it can move to the wellbore. Darcy's law (Bear 1988) predicts that it takes methane over 70 years to migrate just one meter for 100-nanodarcy permeability and a large pressure gradient of 2 kPa per meter. Shale oil production is even more unimaginable due to oil's high viscosity. Reconciling such a dire prediction with the reality of booming shale production has been a huge challenge for the scientific community (Javadpour 2009; Clarkson 2013; Rassenfoss 2015; Cipolla et al. 2010; Wang et al. 2015). Recent studies have been focused on gas transport through nano-scale capillaries and these studies are essentially modifications to the Poiseuille's law and Darcy's law. The popular slip theory believes that gas slips in nano-size capillaries and the slippage enhances flow rate (Javadpour 2009; Clarkson 2013, Ertekin et al. 1986; Beskok & Karniadakis 1999; Javadpour et al. 2007; Civan 2010; Civan et al. 2011; Darabi et al. 2012; Mehmani et al. 2013; Lunati & Lee 2014). This theory, however, is based on rarefied gas dynamics and the kinetic theory for dilute gas (Tsien 1946; Karniadakis et al. 2005; Islam & Patzek 2014); but natural gas is a supercritical fluid with high density in typical shale reservoir conditions (21MPa and above) (Nasrifar & Bolland 2006). The commonly used classification of slip flow regime for Knudsen number in the range $0.001 < Kn < 0.1$ can be misleading, since slip is *inferred* from measured mass flow rate being higher than that given by Poiseuille flow (Beskok & Karniadakis 1999). As shown by the work reported here and elsewhere (Chen & Shen 2018a), compressible Navier-Stokes equations can admit solutions with a no-slip velocity but a slip-like mass flow rate higher than that given by

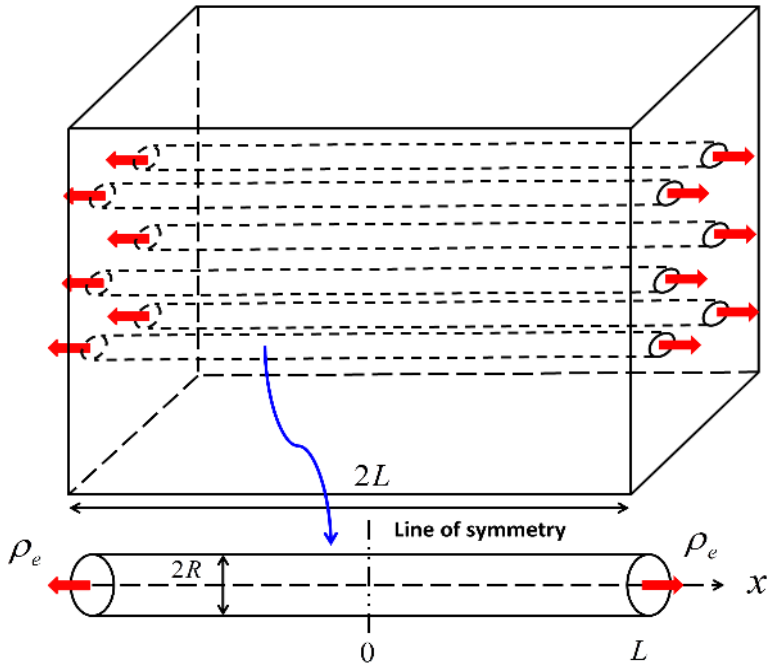

Figure 2.12. Symmetric drainage from a capillary tube embedded in a shale matrix block surrounded by fractures. The capillary has an inner radius R and it penetrates through the entire block of length $2L$. The flow is symmetric about $x = 0$.

Poiseuille flow. Slip may occur for gas in extremely small capillaries less than 10nm in diameter when the pressure is below 10MPa (Javadpour 2009). These extremely small pores, however, are associated with the organic matters that store gas in adsorbed phase; and compared to the dominant larger inorganic pores, they hold very little free-gas which is the gas produced in the first year or two. Desorption is a much slower process and there is no evidence suggesting that adsorbed gas has been produced in the first year (Cipolla et al 2010; Wang et al. 2015). Furthermore, a recent study shows that these extremely small organic nanopores actually trap oil and gas molecules instead of allowing them to flow (Bousige et al. 2016). Together, high gas pressure, little free gas stored in the smallest pores and the trapping effect of the organic pores make wall slip highly questionable as the mechanism responsible for the observed high shale gas production rate. Additionally, no

theory has been proposed to explain why oil can also be produced abundantly from the ultra-tight shale matrix. So far, fluid production from shale has defied explanation from fluid dynamics theory (Rassenfoss 2015).

The single most fundamental problem for shale production is the drainage flow from the meter-size matrix blocks to the surrounding fractures. Such a drainage flow is driven solely by the volumetric expansion of the compressed fluid stored in the nanopores. To explore a unified physical mechanism for both liquid and gas production, here the simplest of such a drainage flow at the pore-scale is studied: the volume-expansion-driven drainage flow of a single phase compressible fluid from a small capillary tube embedded in a matrix block with its ends open to the surrounding fractures (figure 2.12).

2.8.1. Drainage flow from a capillary tube to the surrounding fractures

A straight capillary embedded in a typical shale matrix block has an inner radius R and length $2L$, with the two ends connected directly to the fractures on the sides of the block (figure 2.12). Pressure-depletion induced deformation of the shale matrix on the fluid production occurs on a time scale comparable to the production time scale of the reservoir. Therefore, the shale matrix can be treated as rigid during the early production period. The fluid stored in the tube can be gas or liquid and it is initially at rest with a density ρ_i. The fluid is drained symmetrically from both ends of the tube upon lowering the density at the ends to ρ_e. Fluid in the fractures is maintained at the density ρ_e at all times thereafter. In practice, in order to maintain the mechanical integrity of the matrix block and the adjacent fractures, the exit density (or pressure) is lowered gradually by multiple small steps during production. In each step, the density perturbation can be considered as small and

temperature variation is negligible (small Mach number). Since the capillary is small, and the Mach number is also small, nonlinear inertial effect can be neglected (Morse & Ingard 1968). Gravitational effect is negligible. Thus, the continuity (equation 2.1) and the linearized compressible Navier-Stokes equations (equation 2.2) can be applied to the shale drainage flow system. Rewriting the equations below.

$$\frac{\partial \rho'}{\partial t} + \rho_e \nabla \cdot \mathbf{v}' = 0\,, \tag{2.1}$$

$$\rho_e \frac{\partial \mathbf{v}'}{\partial t} = -\nabla p' + \left(\mu_b + \frac{1}{3}\mu \right) \nabla(\nabla \cdot \mathbf{v}') + \mu \nabla^2 \mathbf{v}'\,, \tag{2.2}$$

Equation (2.2) is justified under acoustic scaling and low Mach number assumption. Because the bulk viscosity is proportional to the relaxation times for the internal modes, to consider the case of large bulk viscosity, the molecular relaxation time of the fluid must be allowed to be large, and there is the possibility that the flow may not be in equilibrium. To ensure that the Navier-Stokes equations are valid, we must require the flow to be near equilibrium, which can be characterized by the condition that the characteristic time for the flow being much larger than the characteristic molecular relaxation time. This requirement is referred to as the local thermodynamic equilibrium (LTE) by Graves & Argrow 1999. Using equation (30) in Cramer (2012), the relaxation time for the vibrational modes for methane at temperature of 300 K and pressure of 1 MPa is about $10^{-7} s$; while the time scale for an acoustic wave in a one-meter block is about $10^{-3} s$ Thus, the local thermodynamic equilibrium condition is satisfied and the use of the Navier-Stokes equations for large bulk viscosity is justified.

By taking the divergence of equation (2.2), using $p' = c^2 \rho'$ and then eliminating velocity from equations (2.1) and (2.2). The damped wave equation for the density perturbation (equation 2.3) could be derived. Rewriting the equations below.

$$\frac{\partial^2 \rho'}{\partial t^2} = \left(c^2 + D_\rho \frac{\partial}{\partial t} \right) \nabla^2 \rho', \tag{2.3}$$

It must be emphasized that this damped wave equation for the density is exact as long as the linearized continuity and Navier-Stokes equations (2.1) and (2.2) hold; and this fundamental equation is well known in the acoustic community (see equation (6.4.22), p282 in Morse & Ingard 1968). Equation (2.3) includes the full viscous effect on the density change. It is also observed that if the wave effects can be neglected, the damped wave equation (2.3) is reduced to a diffusion equation for the density disturbance, with a diffusion coefficient D_ρ. If bulk viscosity is set to zero, as in the Stokes hypothesis, then the density diffusion coefficient for the density disturbance is just the kinematic viscosity of the fluid.

Because of the symmetry about $x = 0$, only one-half of the tube needs to be considered. The end conditions and the initial conditions for the density perturbations are identical to section 2.2, because a symmetric end gives same density boundary condition as a sealed end (Neumann boundary). Again, no wall boundary for the density needs specify as it is determined by the solution itself (section 2.2). Thus, by solving the same initial-boundary-value problem could using the linearized compressible Navier-Stokes equation with no-slip condition (section 2.2−2.3), one could obtain same analytical solutions for the density perturbation equation (2.16), its transversely relaxed solution (2.19), and the irrotational velocity equation (2.20), for this pore-scale shale production problem.

2.8.2. Rotational velocity profile with symmetric end

With symmetric end boundary condition, analytical solutions for the solenoidal velocity fields can be obtained through solving the stream-function and vorticity equation, implementing no-slip wall condition equation (2.6) and axisymetric/symmetric boudnary condition at the tube/channel center.

$$
\begin{aligned}
&\mathrm{v}'_{\mathrm{x},RT}(x,r,t) = \frac{2}{L}\frac{\rho_i-\rho_e}{\rho_e}\sum_{n=0}^{\infty}\frac{(-1)^n}{\sigma_n^2}RE\left[\left(\frac{F_n(r)}{F_n(R)}+\frac{G_n(r)}{rF_n(R)}\right)\Omega_n e^{\Omega_n t}\right]\sin\sigma_n x \\
&\mathrm{v}'_{r,RT}(x,r,t) = -\frac{2}{L}\frac{\rho_i-\rho_e}{\rho_e}\sum_{n=0}^{N_d}\frac{(-1)^n}{\sigma_n}RE\left[\frac{G_n(r)}{F_n(R)}\Omega_n e^{\Omega_n t}\right]\cos\sigma_n x \\
&G_n(r) = J_1\left(\tilde{\sigma}_n r\right) - \frac{J_1\left(\tilde{\sigma}_n R\right)}{J_1\left(\tilde{\eta}_n R\right)}J_1\left(\tilde{\eta}_n r\right) \\
&F_n(r) = G_n'(r) = \frac{\tilde{\sigma}_n}{2}\left[J_0\left(\tilde{\sigma}_n r\right)-J_2\left(\tilde{\sigma}_n r\right)\right] - \frac{J_1\left(\tilde{\sigma}_n R\right)}{J_1\left(\tilde{\eta}_n R\right)}\frac{\tilde{\eta}_n}{2}\left[J_0\left(\tilde{\eta}_n r\right)-J_2\left(\tilde{\eta}_n r\right)\right] \\
&\Omega_n = -\gamma_n + i\omega_n;\ \ \nu_e = \frac{\mu}{\rho_e} \\
&\sigma_n = \frac{(2n+1)\pi}{2L};\ \ \tilde{\sigma}_n = i\sigma_n;\ \ \tilde{\eta}_n = i\sqrt{\sigma_n^2+\frac{\Omega_n}{\nu_e}}
\end{aligned}
\qquad . \quad (2.42)
$$

Since $\nabla\cdot\mathbf{v}'_{RT}=0$, integration of this incompressible condition over the capillary cross-section shows that the volumetric flow rate from the solenoidal velocity $Q_{RT}(x)=\text{constant}=Q_{RT}(0)=0$, for symmetric draining. Thus, the role of the solenoidal velocity is to enforce the no-slip condition on the tube wall for the overall velocity and it has no effect on the drainage rate.

2.8.3. Asymptotic transformation and overall velocity profile

For large tubes, the stream-wise solenoidal velocity $\mathrm{v}'_{x,RT}$, computed from the stream-function solution, is the classical Stokes solution driven by an oscillatory boundary. As the

tube radius is reduced, the Stokes layer occupies a larger portion of the tube. In the small radius limit, $\mathrm{v}'_{x,RT}$ has the asymptotic expression.

$$\begin{aligned}\mathrm{v}'_{x,RTasy,tube} &= \mathrm{v}'_{x,IR}\left[\left(1-2\frac{r^2}{R^2}\right)+O\left(\frac{cR^2}{\nu_e L}\right)\right] \\ &= \left(2\frac{r^2}{R^2}-1\right)\frac{2}{L}\frac{\rho_i-\rho_e}{\rho_e}\sum_{n=0}^{N_d}\frac{(-1)^n}{\sigma_n^2}RE\left[\Omega_n e^{\Omega_n t}\right]\sin\sigma_n x+O\left((\frac{R}{L})^2\right)\end{aligned}, \quad (2.43)$$

where $$RE\left[\Omega_n e^{\Omega_n t}\right] = e^{-\gamma_n t}\left(\gamma_n\cos\omega_n t+\omega_n\sin\omega_n t\right).$$

For $L=1m$ and shale oil and gas (with typical property values listed in the Appendix), $\mathrm{v}'_{x,RT}$ can be very well approximated by the above parabolic profile for tube radius below $1\,\mu m$. The overall stream-wise velocity in the small radius limit is

$$\mathrm{v}'_x = \frac{16L}{\pi^2}\frac{\rho_i-\rho_e}{\rho_e}\left(1-\frac{r^2}{R^2}\right)\sum_{n=0}^{N_d}\frac{(-1)^n\exp(-\gamma_n t)}{(2n+1)^2}\left(\gamma_n\cos\omega_n t+\omega_n\sin\omega_n t\right)\sin\frac{(2n+1)\pi x}{2L}. \quad (2.44)$$

which is parabolic and satisfies the no-slip condition on the wall. This parabolic velocity profile, however, differs significantly from that of a Poiseuille flow: the centerline velocity is independent of the tube radius; whilst the centerline velocity of a Poiseuille flow is proportional to R^2. Furthermore, the velocity is not inversely proportional to shear viscosity as in a Poiseuille flow.

2.8.4. Mechanism of fluid production from the capillary tube

The instantaneous mass flow rate at the tube exit $\dot{m}_e(t)$ can be calculated by either integrating the density perturbation time derivate over one-half of the tube (equation 2.6 with half-tube integral), or by integrating the irritation velocity profile over the capillary cross-section. As equation (2.21) shown in section 2.5, $\dot{m}_e(t)$ oscillates in time with a

frequency of $\omega_0 = \pi c / 2L$, generally in the range over 100 Hz for shale oil and gas when $L = 1m$. The drainage rate $\hat{\dot{m}}_e(t)$ is the period-averaged net mass flow rate which is also the mass decrease in the tube per period divided by the period T $(= 4L/c)$. By taking the Taylor series expansion for $1 - \exp(-\gamma_n T)$, the leading order term can be used as an approximation for the drainage rate for $t >> T$ (equation 2.23).

$$\hat{\dot{m}}_e(t) = M_L \frac{D_\rho}{L^2} \sum_{n=0}^{N} \exp\left[-\frac{D_\rho (2n+1)^2 \pi^2 t}{8L^2} \right], \tag{2.23}$$

Since the period T for a meter-size block is typically of the order of 0.01 second, the drainage rate expression (2.23) can be used virtually for all times of interest to fluid production from shale. As the period-averaged drainage speed corresponding to the drainage rate defined in equation (2.24),

$$V_e(t) = \frac{\hat{\dot{m}}_e(t)}{\rho_e \pi R^2} = \frac{\rho_i - \rho_e}{\rho_e} \frac{D_\rho}{L} \sum_{n=0}^{N} \exp\left[-\frac{D_\rho (2n+1)^2 \pi^2 t}{8L^2} \right], \tag{2.24}$$

an outstanding feature of the drainage speed is discovered that it is independent of the capillary radius. In other words, regardless how small a shale pore is, a compressible shale fluid, gas or liquid, can escape the small pore with a finite speed, even though the mass flow rate might be small due to its R^2 dependence on the capillary radius. Poiseuille's law, on the other hand, predicts an average exit speed proportional to R^2 and inversely proportional to the shear viscosity, giving rise to an infinitesimally small exit velocity for very small capillaries.

Once the producible fluid mass M_L is given, the diffusion coefficient D_ρ is the only fluid property that the drainage rate $\hat{\dot{m}}_e(t)$ depends on. D_ρ is related to the bulk viscosity μ_b. It is well recognized that Stokes' hypothesis of zero bulk viscosity is only valid for

dilute monatomic gas (Graves & Argrow 1999; Rajagopal 2013). The bulk viscosity for a liquid is generally of the same order of magnitude as its shear viscosity. On the other hand, the bulk viscosity of a polyatomic gas increases with temperature and it can become several orders of magnitude higher than its shear viscosity in a wide temperature range (Graves & Argrow 1999, Cramer 2012; Li et al. 2017). In particular, the bulk viscosity for methane, the dominant component of natural gas, is estimated to be 320 times of its shear viscosity at $80^0 C$ (Cramer 2012), a temperature typical for shale. At $80^0 C$ and a pressure of 25MPa, the diffusion coefficients for gas and oil are of the same order of magnitude, $D_\rho = 4.82\times10^{-5}\text{m}^2/\text{s}$, and $D_\rho = 8.43\times10^{-6}\text{m}^2/\text{s}$, respectively; and they differ only by a multiple of 5.72 (appendix A). Thus, we conclude that viscous oil can be produced from small capillaries as efficiently as gas, even though their shear viscosities differ by at least two orders of magnitude.

The scaled drainage rate $\hat{\dot{m}}_e(t)/M_L$ is independent of tube radius and it is plotted against time on log-log scale in figure 2.13 for shale oil and gas. In early times, these drainage rates are two-orders of magnitude higher than those given by the Poiseuille's law. The straight-line portion of the curves corresponds to a power law for the drainage rate $\hat{\dot{m}}_e(t) \approx t^{-1/2}$, typical for diffusive transport. The power law ends when the density diffusion front reaches $x = 0$; thereafter the drainage rate decays exponentially to zero. A drain-out time t_d, defined as the instant when the accumulative produced fluid mass has reached 99% of the producible mass, can be used to measure how fast a fixed amount of stored fluid is produced. This drain-out time computed from (2.23) is

$$t_d = 3.57\frac{L^2}{D_\rho}. \tag{2.25}$$

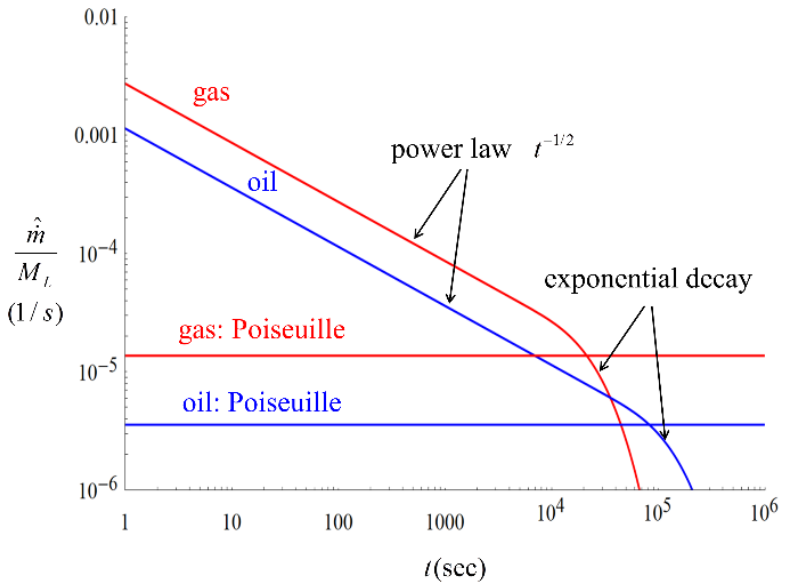

Figure 2.13. Log-log plot of $\hat{m}_e(t)/M_L$ vs time for shale oil and gas for $L=1\,\text{m}$. $\hat{m}_e(t)/M_L$ is independent of radius. the poiseuille's law result is for radius of $10nm$. Gas: $\mu=1.99\times10^{-5}\,\text{Pa}\cdot\text{s}$, $\mu_b=320\mu=6.368\times10^{-3}\,\text{Pa}\cdot\text{s}$, $\rho_i=136.78\text{kg/m}^3$, $\rho_e=132.68\text{kg/m}^3$. $c=584m/s$, $D_\rho=4.82\times10^{-5}\text{m}^2/\text{s}$. Oil: $\mu_b=\mu=2.89\times10^{-3}\,\text{Pa}\cdot\text{s}$, $\rho_i=825\text{kg/m}^3$, $\rho_e=800.25\text{kg/m}^3$, $c=1300\text{m/s}$, $D_\rho=8.43\times10^{-6}\text{m}^2/\text{s}$.

A unique feature of the $\hat{m}_e(t)/M_L$ curves in figure 2.13 is that the area underneath each curve is always unity, reflecting the fact that the accumulative fluid production is the producible mass M_L. Equations (2.23) and (2.25) show that a large diffusion coefficient D_ρ gives a large drainage rate as well as a small drain-out time. Contrary to intuition, a large drainage rate accompanied by a small drain-out time is actually beneficial for fluid production for drainage flows, as a fixed amount of fluid is produced in a shorter time. This characteristic is quite different from open-end tube flows for which maintaining a high drainage rate produces more fluids due to unlimited supply of fresh fluid from upstream. Figure 2.13 indicates that the drainage rates for oil and gas are of the same order of magnitude. Furthermore, the drain-out time ratio between oil and gas is

$t_{d,oil} / t_{d,gas} = D_{\rho,gas} / D_{\rho,oil} = 5.72$. Thus, oil and gas can be produced from the capillary in a similar time span (figure 2.13). The classical Poiseuille theory, on the other hand, gives a significantly larger drain-out time ratio $t_{d,oil} / t_{d,gas} = \mu_{oil} / \mu_{gas} = 145$, as the drain-out time from the Poiseuille theory is proportional to the shear viscosity μ.

Chapter 3

Symmetric Drainage flow of a compressible fluid from a fracture

3.1. Mathematical formulation

In this chapter, we study the symmetric drainage flow of a single-phase compressible fluid from a narrow channel (figure. 3.1). The channel has a narrow gap $2H$ and a length $2L$. The fluid stored in the channel is initially at rest with a density ρ_i with both ends closed. The channel is embedded in a bath of the same compressible fluid maintained at a density ρ_e slightly lower than ρ_i. At $t=0$, the two ends of the channel at $x=-L, L$ are opened fully, and the densities at the exits are maintained at ρ_e all times thereafter. Volumetric expansion causes the fluid to drain from microchannel through the ends symmetrically. The density difference $\rho_i - \rho_e$ is assumed to be small and temperature variation is negligible. For very narrow channels, the Mach number is small; as such the continuity and the compressible Navier-Stokes equations (Chorin & Marsden 1992) can be linearized around the final equilibrium state $(\rho, \mathbf{v}) = (\rho_e, 0)$ so that (Morse & Ingard 1968; Temkin 1981)

$$\frac{\partial \rho'}{\partial t} + \rho_e \nabla \cdot \mathbf{v}' = 0\,, \tag{3.1}$$

$$\rho_e \frac{\partial \mathbf{v}'}{\partial t} = -\nabla p' + \left(\mu_b + \frac{1}{3}\mu\right)\nabla(\nabla \cdot \mathbf{v}') + \mu \nabla^2 \mathbf{v}'\,, \tag{3.2}$$

where the density perturbation $\rho' = \rho - \rho_e$; p' is the pressure perturbation; $\mathbf{v}'$ is the velocity perturbation which is assumed to be symmetric about the channel centerline $y=0$; μ, μ_b are the shear and bulk viscosities of the fluid, respectively. Equations (3.1) and (3.2) can be used to derive a damped wave equation for the density perturbation,

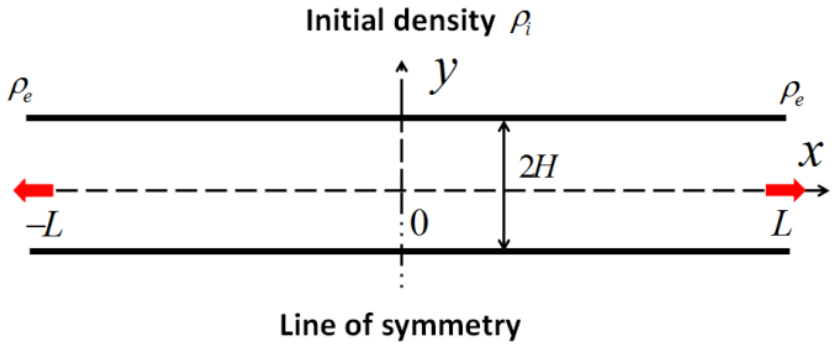

Figure 3.1. Schematic of symmetric drainage flow from a channel. The initial density is ρ_i; and the exit density is ρ_e.

$$\frac{\partial^2 \rho'}{\partial t^2} = \left(c^2 + D_\rho \frac{\partial}{\partial t} \right) \nabla^2 \rho', \tag{3.3}$$

where the diffusion coefficient $D_\rho = (\mu_b + 4\mu/3)/\rho_e$ characterizes the diffusion of a small density disturbance and c is the speed of sound. equation (3.3) is decoupled from the velocity field. It must be emphasized that equation (3.3) is not an *ad hoc* equation: it is as rigorous as the linearized system of equations (3.1) and (3.2). The boundary and initial conditions for the density perturbation are:

$$x = 0 : \frac{\partial \rho'}{\partial x} = 0; x = L : \rho' = 0 ; \tag{3.4}$$

$$t = 0 : \rho' = \rho_i - \rho_e ; \frac{\partial \rho'}{\partial t} = 0 . \tag{3.5}$$

The boundary condition on $x = 0$ is due to symmetry. Unlike the velocity, the boundary value of the density on the channel wall does not need to be specified (see below). Of particular interest is that the mass flow rate at the exit $\dot{m}_e(t)$ can be computed once the instantaneous density distribution is obtained without the need for explicit knowledge of the corresponding velocity field, as the integral of the continuity equation over one half of the channel (due to symmetry) gives

$$\dot{m}_e(t) = -\int_{\text{half channel}} \frac{\partial \rho'}{\partial t} d\mathrm{v} \,. \tag{3.6}$$

The velocity field can be computed once the density distribution for the linearized flow is obtained. From the Helmholtz decomposition theorem (Aris 1989; Leal 2010; Panton 2013), the velocity field $\mathbf{v}'$ can be decomposed into the sum of an irrotational part $\mathbf{v}'_{IR}$ and a rotational part $\mathbf{v}'_{RT}$,

$$\mathbf{v}' = \mathbf{v}'_{IR} + \mathbf{v}'_{RT} \,, \tag{3.7}$$

where the irrotational part is a potential flow and the rotational part is solenoidal (incompressible):

$$\nabla \times \mathbf{v}'_{IR} = 0 \,,\ \mathbf{v}'_{IR} = \nabla \Phi \,, \tag{3.8}$$

$$\nabla \cdot \mathbf{v}'_{RT} = 0 \,. \tag{3.9}$$

In the above, Φ is the scalar velocity potential for the irrotational flow. The pressure can also be split into two corresponding parts,

$$p' = p'_{IR} + p'_{RT} \,, \tag{10}$$

with p'_{IR} corresponding to the irrotational but compressible part of the velocity $\mathbf{v}'_{IR}$, and p'_{RT} corresponding to the solenoidal part of the velocity. As commented by Panton (Panton 2013, p430), the Helmholtz decomposition theorem places the expansion motions in the potential component of the velocity. Thus, any change in fluid density is only associated with the potential component $\mathbf{v}'_{IR}$. In other words, the thermodynamic relation between density and pressure only applies to the pressure associated with the potential component p'_{IR}; and the pressure associated with the solenoidal component p'_{RT} acts as a Lagrangian multiplier that enforces the incompressibility condition on the solenoidal velocity $\mathbf{v}'_{RT}$ (a

practice widely known and implemented in the computational fluid dynamics community). The two parts of the velocity field are called the longitudinal mode and transverse mode respectively in the acoustic literature (Morse & Ingard 1968; Temkin 1981).

Using the vector identity

$$\nabla^2\mathbf{v}'=\nabla(\nabla\cdot\mathbf{v}')-\nabla\times(\nabla\times\mathbf{v}'), \tag{3.11}$$

equation (3.2) can be written as

$$\rho_e\frac{\partial\mathbf{v}'}{\partial t}=-\nabla p'+\left(\mu_b+\frac{4}{3}\mu\right)\nabla(\nabla\cdot\mathbf{v}')-\mu\nabla\times(\nabla\times\mathbf{v}'). \tag{3.12}$$

With the decomposition (3.7)−(3.10), the irrotational field and the solenoidal field satisfy the following sets of equations. For irrotational field $\mathbf{v}'_{IR}$:

$$\frac{\partial\rho'}{\partial t}+\rho_e\nabla\cdot\mathbf{v}'_{IR}=0, \tag{3.13}$$

$$\rho_e\frac{\partial\mathbf{v}'_{IR}}{\partial t}=-\nabla p'_{IR}+\left(\mu_b+\frac{4}{3}\mu\right)\nabla(\nabla\cdot\mathbf{v}'_{IR}), \tag{3.14}$$

$$p'_{IR}=c^2\rho'. \tag{3.15}$$

For solenoidal field $\mathbf{v}'_{RT}$:

$$\nabla\cdot\mathbf{v}'_{RT}=0, \tag{3.16}$$

$$\rho_e\frac{\partial\mathbf{v}'_{RT}}{\partial t}=-\nabla p'_{RT}+\mu\nabla^2\mathbf{v}'_{RT}. \tag{3.17}$$

In the linear theory considered here, these two modes are only coupled through the no-slip condition imposed on the overall velocity $\mathbf{v}'$,

$$y=\pm H:\mathbf{v}'=\mathbf{v}'_{IR}+\mathbf{v}'_{RT}=0. \tag{3.18}$$

3.2. Acoustic waves and transverse density relaxation in a narrow channel

In general, any function $\rho'(x,\mathrm{y},t)$ can be expressed as the sum of a part independent of y and a part that vanishes on the channel wall,

$$\rho'(x,y,t)=\rho'(x,H,t)+\left[\rho'(x,y,t)-\rho'(x,H,t)\right]. \tag{3.19}$$

With this decomposition, the initial-boundary-value-problem for the density perturbation (3.3)–(3.5) can be solved using the method of separation of variables without the need of imposing any boundary condition for the density on the channel wall. The complete solution for $\rho'(x,\mathrm{y},t)$ is then

$$\rho'(x,y,t)=\frac{2(\rho_i-\rho_e)}{L}\left[\begin{array}{l}\displaystyle\sum_{n=0}^{N_d}\frac{(-1)^n}{\sigma_n}e^{-\gamma_n t}\cos\omega_n t\cos\sigma_n x\\ \displaystyle+\sum_{n=N_d+1}^{\infty}\frac{(-1)^n}{\sigma_n}e^{-\gamma_n t}\cosh\gamma_n\sqrt{1-\varepsilon_n}\,t\cos\sigma_n x\\ \displaystyle+RE\sum_{n=0}^{\infty}\sum_{m=1}^{\infty}A_{nm}\cos(\alpha_m y)\left(e^{K_{nm}^{+}t}-e^{K_{nm}^{-}t}\right)\cos\sigma_n x\end{array}\right], \tag{3.20}$$

where "*RE*" stands for the real part and

$$\begin{aligned}
&A_{nm}=\frac{\sigma_n}{\alpha_m H}\frac{D_\rho(-1)^{n+m-1}}{K_{nm}^{+}-K_{nm}^{-}};\\
&K_{nm}^{\pm}=-\frac{D_\rho}{2}\left(\sigma_n^2+{\alpha_m}^2\right)\pm\sqrt{\frac{D_\rho^2}{4}\left(\sigma_n^2+{\alpha_m}^2\right)^2-c^2\left(\sigma_n^2+{\alpha_m}^2\right)};\\
&\sigma_n=\frac{(2n+1)\pi}{2L};\ \ \alpha_m=\frac{(2m-1)\pi}{2H};\\
&\gamma_n=\frac{D_\rho}{2}\sigma_n^2;\ \ \omega_n=c\sigma_n\sqrt{1-\frac{D_\rho^2\sigma_n^2}{4c^2}};\\
&\varepsilon_n=\frac{4c^2}{D_\rho^2\sigma_n^2}<1,\ n>N_d;\quad N_d=floor\left[\frac{2cL}{\pi D_\rho}-\frac{1}{2}\right].
\end{aligned} \tag{3.21}$$

The single sum series in (3.20) is the part of ρ' that is independent of the coordinate y, where N_d is an integer such that ω_n becomes imaginary when $n > N_d$. For meter-length channels, and typical fluid properties $c = 300\text{m/s}, D_\rho = 10^{-5}\text{m}^2/\text{s}$, $N_d = O(10^7)$. The part of the series with $n > N_d$ is purely diffusive (non-oscillatory). The decay rate for this diffusive portion of the series ($n > N_d$) is about $\exp(-c^2 t / D_\rho)$ or $\exp(-2\gamma_n t)$, whichever is smaller. For $c = 400\text{m/s}$, $D_\rho = 10^{-5}\text{m}^2/\text{s}$, $\exp(-c^2 t / D_\rho) \sim \exp(-10^9 t)$, which is an extremely fast decay; whilst $\exp(-2\gamma_n t)$ always decays faster than the terms in the part of series with $n \le N_d$, which decays as $\exp(-\gamma_n t)$. Thus, the purely diffusive part of the series ($n > N_d$) can be neglected in the calculations for large times due to their faster decay.

The double-sum-series in equation (3.20) contains the $y-$dependence of the density profile which vanishes on the channel wall equation (3.19). The slowest decaying mode in the double-sum-series is the $(n,m) = (0,1)$ mode. A Taylor series expansion for small gap gives, to the leading order,

$$K_{01}^{+} = -\frac{c^2}{D_\rho{}^2}, \tag{3.22}$$

$$K_{01}^{-} = -\frac{5.81 D_\rho}{H^2}. \tag{3.23}$$

K_{01}^{+} is the aeroacoustics mode, which decays with a rate of $\exp(-c^2 t / D_\rho)$, independent of the length and the gap of the channel; and as shown above, $\exp(-c^2 t / D_\rho)$ decays very fast as $\exp(-10^9 t)$. K_{01}^{-} is the highly damped viscous mode for narrow channels. For example, for a micron-size gap, $H = 10^{-6}\text{m}$ and $D_\rho = 10^{-5}\text{m}^2/\text{s}$, $K_{01}^{-} = -5.81\times 10^7/\text{s}$. Thus, for a micron-size gap, after a very short-time of the order $O(10^{-7}\text{ s})$, the double-sum-series in (3.20) quickly decays to zero and the density relaxes to a profile uniform over the channel

cross-section with the density perturbation given by the single-sum series. This density relaxation occurs even faster for nano-size channels. In other words, the acoustic waves quickly approach the plane wave solution in a narrow channel. This fast relaxation of the density in the transverse direction is due to strong transverse viscous diffusion (strong transverse damping effect) in narrow channels. The transversely relaxed density perturbation is given by

$$\rho'(r,x,t) = \frac{2}{L}(\rho_i - \rho_e)\sum_{n=0}^{N_d} \frac{(-1)^n}{\sigma_n} e^{-\gamma_n t} \cos\omega_n t \cos\sigma_n x \tag{3.24}$$

after neglecting the fast decaying purely diffusive modes.

Equation (3.24) shows that in narrow channels, any density variation in the cross-sectional direction is smoothed out very quickly, while viscous damping of the longitudinal variation of density is extremely slow, on the diffusion timescale D_ρ / L^2 , since $\gamma_n \approx D_\rho / L^2$. The density perturbation solution (3.24) represents a damped standing acoustic wave in the channel, with a density node at the exit and antinode at the symmetry line $x = 0$.

3.3. Velocity and the pressure fields

3.3.1. *Irrotational field*

For the plane wave solution of the density, equation (3.24), the irrotational velocity obtained from the continuity equation (3.13) becomes $\mathbf{v}'_{IR} = \mathrm{v}'_{x,IR}(x,t)\mathbf{e}_x$ which is given by

$$\mathrm{v}'_{x,IR}(x,t) = \frac{2}{L}\frac{\rho_i - \rho_e}{\rho_e}\sum_{n=0}^{N_d} \frac{(-1)^n}{\sigma_n^2}\left[\gamma_n \cos\omega_n t + \omega_n \sin\omega_n t\right] e^{-\gamma_n t} \sin\sigma_n x \tag{3.25}$$

This irrotational part of the instantaneous velocity is independent of y. Since $\gamma_n << \omega_n$ when $n < N_d$, the instantaneous irrotational velocity $\mathbf{v}'_{IR}$ scales with the speed of sound as $c(\rho_i - \rho_e)/\rho_e$, not the viscous velocity scale as in the Poiseuille's law.

The compressible pressure perturbation resulting from the irrotational velocity $\mathbf{v}'_{IR}$ is related to the density change by $p'_{IR} = c^2\rho'$. The compressible pressure perturbation is given by

$$p'_{IR} = c^2\rho'(x,t) = \frac{2}{L}c^2(\rho_i - \rho_e)\sum_{n=0}^{N_d}\frac{(-1)^n}{\sigma_n}e^{-\gamma_n t}\cos\omega_n t\cos\sigma_n x\,. \tag{3.26}$$

3.3.2. *Rotational field*

The solenoidal velocity $\mathbf{v}'_{RT}$ is two-dimensional,

$$\mathbf{v}'_{RT} = \mathbf{e}_x \mathrm{v}'_{x,RT}(x,y,t) + \mathbf{e}_y \mathrm{v}'_{y,RT}(x,y,t)\,, \tag{3.27}$$

where $\mathbf{e}_x$, $\mathbf{e}_y$ are the unit base vectors in the x, y directions, respectively. The solenoidal velocity $\mathbf{v}'_{RT}$ can be determined by the incompressibility condition (3.16) and the linearized vorticity diffusion equation

$$\frac{\partial\boldsymbol{\omega}}{\partial t} = \nu_e\nabla^2\boldsymbol{\omega}\,, \tag{3.28}$$

$$\boldsymbol{\omega} = \nabla\times\mathbf{v}' = \nabla\times\mathbf{v}'_{RT}\,, \tag{3.29}$$

where the kinematic viscosity $\nu_e = \mu/\rho_e$. A stream-function $\psi(x,y,t)$ can be introduced such that

$$\mathrm{v}'_{x,RT} = \frac{\partial\psi}{\partial y},\ \ \mathrm{v}'_{y,RT} = -\frac{\partial\psi}{\partial x}\,. \tag{3.30}$$

Thus, the vorticity equation becomes

$$\frac{\partial}{\partial t}\nabla^2\psi = \nu_e \nabla^4 \psi \,. \tag{3.31}$$

The no-penetration and the no-slip boundary condition on the wall for the overall velocity $\mathbf{v}'$ become

$$y = \pm H : \frac{\partial \psi}{\partial y} = -\,\mathrm{v}_{x,IR};\ \frac{\partial \psi}{\partial x} = 0\,. \tag{3.32}$$

Since the flow is symmetric about the centerline $y = 0$, $\mathrm{v}'_{x,RT}$ must be an even function of y. This requires ψ to be an odd function of y. The solenoidal velocity is driven by the no-slip condition imposed on the overall velocity $\mathbf{v}'_{RT}$, with the stream-function given by

$$\psi(x,y,t) = \frac{2}{L}\frac{\rho_i - \rho_e}{\rho_e}\sum_{n=0}^{N_d}\frac{(-1)^n}{\sigma_n^2} RE\left[\frac{G_n(y)}{F_n(h)}\Omega_n e^{\Omega_n t}\right]\sin\sigma_n x \tag{3.33}$$

where

$$\begin{aligned} G_n(y) &= \sinh(\sigma_n y) - \frac{\sinh(\sigma_n h)}{\sinh(\eta_n h)}\sinh(\eta_n y) \\ G_n'(y) &= F_n(y) = \sigma_n \cosh(\sigma_n y) - \eta_n \frac{\sinh(\sigma_n h)}{\sinh(\eta_n h)}\cosh(\eta_n y) \end{aligned} \tag{3.34}$$

The solenoidal velocity components are

$$\begin{aligned} &\mathrm{v}'_{x,RT}(x,y,t) = \frac{2}{L}\frac{\rho_i - \rho_e}{\rho_e}\sum_{n=0}^{N_d}\frac{(-1)^n}{\sigma_n^2} RE\left[\frac{F_n(y)}{F_n(H)}\Omega_n e^{\Omega_n t}\right]\sin\sigma_n x; \\ &\mathrm{v}'_{y,RT}(x,y,t) = -\frac{2}{L}\frac{\rho_i - \rho_e}{\rho_e}\sum_{n=0}^{N_d}\frac{(-1)^n}{\sigma_n} RE\left[\frac{G_n(y)}{F_n(H)}\Omega_n e^{\Omega_n t}\right]\cos\sigma_n x. \\ &G_n(y) = \sinh(\sigma_n y) - \frac{\sinh(\sigma_n H)}{\sinh(\eta_n H)}\sinh(\eta_n y) \\ &F_n(y) = G_n'(y) = \sigma_n \cosh(\sigma_n y) - \eta_n \frac{\sinh(\sigma_n H)}{\sinh(\eta_n H)}\cosh(\eta_n y) \\ &\Omega_n = -\gamma_n + i\omega_n;\ \ \nu_e = \frac{\mu}{\rho_e}; \\ &\sigma_n = \frac{(2n+1)\pi}{2L};\ \ \eta_n = \sqrt{\sigma_n^2 + \frac{\Omega_n}{\nu_e}}. \end{aligned} \tag{3.35}$$

In the small gap limit, the stream-wise solenoidal velocity component is given by

$$\begin{aligned} \mathrm{v}'_{x,RT} &= \frac{\mathrm{v}'_{x,IR}}{2}\left(1-3\frac{y^2}{H^2}\right)+O\left(H^2\right) \\ &= \left(1-3\frac{y^2}{H^2}\right)\frac{1}{L}\frac{\rho_i-\rho_e}{\rho_e}\sum_{n=0}^{N_d}\frac{(-1)^n}{\sigma_n^2}e^{-\gamma_n t}\left(\gamma_n\cos\omega_n t+\omega_n\sin\omega_n t\right)\sin\sigma_n x+O\left(\left(\frac{H}{L}\right)^2\right) \end{aligned} . \quad (3.36)$$

Thus, in the small gap limit, the stream-wise solenoidal velocity becomes parabolic; however, it slips on the wall so that the overall velocity satisfies the no-slip condition. Clearly, the volumetric flow rate due to the solenoidal velocity at any cross-section is zero,

$$Q_{RT}=\int_{-H}^{H}\mathrm{v}_{x,RT}\,dy=\frac{\mathrm{v}_{x,IR}}{2}\int_{-H}^{H}\left(1-3\frac{y^2}{H^2}\right)dy=0. \quad (3.37)$$

This result is general, regardless of the channel gap size, as the volume integration of the incompressibility condition $\nabla\cdot\mathbf{v}'_{RT}=0$ between $x=0$ and x gives

$$0=\int\nabla\cdot\mathbf{v}'_{RT}\,d\mathrm{v}=\oiint_{boundary}n\cdot\mathbf{v}'_{RT}\,da=Q_{RT}(x)-Q_{RT}(0)=Q_{RT}(x) \quad (3.38)$$

after applying the no-penetration condition on the channel wall and the symmetry condition at $x=0$. Thus, the solenoidal velocity $\mathbf{v}'_{RT}$ makes no contribution to the mass flow rate and its sole role is to enforce the no-slip condition on the channel wall for the overall velocity.

In the small gap limit, the overall stream-wise velocity is also parabolic,

$$\begin{aligned} \mathrm{v}'_x &= \mathrm{v}'_{x,IR}+\mathrm{v}'_{x,RT} \\ &= \frac{3}{2}\left(1-\frac{y^2}{H^2}\right)\mathrm{v}'_{x,IR}=\left(1-\frac{y^2}{H^2}\right)\frac{3}{L}\frac{\rho_i-\rho_e}{\rho_e}\sum_{n=0}^{N_d}\frac{(-1)^n}{\sigma_n^2}e^{-\gamma_n t}\left(\gamma_n\cos\omega_n t+\omega_n\sin\omega_n t\right)\sin\sigma_n x \end{aligned} . \quad (3.39)$$

While the overall stream-wise velocity is parabolic in the small gap limit, it differs from the plane Poiseuille flow solution

$$\mathrm{v}'_x = -\frac{H^2}{2\mu}\frac{dp}{dx}\left(1-\frac{y^2}{H^2}\right) \tag{3.40}$$

in at least two significant aspects:

(a) The centerline velocity is independent of the radius/height; whilst the Poiseuille flow solution (3.40) has a centerline velocity proportional to H^2;

(b) The velocity does not scale with the inverse of viscosity as in the Poiseuille flow solution (3.40).

The incompressible part of the pressure perturbation associated with the solenoidal field is computed with the plane wave solution of the rotational velocity solution equation (3.35) through incompressible linear momentum equation. Noticed, the rotational pressure profile could be obtained just from the x-direction equation only. In order to simultaneously satisfy the equation for the 2nd direction (y-directions), a complete complex form of the rotational velocity solution equation (3.35) need to be used, instead of using an asymptotic expression equation.

$$\begin{aligned}
&p'_{RT} = \frac{2}{L}\frac{\rho_i-\rho_e}{\rho_e}\sum_{n=0}^{N_d}\frac{(-1)^n}{\sigma_n^3}RE\left[\left(\mu\sigma_n^2-\mu\nabla_y^2+\rho_e\Omega_n\right)\frac{F_n(y)}{F_n(h)}\Omega_n e^{\Omega_n t}\right]\cos\sigma_n x\\
&F_n(y) = \sigma_n\cosh(\sigma_n y)-\eta_n\frac{\sinh(\sigma_n h)}{\sinh(\eta_n h)}\cosh(\eta_n y)\\
&\nabla_y^2 F_n(y) = F_n''(y) = \sigma_n^3\cosh(\sigma_n y)-\eta_n^3\frac{\sinh(\sigma_n h)}{\sinh(\eta_n h)}\cosh(\eta_n y)\\
&\Omega_n = -\gamma_n + i\omega_n;\ \ \nu_e = \frac{\mu}{\rho_e}\\
&\sigma_n = \frac{(2n+1)\pi}{2L};\ \ \eta_n = \sqrt{\sigma_n^2+\frac{\Omega_n}{\nu_e}}
\end{aligned} \tag{3.41}$$

This pressure is induced by the solenoidal velocity field which in turn is driven by the requirement of no-slip condition for the overall velocity. The inverse square dependence

on the gap H is the hallmark of the lubrication theory, which only appears in the incompressible pressure (3.41), not in the compressible part of the pressure which is gap independent, equation (3.26).

The work above reveals that there are two flow mechanisms for a viscous low Mach number flow: the compressible part of the flow is driven by the fluid's volumetric expansion whilst the incompressible part of the flow is driven by the incompressible pressure gradient or a boundary velocity. For the drainage flow considered, the compressible part is irrotational and it slips on the channel wall. The incompressible part is driven by a slip velocity on the channel wall that makes the overall velocity satisfying the no-slip condition. Only the incompressible part of the flow can be approximated by a lubrication theory. However, for drainage flows, the incompressible part of the flow generates no net mass flow rate as shown by equation (3.38). Thus, a lubrication-based theory is incapable of capturing the correct mass flow rate.

Figure 3.2 shows a sequence of the instantaneous streamline plots over one period for the solenoidal velocity $\mathbf{v}'_{RT}$ for a channel with a gap of 20μm ($H = 10\mu\text{m}$), and half-length of $L = 1\text{m}$. Fluid property values are listed in the appendix A. In the plots, only the top-half of the channel is shown and the coordinates x, y are made dimensionless by L, H, respectively, so that they run from 0 to 1 and 0 to 1/2, respectively in the plots. However, the velocity values are dimensional, as indicated by the color bar. The period of oscillation is $T = 0.006849s$ and the streamlines plots starts at the time instant of $t_0 = 10^4 T = 68.49s$. Eight time instants are shown, with an increment of $T/8$ starting from t_0. The solenoidal velocity slips on the channel wall and for the first half of the period, the slip velocity is in the negative x-direction; whilst for the second half, it is in the positive x-

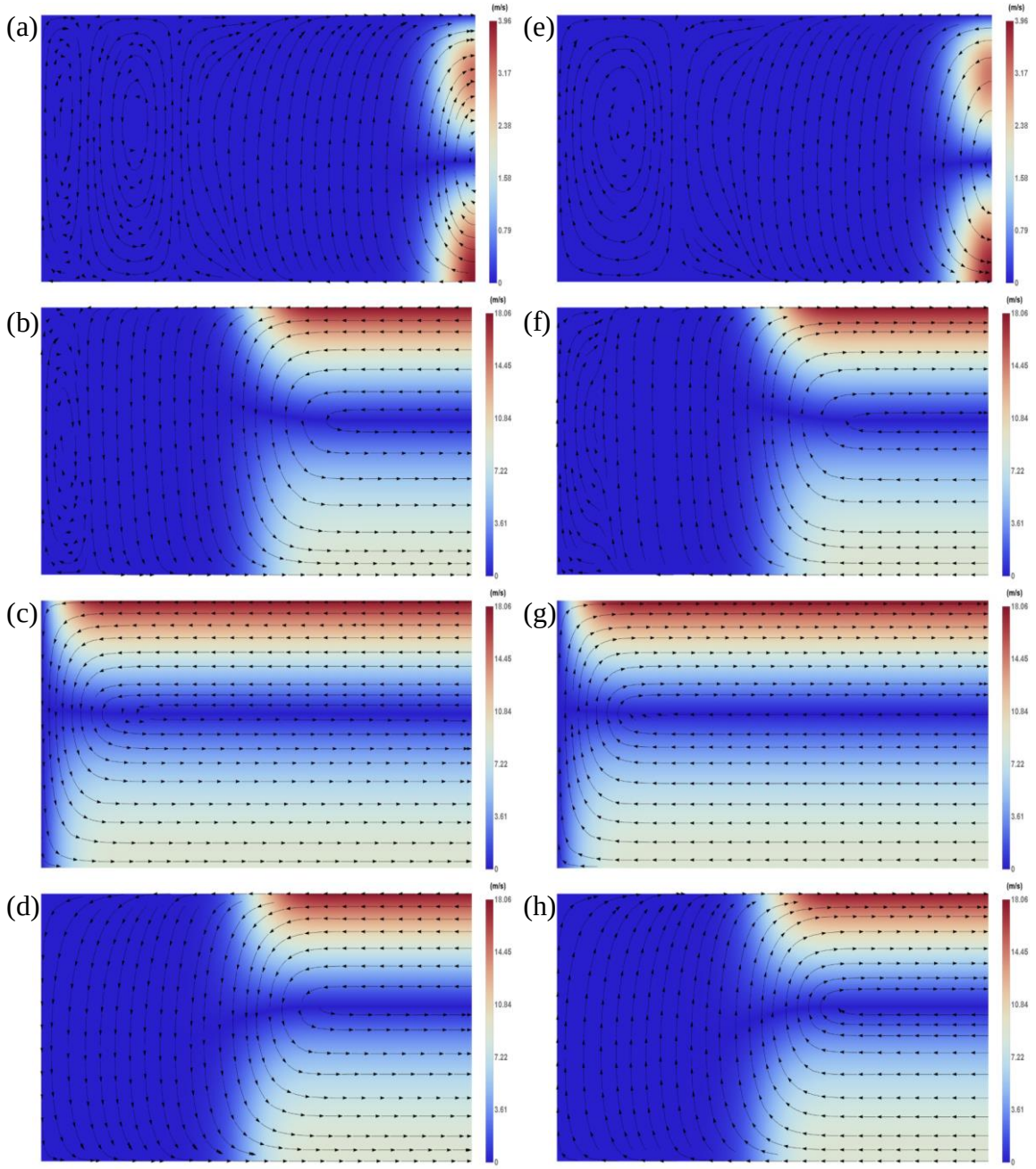

Figure 3.2. Instantaneous streamlines for the solenoidal velocity over one period. Only the upper-half of the channel is shown. The horizontal and vertical coordinates are dimensionless x, y running from 0 to 1 and 0 to 1/2, respectively. The flow is incompressible and rotational. From plot (a) to plot (h), each plot is corresponding to time instance $t_0 \sim t_0 + 7T/8$ with $T/8$ increment.

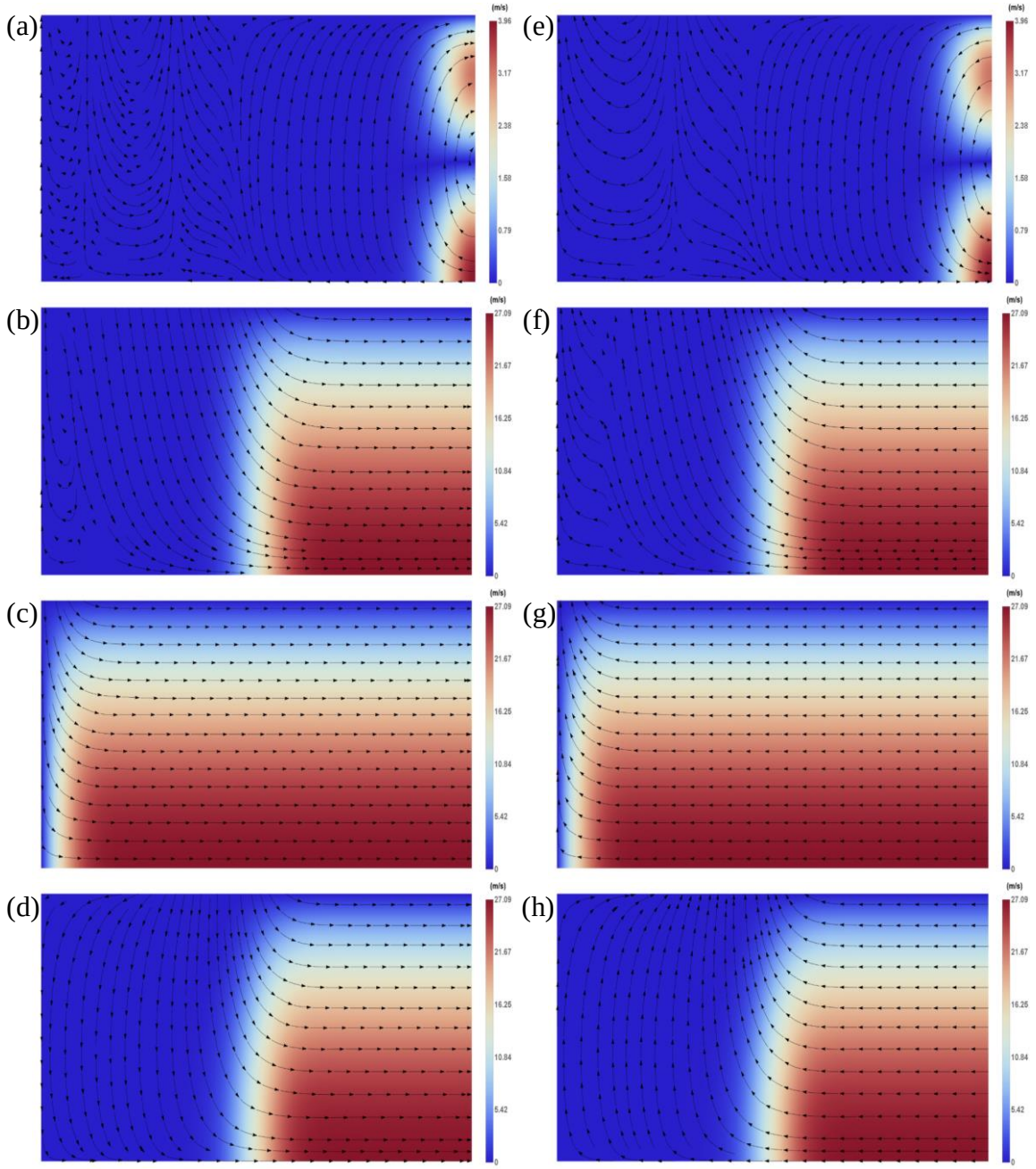

Figure 3.3. Instantaneous streamlines for the overall velocity over one period. Only the upper-half of the channel is shown. The velocity satisfies no-slip on the wall. Fluid production is achieved by the decay of the amplitude of oscillation. The horizontal and vertical coordinates are dimensionless x, y running from 0 to 1 and 0 to 1/2, respectively. The flow is incompressible and rotational. From plot (a) to plot (h), each plot is corresponding to time instance $t_0 \sim t_0 + 7T/8$ with $T/8$ increment.

direction. The obvious pattern of these instantaneous streamlines is that the solenoidal flow near the wall and that around the central region are always in the opposite directions, resulting in a zero mass flow rate over any cross-section as shown analytically by equation (3.38).

Figure 3.3 shows the corresponding instantaneous streamlines for the overall velocity $\mathbf{v}'$ over the same period. A standout feature of these streamlines is that the overall velocity satisfies the no-slip condition; and except for the short times around the start and the end of the period, significant flows occur only near the central region of the channel. For the first half period, fluid moves out of the channel; whilst for the second half, fluid is sucked back into the channel. Because of the decay of the velocity in time, there is a net amount of fluid produced during one period as more fluid moves out than the amount sucked back in. This net production will be determined analytically in the next section. Also noticeable is that the instantaneous velocity is relatively large, sine it scales with the speed of sound as alluded to earlier. The period-averaged velocity, however, is much smaller, as will be shown in the next section. Finally, we emphasize that when the property values are varied, these flow patterns remain qualitatively the same for narrow channels.

3.4. Large-timescale diffusive behavior and the drainage rate

The instantaneous velocity and pressure fields are damped wave solutions. The slowest decaying component has a period of the oscillation of $T = 4L/c$, which is about $O(10^{-2}s)$ for meter-long channels and it is even shorter for centimeter-long channels. This is a quite short time compared to the timescale of interest in most of applications. For sampling time much greater than the period, the behavior of the system is diffusive, even though its very

short-timescale behavior is ballistic with the instantaneous velocity scaling with $c(\rho_i - \rho_e)/\rho_e$. The large-timescale behavior of the system can be obtained by averaging the instantaneous fields over the period. For example, for the irrotational velocity $\mathrm{v}'_{x,IR}(x,t)$, its period-averaged value, denoted by an overbar, is given by

$$\overline{\mathrm{v}'_{x,IR}(x,t)} = \frac{1}{T}\int_t^{t+T} \mathrm{v}'_{x,IR}(x,\xi)d\xi = \frac{2}{L}\frac{\rho_i - \rho_e}{\rho_e}\sum_{n=0}^{N_d}\frac{(-1)^n}{\sigma_n^2}\frac{e^{-\gamma_n t} - e^{-\gamma_n (t+T)}}{T}\sin\sigma_n x, \quad (3.42)$$

where $t = kT,\ k >> 1$ is an integer. For small T,

$$\frac{e^{-\gamma_n t} - e^{-\gamma_n (t+T)}}{T} \approx -\frac{d}{dt}e^{-\gamma_n t} = \gamma_n e^{-\gamma_n (t+T)}.$$

Thus,

$$\overline{\mathrm{v}'_{x,IR}(x,t)} = \frac{\rho_i - \rho_e}{\rho_e}\frac{D_\rho}{L}\sum_{n=0}^{N_d}(-1)^n e^{-\gamma_n t}\sin\sigma_n x. \quad (3.43)$$

equation (3.43) clearly shows that the period-averaged irrotational velocity is diffusive, and it scales with the diffusive characteristic velocity D_ρ / L. This is very similar to the motion of a Brownian particle in a liquid which shows ballistic behavior in short-timescale and diffusive behavior in large-timescale (Huang et al. 2011).

The period-averaged pressure perturbation also shows a diffusive nature (figure 3.4), with the pressure for the irrotational field and solenoidal field given respectively by

$$\overline{p'_{IR}(x,t)} = \frac{1}{T}\int_t^{t+T} p'_{IR}dt = \frac{D_\rho^2}{2L}(\rho_i - \rho_e)\sum_{n=0}^{N_d}(-1)^n \sigma_n e^{-\gamma_n t}\cos\sigma_n x, \quad (3.44)$$

$$\overline{p'_{RT}(x,t)} = \frac{1}{T}\int_t^{t+T} p'_{RT}dt = RE\left[\frac{e^{\Omega_n T} - 1}{\Omega_n T}p'_{RT,channel}\right]. \quad (3.45)$$

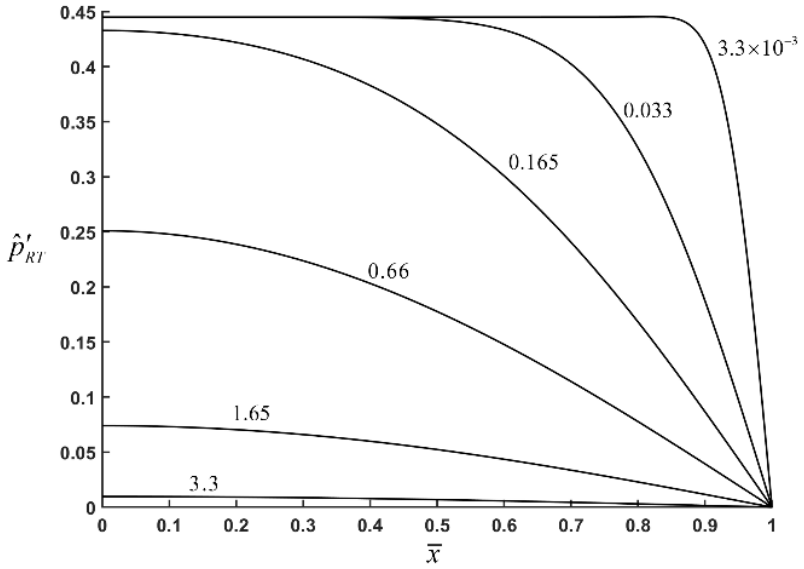

Figure 3.4. Diffusive decay of the Period-Averaged rotational pressure, with dimensionless time $\bar{t} = D_\rho t / L^2$ shown above each curve. $D_\rho = 4.82\times10^{-5}\,\mathrm{m}^2/\mathrm{s}$, $H = 10\mathrm{um}$ and $L = 1\mathrm{m}$.

The drainage rate is the mass flow rate calculated from the period-averaged irrotational velocity at the exit, as the solenoidal velocity produces no mass flow rate at any cross-section equation (3.38). Thus, if the channel width is W, from equation (3.41) we have the drainage rate

$$\overline{\dot{m}_e(t)} = \rho_e \, \overline{\mathrm{v}'_{x,IR}(L,t)}\, 2HW = 2\left(\rho_i - \rho_e\right)\frac{D_\rho}{L} HW \sum_{n=0}^{N_d} \exp\left[-\frac{D_\rho (2n+1)^2 \pi^2 t}{8L^2}\right]. \quad (3.46)$$

The channel cross-sectional area averaged exit velocity is simply

$$V_e(t) = \overline{\mathrm{v}'_{x,IR}(L,t)} = \frac{\rho_i - \rho_e}{\rho_e}\frac{D_\rho}{L}\sum_{n=0}^{N_d} \exp\left[-\frac{D_\rho (2n+1)^2 \pi^2 t}{8L^2}\right]. \quad (3.47)$$

The same result can be obtained by applying equation (3.6) and the density solution (3.24) to the instantaneous mass flow rate at the exit

$$\dot{m}_e(t) = -\int_{Tube} \frac{\partial \rho'}{\partial t}\, d\mathrm{v} = \frac{16HWL(\rho_i - \rho_e)}{\pi^2} \sum_{n=0}^{N_d} \frac{\exp[-\gamma_n t]}{(2n+1)^2}\left(\gamma_n \cos\omega_n t + \omega_n \sin\omega_n t\right). \quad (3.48)$$

Equation (3.48) shows that the instantaneous mass flow rate experiences oscillations, with production greater than intake in any given period due to the damping of the oscillation. Thus, when viewed in the short-timescale, fluid is produced in a huff-n-puff process. When the instantaneous mass flow rate (3.48) is averaged over a period, it produces the same result for the drainage rate $\overline{\dot{m}_e(t)}$ as given by equation (3.46).

A standout feature of the drainage rate formula (49) is that it scales linearly with the channel gap H instead of H^3 as given by the Poiseuille's law. Thus, (3.46) is a slip-like mass flow rate, despite the corresponding velocity profile satisfies the no-slip condition on the channel wall. The drainage rate can be very high in short-times, decreasing diffusively as $t^{-1/2}$ as time is increased. The drainage speed (3.47) is independent of the channel gap vs. the H^2 dependence from the Poiseuille's law. Furthermore, the drainage rate and the drainage speed are proportional to the fluid viscosity via the diffusion coefficient D_ρ, in stark contrast to the inverse proportionality to the fluid viscosity provided by the Poiseuille's law. Altogether, it shows that the fluid volumetric expansion driven drainage flow considered here is controlled by an entirely different mechanism than Poiseuille-type of flows, with the latter only suitable for displacement type of flows.

For any given density drop $\Delta\rho = \rho_i - \rho_e$, the mass of the producible fluid from the channel is fixed; for half of the channel considered in the symmetric drainage problem, this producible fluid mass is $M_L = 2HWL(\rho_i - \rho_e)$. The drainage rate in (3.46) can be expressed as

$$\overline{\dot{m}_e(t)} = M_L \frac{D_\rho}{L^2} \sum_{n=0}^{N_d} \exp\left[-\frac{D_\rho (2n+1)^2 \pi^2 t}{8L^2} \right]. \tag{3.49}$$

Here, $M_L D_\rho / L^2 \approx$ (fluid mass to be drained)/(characteristic drainage time), and it is the characteristic production rate for the drainage flow. Therefore, the dimensionless mass flow rate is

$$\dot{m}_D(t_D) = \frac{\overline{\dot{m}_e(t)}\, L^2}{M_L D_\rho} = \sum_{n=0}^{N_d} \exp\left[-\frac{(2n+1)^2 \pi^2}{8} t_D \right], \tag{3.50}$$

where the dimensionless time $t_D = D_\rho t / L^2$. When $t_D = 7.5$, $\dot{m}_D = 10^{-4}$. Thus, the drain-out time is

$$t_{D,drain-out} = 7.5, \tag{3.51}$$

or

$$t_{d,drian-out} = 7.5 \frac{L^2}{D_\rho}. \tag{3.52}$$

The constant becomes 3.75 if drain-out is defined as $\dot{m}_D = 10^{-2}$. The Poiseuille flow theory, on the other hand, gives a drain-out time proportional to the kinematic viscosity, $t_d \propto \nu_e$, instead of the inverse of the kinematic viscosity as shown by equation (3.38). The single curve of $\dot{m}_D(t_D)$ is plotted in figure 3.5 on a log-log scale. The mass flow rate decays diffusively with the power $t_D^{-1/2}$ before exponential decay sets in.

The drainage rate shown by equation (3.46) also applies to the case of a half-sealed channel in which the symmetry line at $x = 0$ is replaced by a sealed end. This is due to the fact that the density solution for this situation is exactly the same as the symmetric drainage problem, although the velocity fields are different.

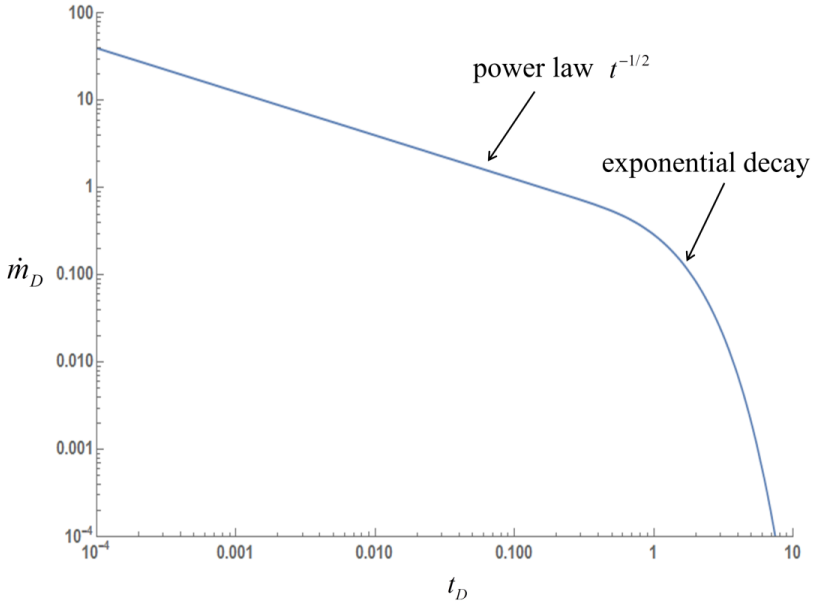

Figure 3.5. Log-log plot of the dimensionless drainage rate vs dimensionless time.

Chapter 4

Drainage flow from a micro-conduit to a reservoir or contraction

In Chapter 2 & 3, it is shown that even with the no-slip boundary condition, a volumetric-expansion driven low Mach number viscous drainage flow in a small conduit can exhibit a slip-like mass flow rate which surpass that given by the classical Poiseuille flow solution. However, one may question the use of the boundary condition of a prescribed density at the exit, even though this condition has been widely used for both incompressible and compressible flows through conduits. In this chapter, numerical simulations will be performed to examine whether a prescribed density exit boundary condition is a reasonable approximation to a realistic slender-conduit-reservoir system. By performing a quantitative analysis, we can obtain better insight on how the reservoir affect the propagating wave inside a micro-conduit. The work in this chapter extends the unsteady gas drainage flow study presented in Chapters 2 & 3.

4.1. Numerical model

The software package COMSOL 5.3 is used for the numerical simulations, with the same micro-conduit conditions as in Chapter 2, figure 2.1, and equations (2.16)–(2.17). However, instead of fixing the density at the conduit exit, the micro-conduit is connected to a reservoir or a contraction to mimic the more realistic outflow condition (figure 4.1). The reservoir/contraction can be viewed as a large bath containing the same compressible fluid maintained at a slightly lower density ρ_e, separated by a diaphragm from the micro-conduit filled with the same fluid with a higher density $\rho = \rho_i$. At $t = 0$, the diaphragm is broken instantaneously and the higher density gas in the micro-conduit starts to drain into

the reservoir/contraction by volumetric expansion. The exit density becomes time dependent and is influenced by the flow condition on both sides of the exit junction (micro-conduit and reservoir). The density difference is assumed to be small relative to the initial density, $\Delta\rho \ll \rho_i$, and isothermal flow is also assumed. The problem can be considered as a *generalized* weak shock-tube problem, except that we allow the tube cross section to change abruptly at the diaphragm junction.

4.2. Governing equation and boundary conditions

Since the mass drainage rate is controlled by the density change inside the micro-conduit, the damped wave equation for the density perturbation, equation (2.15), is used as the governing equation for the numerical simulation instead of the linearized Navier-Stokes equations. This significantly reduces the computational cost. Our focus in this chapter is to investigate how the reservoir/contraction affect the drainage rate and the density wave evolution, both of which can be acquired by solving the density distribution inside the conduit. Neumann boundary condition is implemented at the conduit walls as well as the reservoir side-walls. At the outer edge of the reservoir/contraction, an acoustic wave absorbing boundary condition is used to mimic an infinite long reservoir by a truncated computational domain. After testing several non-reflecting wave boundary conditions, an acoustic wave absorbing layer called perfectly matched layers (PML) is selected as the outer going boundary of the reservoir.

PML is widely used in acoustic and electromagnetic simulations as an artificial absorbing layer for wave equations. Within the layer, PML applies a complex stretching function to the coordinate in each direction so that the oscillatory wave solution will be

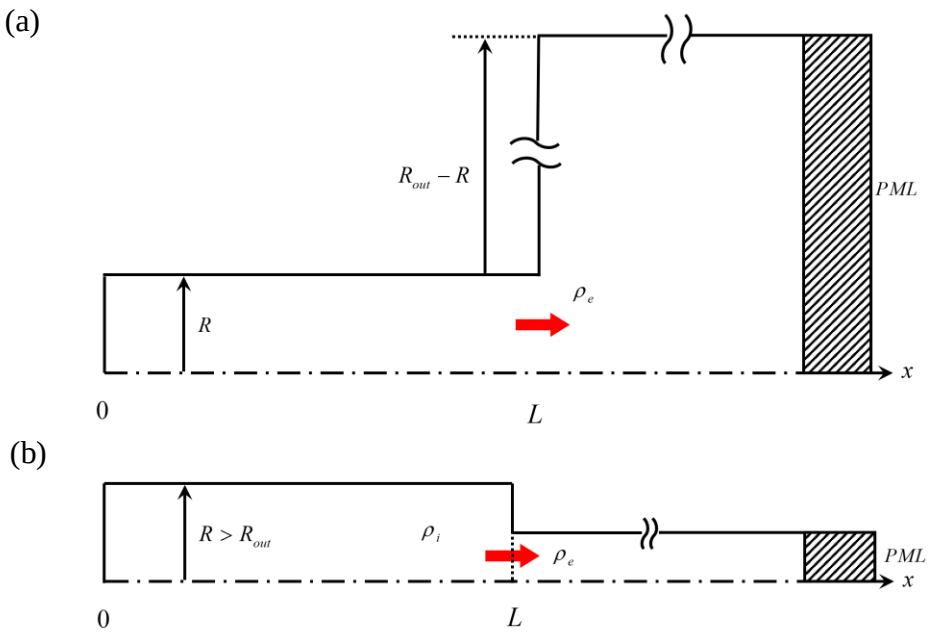

Figure 4.1. Drainage from a capillary tube to (a) a reservoir; (b) a contraction, filled with the same fluid at a lower density. Perfectly Matched Layer is placed at the far end of the reservoir to mimic the non-reflection outflow boundary condition.

attenuated exponentially (Johnson 2008). For our simulation, a rational stretching function with a scaling factor 6 and scaling curvature parameter 3 are selected for best result. Detailed numerical method verification is shown in the Appendix E.

4.3. Fundamentals of wave reflection, transmission and the reflection coefficient

In section 2.3, an oscillating wave pattern emerges for the density perturbation within the micro-conduit during the drainage process. Reflections occur whenever the density wave reaches the sealed end $x = 0$ or the exit $x = L$. Since the exit density is fixed, the wave inside is a standing wave, which is only an approximation to a realistic system. By connecting the conduit to a reservoir or a contraction, however, part of the propagating waves leaks into the reservoir (or contraction) and the rest is reflected back upon the arrival of the wave at the exit. The "leakage" of the wave can be studied by a wave reflection and

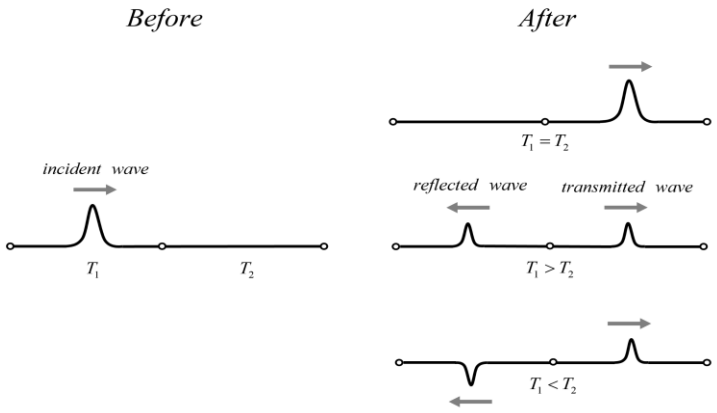

Figure 4.2. Incident, reflected and transmitted wave propagating on two strings with different tensions.

transmission analysis with a sudden change in radius/height (or area) of the conduit. Thus, before presenting the numerical simulation results, it will be constructive to review some basics of acoustic wave reflection and transmission.

In classical acoustic or electromagnetic wave transport analysis, the reflection coefficient $\Re$ is widely used to interpret the wave reflecting mechanism while the wave is passing through a junction between two different media (Schwartz 2016). As shown in figure 4.2, two strings with different tensions are connected to each other. As a right-going incident wave pass through the junction, different reflecting mechanism can be expected depending on the string tensions. With a unified tension $T_1 = T_2$ condition, the wave passes through the junction completely without any reflections. If $T_1 > T_2$, a fraction of the wave is reflected while the rest is transmitted to the second string. On the other hand, if $T_1 < T_2$, the same wave reflection occurs but with a phase flip.

One can use the reflection coefficient $\Re$ to analyze such wave reflection mechanism. By definition, the reflection coefficient is the intensity ratio of the reflection wave over the incident wave. For the incident wave propagation example shown above, one can derive a

reflection coefficient in terms of impedance from a 1-D wave equation by decomposing the incident wave into the reflecting and transmitting components and imposing continuity at the junction (Schwartz 2016). As shown in equation (4.2) below, $\Re$ equals to the ratio of the impedance difference over the impedance sum, with the impedance defined as the tension over the wave speed, $Z = T/\mathrm{v}$. For a propagating sound wave, the impedance is also defined as a product of the medium density and the speed of sound, $Z = \rho c$, which leads to the reflection coefficient:

$$\Re = \frac{I_{reflection}}{I_{incident}} = \frac{Z_1 - Z_2}{Z_1 + Z_2} = \frac{(\rho c)_1 - (\rho c)_2}{(\rho c)_1 + (\rho c)_2}. \tag{4.1}$$

Subscript "1" and "2" represent properties of the two different media as the incident wave is passing from "1" to "2". Z stands for the specific impedance which is equal to the product of medium density and speed of sound.

The flow behavior in the drainage flow system can be related to the reflection coefficient, since the density wave inside the capillary will experience a reflection at the capillary exit when it propagates from the capillary (medium "1") to the reservoir or contraction (medium "2") through the tube exit (junction). It is noted that for a wave propagating through different size cavities as from a tube to a reservoir or a contraction, one must consider the impedance per area as the relevant quantity, i.e. $Z = \rho c/A$. In the linearized theory considered in this study, the change in the density and speed of sound is small compared to the change in the cross-sectional area for the case of practical interest. Then the impedance is effectively equal to the reciprocal of the area, $Z = 1/A$, which simplifies the reflection coefficient to,

$$\Re = \frac{\frac{1}{A_1} - \frac{1}{A_2}}{\frac{1}{A_1} + \frac{1}{A_2}} = \frac{A_2 - A_1}{A_2 + A_1} = \frac{A_2 / A_1 - 1}{A_2 / A_1 + 1}. \tag{4.2}$$

Notice that the reflection coefficient of the junction is positive, $\Re > 0$, and it is an monotonic increasing function of the area expansion ratio A_2 / A_1 when $A_2 / A_1 > 1$ (reservoir). The reflection coefficient becomes negative, $\Re < 0$, for a reflection by a contraction $A_2 / A_1 < 1$, indicating a phase shift of 180 degrees for the reflected wave from the incident wave. The magnitude of the reflection coefficient increases with decreasing contraction ratio A_2 / A_1 (<1).

It should be emphasized that the reflection coefficient $\Re$ only describes the amplitude of the reflected wave and the transmitted wave. It is not suitable to $\Re$ as a boundary condition. This issue will be discussed further below.

4.4. Drainage flow into finite size reservoirs and contractions

4.4.1. *Evolution of the density waves*

4.4.1.1. *Capillary size extension of the tube: the weak shock-tube problem*

We first consider a drainage flow from a tube with an extension to infinity by a tube with the same size ($R_{out} = R$). Here we use a subscript "out" for any quantity associated with the reservoir, contraction, or simple extension by an identical tube. This is the classical weak shock-tube problem. Assuming $L >> R$, we use a finite extension with the same length as the capillary and the perfectly matched layer (PML) at the end of the extension to model the outflow boundary condition with the finite computational domain (figure 4.3). All demonstrated examples have $R = 1\mu\text{m}$, $L / R = 50$, $c = 450\text{m/s}$ and $D_\rho = 5\times10^{-5}\text{m}^2/\text{s}$.

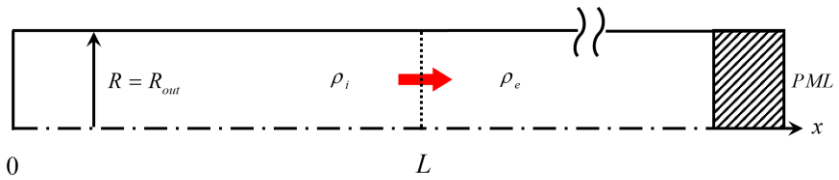

Figure 4.3. The weak shock-tube problem in a semi-infinite tube modelled by a finite extension with a Perfectly Matched Layer placed at the far end.

Figure 4.4a shows the normalized density perturbation $\bar{\rho}' = \rho' / (\rho_i - \rho_e)$ at different time instances for capillary size extension ($R_{out} = R$). As the diaphragm breaks, two density waves propagating in opposite directions are initiated at the exit: a compressional wave to the right into the "reservoir" and a rarefaction wave to the left into the capillary tube. The density (perturbation) at the exit is at $\bar{\rho}'_e = 0.5$; and the amplitudes of the right-propagating $\tilde{A}_{out}$, and left-propagating waves $\tilde{A}_{tube}$, measured from the density level at the exit, $\bar{\rho}'_e = 0.5$ are both 0.5, $\tilde{A}_{out} = \tilde{A}_{tube} = 0.5$. The equal amplitudes of the two waves represent an equal split. When the inward propagating wave reaches the sealed-end at $x = 0$, it is reflected completely, as a complete reflection boundary condition is assumed there, $(\partial\rho/\partial x = 0)$. The reflected wave then moves towards the exit, with the density ahead of the wave front being the same as the density at the exit, $\bar{\rho}'_e = 0.5$, and the density behind the wave front being $\bar{\rho}' = 0$. When the reflected wave arrives the exit $x = L$, no reflection is experienced as the reflection coefficient for this case is zero, $\Re = 0$ (equation 4.2 with $A_1 = A_2$). The sealed-end reflected wave is completely transmitted into the reservoir; and as soon as the sealed-end reflected wave has passed the exit/junction, the drainage process is completed. During the drainage process, no oscillation of the density inside the tube occurs, and the process is monotonic.

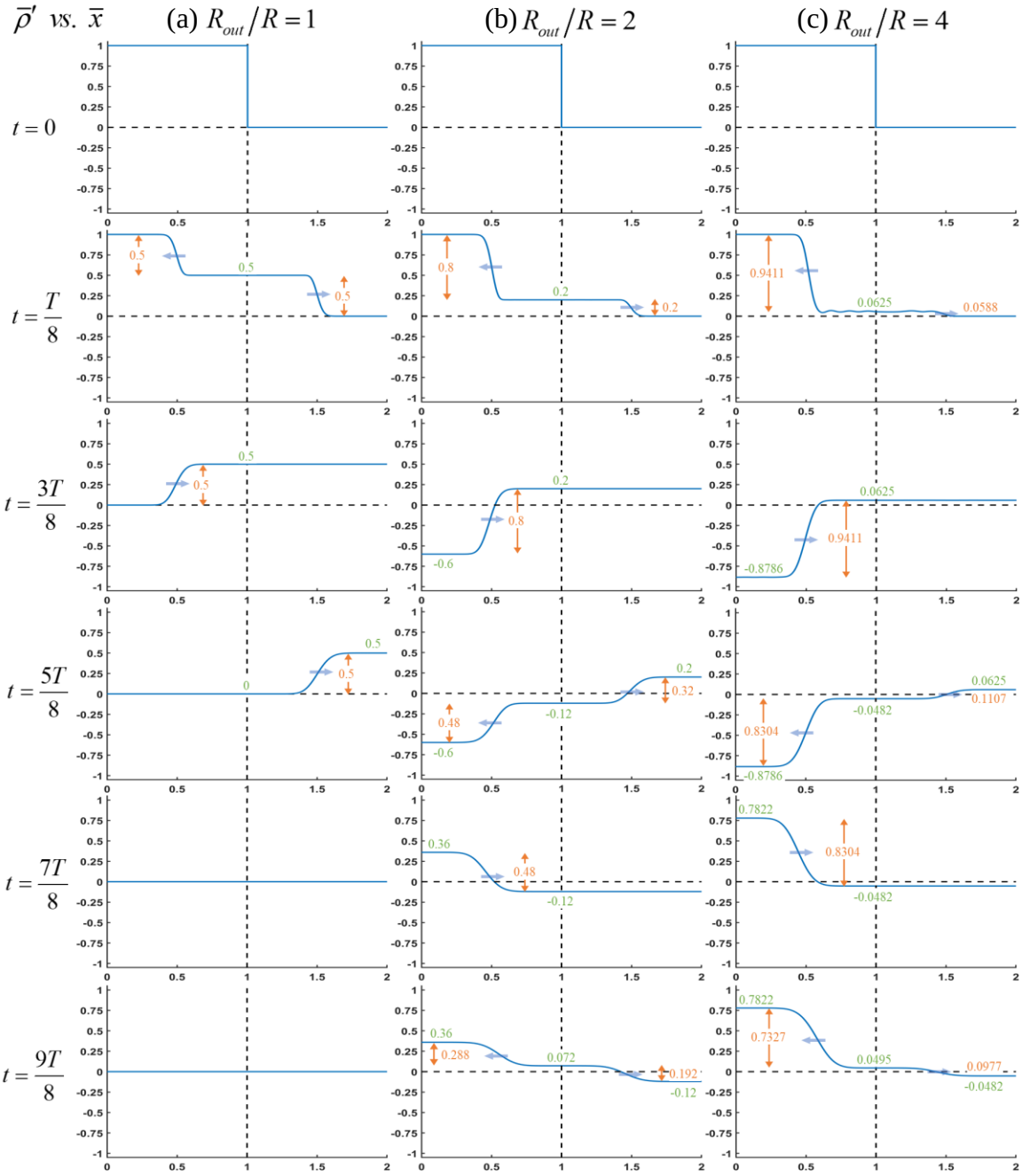

Figure 4.4. Comparison of density wave oscillations inside the tube $(0 \le \bar{x} \le 1)$ and the reservoir $(\bar{x} > 1)$ at different time instances, with the wave direction marked by the blue arrow. (a) capillary size extension $R_{out}/R = 1$. (b) reservoir with $R_{out}/R = 2$. (c) reservoir with $R_{out}/R = 4$. Each red number represents the wave amplitude while the green number shows the current density perturbation level.

4.4.1.2. *Drainage into a reservoir*

Drainage to a reservoir, i.e. $R_{out}/R>1$, is considered in this section. We shall use $R_{out}/R=2$ as an example to illustrate the characteristics of the wave motion. When the diaphragm is broken, the density at the exit drops to $\bar{\rho}_e'=0.2$. The amplitudes of the two initial split waves are no longer equal: the compressional wave propagating out of the capillary into the reservoir has an amplitude of $\tilde{\mathrm{A}}_{out}=0.2$; whilst the inward propagating rarefaction wave has an amplitude of $\tilde{\mathrm{A}}_{tube}=0.8$ (figure 4.4 panel (b) at $t=T/8$). The sum of the amplitudes is still 1.0, but the ratio of the inward-to-outgoing wave-amplitude is $\tilde{\mathrm{A}}_{tube}:\tilde{\mathrm{A}}_{out}=4:1$. This initial amplitude ratio is determined by the cross-sectional area ratio $A_{out}:A=4:1$, which also can be used to determine the exit density level at different time instances as shown below.

As the inward propagating rarefaction wave reaches the sealed-end at $x=0$, it is reflected completely; and the density behind the wave front drops to $\bar{\rho}'=-0.6$. The wave, however, remains the rarefaction type, as the density ahead of the wave front equals density at the tube exit, which is higher than the density behind the wave front. The reflection by the sealed-end doesn't change the wave amplitude as it is still $\left|\bar{\rho}'-\bar{\rho}_e'\right|=0.8$, since the sealed-end is assumed to provide a perfect reflection. Then, the sealed-end-reflected wave travels towards the exit at $x=L$; and once it reaches the exit, a part of the rarefaction wave is transmitted through the exit to the reservoir, while the rest is reflected back to the capillary tube and becomes a compressional wave. The part of the wave that transmits through the exit represents a "leakage" of the fluid into the reservoir. The exit-reflected wave amplitude is determined by the reflection coefficient of the exit/junction, which is $\Re=0.6$ based on equation (4.2). Thus, the amplitude of the exit-reflected wave is

$$\left|\bar{\rho}'-\bar{\rho}'_e\right|_{reflection} = \Re\left|\bar{\rho}'-\bar{\rho}'_e\right|_{incident} = 0.6\times 0.8 = 0.48, \tag{4.3}$$

which is indeed the amplitude of the exit-reflected wave (figure 4.4 panel (b) at $t = 5T/8$).

The incident wave to the exit has an amplitude of 0.8 before splitting into the transmitted and reflected parts at the exit. The sum of the amplitudes of the exit-reflected wave and transmitted wave remains 0.8. This gives the transmitted wave an amplitude of $0.8-0.48=0.32$ (or $(1-\Re)\times 0.8$), i.e. amplitude $\left|\bar{\rho}'-\bar{\rho}'_e\right|_{transmitted} = 0.32$. Since the transmitted wave is a continuation of the incident rarefaction wave, the density ahead of the transmitted wave front is still the previous density at the exit, which is $\bar{\rho}' = 0.2$. Thus, the density behind the transmitted rarefaction wave must be the wave front density minus the amplitude, $0.2-0.32=-0.12$. This is indeed the new value of the density at the exit after the passage of the transmitted wave, as shown by the right-propagating wave portion in figure 4.4 panel (b) at $t = 5T/8$. Thus, unlike the previous case of weak shock-tube problem without an area expansion, the passage of the transmitted rarefaction wave through the exit to the large reservoir reduces the density at the exit, which for the present case, from the initial value of 0.2 to -0.12.

The exit-reflected wave is compressional instead of the incident rarefaction wave, as shown on the $t = 5T/8$ frame in panel (b) of figure 4.4: the density ahead of the wave front is lower than that behind the wave front. This compressional wave is then perfectly reflected by the sealed-end without a change in amplitude, which then travels towards the tube exit as a compressional wave (see the $t = 7T/8$ frame in panel (b) of figure 4.4). This incident compressional wave to the exit is then split into a new exit-reflected part and a transmitted part, determined yet again by the same reflection coefficient of the exit/junction, $\Re = 0.6$. The new exit-reflected wave now becomes a rarefaction wave, with an amplitude

of $0.6\times0.48=0.228$ and propagating back towards the sealed-end. The transmitted part of the wave remains compressional, with the density ahead of the wave front being the same as the incident compressional wave front, i.e. the previous value of the density at the exit, which is -0.12. Since the transmitted compressional wave has an amplitude of $(1-\Re)\times0.48=0.192$, the passage of the transmitted compressional wave *raises* the density at the exit from –0.12 to $0.192-0.12=0.072$ (see the $t=7T/8$ frame in panel (b) of figure 4.4).

The wave reflection-transmission process described above at the tube exit repeats for each cycle, with each cycle comprised of a rarefaction phase of one-half period and a compressional phase of one-half period. When the rarefaction wave hits the exit, it splits into an exit-reflected compressional wave propagating back towards the sealed-end and a transmitted rarefaction wave with the density ahead of the rarefaction wave being the exit density before the wave split. The amplitudes of the two split waves are determined by the reflection coefficient of the exit/junction $\Re$ given by equation (4.2). The amplitude of the transmitted rarefaction wave and the density ahead of the transmitted rarefaction wave front then determines the new exit density, which decreases whenever a rarefaction wave hits the exit. Similarly, for the other half of the period when the compressional wave hits the exit, the exit-reflected wave becomes a rarefaction wave, while the transmitted wave is compressional with the density ahead of the compressional wave front being the exit density before the wave split. The density at the exit after the wave split increases. Thus, over one complete period, the wave transmitted to the reservoir and the exit-reflected wave alternate between rarefaction/compressional; and the exit density oscillates, experiences a decrease and then an increase. The repeated splitting of the wave amplitude at the exit

together with bulk viscous damping cause the wave amplitude to decrease in time. The exit density also decreases in time in a stair-step fashion, which is in stark contrast to the idealized model for a capillary tube without a reservoir/contraction but with fixed exit density.

4.4.1.3. *Drainage into a contraction*

For drainage flow into a contraction, $R_{out}/R<1$. the characteristics of the density wave differs significantly from that for drainage into a reservoir. The case of $R_{out}/R=0.5$, $A_{out}/A=0.25$ is shown in figure 4.5 panel (b) & (c). As the diaphragm breaks, an inward left-propagating rarefaction wave and an outgoing (right-propagating) compressional wave to the contraction are initiated, with their amplitudes determined by the area contraction ratio. The initial density drop of 1.0 across the diaphragm is split according to the area contraction ratio of 1:4, with the outgoing right-propagating compressional wave having an amplitude that is 4 times of that of the left-propagating rarefaction wave, $\tilde{A}_{out}:\tilde{A}_{tube}=4:1$. Thus, the amplitude of the outgoing right-propagating compressional wave is 0.8, whilst the amplitude of the left-propagating rarefaction wave is 0.2. The density (density perturbation) ahead of the outgoing right-propagating compressional wave is zero. Thus, the density at the exit immediately after the wave formation is $\bar{\rho}_e'=0.8$. The inward left-propagating rarefaction wave is perfectly reflected by the sealed-end without changing its rarefaction nature or its amplitude, which then travels towards the exit of the tube at $x=L$ ($t=3T/8$ frame in panel (b) of figure 4.5). The exit of the tube (junction) has a reflection coefficient $\Re=-0.6$. The part of the sealed-end reflected rarefaction wave that has transmitted through the exit into the contraction has an amplitude of

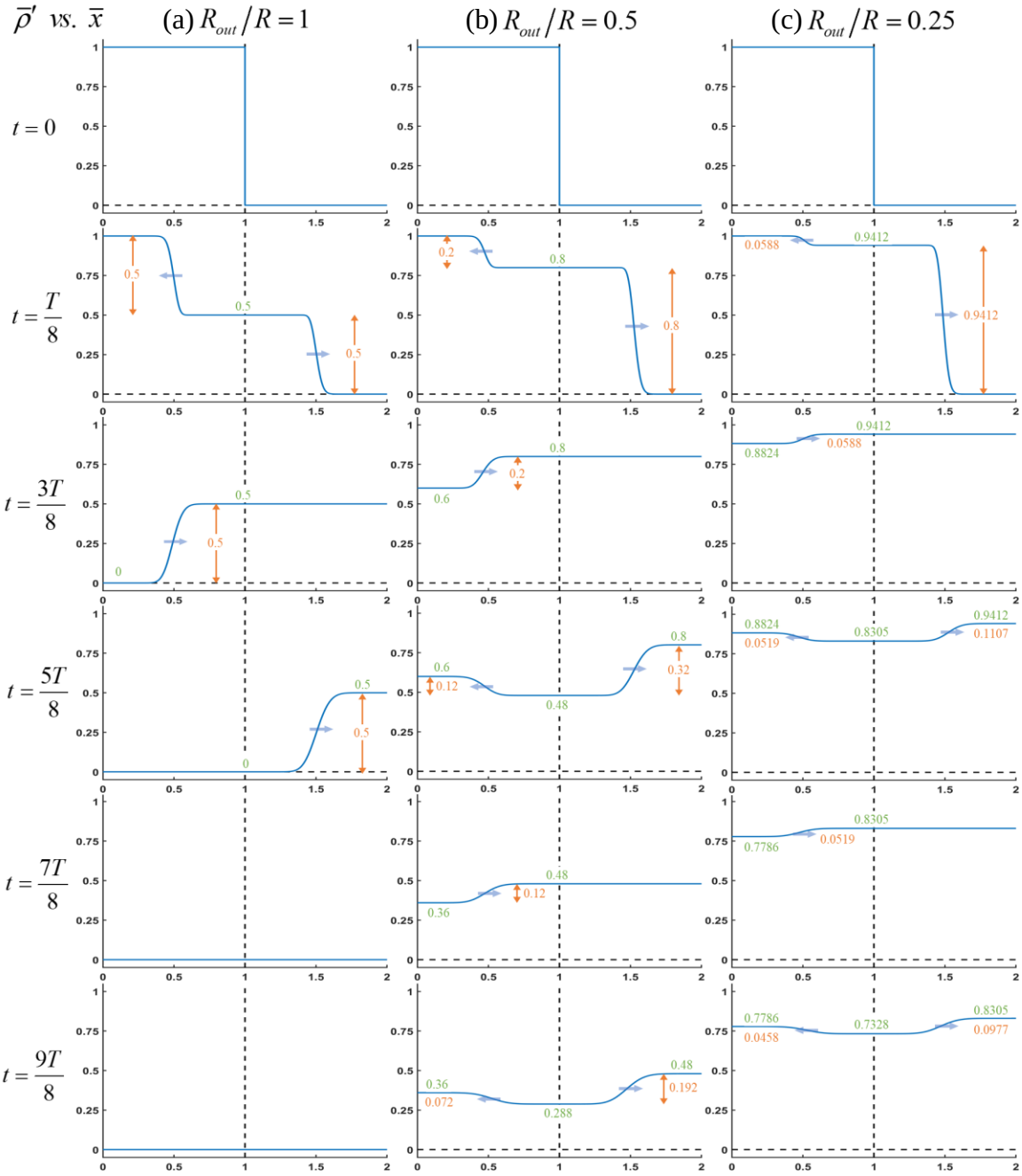

Figure 4.5. Comparison of density wave oscillations inside the tube $(0 \le \bar{x} \le 1)$ and the reservoir $(\bar{x} > 1)$ at different time instances, with blue wave direction marker. (a) capillary size extension $R_{out} = R$. (b) contraction with $R_{out}/R = 0.5$. (c) reservoir with $R_{out}/R = 0.25$. Each red number represents the wave amplitude while the green number shows the current density perturbation level.

$(1-\Re)\times 0.2 = 0.32$, since the incident wave to the exit has an amplitude of 0.2. Since the density ahead of transmitted rarefaction wave is the exit density before the transmission, $\bar{\rho}_e' = 0.8$, the density behind the transmitted rarefaction wave is then $0.8-0.32=0.48$, which should be the new exit density after the passage of the transmitted wave, i.e. $\bar{\rho}_e' = 0.48$ ($t = 5T/8$ frame in panel (b) of figure 4.5).

The part of the sealed-end reflected rarefaction wave that gets reflected by the exit has an amplitude of $\Re\times 0.2 = -0.12$. This negative value indicates a phase shift of 180 degrees of the exit-reflected wave: the exit-reflected wave remains a rarefaction wave as the incident wave, instead of changing to a compressional wave as in the case for a positive reflection coefficient (see the reservoir case). Thus, the density ahead of the exit-reflected wave is $\bar{\rho}_e' + 0.12 = 0.48 + 0.12 = 0.60$, as shown by the inward propagating part in $t = 5T/8$ frame of panel (b) in figure 4.5. This rarefaction wave gets a perfect reflection from the sealed-end, maintain its amplitude and travels towards the exit as the same rarefaction wave, as shown in $t = 7T/8$ in panel (b) of figure 4.5. Once the rarefaction wave hits the exit again, the exit-reflected wave remains as a rarefaction wave, once again due to the negative reflection coefficient of the exit. In other words, the wave inside the tube remains as a rarefaction wave during its life-time. The transmitted wave is still a rarefaction wave, with an amplitude of $(1-\Re)\times 0.12 = 0.192$. This allows us to compute a new exit density as $0.48-0.192=0.288$ (see $t = 9T/8$, panel (b), figure 4.5).

Thus, for drainage into a contraction, after the initial compressional wave traveling into the contraction, only rarefaction waves exist inside the capillary thereafter; whilst for drainage into a reservoir, rarefaction and compressional wave alternate in both the tube and the reservoir. It is worth noting that the density at the exit drops in a stair-step fashion,

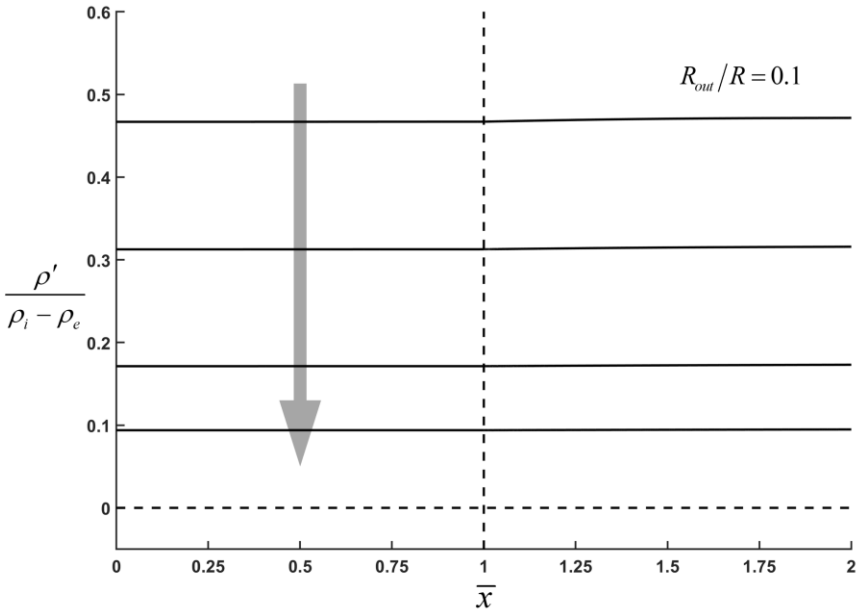

Figure 4.6. Density profile near the tube exit $\overline{x} = 1$ for a strong contraction $R_{out}/R = 0.1$.

without oscillating about zero as experienced by that for the drainage flow into a reservoir.

As the contraction ratio increases (see figure 4.5 panel (c) for the case of $R_{out}/R = 0.25$), the initial amplitude of the inward propagating rarefaction wave becomes much smaller. As a result, the transmitted wave through the exit has an even smaller amplitude. This means that the "leakage" of the fluid via the wave transmission at the exit is small, and the density at the exit drops very slowly. This leads to a prolonged drainage time to empty the tube. In the extreme case of very large contraction, such as $R_{out}/R = 0.1$ shown in figure 4.6, the wave amplitude is so small and the drainage is so slow that it looks like there is no wave inside the system at all. The process looks like quasi-steady. However, this quasi-steady flow must be still described by the wave dynamics, not by incompressible flow of the lubrication type. Such a continuous slow decaying pattern could be used to interpret pressure-driven micro-scale gas flow experiments; as such experiments are usually conducted by connecting a gas storage tank to a conduit via various contraction tubings.

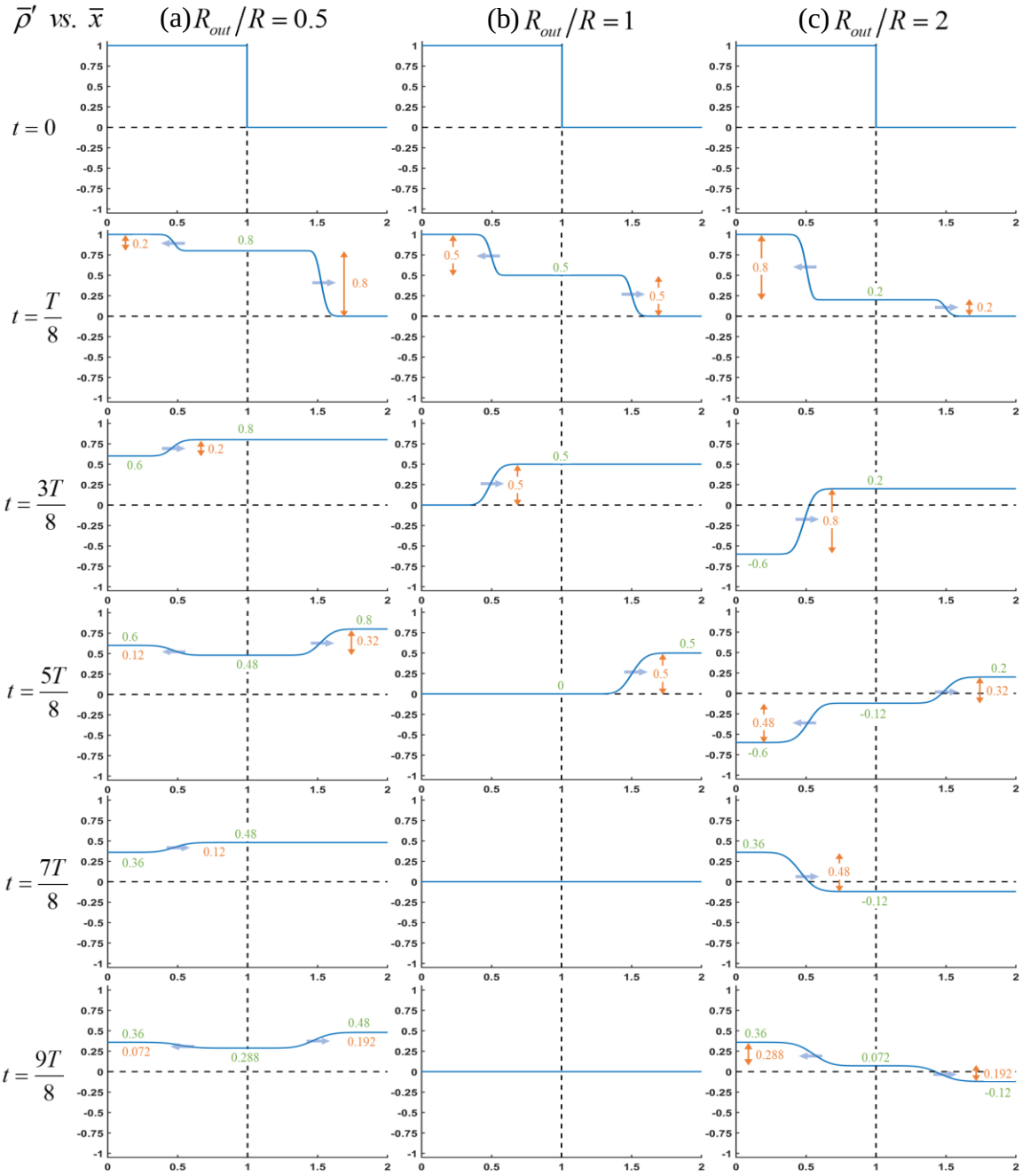

Figure 4.7. Comparison of density wave oscillations inside the tube $(0 \le \bar{x} \le 1)$ and the reservoir $(\bar{x} > 1)$ at different time instances, with blue wave direction marker. (a) contraction with $R_{out}/R = 0.5$. (b) capillary size extension $R_{out} = R$. (c) reservoir with $R_{out}/R = 2$. Each red number represents the wave amplitude while the green number shows the current density perturbation level.

Figure 4.7 illustrates the different characteristics of density wave motion in drainage flows into a contraction (panel a), no-area change (panel b), and a reservoir (panel c).

4.4.2. *The initial wave split ratio*

When the diaphragm breaks, the initial density drop across the exit (diaphragm) is split into two waves propagating in opposite directions: a compressional outgoing wave with an amplitude $\tilde{A}_{out}$ into the reservoir (contraction); and an inward rarefaction wave with an amplitude $\tilde{A}_{tube}$ into to the capillary/channel. The amplitudes of these two waves are measured from the exit density. After simulating many cases with different area expansion/contraction ratios, it is found that the initial wave split ratio Λ, defined as the ratio of the outgoing wave over the inward moving wave, $\Lambda = \tilde{A}_{out} / \tilde{A}_{tube}$, is equal to the reciprocal of the corresponding cross-sectional area ratio, i.e.

$$\begin{aligned} \text{Circular tube}: \quad & \Lambda = \frac{R^2}{R_{out}^2} \\ \text{Channel}: \quad & \Lambda = \frac{(Hw)_{channel}}{(Hw)_{out}}, \end{aligned} \tag{4.4}$$

where H is the channel half-height and w is the channel half-width.

Thus, the amplitude of the wave in the smaller section is always larger than the amplitude of the wave in the larger section. The initial wave split ratio Λ is also related to the reflection coefficient, equation (4.2), by

$$\Re = \frac{1-\Lambda}{1+\Lambda}. \tag{4.5}$$

Since the sum of the two amplitudes equals to the initial density drop of one (all in terms of the dimensionless density perturbation),

$$\tilde{A}_{out} + \tilde{A}_{tube} = 1, \tag{4.6}$$

we find the two amplitudes as

$$\begin{aligned} \tilde{A}_{out} &= \frac{\Lambda}{1+\Lambda} \\ \tilde{A}_{tube} &= \frac{1}{1+\Lambda} \end{aligned}. \tag{4.7}$$

with Λ given by the duct contraction ratio specified by equation (4.4).

The density (perturbation) at the exit immediately after the initial wave split is given by

$$\bar{\rho}'_{e,0} = \tilde{A}_{out} = \frac{\Lambda}{1+\Lambda}. \tag{4.8}$$

Thus, the amplitudes of the two initial waves as well as the density at the exit are completely determined by the cross-section expansion/contraction ratio at the exit, given by equation (4.4).

4.4.3. *Dimensionless density perturbation at the sealed-end and the exit*

The dimensionless density perturbation at the sealed-end, $\bar{\rho}'_s$, and at the exit, $\bar{\rho}'_e$, are plotted against the number of period in figure. 4.8 for $R_{out}/R = 1.0,\ 2.0,\ 0.5$ (extended tube, reservoir, contraction, respectively). The period is $T = 4L/c$.

For the extended tube (i.e. weak shock-tube problem), both $\bar{\rho}'_s$ and $\bar{\rho}'_e$ only experience a step drop to zero, which occurs one-half period apart (the blue lines). For a reservoir, both $\bar{\rho}'_s$ and $\bar{\rho}'_e$ oscillate about the final equilibrium value of zero with a time-decaying amplitude, and $\bar{\rho}'_e$ lags $\bar{\rho}'_s$ by one-half period. For the contraction, $\bar{\rho}'_s$ and $\bar{\rho}'_e$ do not oscillate about zero: they drop in a stair-step fashion with a decreasing step size, and again $\bar{\rho}'_e$ lags $\bar{\rho}'_s$ by one-half period.

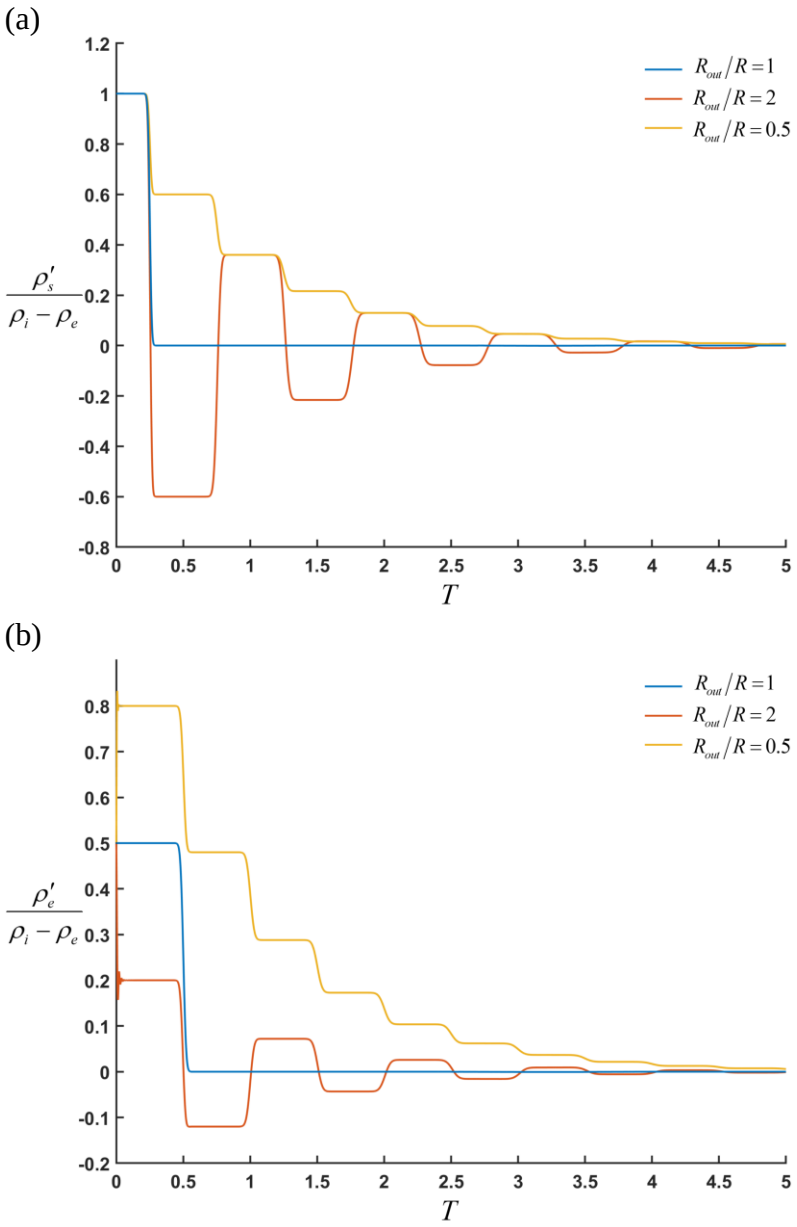

Figure 4.8. Dynamic density (dimensionless density perturbation) variation: (a) at the sealed end $x=0$; (b) at the tube exit $x=L$. T is the period of oscillation. Note that only for drainage to a reservoir that the density oscillates about zero (the final equilibrium value for the dimensionless density perturbation).

As described above, after the initial wave split, the inward propagating wave in the small capillary (channel) travels towards the sealed-end, where it is reflected completely. The density at the sealed-end $\bar{\rho}_s'$ changes and its value can be computed using the reflection

coefficient of the sealed end (which equals 1). The sealed-end-reflected wave travels towards the exit. The partial reflection and partial transmission of the sealed-end-reflected wave at the exit changes the density at the exit $\bar{\rho}'_e$. The new exit density can be computed using the reflection coefficient of the exit (junction) given by equation (4.2). Starting from the initiation, the wave will be reflected by the sealed-end and the exit once every one-half period. The repeated reflections by the sealed end and the exit allows us to derive recursive formulas for the density at the sealed-end and the exit:

$$\begin{aligned}
&\bar{\rho}'_{s,0} = 1, \;\; \bar{\rho}'_{e,0} = \frac{\Lambda}{1+\Lambda} \\
&\bar{\rho}'_{s,n} = 2\bar{\rho}'_{e,n} - \bar{\rho}'_{s,n-1}, \qquad \left(n-0.5\right)\frac{T}{2} \le t \le \left(n+0.5\right)\frac{T}{2}, \;\; n = 1,2,3\ldots \\
&\bar{\rho}'_{e,n} = \frac{\Lambda}{1+\Lambda}\bar{\rho}'_{s,n-1}, \qquad \left(n-1\right)\frac{T}{2} \le t \le n\frac{T}{2}, \;\; n = 1,2,3\ldots
\end{aligned} \tag{4.9}$$

where $T = 4L/c$ is the oscillation period.

4.4.4. *Instantaneous mass inside the conduit and the mechanism of mass production*

4.4.4.1. *Extended conduit (weak shock-tube problem)*

The instantaneous mass inside the conduit can be calculated by integrating the density perturbation distribution in the conduit (figure 4.9). For the same size extension $R_{out}/R = 1$, the drainable gas inside the conduit only experiences a rarefaction phase without any oscillation As a result, the normalized excess mass M/M_L inside the conduit decreases linearly from 1 to 0 (figure 4.9a). This numerical result agrees with the analytical solution obtained from the Green's function for the pressure (corresponding to an initially concentrated impulse) of the damped wave equation given by Buckingham (2005). The

analytical result also shows no oscillation in the excess density inside the channel, and the excess density always stays above zero. Detailed derivation is shown in Appendix D.

4.4.4.2. *Reservoir*

While the exit reflection coefficient $\Re$ as given by equation (4.2), is useful for describing the amplitudes of the exit-reflected and transmitted waves, it cannot be used as a boundary condition at the exit. In our simulation, a non-reflecting outflow boundary condition is imposed at the far end of the reservoir via the perfectly matched layer (PML); and no boundary condition at the tube exit is imposed. Both the density and its gradient at the exit change with time and they are determined from the numerical simulations. Thus, the numerically computed solution for a realistic configuration is not a standing wave, which is the case for the idealized model with the reservoir and prescribed exit density.

For a reservoir, $R_{out}/R>1$, starting from a rarefaction density wave, the wave inside the tube alternates between rarefaction wave and compressional wave, with each wave type taking up one-half period and the switching occurs when the wave front arrives at the exit. When the rarefaction wave arrives at the exit at odd-multiple of half-period (i.e. $t=(2n+1)T/2$), part of the wave transmits past the exit as a "puff", with the exit density $\overline{\rho}_e'$ experiencing a sudden drop (see the red curve in figure. 4.8b at $t=0.5T, 1.5T$). This drop in the exit density transports fluid mass through the exit. On the other hand, the exit-reflected part of the wave remaining inside the tube becomes compressional, traveling back towards the sealed-end. When this compressional wave, after being reflected by the sealed-end, returns to the exit at the end of each period (even-multiple of half-period, such as $t=T, 2T$ in figure 4.8b for the red curve), the transmitted wave through the exit creates a "huff", with a step jump in the exit density. This jump in the exit density causes the gas

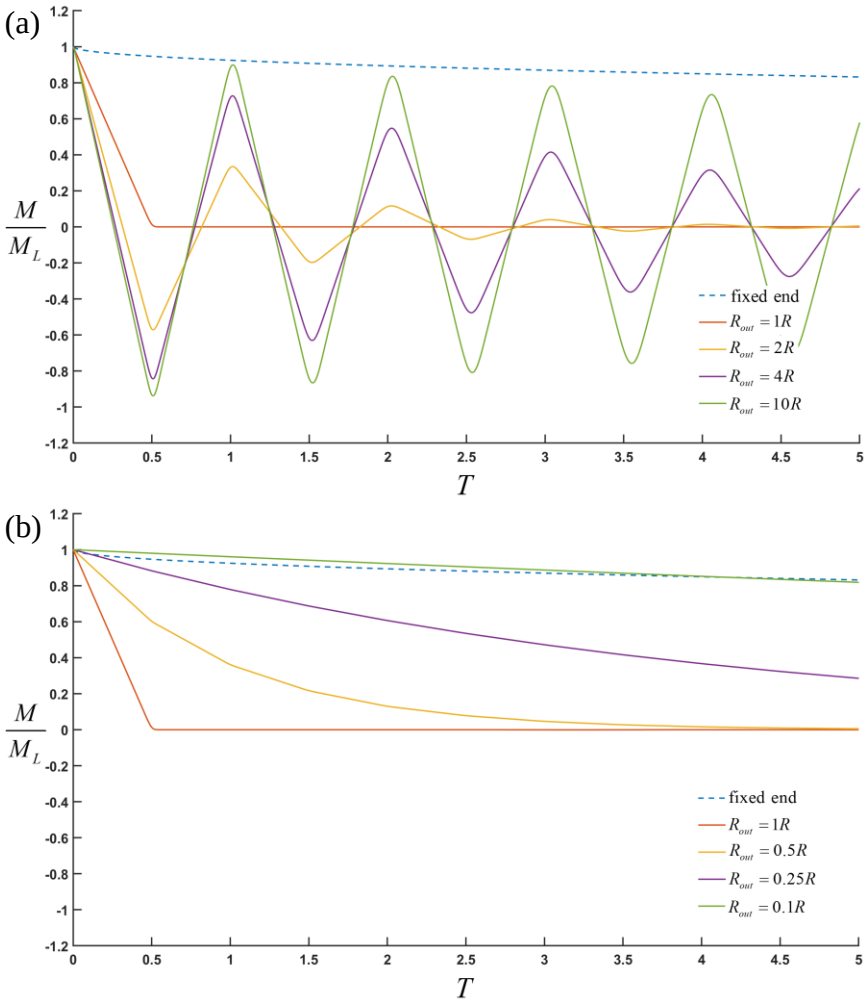

Figure 4.9. Instantaneous mass inside the capillary. (a) reservoirs; (b) contractions. The dash line represents the mass envelope curve with the prescribed exit density boundary (section 2.7).

from the reservoir to move back into the tube. This huff-n-puff action creates an oscillation in the exit density, which in turn induces an oscillation of the mass inside the tube, as shown in figure 4.9a. The time-decay in the amplitude of the wave due to the reflection and split by the exit and viscous damping ensures that a net mass drainage results in each period. The amplitude of the oscillation depends on the initial wave split ratio and the reflection coefficient of the exit, which in turn both depend on the reservoir-to-tube expansion ratio. For a given conduit size, a larger size reservoir gives a larger reflection coefficient at the

exit. A large exit reflection coefficient slows down the drainage process by reflecting a larger portion of the density perturbation wave back into the tube and a smaller decrease in the wave amplitude when the wave arrives at the exit. As a result, the density wave oscillates inside the tube for a longer time, resulting in a longer drain-out time. This effect from the reservoir expansion ratio is clearly demonstrated in figure 4.9a. For the reservoir radius expansion ratio of $R_{out}/R = 2$ (the yellow curve in figure 4.9a), the mass inside oscillates with a time-decaying amplitude. After about 3 period (n = 3), the amplitude approaches zero and the gas is drained out. As the reservoir radius expansion ratio is increased to $R_{out}/R = 4$, the amplitude of the mass oscillation is much larger and it decays much slowly in time, significantly increases the drain-out time (the purple curve). Such a trend persists for larger reservoir radius expansion ratio $R_{out}/R = 10$ (green curve).

It is noted that as the reservoir radius expansion ratio R_{out}/R becomes very large, the envelope of the instantaneous mass approaches the envelope of the instantaneous mass computed using a *fixed exit density boundary condition* at the tube exit without a reservoir, which is the blue dashed curve in figure 4.9a. The case of infinitely large reservoir gives the slowest drain-out time.

As we have mentioned earlier, the reflection coefficient at the exit cannot be used as a boundary condition: for a very large reservoir, the exit reflection coefficient is $\Re = 1$. This would have indicated a perfect reflection, which would have implied $\partial\rho / \partial x\big|_{x=L} = 0$. If such a boundary condition is used, then no fluid will be able to leak into the reservoir by any means, and the wave would have been locked inside, only being damped out by viscous dissipation. The physics in a real system is such that no boundary condition is imposed at the exit, and the exit density oscillates with a time-decaying amplitude.

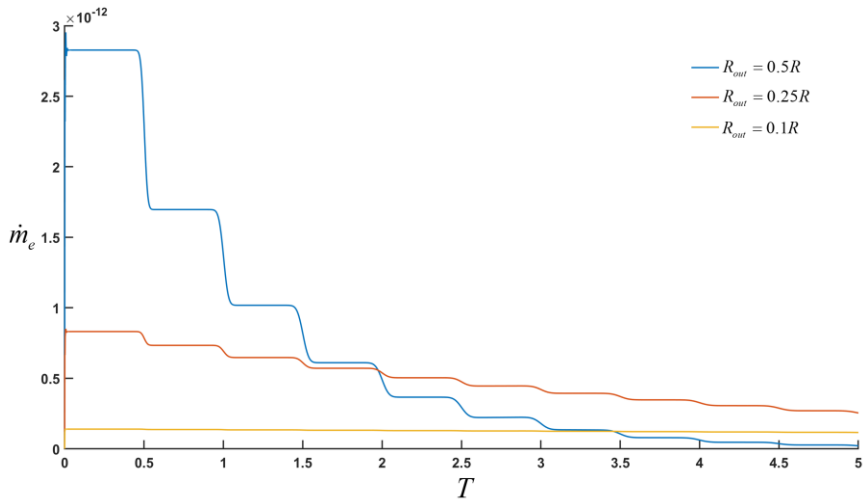

Figure 4.10. Instantaneous mass flow rate vs. oscillation period for different size contraction.

4.4.4.3. *Contraction*

For a contraction, $R_{out}/R < 1$, the reflection coefficient at the exit is negative, $\Re < 0$. This causes a phase shift of the wave upon reflection by the exit. Thus, as discussed above, the wave inside the tube is always a rarefaction wave. Therefore, gas leaks out of the tube every time the wave hits the exit, and there is no huff-n-puff action as in the case of drainage into a reservoir. The mass inside drops with time without oscillation (figure 4.9b). In fact, the mass inside drops in a piece-wise linear fashion: in each half-period, the mass decreases linearly, with the slope changing at the end of the period. Thus, the mass flow rate, which is the time rate of change of the instantaneous mass inside the tube, drops in a stair-step fashion every half oscillation period (figure 4.10)

Decreasing the ratio R_{out}/R slows down the drainage significantly. When $R_{out}/R \to 0$, the mass inside the capillary tends to its original value, and no drainage occurs, as expected.

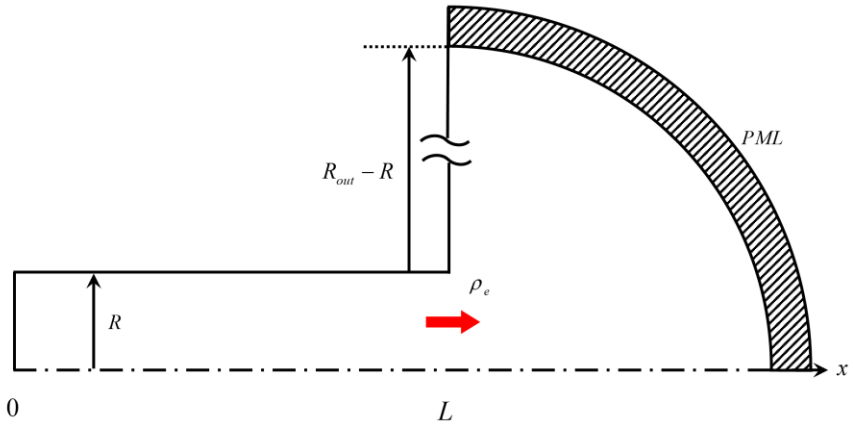

Figure 4.11. Drainage from a capillary tube connected to a large reservoir filled with same fluid. Perfectly Matched Layer is placed at the far end of the reservoir.

4.5. Drainage flow into an infinite large reservoir

The case of an infinitely large reservoir deserves special attention. Since the reservoir is unbounded, the no-reflection boundary condition has to be implemented over a larger circle if a finite computational domain is to be used. In our simulation, a quarter sector shape reservoir with a ring PML (figure 4.11) is used to mimic the infinitely large reservoir. Such modification not only removes the wave reflection from the reservoir side-wall (figure 4.1a), but also further reduce the numerical error generated from the PML algorithm by avoiding non-zero wave contact angle to the layer. Reservoir radius was set to $R_{out} = \max\left[250R, 2L\right]$, ensuring a large enough split ratio. The thickness of the PML was set to $\delta_{PML} = 0.25R_{out}$.

4.5.1. *Density pulse wave transmission*

For an infinitely large reservoir, the exit density quickly drops to zero during the initial wave split from equation (4.8), as $\Lambda \to 0$. One could have calculated the amplitudes of the two initial split wave as $\tilde{A}_{tube} = 1$ and $\tilde{A}_{out} = 0$, from equation (4.7). In reality, however,

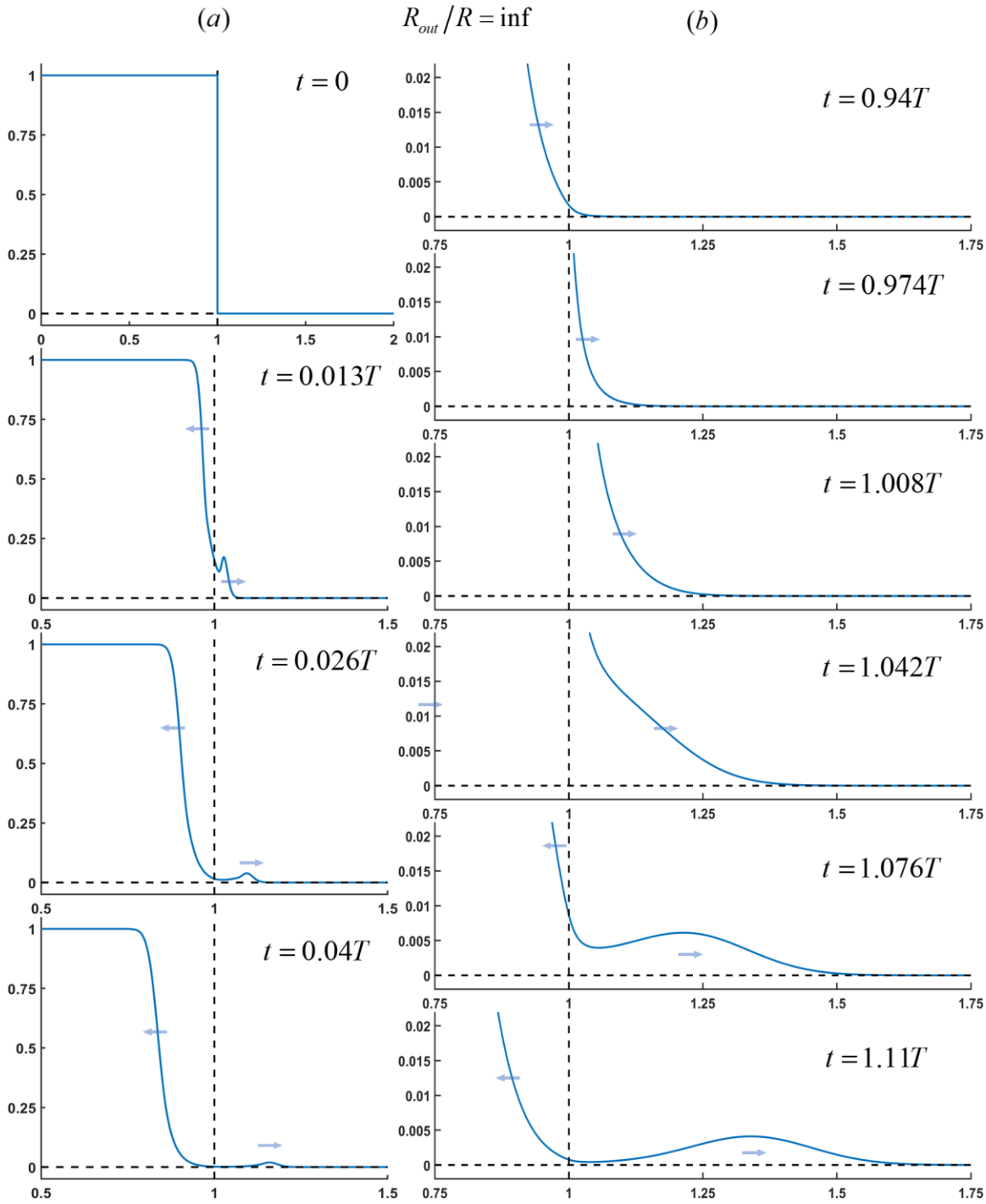

Figure 4.12. Density wave oscillations inside the tube $(0 \le \bar{x} \le 1)$ and the infinite large reservoir $(\bar{x} > 1)$ at different time instances. (a) Initial wave split. (b) A density pulse passes into the infinitely large reservoir when the rarefaction wave is getting reflected at the exit and becomes a compressional wave.

the initial density wave split has a little twist, as a small pulse is formed and sent into the reservoir before the exit density drops to zero. (figure 4.12a). Such pulse transmission does not signify the breakdown of the initial wave split ratio theory described above as $\tilde{A}_{out} = 0$ only shows the steady outgoing-wave amplitude solely affected by the area difference, which in this case, is indeed zero. This indicates that, while the exit has a reflection coefficient $\Re \to 1$, the "perfect" reflect differs from that from a rigid surface such as the sealed-end. It is a "soft" or "elastic" perfect reflection: the exit allows a small pulse to pass through, while the perfect reflection of the incident wave is slightly delayed (i.e. not instantaneous), with a negligible change in amplitude $\tilde{A}_{tube} = 1$.

The density pulse transmission is also observed whenever the sealed-end-reflected density wave arrives at the exit. As equation (4.2) shown above, the reflection coefficient at the exit is $\Re \to 1$. However, the infinitely large reservoir with small impedance per area $Z_2 = 1/A_2$ could not reflect all the incident wave instantaneously without letting it pushes through the exit for a short distance. Thus, a density pulse is sent to pass through the exit during the exit-reflection time window (figure 4.12b). Noticed, as the sealed-end-reflected wave passes through the exit before getting reflected, the overall distance for the wave to travel within each oscillation period is actually a little bit longer than the tube length L. Since the wave speed is constant, the actual oscillation period will be slightly larger than $T = 4L/c$.

As shown in figure 4.13b, the dimensionless density perturbation at the exit $\bar{\rho}'_e$ is plotted against the oscillation period $T = 4L/c$, for 3 different size reservoirs ($R_{out}/R = 2$, 5 and 250). The first 2 cases represent finite size reservoir (figure 4.1a) and the last case represents infinitely large reservoir (figure 4.11). As the sealed-end-reflected wave reaches

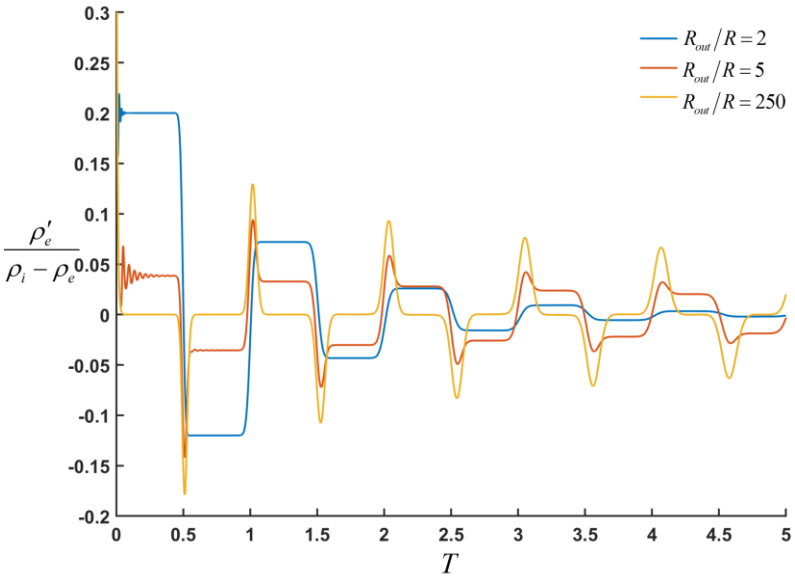

Figure 4.13. Dimensionless density perturbation at the exit level variation at the tube exit $x=L$. T stands for the oscillation period.

to the exit about every half oscillation period $t \sim 0.5T, T...$, the exit density spikes because the density wave is pushing through the exit (pulse transmission) during the exit-reflection time window. Most importantly, this pulsatile change is unified even for the small size reservoir (blue curve in figure 4.13) simply because its exit density doesn't recover to prior value but maintained at a new level as the transmitted wave doesn't has enough space to disperse but being confined within the small reservoir. The red curve in figure 4.13b, $R_{out}/R=5$, clearly shows that the pulse transmission exits even for finite size reservoir.

4.5.2. *Continuous leaking and pulse leaking*

After discovering the full picture of the density wave evolution with different size reservoirs, we introduce two leaking mechanisms as the "Continuous Leaking" (CL) and the "Pulse Leaking" (PL), corresponding to two different density wave evolutions (wave reflection and pulse transmission). Both leaking mechanisms exist for different size

reservoir. With small expansion area ratio, the continuous leaking dominates, as a large fraction of each sealed-end-reflected wave will pass through the exit. As the expansion area ratio increases, the leaking fraction decreases (or $\Re$ increases). The leaking mechanism gradually change to a pulse leaking with a small density pulse passes through the exit during each exit-reflection time period. Unlike the continuous leaking, which is determined by the reflection coefficient $\Re$ (or area ratio), the pulse leaking mechanism only depends on the sealed-end-reflected wave energy as a steeper wave can push through the exit further before getting reflected. This aspect needs to be investigated further.

4.6. Summary the influence factors for drainage with a reservoir or a contraction

To summary, we discovered that the same size extension, reservoir and contraction affects the mass production driven by the volume-expansion from a micro-conduit by at least 5 aspects.

(a) Diffusion coefficient D_ρ, which controls the density wave damping effect while it is propagating inside the micro-conduit (section 2.7).

(b) Continuous leaking of the density wave amplitude caused by the density wave reflection at the conduit exit, controlled by the reflection coefficient at the exit $\Re$, which depends on the area ratio at the exit or the initial wave split ratio Λ. This leaking mechanism decreases with an increasing reservoir size.

(c) Pulse leaking of density wave caused by the pulse transmission during density wave reflects at the conduit exit, This leaking mechanism exits for any size reservoir or contraction and it becomes dominant when the continuous leakage is minimal when $\Re \to 1$. Contrary to continuous leakage, this leakage effect does not depend on the size of the

reservoir or contraction ($\Re$ or Λ), but the kinematic energy of the sealed-end-reflected density wave within each oscillation. This result requires further study and quantification.

(d) Oscillation period is increased slightly due to the extended distance for the wave to travel through the exit during non-instantaneous reflection of the exit.

(e) Instantaneous mass arising at each half period due to the exit density spikes. This last aspect results in a slightly higher mass envelope curve than the drainage flow with *fixed exit density boundary condition* used in Chapter 2, especially for minimal wave leaking case which will be discussed later.

4.7. Mass flow rate and effective diffusion coefficient for an infinite reservoir

In Chapter 2, we have derived an analytical solution for the mass flow rate (drainage rate) for time much larger than the period of acoustic oscillation for drainage flow from a very narrow tube with a fixed exit density $\rho_e' = 0$ in the absence of a reservoir. This solution is the leading order solution for a very narrow tube, $R/L \to 0$. Compared to a realistic application, two important factors are missing in this solution: (a) in reality, the tube is not infinitely thin, i.e. R/L is small but not zero; (b) the tube is always connected to a reservoir, even though the reservoir may be very large compared to the tube. When the condition (b) is taken into consideration, the density at the exit is no longer fixed, as illustrated by the examples shown in the previous sections. The analytical solution is a standing wave solution, which must be corrected by time-decaying exit density when a reservoir is present.

The analytical solution for drainage flow from a tube with a fixed exit density (equation 2.29), however, is simple to use, and it is a diffusion solution. It would be of tremendous

engineering value if we can adopt this analytical solution and use it for realistic situations with a narrow tube and a large reservoir (i.e. extending the solution to finite size tube and large reservoir, with the latter relaxing the fixed exit density condition) by modifying the diffusion coefficient from D_ρ to an effective diffusion coefficient D_{eff}. To this end, we perform a large number of numerical drainage flow simulations for various sizes of the capillary tubes with a very large reservoir. The simulations are carried out till 99% of the mass (drainable mass) has drained out the tube. We then use the above-mentioned analytical solution to compare with the numerical simulation, and to extract an effective diffusion coefficient.

4.7.1. *Normalized excess mass reduction and its approximations*

Due to the computational cost, only relatively short micro-capillaries are simulated here for the entire drainage process; and variation of the capillary tube length will be considered later. Here $R = 1\mu\text{m}$, $L = 50\text{um}$, $c = 450\text{m/s}^2$, $D_\rho = 5\times10^{-5}\text{m}^2/\text{s}$, $R_{out}/R = 250$. This size of the reservoir with PML is large enough that a further increase in the reservoir size does not change the mass reduction anymore. Small initial density levels were used in the present simulation $\rho_i = 1.01\text{kg/m}^3$, $\rho_e = 1\text{kg/m}^3$. It is noted that the initial density perturbation level $\rho'_{t=0} = \rho_i - \rho_e$ does not affect the percentage of mass reduction governed by the damped wave equation (2.15).

The normalized excess mass, which is integrated from the density perturbation profile over the conduit, oscillates about zero (its final equilibrium value) with a time-decaying amplitude (blue lines in figure 4.14a). The red line is the envelope of the normalized excess mass; whilst the yellow line is the envelope of the excess mass computed from the ideal

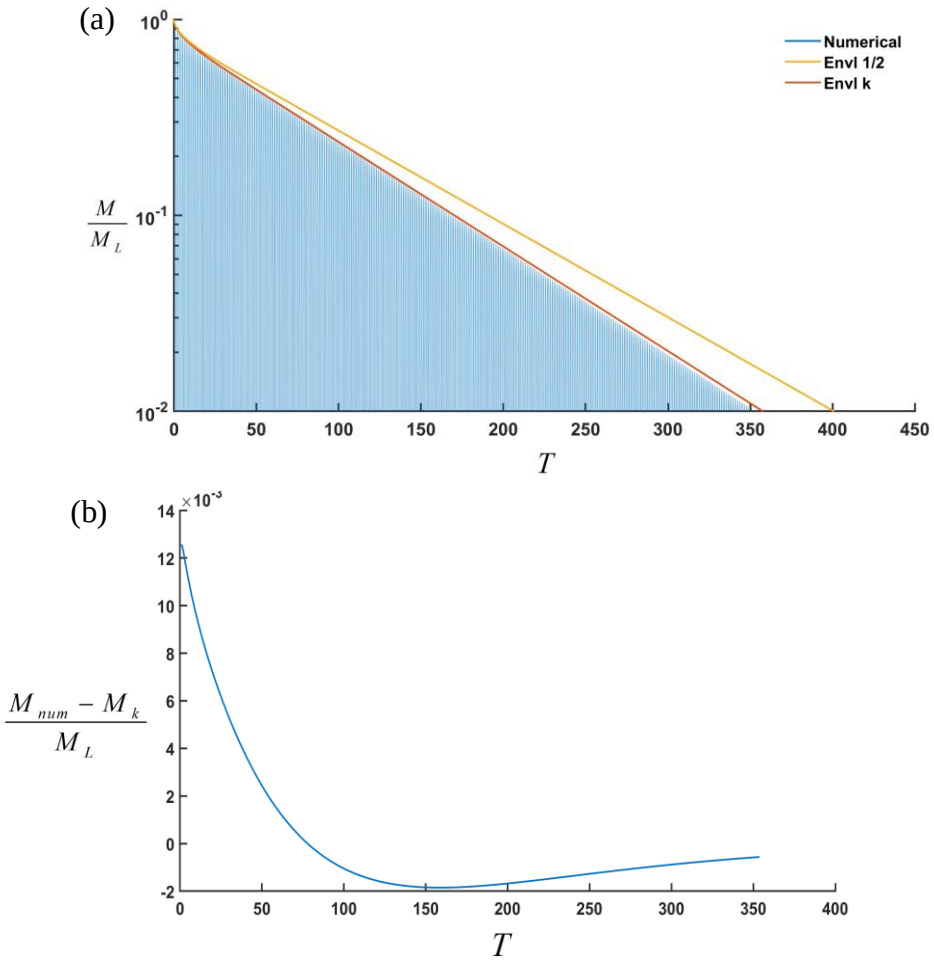

Figure 4.14. (a) Normalized instantaneous excess mass vs. oscillating period $T = 4L/c$. M_L is the total amount of producible fluid from the capillary. The oscillatory blue curve represents numerical simulation with a large reservoir. The yellow curve is the analytical solution for the excess mass envelope for the idealized system. The red curve represents modified mass solution with a revised multiplier k. (b) Error of the ideal system vs. oscillating period.

model with a fixed exit density without the reservoir. The envelope comparison shows that, with the pulse leakage occurring twice every period as described above, the excess mass of the real system decreases faster than that of the ideal system. This difference in the instantaneous excess mass can also be described as a relative error of using the idealized system (tube without reservoir with a prescribed exit density) to model the realistic system, which is plotted in figure 4.14b.

Figure 4.14a also shows that if one insists on using the ideal system to model the realistic system, one can modify the diffusion coefficient in the ideal system from $D_\rho / 2$ to kD_ρ, with $k > 0.5$. Indeed, we will extract an approximate expression for the dimensionless multiple k in the following sub-section.

4.7.2. *Effective diffusion coefficient*

As discussed earlier, we wish to modify the diffusion coefficient in the idealized system so that the analytical solution of the idealized system can be used to compute the mass flow rate of a realistic system with a reservoir. To this end, curve-fitting is performed using linear regression method (Draper 1998). The diffusion coefficient in the analytical solution of the envelope of the excess mass of the idealized system is changed to $D_{eff} = kD_\rho$. The sum of square due to error (SSE) is calculated from the difference between the envelope of the numerically computed excess mass for the realistic system and that of the idealized system at the same time instance,

$$SSE = \sum_{i=1}^{n} \left(m_i - m_{envl,i} \right)^2 , \tag{4.10}$$

where the sum is carried out the discrete time instants computed. The effective diffusion coefficient is found by minimizing SSE. With this procedure, we can find an effective diffusion coefficient that gives a maximum error below 2.2% of the total producible mass M_L. Detailed error plots will be shown in the following section.

Numerical simulations show that the mass envelope depends on the parameter cR/D_ρ, which is the acoustic Reynolds number based on the tube radius. We can define the acoustic Reynolds number in terms of the tube cross-sectional area as $Re_a = c\sqrt{\pi R^2}\Big/D_\rho$. Another

$R(\mu\text{m})$	L/R	Re_a	k_{optimal}
0.25	25	3.988	0.494268
0.5	25	7.976	0.533664
1	25	15.952	0.612598
0.25	50	3.988	0.497274
0.5	50	7.976	0.518317
1	50	15.952	0.560438
0.25	100	3.988	0.498684
0.5	100	7.976	0.509563
1	100	15.952	0.531333
0.25	200	3.988	0.499405
0.5	200	7.976	0.504936
1	200	15.952	0.516015

Table 4.1. Effective diffusion coefficient multipliers for micro-capillary drainage flow

dimensionless parameter that comes into play is the tube length-to-radius ratio, L/R, as the drainage process will become more diffusively dominant with smaller pulse leakage for a longer tube. For an infinitely large reservoir, the effective diffusion coefficients kD_ρ for various parameters are computed and listed in table 4.1. Other flow properties held constants in these computations are: $c = 450\text{m/s}^2$, $D_\rho = 5\times10^{-5}\text{m}^2/\text{s}$, $R_{out}/R = 250$, $\rho_i = 1.01\text{kg/m}^3$, $\rho_e = 1\text{kg/m}^3$. Six significant digits were kept for k during the regression procedure for better accuracy.

4.7.3. *Acoustic Reynolds number and length-to-radius ratio dependence*

4.7.3.1. *Micro-capillary and 3D micro-channel*

As shown in figure 4.15a, with constant length-to-radius L/R, the effective diffusion coefficient k is linearly proportional to the acoustic Reynolds number Re_a. Higher length-to-radius ratio results in a smaller linear slope. On the other hand, with constant Re_a, k

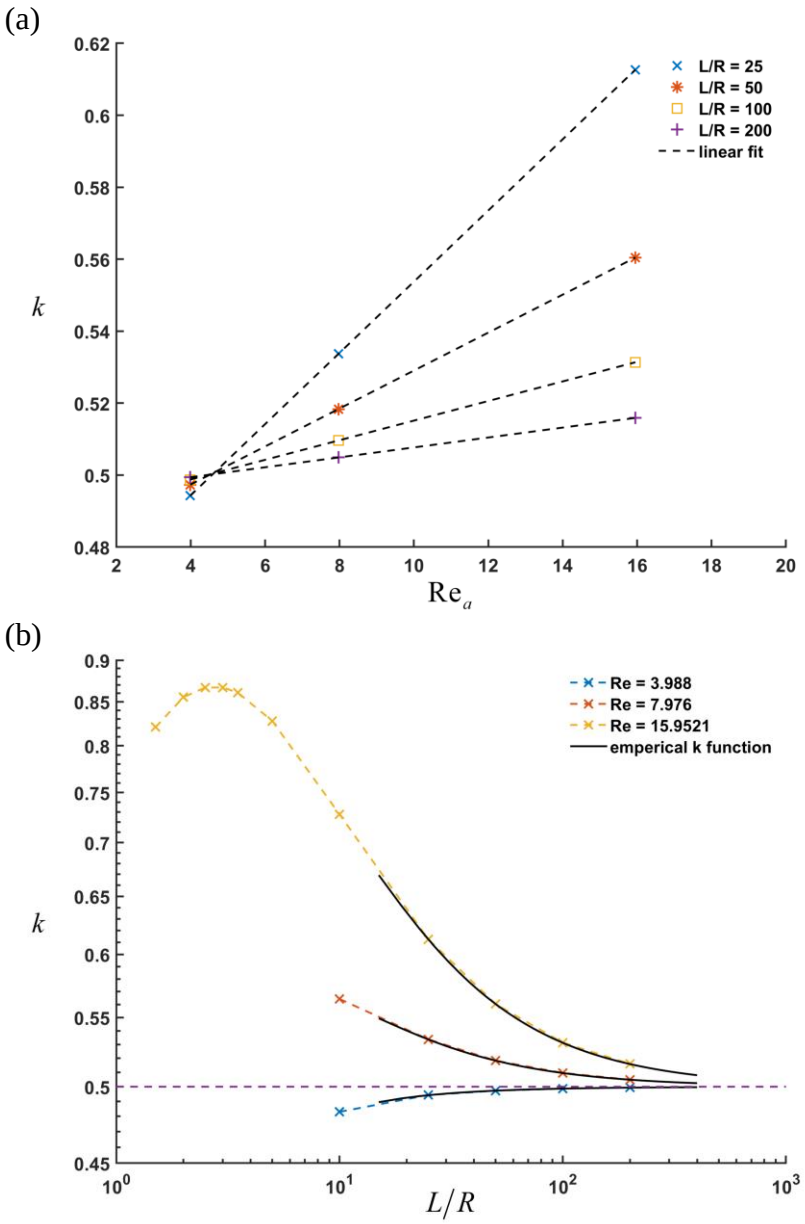

Figure 4.15. Effective diffusion coefficient multiplier relationship with (a) acoustic Reynolds number and (b) Length-to-Radius ratio of the micro-capillary.

converges to 0.5 smoothly with increasing L/R (figure 4.15b).

As discussed earlier, $k = 0.5$ stands for a drainage flow solution computed from an ideal model using fixed outlet condition without a reservoir. Any deviation from $k = 0.5$ indicates a variation of the overall drainage speed affected by the reservoir. Thus, by

increasing the acoustic Reynolds number (or tube radius), the pulse leaking effect is enhanced. As a result, the drainage flow with infinitely large reservoir gains additional draining speed than the ideal model. The second parameter L/R, however, lower the reservoir influence, with respect to the overall drainage speed. As the conduit length L increases, the density wave travels a longer distance inside the capillary. Since the pulse leaking only happens twice in every oscillating period when the density wave is reflected at the conduit exit, the whole drainage process becomes more diffusive dominant as it takes less oscillating period to drain completely. It is worth noting that, with longer conduit, the oscillating period but the drainage time is longer as $T = 4L/c$. As a result, the overall draining process with infinitely large reservoir approaches to the ideal model ($k \to 0.5$).

Noticed, for $Re_a = 3.988$ ($R = 0.25\mu m$), the effective diffusion coefficient multiplier converges to $k = 0.5$ from below, which indicates a drainage rate reduction as the opposite to a higher Reynolds numbers. This departure reveals the fifth aspect shown in section 4.6. Under such a small acoustic Reynolds number, the drainage enhancement caused by the pulse leaking is very weak. The instantaneous mass arising at each half period due to the exit density spikes exceeds the pulse leaking effect. Thus, the overall drainage process with $Re_a = 3.988$ is slower than the ideal model.

Additional effective diffusion coefficient multipliers were calculated from the numerical simulation for small length-to-radius ratio $L/R < 25$. As figure 4.15b shown above, k first increases to a maximum before it starts converging 0.5 with increasing L/R. Because small L/R leads to a short oscillation period $T = 4L/c$. In other words, the interval between each exit-reflection is reduced. There is such a L/R limit so that the exit density perturbation can never recover back to 0 between each “spike”. Thus, the pulse leaking

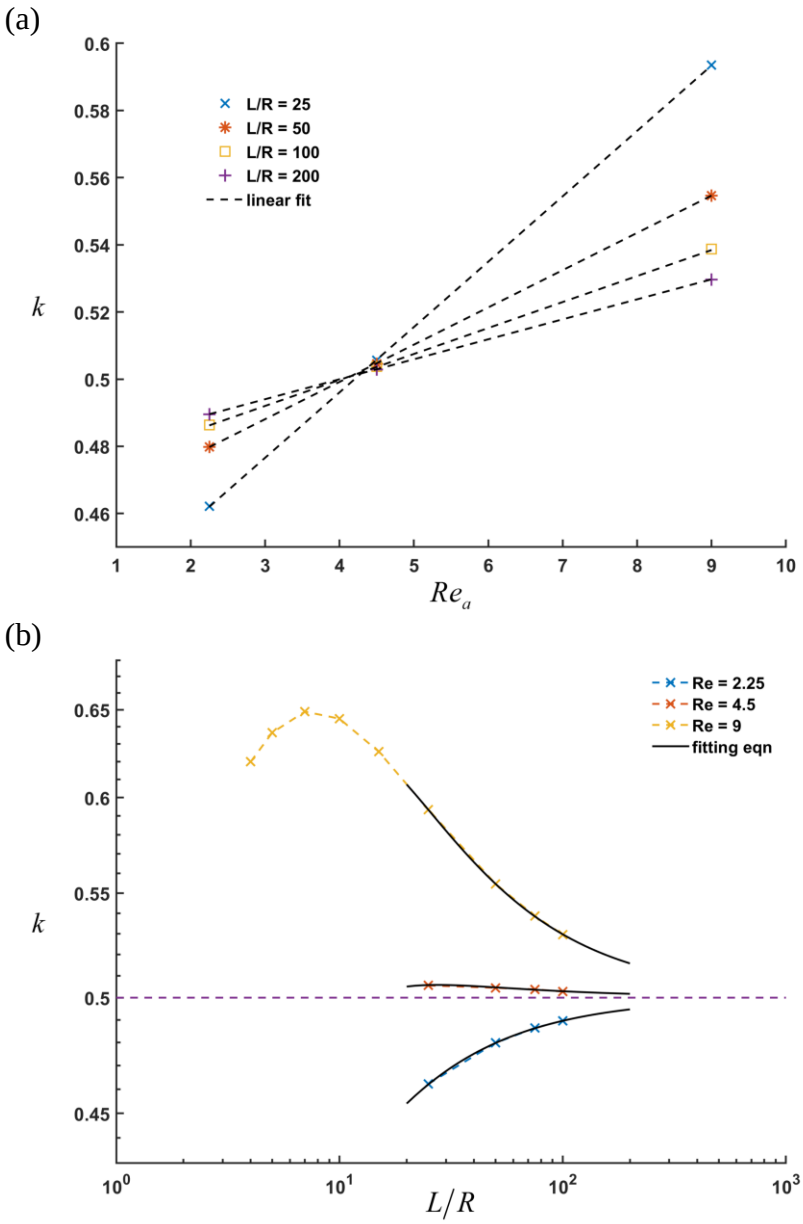

Figure 4.16. Effective diffusion coefficient multiplier relationship with (a) acoustic Reynolds number and (b) Length-to-Radius ratio of the 3D micro-channel with $w = 4H$.

starts behaving like a continuous leaking while the tube length is getting too small. As discussed earlier, the continuous leaking only depends on the reflection coefficient (or the expanded area ratio). Thus, increasing conduit length only reduces the drainage speed from the ideal model (equation 2.32) while the continuous leaking drainage enhancement can

remain as a constant. It indicates that the drainage rate enhancement caused by CL is proportional to the conduit length. Therefore, the effective diffusion coefficient multiplier shows two different trends with increasing L/R. Such short length influence is excluded from the present analysis and $L/R = 25$ is tested to be large enough as shown in figure 4.15b.

For 3D micro-channel drainage flow to an infinitely large reservoir, the acoustic Reynolds number is defined as $Re_a = c\sqrt{4Hw}/D_\rho$ where w stands for channel half-width and the ratio of length over half-height is L/H. Its effective diffusion coefficient multiplier shows same linear relationship in terms of the acoustic Reynolds number Re_a and a 0.5 convergence trend with increasing L/H (figure 4.16). Flow properties used for the 3D channel simulation are: $w = 4H$, $c = 450\text{m/s}^2$, $D_\rho = 2\times10^{-4}\text{m}^2/\text{s}$, $H_{\text{out}} / H = 250$. Detailed effective diffusion coefficient multipliers for different size 3D channel are listed in table B2−B4 in the Appendix B.

4.7.3.2. *2D micro-channel*

The case of an 2D micro-channel drainage flow to infinitely large reservoir deserves special attention. Since the spatial dimension is one degree lower, the pulse leaking wave propagates into a large 2D area instead of a 3D volume. Thus, the pulse leaking wave front no longer have enough space to quickly disperse and propagate away from the channel exit compares to the capillary or 3D channel. As a result, the exit density perturbation recovers slowly to 0 during the exit-reflection time period. As discussed in the above section, a slow recovery of the exit density indicates the pulse leaking converts to a continuous leaking mechanism. Thus, the effective diffusion coefficient multiplier shows a monotonic

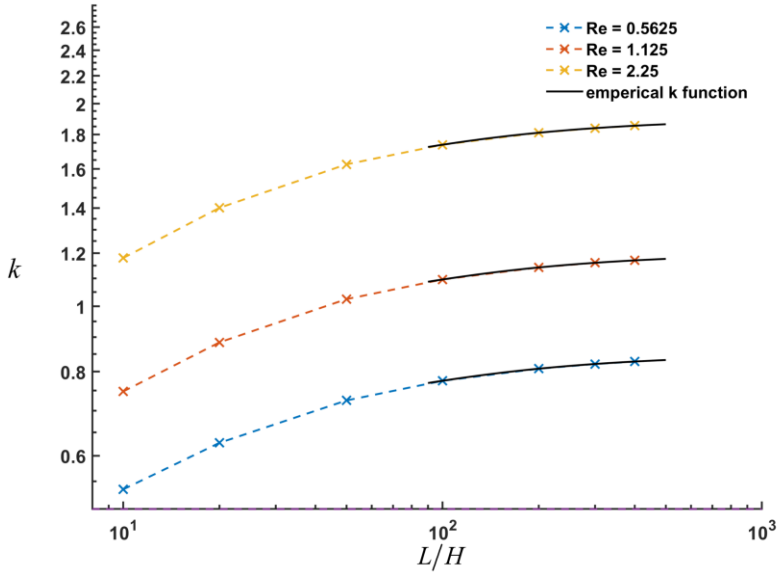

Figure 4.17 Effective diffusion coefficient multiplier relationship with Length-to-Height ratio of the 2D micro-channel.

increasing behavior in terms of the ratio of length over half-height L/H (figure 4.17) instead of converging to 0.5. Detailed effective diffusion coefficient multipliers for different size 2D channel are listed in table B5 in the Appendix B.

4.7.4. *Empirical function of the effective diffusion coefficient multiplier*

4.7.4.1. *Curve fitting for acoustic Reynolds number and length-to-radius ratio*

After finding the effective diffusion coefficient multiplier dependence on both parameters, an empirical function for the multiplier k in terms the acoustic Reynolds number Re_a and the length-to-radius ratio L/R can be generated by performing a curve fitting on each parameter separately. Noticed, only data with $L/R \geq 25$ are used for the empirical derivation in order to neglect the short length behavior discussed above.

Linear fitting equations can be generated for each L/R case by using MATLAB curve fitting toolbox with root mean square error (RMSE) less than 3.8×10^{-5}. After collecting

L/R	Slope $\times 10^{-3}$	Interception $\times 10^{-1}$
25	9.8913	4.5480
50	5.2797	4.7621
100	2.7290	4.8780
200	1.3884	4.9387

Table 4.2. Linear parameters with different length-to-radius ratio

the linear parameters (table 4.2), a second curve fitting technique can be implemented based on each linear parameter in terms of the reciprocal of length-to-radius ratios R/L. After testing multiple fitting equations (polynomial, power, exponential and rational fit), second order polynomial fits the data perfectly with RMSE less than 2.5×10^{-5}. Thus, an empirical equation could be generated equation (4.11), which shows the effective diffusion coefficient multiplier is linear dependent on the acoustic Reynolds number with linear slopes and interceptions which both quadratically dependent on the reciprocal of the length-to-radius ratio.

$$k_{emp}=\left[-0.8249\left(\frac{R}{L}\right)^2+0.28\left(\frac{R}{L}\right)+9.711\times10^{-6}\right]\frac{c\sqrt{\pi R^2}}{D_\rho}+\left[3.047\left(\frac{R}{L}\right)^2-1.253\left(\frac{R}{L}\right)+0.5\right], \quad (4.11)$$

Equation (4.11) reproduces the optimal effective diffusion coefficient multipliers derived from the least square regression shows in section (4.7.2). The maximum relative error between k_{optimal} and $k_{\text{empirical}}$ is less than 0.014%. It also satisfies the 0.5 converging relationship $k\to0.5$ (figure 4.15b) as the length-to-radius ratio approaching to infinity (or $R/L\to0$). However, empirical equation (4.11) has a restriction. The first bracket contains a non-zero the constant term (9.711×10^{-6}). In order to satisfy the converging relations while $R/L\to0$, the acoustic Reynolds number has to satisfy the condition

$9.711\times10^{-6}\,Re_a \ll 0.5$, which results in $Re_a \ll 5.1488\times10^{4}$. With general fluid property $c = 450\text{m/s}$ and $D_\rho = 5\times10^{-5}\text{m}^2/\text{s}$, the acoustic Reynolds number limit results in a tube radius limit, $R \ll 3.2277\text{mm}$. Thus, the empirical equation (4.11) only works for micro-tubes with radius less than 3.2 mm.

4.7.4.2. *Combination of ballistic and diffusive transport*

By substituting the empirical multiplier of the effective diffusion coefficient into the ideal model, we artificially embed the ballistic transport of the wave into the ideal diffusion model. As equation (4.12) shown below, $\gamma = kD_\rho$ is the sum of a ballistic transport depends on the speed of sound (first term) and a diffusive transport, which is determined by the diffusion coefficient D_ρ (second term). Thus, by using the empirical equation (4.11), we approximate a realistic drainage flow to infinitely large reservoir by simply using the analytical solution from an idealized diffusion model.

$$\gamma = kD_\rho = f_B\left(\frac{R}{L}\right)c\sqrt{\pi R^2} + f_D\left(\frac{R}{L}\right)D_\rho\,. \tag{4.12}$$

4.7.4.3. *Empirical function limits for larger size micro-capillary*

Since the empirical function was derived only from 12 data points with micron sized tube radius (table 4.1), it is necessary to verify it also available for a larger tube radius (higher Reynolds number) and length-to-radius ratio outside the testing range. We calculated the instantaneous excess mass reduction by substituting the empirical multiplier to the ideal model (equation 2.32) and taking the integral. Comparison plots can be generated for the numerical and analytical mass solutions. In figure 4.18a,b below, comparisons are first conducted within the test range ($Re_a = 3.988,\ 7.976,\ 15.9521$ and

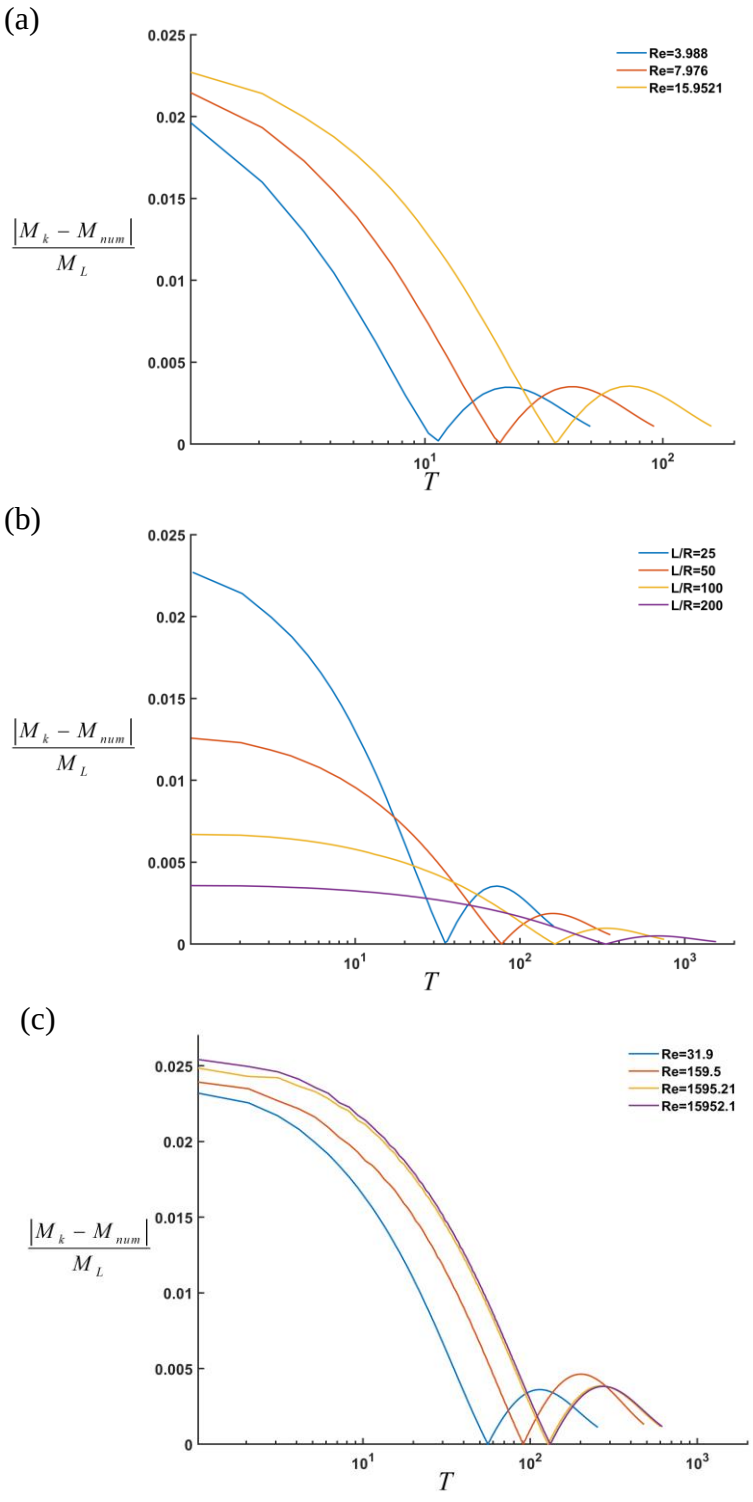

Figure 4.18. (a) Mass relative error of using diffusion model with effective diffusion coefficient vs oscillation period (a) for original Re_a data with $L/R = 25$. (b) for different L/R with $Re_a = 15.9521$. (c) for higher Re_a verification with $L/R = 25$.

$L/R = 25, 50, 100, 200$); maximum error appears at the beginning of each drainage process. As the acoustic Reynolds number increases or length-to-radius ratio decreases, the analytical solution deviates further from the numerical result. Thus, to find the empirical function limit, we only need to test the analytical solution for larger tube radius and short length ($Re_a > 15.9521,\ L/R = 25$). As shown in figure 4.18c, the maximum error even for the highest acoustic Reynolds number is below 2.55%. It indicates that the analytical solution with empirical effective diffusion coefficient can approximate the drainage flow system very well, even for a 1mm size capillary ($Re_a = 15952.1$), which is also within the equation limit discussed in section (4.7.4.1).

The empirical function of the effective diffusion coefficient multiplier for a 3D micro-channel with multiple width are also generated using the same two-step curve fitting technique, only the case of $w = 2H$ is shown below; The empirical equation for other channel cases are shown in the Appendix B.

$$k_{emp} = \left[-1.873\left(\frac{h}{L}\right)^2 + 0.4374\left(\frac{h}{L}\right) + 7.967\times10^{-5} \right]\frac{c\sqrt{4hw}}{D_\rho} + \left[6.507\left(\frac{h}{L}\right)^2 - 1.88\left(\frac{h}{L}\right) + 0.4998 \right] \tag{4.12}$$

For the 2D micro-channel drainage flow, the empirical function of the effective diffusion coefficient multiplier is given by.

$$k_{emp} = \left[124.5\left(\frac{h}{L}\right)^2 - 6.614\left(\frac{h}{L}\right) + 0.6242 \right]\frac{ch}{D_\rho} + \left[124.4\left(\frac{h}{L}\right)^2 - 5.735\left(\frac{h}{L}\right) + 0.4994 \right]. \tag{4.13}$$

4.8. Effective diffusion coefficient for finite size reservoirs and contractions

4.8.1. *Reservoirs*

4.8.1.1. *Effective diffusion coefficient and area ratio dependence*

For drainage flow to a finite size reservoir, the same diffusion model can be used with an effective diffusion coefficient to approximate the numerical simulation result. To determine the optimal effective diffusion coefficient multiplier, the same linear regression model is implemented to calculate the minimum sum of square error (equation 4.10). k_{optimal} for different size reservoirs were listed in table C1 in the Appendix C.

As shown in figure 4.19, the analytical approximation with optimal effective diffusion coefficient starts deviates from the numerical result as the reservoir size decreases from $R_{out}/R = 10$ to $R_{out}/R = 1$. This is because the drainage process becomes more ballistic dominant with higher fraction of wave leaking into the reservoir during the exit-reflection period (small $\Re$), especially for the same size extension $R_{out}/R = 1$, where the drainage is finished in just half period. Thus, even with optimal effective diffusion coefficient, the diffusion model has its limit to fully approximate such ballistic dominant drainage. However, the maximum relative error for the capillary size extension approaches to 16% and it is quick reduced to 6% as the reservoir becomes 10 times larger (figure 4.20a,b). Thus, we conclude that the diffusion model with effective diffusion coefficient still suffice even for small size reservoir drainage flow.

As shown in figure 4.21, a capillary size reservoir results in a largest k value; as the reservoir size increases, the multiplier decreases and converges to a value for the infinite large reservoir as derived in the above section. For different length-to-radius ratio, the curves have similar trend.

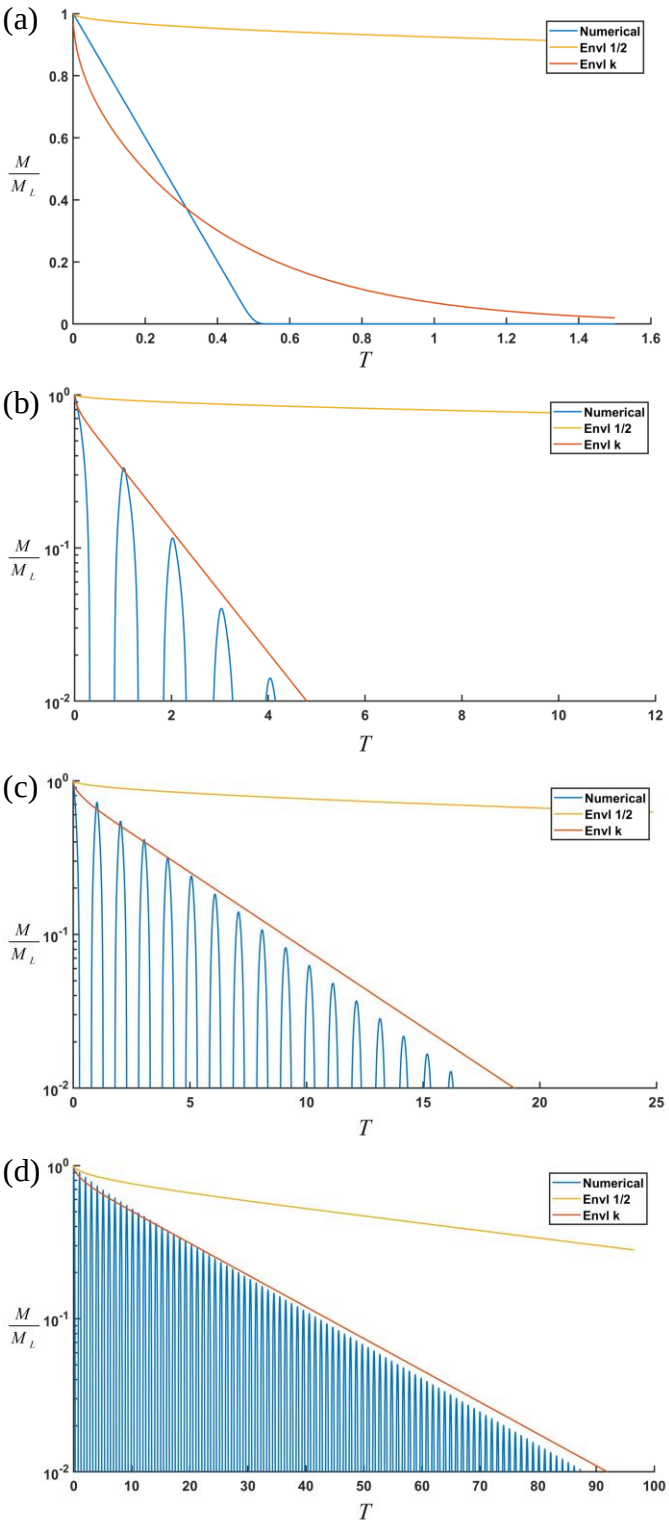

Figure 4.19. Normalized instantaneous mass reduction vs. oscillating period with multiple size reservoirs, $R = 1\mu\text{m}$, $L = 50\mu\text{m}$, $c = 450\text{m/s}^2$, $D_\rho = 5\times10^{-5}\text{m}^2/\text{s}$. (a) $R_{out}/R = 1$, (b) $R_{out}/R = 2$, (c) $R_{out}/R = 4$, (d) $R_{out}/R = 10$.

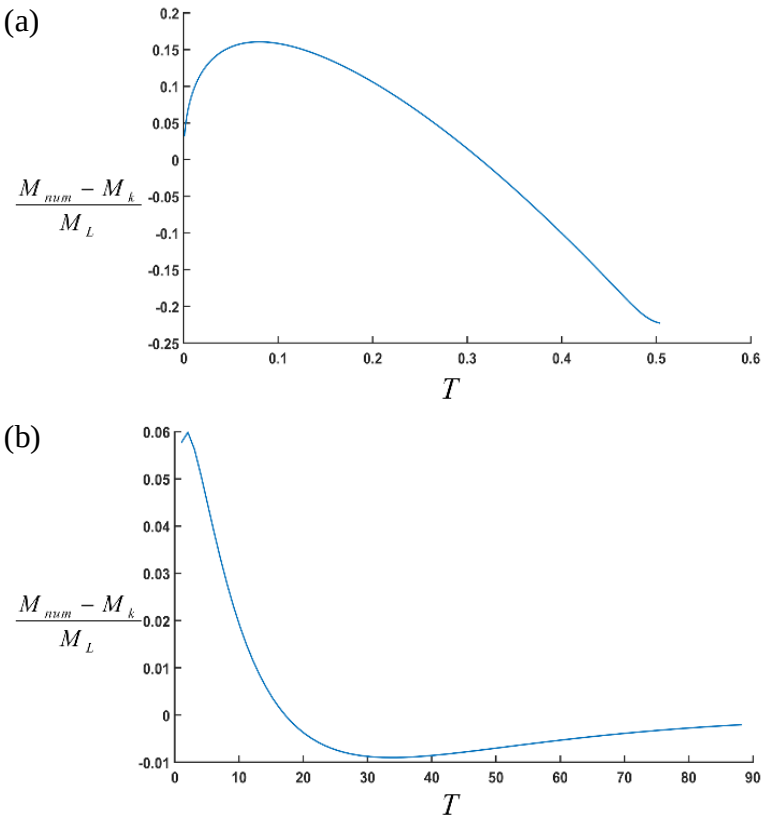

Figure 4.20. Relative error vs oscillation period for a whole drainage process with (a) capillary sized reservoir $R_{out}/R = 1$ and (b) expanded reservoir with $R_{out}/R = 10$.

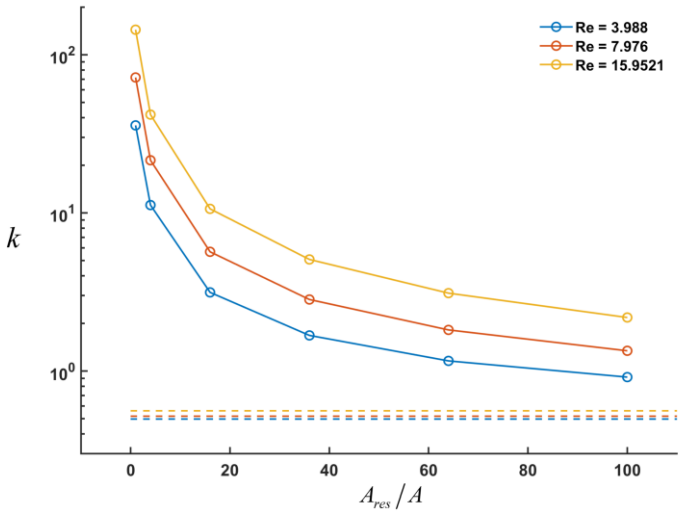

Figure 4.21. Effective diffusion coefficient multiplier vs. area ratio with different acoustic Reynolds number. The length-to-ratio $L/R = 50$. Dash lines represents the multiplier value for an infinitely large reservoir at different acoustic Reynolds number condition.

4.8.1.2. *Empirical function of the effective diffusion coefficient multiplier*

Following the same curve fitting procedure used in section 4.7.4, with enough k_{optimal} collected, an empirical function of the effective diffusion coefficient multiplier with the finite size reservoir could be generated. However, besides the acoustic Reynolds number and the Length-to-radius ratio, a finite size reservoir drainage flow system has a third dependent variable, which is the reservoir tube area ratio A_{out}/A. A proper curve fitting procedure was found as

(1) Linear fitting to each optimal multiplier in terms of the acoustic Reynolds number Re_a.

(2) Second order polynomial fitting to the linear parameters acquired above in terms of the area ratio A/A_{out}.

(3) Second order polynomial fitting to the quadratic parameters acquired in the second step in terms of the length-to-radius ratio L/R.

$$k = \left[f_1 \left(\frac{A}{A_{out}} \right)^2 + f_2 \frac{A}{A_{out}} + f_3 \right] \frac{c\sqrt{\pi R^2}}{D_\rho} + \left[f_4 \left(\frac{A}{A_{out}} \right)^2 + f_5 \frac{A}{A_{out}} + f_6 \right] \qquad (4.14)$$

$$f_i = a_i \left(\frac{L}{R} \right)^2 + b_i \left(\frac{L}{R} \right) + c_i \quad i = 1, 2....6$$

$$\begin{bmatrix} \mathbf{a} & \mathbf{b} & \mathbf{c} \end{bmatrix} = \begin{bmatrix} 1.2196\times10^{-5} & -0.03088 & -0.04456 \\ -1.1910\times10^{-5} & 0.2117 & 0.04160 \\ -2.7647\times10^{-7} & -1.8087\times10^{-4} & 0.002807 \\ 7.8605\times10^{-5} & -0.05292 & -1.5721 \\ -5.7372\times10^{-5} & 0.0494 & 0.9172 \\ -2.0251\times10^{-6} & 1.1322\times10^{-3} & 0.4174 \end{bmatrix}$$

With a root mean square error (RMSE) less than 0.2969, The empirical equation (4.14) reproduced each optimal multiplier of the effective diffusion coefficient well. It's worth

noting that, the optimal multiplier for $A_{out}/A = 1$ are at least 2 order magnitude larger than the one for $A_{out}/A = \inf$. Thus, the empirical function (4.14) does not reproduce $k_{\text{empirical}}$ as accurate as the empirical function (4.11), which is derived only for the drainage flow to infinitely large reservoir. In other words, equation (4.14) works best for small size expanded reservoir and has increasing relative error outputs as $A_{out}/A \to \inf$.

4.8.2. *Contractions*

4.8.2.1. *Effective diffusion coefficient and area ratio dependence*

For drainage flow to finite size contractions, the fluid mass within the capillary drains as a linear piecewise function. By same diffusion model with optimal effective diffusion coefficient to approximate the drainage process, the relative error for the approximation is within an acceptable range as the maximum relative error approaches 11% at the beginning of the drainage process for a contraction with $R_{out}/R = 0.1$ (figure 4.23).

As shown in figure 4.24, the effective diffusion coefficient multiplier is a monotonic decreasing function against the reciprocal of the contract area ratio (A/A_{out}), as the smaller the contraction becomes, the less fluid can drain, which leads to a complete stall ($k \to 0$) as $A/A_{out} \to \inf$.

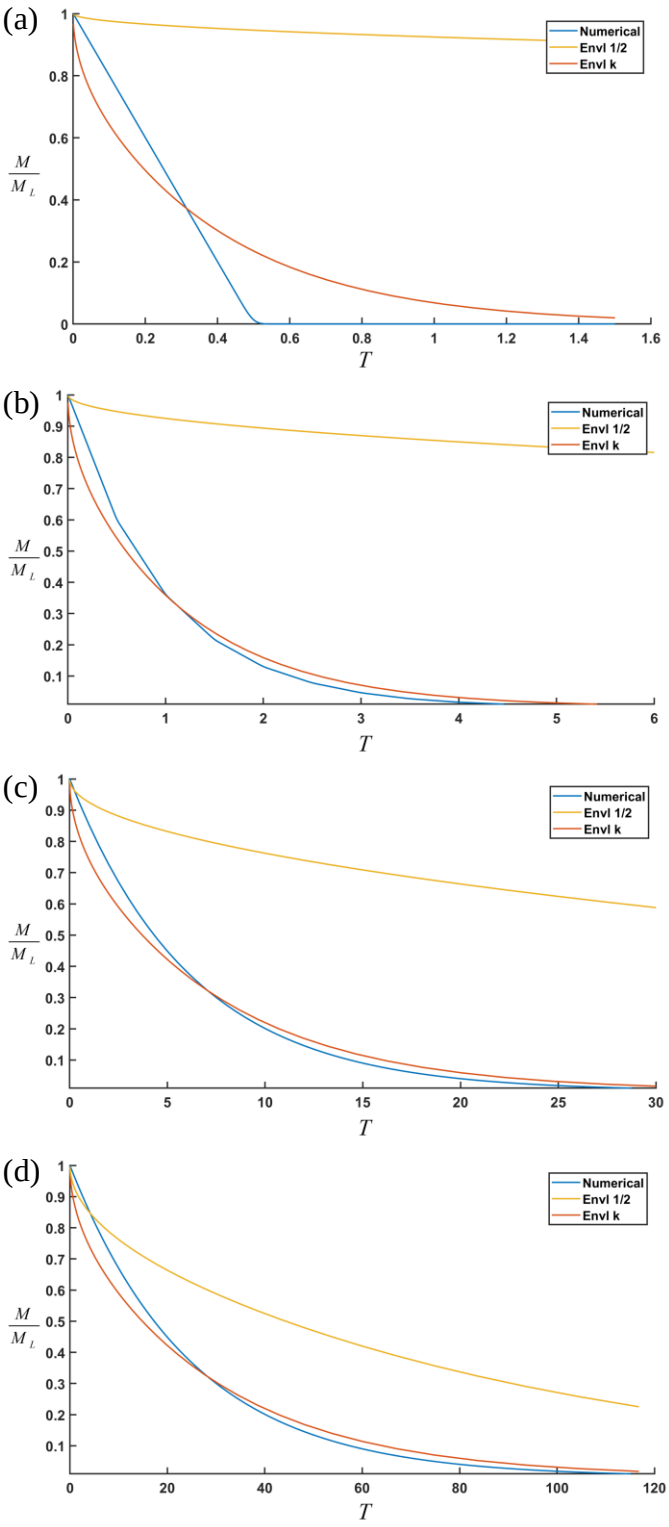

Figure 4.22 Normalized instantaneous mass reduction vs. oscillating period with multiple size reservoirs, $R = 1\mu\text{m}$, $L = 50\mu\text{m}$, $c = 450\text{m/s}^2$, $D_\rho = 5\times10^{-5}\text{m}^2/\text{s}$. (a) $R_{out}/R = 1$, (b) $R_{out}/R = 0.5$, (c) $R_{out}/R = 0.2$, (d) $R_{out}/R = 0.1$.

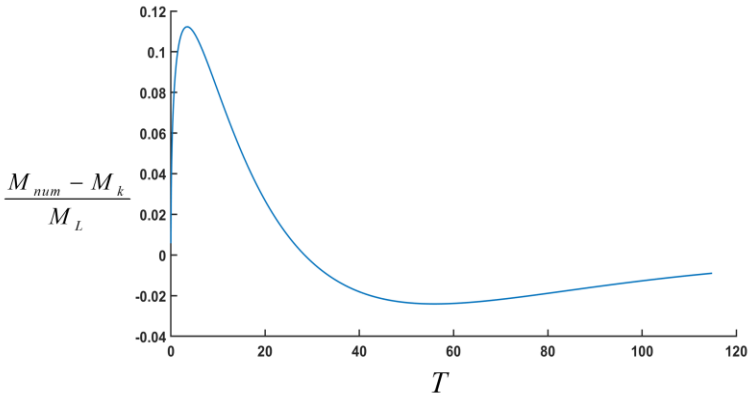

Figure 4.23. Relative error vs oscillation period for a whole drainage process with contracted reservoir $R_{out}/R = 0.1$.

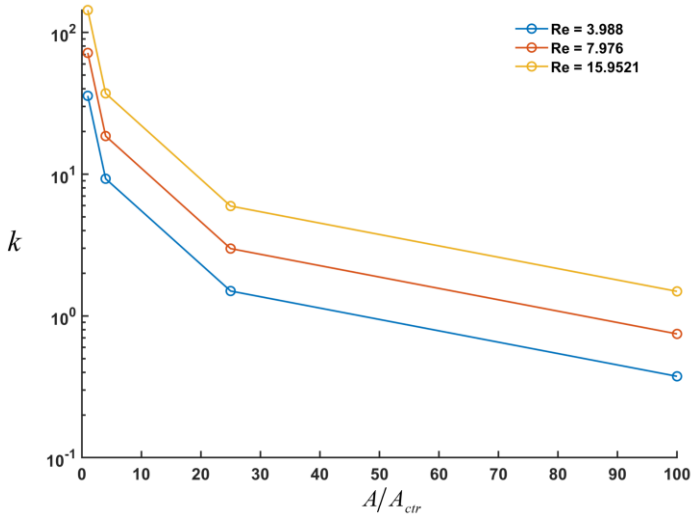

Figure 4.24. Effective diffusion coefficient multiplier vs. area ratio with different acoustic Reynolds number. The length-to-ratio $L/R = 50$.

4.8.2.2. *Empirical function of the effective diffusion coefficient multiplier*

For drainage flow with contracted reservoir, same analysis was conducted. The optimal multipliers were calculated for $A_{out}/A = 0.25$, $A_{out}/A = 0.04$ and $A_{out}/A = 0.01$. k_{optimal} data are listed in table C2 in the Appendix C. A new empirical function for contracted finite size reservoir was derived for the contraction, equation (4.15), with a root mean square

error (RMSE) less than 0.02348. Noticed, a second order polynomial curve fitting was conducted in terms of the contracted area ratio A_{out}/A instead of its reciprocal, which is different than equation (4.14).

$$k = \left[f_1 \left(\frac{A_{out}}{A} \right)^2 + f_2 \frac{A_{out}}{A} + f_3 \right] \frac{c\sqrt{\pi R^2}}{D_\rho} + \left[f_4 \left(\frac{A_{out}}{A} \right)^2 + f_5 \frac{A_{out}}{A} + f_6 \right] \tag{4.15}$$

$$f_i = a_i \left(\frac{L}{R} \right)^2 + b_i \left(\frac{L}{R} \right) + c_i \quad i = 1, 2....6$$

$$\begin{bmatrix} \mathbf{a} & \mathbf{b} & \mathbf{c} \end{bmatrix} = \begin{bmatrix} -3.7088\times10^{-7} & -7.8325\times10^{-3} & -2.6124\times10^{-3} \\ 3.7964\times10^{-7} & 0.18853 & 2.4449\times10^{-3} \\ -8.3235\times10^{-9} & -4.3391\times10^{-5} & -5.4618\times10^{-5} \\ 1.0834\times10^{-5} & -8.9024\times10^{-3} & 2.1534\times10^{-3} \\ 8.5852\times10^{-6} & 6.5225\times10^{-3} & -0.24512 \\ -2.3894\times10^{-7} & 1.1655\times10^{-5} & 4.9019\times10^{-3} \end{bmatrix}$$

Chapter 5

Steady compressible gas flow through a micro-conduit

5.1. Self-diffusion embedded in the compressible Navier-Stokes equations

The conservative forms of the continuity and the compressible Navier-Stokes equations. (Anderson, 1995) are

$$\frac{\partial \rho}{\partial t} + \nabla \cdot (\rho \mathbf{v}) = 0\,, \tag{5.1}$$

$$\frac{\partial (\rho \mathbf{v})}{\partial t} + \nabla \cdot \left(\rho \mathbf{v} \otimes \mathbf{v}\right) = -\nabla p + \left(\mu_b + \mu/3\right)\nabla(\nabla \cdot \mathbf{v}) + \mu \nabla^2 \mathbf{v}\,, \tag{5.2}$$

where ρ, p, $\mathbf{v}$ are the density, pressure and velocity of the fluid; μ_b is the bulk viscosity, and μ is the shear viscosity. An equation of state such as the ideal gas law is supplied to link the pressure and the density. Since compressible flows through micro-conduits are low Mach number flows (global Mach number $M << 1$), the energy equation is not included here as temperature change is assumed to be small. This assumption is adopted in most of studies on micro-flows. In the following, we will show how self-diffusion arises from these governing equations. for compressible flow through a long and narrow micro-conduit.

5.1.1. *Self-diffusion in transient flow perturbing an equilibrium state*

For a flow perturbing an equilibrium state, linearization of equations. (5.1) and (5.2) lead to the well-known linear acoustic equations. governing the propagation of small amplitude acoustic waves (Lighthill, 1978; Pierce, 1983):

$$\frac{\partial \rho'}{\partial t} + \rho_0 \nabla \cdot \mathbf{v}' = 0\,, \tag{5.3}$$

$$\rho_0 \frac{\partial \mathbf{v}'}{\partial t} = -\nabla p' + \left(\mu_b + 4\mu/3\right)\nabla(\nabla \cdot \mathbf{v}') - \mu \nabla \times (\nabla \times \mathbf{v}')\,, \tag{5.4}$$

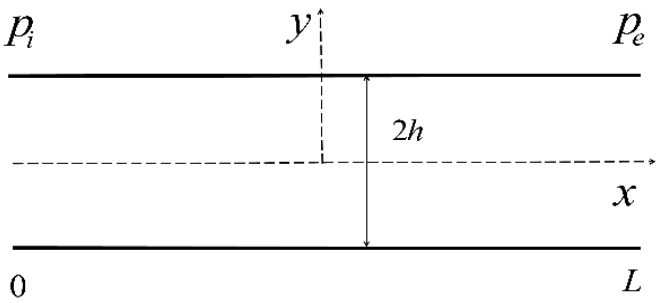

Figure 5.1. Micro-flow through a channel. For a micro-capillary, the radius of the capillary is R.

where $\rho' = \rho - \rho_0$ is the density perturbation from the equilibrium density ρ_0; p' is the pressure perturbation; $\mathbf{v}'$ is the velocity. Density perturbation satisfies a damped wave equation of the form (Lighthill 1978; Morse & Ingard 1968; Temkin 1981)

$$\frac{\partial^2 \rho'}{\partial t^2} = \left(c^2 + D_0 \frac{\partial}{\partial t} \right) \nabla^2 \rho', \tag{5.5}$$

where c is the speed of sound and

$$D_0 = (\mu_b / \mu + 4/3) \frac{\mu}{\rho_0}, \tag{5.6}$$

is the damping coefficient for the density wave. The damping term in (5.5) is called "sound-absorption" in the acoustic literature (Herzfeld & Litovitz 1959).

For transient flows in semi-sealed long and narrow capillaries (figure 5.1), it is shown that density relaxes quickly in the transverse direction and it becomes uniform in the cross-section shortly after start-up (Chen & Shen 2018a). Thus, $\rho = \rho(x,t)$, with x being the longitudinal direction. The second term on the right-hand-side (rhs) of equation (5.4) then becomes $-\mathbf{e}_x D_0 \partial^2 \rho' / \partial x \partial t$, where $\mathbf{e}_x$ is the unit base vector in the x-direction. This leads to the damping of the acoustic wave by the second term on the rhs of equation (5.5), which is due to the self-diffusion induced by the local density gradient $\partial \rho' / \partial x$. Since equation

(5.5) is derived from the linearized compressible Navier-Stokes equations., we conclude that the linearized compressible Navier-Stokes equations include self-diffusion effect for transient flows via sound-absorption.

5.1.2. *Self-diffusion in steady flow through a micro-conduit*

Consider the motion of a compressible fluid through a circular capillary with radius R and length L (figure 5.1). The capillary is long and narrow such that $R \ll L$. Steady-state flow is the long-time solution of a start-up flow. Self-diffusion effect in a transient start-up flow does not vanish at large times, as the dilatation $\nabla \cdot \mathbf{v}$ term in equation (5.2) remains in the momentum equation for steady compressible flows. The mathematical theory for low Mach number flows developed by Klainerman & Majda (1982) can be employed to show that self-diffusion is persistent for steady compressible flow through a small capillary.

To this end, the governing equations (5.1), (5.2) are first made dimensionless with the scales used by Klainerman & Majda (1982). Let v_{ref} be a reference fluid particle velocity, L_{ref} a reference length, and a reference time is defined as $t_{ref} = L_{ref} / \mathrm{v}_{ref}$. The reference pressure and density are p_{ref}, ρ_{ref}, respectively. A reference speed of sound can be defined as $c_{ref} = \sqrt{p_{ref} / \rho_{ref}}$ (a constant factor is dropped for convenience; see Klainerman & Majda 1982). The dimensionless velocity, pressure, density, coordinates, and time are $\bar{\mathbf{v}} = \mathbf{v} / \mathrm{v}_{ref}, \bar{p} = p / p_{ref}$, $\bar{\rho} = \rho / \rho_{ref}, \bar{\mathbf{x}} = \mathbf{x} / L_{ref}, \bar{t} = t / t_{ref}$. A global Mach number is defined as $M = \mathrm{v}_{ref} / c_{ref}$ and a Reynolds number is defined as $\mathrm{Re} = \rho_{ref} \mathrm{v}_{ref} L_{ref} / \mu$, both of which are assumed to be small. The dimensionless governing equations. are then

$$\frac{\partial \bar{\rho}}{\partial \bar{t}} + \bar{\nabla} \cdot (\bar{\rho} \bar{\mathbf{v}}) = 0, \tag{5.7}$$

$$\frac{\partial(\bar{\rho}\bar{\mathbf{v}})}{\partial\bar{t}}+\bar{\nabla}\cdot\left(\bar{\rho}\bar{\mathbf{v}}\otimes\bar{\mathbf{v}}\right)=-\frac{1}{M^2}\bar{\nabla}\bar{p}+\frac{\mu_b/\mu+1/3}{\mathrm{Re}}\bar{\nabla}(\bar{\nabla}\cdot\bar{\mathbf{v}})+\frac{1}{\mathrm{Re}}\bar{\nabla}^2\bar{\mathbf{v}}\,. \tag{5.8}$$

It is known that the limit of $M\to 0$ is singular as these governing equations change types (Klainerman & Majda 1981). For inviscid isentropic flows, Klainerman & Majda (1982) have rigorously proved that for a given initial data, the linearized acoustics is a *uniformly* valid principal correction in the deviation of the compressible flow solution from the incompressible solution as the global Mach number $M\to 0$; and they have derived the following asymptotic results:

$$\left|\bar{\mathbf{v}}-\left(\bar{\mathbf{v}}^I+M\ \tilde{\mathbf{v}}^A\right)\right|\le\Delta_5 M^2\,, \tag{5.9}$$

$$\left|\bar{p}-\left(\bar{p}_0+M^2(\tilde{p}^I+\tilde{p}^A)\right)\right|\le\Delta_6 M^3\,, \tag{5.10}$$

where $|\ |$ stands for the magnitude, superscripts *"I", "A"* stand for incompressible and acoustic quantities, respectively; $\Delta_5>0$, $\Delta_6>0$ are fixed constants, and $\bar{p}_0$ is a background thermodynamic pressure. The asymptotic results (5.9) and (5.10) have been extended by Klein (1995) to non-isentropic flows and by Munz et al. (2003, 2007) to the general heat conducting viscous compressible Navier-Stokes equations. These asymptotic results allow us to decompose a low Mach number flow into the sum of two fields, the limiting incompressible field and a linearized acoustic field, $\bar{\mathbf{v}}=\bar{\mathbf{v}}^I+\bar{\mathbf{v}}^A+O(M^2)$ with $\bar{\nabla}\cdot\bar{\mathbf{v}}^I=0$ and $\bar{\mathbf{v}}^I=\lim_{M\to 0}\bar{\mathbf{v}}$. Specifically,

$$\bar{\mathbf{v}}=\bar{\mathbf{v}}^I+\bar{\mathbf{v}}^A+O(M^2)=\bar{\mathbf{v}}^I+M\ \tilde{\mathbf{v}}^A+O(M^2)\,, \tag{5.11}$$

$$\bar{p}-\bar{p}_0=\bar{p}^I+\bar{p}^A+O(M^3)=M^2\tilde{p}^I+M^2\tilde{p}^A+O(M^3)\,. \tag{5.12}$$

Density can also be expanded,

$$\bar{\rho}=1+M^2\tilde{\rho}_2+O(M^4)\,. \tag{5.13}$$

These asymptotic expansions are valid for all times. In the absence of a continuous acoustic excitation and flow instabilities, a condition met by low Reynolds number steady micro-flows, the two flow fields are expected to approach steady-state solutions at large times which are governed by the corresponding steady-state equations:

$$\bar{\nabla}\cdot(\bar{\rho}\bar{\mathbf{v}})=0\,, \tag{5.14}$$

$$\bar{\nabla}\cdot\left(\bar{\rho}\bar{\mathbf{v}}\otimes\bar{\mathbf{v}}\right)=-\frac{1}{M^2}\bar{\nabla}\bar{p}+\frac{\mu_b/\mu+4/3}{\mathrm{Re}}\bar{\nabla}(\bar{\nabla}\cdot\bar{\mathbf{v}})-\frac{1}{\mathrm{Re}}\bar{\nabla}\times(\bar{\nabla}\times\bar{\mathbf{v}})\,, \tag{5.15}$$

where the vector identity $\nabla^2\mathbf{a}=\nabla(\nabla\cdot\mathbf{a})-\nabla\times(\nabla\times\mathbf{a})$ has been used.

For steady flows, we replace the superscript "*A*" by "*D*" in the expansion (5.11) and (5.12), with

$$\bar{\mathbf{v}}^D=\lim_{t\to\infty}\bar{\mathbf{v}}^A,\ \bar{p}^D=\lim_{t\to\infty}\bar{p}^A\,, \tag{5.16}$$

while maintaining the superscript "*I*" for the limiting steady incompressible field. Thus, for steady flows,

$$\bar{\mathbf{v}}=\bar{\mathbf{v}}^I+\bar{\mathbf{v}}^D+O(M^2)=\bar{\mathbf{v}}^I+M\ \tilde{\mathbf{v}}^D+O(M^2)\,, \tag{5.17}$$

$$\bar{p}-\bar{p}_0=\bar{p}^I+\bar{p}^D+O(M^3)=M^2\tilde{p}^I+M^2\tilde{p}^D+O\,(M^3)\,. \tag{5.18}$$

The momentum equation for the limiting incompressible flow is (with $\bar{\rho}=1$)

$$\bar{\nabla}\cdot\left(\bar{\mathbf{v}}^I\otimes\bar{\mathbf{v}}^I\right)=-\bar{\nabla}\tilde{p}^I-\frac{1}{\mathrm{Re}}\bar{\nabla}\times(\bar{\nabla}\times\bar{\mathbf{v}}^I)\,. \tag{5.19}$$

Subtracting equation (5.19) from equation (5.15) and substituting equations (5.17) and (5.18) into the result gives

$$\bar{\nabla}\cdot\left(\bar{\rho}\bar{\mathbf{v}}\otimes\bar{\mathbf{v}}\right)-\bar{\nabla}\cdot\left(\bar{\mathbf{v}}^I\otimes\bar{\mathbf{v}}^I\right)=-\bar{\nabla}\tilde{p}^D+\frac{\mu_b/\mu+4/3}{\mathrm{Re}}\bar{\nabla}(\bar{\nabla}\cdot\bar{\mathbf{v}}^D)-\frac{1}{\mathrm{Re}}\bar{\nabla}\times(\bar{\nabla}\times\bar{\mathbf{v}}^D)\,, \tag{5.20}$$

where for each of the three contributions on the right-hand side, only the leading order term has been retained. The limiting incompressible field $\bar{\mathbf{v}}^I$ is driven by the pressure gradient while the compressible field $\bar{\mathbf{v}}^D$ is driven by the density gradient. Since micro-flows are weak flows with very low mass flow rates, we seek a leading-order solution that is linear in each driving mechanism (gradient), which takes the form

$$\bar{\mathbf{v}}^I = \tilde{\mathbf{v}}_p \frac{\partial \bar{p}}{\partial \bar{x}}, \bar{\mathbf{v}}^D = \tilde{\mathbf{v}}_\rho \frac{\partial \bar{\rho}}{\partial \bar{x}}, \tag{5.21}$$

and we neglect any interactive term that involves the product of the two velocities, i.e. the product of the two gradients, in the governing equations. Thus, there is no coupling between the incompressible field $\bar{\mathbf{v}}^I$ and the compressible field $\bar{\mathbf{v}}^D$ other than conservation of the overall mass. This approximation is used either explicitly or implicitly in all models involving density gradient for compressible micro-flows, for example the diffusive flux theories; and it puts the two flow driving mechanisms on equal footings.

With the assumption (5.21) and the density expansion (5.13), after neglecting the product term $\frac{\partial \bar{p}}{\partial \bar{x}} \frac{\partial \bar{\rho}}{\partial \bar{x}}$, equation (5.20) becomes

$$\bar{\nabla} \cdot \left(\bar{\rho} \bar{\mathbf{v}}^D \otimes \bar{\mathbf{v}}^D \right) = -\bar{\nabla} \tilde{p}^D + \frac{\mu_b / \mu + 4/3}{\mathrm{Re}} \bar{\nabla} (\bar{\nabla} \cdot \bar{\mathbf{v}}^D) - \frac{1}{\mathrm{Re}} \bar{\nabla} \times (\bar{\nabla} \times \bar{\mathbf{v}}^D). \tag{5.22}$$

The Helmholtz decomposition (Aris 1989; Leal 2010; Panton 2013) can be used to further decompose $\bar{\mathbf{v}}^D = M\ \tilde{\mathbf{v}}^D$ to the sum of an irrotational part and a solenoidal part,

$$\tilde{\mathbf{v}}^D = \tilde{\mathbf{v}}^{IR} + \tilde{\mathbf{v}}^{RT}, \tag{5.23}$$

where $\nabla \times \tilde{\mathbf{v}}^{IR} = 0$, $\tilde{\mathbf{v}}^{IR} = \nabla \Phi$, $\nabla \cdot \tilde{\mathbf{v}}^{RT} = 0$. Φ is the scalar velocity potential for the irrotational velocity. Thus, $\bar{\nabla} \times \tilde{\mathbf{v}}^D = \bar{\nabla} \times \tilde{\mathbf{v}}^{RT}$ and the momentum equation (5.22) becomes

$$M^2 \bar{\nabla} \cdot \left(\tilde{\mathbf{v}}^D \otimes \tilde{\mathbf{v}}^D \right) + O(M^4) = -\bar{\nabla} \tilde{p}^D - \frac{\mu_b / \mu + 4/3}{\mathrm{Re}} M^3 \bar{\nabla} (\tilde{\mathbf{v}}^D \cdot \bar{\nabla} \tilde{\rho}_2) - \frac{M}{\mathrm{Re}} \bar{\nabla} \times (\bar{\nabla} \times \tilde{\mathbf{v}}^{RT}), \tag{5.24}$$

where the continuity equation

$$\bar{\nabla}\cdot\bar{\mathbf{v}}^{D}=-\bar{\mathbf{v}}^{D}\cdot\bar{\nabla}\ln\bar{\rho} \tag{5.25}$$

has been used. For micro-flows through an open conduit with small to moderate ratios between the inlet pressure and the outlet pressure, Cai et al. (2007) has shown that $M\sim\mathrm{Re}\sim\varepsilon=R/L$. Thus, $M/\mathrm{Re}=O(1)$. Therefore, in the limit of $M\to 0$, the order $O(1)$ and $O(M^2)$ equations of (5.24) become, respectively,

$$O(1):-\bar{\nabla}\tilde{p}^{D}-\frac{M}{\mathrm{Re}}\bar{\nabla}\times(\bar{\nabla}\times\tilde{\mathbf{v}}^{RT})=0; \tag{5.26}$$

$$O(M^2):\bar{\nabla}\cdot\left(\tilde{\mathbf{v}}^{D}\otimes\tilde{\mathbf{v}}^{D}\right)=-\left(\mu_b/\mu+4/3\right)\frac{M}{\mathrm{Re}}\bar{\nabla}(\tilde{\mathbf{v}}^{D}\cdot\bar{\nabla}\tilde{\rho}_2). \tag{5.27}$$

In dimensional forms, the solenoidal part of the diffusive velocity is then governed by the incompressibility and the creeping flow equations.

$$\nabla\cdot\mathbf{v}^{RT}=0, \tag{5.28}$$

$$-\nabla p^{D}+\mu\nabla^{2}\mathbf{v}^{RT}=0. \tag{5.29}$$

As will be shown in Section 3 below, the solenoidal velocity is induced by the irrotational part of the diffusive velocity and its role is to ensure that the diffusive velocity satisfies the no-slip condition on the wall.

Equation (5.27) reflects a balance between the convective acceleration and an equivalent body force induced by the self-diffusion of the fluid mass. It is noticed that, with a difference of a term of the higher order $O(M^4)$, equation (5.27) is the same as the equation

$$\bar{\nabla}\cdot\left(\bar{\rho}\bar{\mathbf{v}}^{D}\otimes\bar{\mathbf{v}}^{D}\right)=-\frac{\mu_b/\mu+4/3}{\mathrm{Re}}\bar{\nabla}\left(\bar{\mathbf{v}}^{D}\cdot\bar{\nabla}\ln\bar{\rho}\right), \tag{5.30}$$

which in dimensional form is

$$\nabla\cdot\left(\rho\mathbf{v}^{D}\otimes\mathbf{v}^{D}\right)=-\left(\mu_{b}+4\mu/3\right)\nabla\left(\mathbf{v}^{D}\cdot\nabla\ln\rho\right). \tag{5.31}$$

It is observed that deviation of a compressible gas flow from the Hagen-Poiseuille solution stems from the continuous volumetric expansion of the gas along the conduit (rarefication effect) which makes the flow a developing flow instead of a fully developed flow. This effect is characterized by the convective acceleration of the fluid which is balanced by the density gradient induced body force as shown by equation (5.31).

In a cylindrical coordinate, the velocity for an axisymmetric flow is given by $\mathbf{v}=\mathbf{e}_{r}\mathrm{v}_{r}(r,x)+\mathbf{e}_{x}\mathrm{v}_{x}(r,x)$, where $\mathbf{e_r},\mathbf{e_x}$ are the unit base vectors in the *r*, *x* directions, respectively. Density relaxes for compressible flow in long and narrow capillaries and it is a function of x only (Chen & Shen 2018a),

$$\mathbf{v}^{D}\cdot\nabla\ln\rho=\mathrm{v}_{x}^{D}\frac{d}{dx}\ln\rho. \tag{5.32}$$

The x-direction component of equation (5.31) is

$$\frac{2}{r}\frac{\partial}{\partial r}\left(\rho r\mathrm{v}_{r}^{D}\mathrm{v}_{x}^{D}\right)+\frac{\partial}{\partial x}\left(\rho\mathrm{v}_{x}^{D}\mathrm{v}_{x}^{D}\right)=-\left(\mu_{b}+4\mu/3\right)\frac{\partial}{\partial x}\left(\mathrm{v}_{x}^{D}\frac{d}{dx}\ln\rho\right). \tag{5.33}$$

This is the momentum balance equation at a length scale comparable to the length of the tube. At this long length scale, density gradient drives a large-scale compressible flow, which is decoupled from the incompressible field $\bar{\mathbf{v}}^{I}$ when the leading order approximation (5.21) is adopted. Integrating equation (5.33) over the cross-section and utilizing the no-penetration condition for v_{r}^{D} on the tube wall gives

$$\frac{\partial}{\partial x}\int_{0}^{R}2\pi r\rho\left(\mathrm{v}_{x}^{D}\right)^{2}dr=-\left(\mu_{b}+4\mu/3\right)\frac{\partial}{\partial x}\left[\left(\int_{0}^{R}2\pi r\mathrm{v}_{x}^{D}dr\right)\frac{d}{dx}\ln\rho\right]. \tag{5.34}$$

The velocity $\mathbf{v}^D$ is induced by the density gradient. Thus, when $d\rho/dx=0$, $\mathbf{v}^D=0$. Integrating (5.34) with respect to x then leads to

$$\rho\int_0^R 2\pi r\left(\mathrm{v}_x^D\right)^2 dr=-\left(\mu_b+4\mu/3\right)\left(\int_0^R 2\pi r\mathrm{v}_x^D dr\right)\frac{d}{dx}\ln\rho\,. \tag{5.35}$$

Thus, the mass flow rate from the density gradient induced flow and the corresponding mass flux are given respectively by

$$\dot{M}_D=\rho\int_0^R 2\pi r\mathrm{v}_x^D dr=-\pi R^2 C_m D_\rho\frac{d\rho}{dx}, \tag{5.36}$$

$$\dot{m}_D=-C_m D_\rho\frac{d\rho}{dx}=-D_m\frac{d\rho}{dx}, \tag{5.37}$$

$$D_\rho=\left(\mu_b/\mu+4/3\right)\nu,\nu=\mu/\rho, \tag{5.38}$$

$$C_m=\frac{2}{R^2}\frac{\left(\int_0^R r\mathrm{v}_x^D dr\right)^2}{\int_0^R r\left(\mathrm{v}_x^D\right)^2 dr}. \tag{5.39}$$

Therefore, the cross-section averaged mass flux $\dot{m}_D$ obeys the Fick's law of diffusion with a diffusion coefficient $D_m=C_m D_\rho$. D_ρ is the self-diffusion coefficient in the free-space which is comparable to that from the kinetic theory of gas that gives $D_{11}=1.3\nu$ (Hirschfelder, Curtiss & Bird 1954). C_m is a shape correction factor caused by a non-uniform velocity profile v_x^D and it is independent of the strength of v_x^D. For a uniform flow, $C_m=1$; and for a parabolic profile that does not slip on the tube wall with the form $1-r^2/R^2$, $C_m=3/4$.

Physically, the compressibility-driven large-scale flow $\mathbf{v}^D$ is the aftereffects of the attenuated acoustic wave field at large times, as the acoustic waves associated with the

start-up process evolves into a diffusive field at large time (Hagen et al. 1997; Federhoff 2010; Frydel & Diamant 2012; Chen & Shen 2018a). It should be emphasized that the mass flux diffusive law (5.37) is derived from the compressible Navier-Stokes equations. Thus, the self-diffusion effect is already embedded in the classical Navier-Stokes formulation for compressible flow in small capillaries. Self-diffusion of a compressible fluid generates an equivalent body force in the bulk of the fluid: the dilatation term $\left(\mu_b + 4\mu/3\right)\nabla(\nabla\cdot\mathbf{v})$ in the momentum equation is directly related to the density gradient as it can be expressed as $-\nabla\left(D_\rho D\rho/Dt\right)$ after using the continuity equation (with D/Dt being the substantial derivative). This term is equivalent to a body force that only manifests itself at a length scale comparable to the length of the tube. This body force is proportional to the fluid's local kinematic viscosity and for transient flow in linear acoustics, it causes a damping of the acoustic wave. For steady-state flow, the equivalent body force becomes $-\nabla\left(D_\rho \mathrm{v}_x d\rho/dx\right)$ and it drives a diffusive flow field described by the mass flux equation (5.37), which is maintained by the balance of this body force with the convective acceleration at the large length scale. *Such a diffusive motion is completely absent in an inviscid compressible flow or an incompressible flow*. This dual effect of viscosity (which drives the diffusive flow) also occurs in acoustic streaming (Rayleigh 1945). Convection with a non-uniform velocity only modifies the self-diffusion coefficient.

Similar mass diffusive law can be derived for micro-flows in a channel with a thin gap $2H$ and a large width W ($H/W \ll 1$). The velocity is given by

$$\mathbf{v} = \mathbf{e}_\mathbf{x}\mathrm{v}_x(x,y) + \mathbf{e}_\mathbf{y}\mathrm{v}_y(x,y), \tag{5.40}$$

where y is measured from the centerline of the channel and the x-axis is along the centerline. The corresponding mass flux is given by

$$\dot{m}_{D,ch} = \frac{\dot{M}_{D,ch}}{2wh} = -D_{m,ch}\frac{d\rho}{dx}, \tag{5.41}$$

with

$$D_{m,ch} = C_{m,ch} D_{\rho}, \tag{5.42}$$

$$C_{m,ch} = \frac{\left(\int_{-h}^{h} \mathrm{v}_{x,\rho} dy\right)^2}{4h\int_{-h}^{h} \mathrm{v}_{x,\rho}^2 dy}. \tag{5.43}$$

For no-slip flow of the parabolic form $1-y^2/h^2$, the shape correction factor $C_{m,ch} = 5/6$.

It should be pointed out that back in the 1960s Lund & Berman (1966) has already recognized the importance of self-diffusion in low Mach number viscous compressible flow through a narrow conduit. Such an effect is completely absent in models based on a slip boundary condition (Jaishankar & McKinley 2014). In the context of modern microfluidics applications, Brenner (2005) and Durst et al. (2006) brought the importance of self-diffusion to the attention of the research community. Our analysis in this section confirms the assertions of these previous works. In addition, the analysis here shows that self-diffusion effect is already included in the compressible Navier-Stokes equations. and no constitutive modification is necessary. In this regard, the ENSE theory can be considered as already embedded in the classical formulation.

5.2. No-slip flow with a slip-like mass flow rate

As shown in equation (5.17), the velocity for a low Mach number flow through a small capillary is the sum of an incompressible field $\mathbf{v}^I$ and a diffusive field $\mathbf{v}^D$. These two velocity fields as well as the mass flow rates are found for flow through a long and narrow circular tube in this section.

5.2.1. *Incompressible field*

The incompressible field $\mathbf{v}^I$ is governed by the incompressible flow equations. which for small Reynolds numbers are reduced to the creeping flow equations

$$\nabla \cdot \mathbf{v}^I = 0\,, \tag{5.44}$$

$$0 = -\nabla p^I + \mu \nabla^2 \mathbf{v}^I\,. \tag{5.45}$$

For long and narrow capillaries, the lubrication approximation can be used and the solution of equations (5.44) and (5.45) subject to the no-slip condition is the well-known Hagen-Poiseuille velocity

$$\mathbf{v}^I = -\frac{R^2}{4\mu}\frac{\partial p^I}{\partial x}\left(1 - r^2 / R^2\right)\mathbf{e}_{\mathbf{x}}\,. \tag{5.46}$$

5.2.2. *Diffusive field*

To find the diffusive field $\mathbf{v}^D$, the Helmholtz decomposition is used to decompose $\mathbf{v}^D$ into two parts, $\mathbf{v}^D = \mathbf{v}^{IR} + \mathbf{v}^{RT}$, as in (5.23); and $\mathbf{v}^D$ satisfies the no-penetration and no-slip condition on the tube wall. An average diffusive speed $V_D(x)$ can be defined through the mass flux equation (5.37)

$$\dot{m}_D = \rho V_D = -C_m \frac{\mu_b + 4\mu/3}{\rho} \frac{d\rho}{dx}. \tag{5.47}$$

Thus,

$$V_D = -C_m \frac{\mu_b + 4\mu/3}{\rho^2} \frac{d\rho}{dx}. \tag{5.48}$$

The irrotational part of $\mathbf{v}^D$ is then

$$\mathbf{v}^{IR} = V_D(x)\mathbf{e}_\mathbf{x}. \tag{5.49}$$

The solenoidal part of the velocity satisfies the incompressible creeping flow equations (5.28) and (5.29) and the boundary condition

$$r = R: \mathrm{v}_r^{RT} = 0; \mathrm{v}_x^{RT} = -\mathrm{v}_x^{IR} = -V_D(x). \tag{5.50}$$

The boundary condition (5.50) ensures that the diffusive velocity $\mathbf{v}^D$ satisfies the no-slip condition on the capillary wall. Thus, the solenoidal field $(p^D, \mathbf{v}^{RT})$ is driven by the irrotational flow $\mathbf{v}^{IR}$ via the boundary condition (5.50). The solenoidal velocity $\mathbf{v}^{RT}$ can be conveniently found by using the stream-function-vorticity formulation for an axisymmetric flow, with the stream function $\psi(r,x)$ defined by

$$\mathrm{v}_r^{RT} = -\frac{1}{r}\frac{\partial\psi}{\partial x}, \mathrm{v}_x^{RT} = \frac{1}{r}\frac{\partial\psi}{\partial r}. \tag{5.51}$$

Thus,

$$E^4\psi = 0, \tag{5.52}$$

with

$$E^2 = r\frac{\partial}{\partial r}\left(\frac{1}{r}\frac{\partial}{\partial r}\right) + \frac{\partial^2}{\partial x^2}. \tag{5.53}$$

The boundary condition becomes

$$r = R: \frac{\partial\psi}{\partial x} = 0; \frac{\partial\psi}{\partial r} = -R\,V_D. \tag{5.54}$$

On the centerline, the velocity and the vorticity must be bounded. For long and narrow capillaries, the lubrication approximation can be used to simplify E^2. In addition, the flow rate for the diffusive field must vanish when $d\rho/dx = 0$. The solution for the stream-function is then

$$\psi = \frac{V_D(x)}{2} r^2 \left(1 - \frac{r^2}{R^2}\right), \tag{5.55}$$

and the components for the solenoidal velocity are given by

$$\begin{aligned} \mathrm{v}_r^{RT} &= \frac{1}{2} r \left(\frac{r^2}{R^2} - 1\right) \frac{dV_D}{dx} \\ \mathrm{v}_x^{RT} &= V_D(x) \left(1 - \frac{2r^2}{R^2}\right) \end{aligned} . \tag{5.56}$$

Finally, the diffusive velocity field is given by $\mathbf{v}^D = \mathbf{v}^{IR} + \mathbf{v}^{RT} = \mathbf{e_r} \mathrm{v}_r^{RT} + \mathbf{e_x} \left(V_D + \mathrm{v}_x^{RT}\right)$, which has the components

$$\begin{aligned} \mathrm{v}_r^D &= -\frac{1}{2} r \left(1 - \frac{r^2}{R^2}\right) \frac{dV_D}{dx} \\ \mathrm{v}_x^D &= 2V_D \left(1 - \frac{r^2}{R^2}\right) \end{aligned} . \tag{5.57}$$

The diffusive velocity (5.57) satisfies the no-slip condition on the wall. When the velocity profile (5.57) is substituted into the shape correction factor equation (5.39), we obtain the shape correction factor $C_m = 3/4$, and

$$V_D = -\frac{3\mu_b/4 + \mu}{\rho^2} \frac{d\rho}{dx}. \tag{5.58}$$

The self-diffusion coefficient is then

$$D_m = \frac{3\mu_b/4 + \mu}{\rho}. \tag{5.59}$$

When the bulk viscosity is taken as zero, this diffusion coefficient is reduced to that from

the ENSE theory Durst et al. 2006.

The above results show that the diffusive velocity field induced by self-diffusion can also satisfy the no-slip condition. This is in contrast to ENSE, which allows the diffusive velocity to slip on the capillary wall.

5.2.3. *No-slip flow with a slip-like mass flow rate*

The total velocity is

$$\mathbf{v} = \mathbf{v}^I + \mathbf{v}^D = -\frac{1}{2}\frac{dV_D}{dx} r\left(1-\frac{r^2}{R^2}\right)\mathbf{e_r} + \left[-\frac{R^2}{4\mu}\frac{dp}{dx}\left(1-\frac{r^2}{R^2}\right) + 2V_D\left(1-\frac{r^2}{R^2}\right)\right]\mathbf{e_x}. \quad (5.60)$$

This velocity profile satisfies the no-slip condition on the tube wall. The volumetric flow rate and mass flow rate are given, respectively, by

$$Q_T = Q_{HP} + Q_D = -\frac{\pi R^4}{8\mu}\frac{dp}{dx} + \pi R^2 V_D . \quad (5.61)$$

$$\dot{M}_T = \rho Q_T = -\frac{\pi R^4 \rho}{8\mu}\frac{dp}{dx} + \pi R^2 \rho V_D = -\frac{\pi R^4 \rho}{8\mu}\frac{dp}{dx} + \pi R^2 \dot{m}_D . \quad (5.62)$$

Here subscripts T, HP, D stand total, Hagen-Poiseuille and diffusive contributions respectively. The mass flow rate for the no-slip flow, equation (5.62) is the same as that of the slip-theory of ENSE if the self-diffusion coefficient in ENSE is adjusted to take into account bulk viscosity. Conservation of mass requires the mass flow rate to be a constant. For an ideal gas, $p = \rho \tilde{R} T$, with T being the temperature and $\tilde{R}$ the gas constant. An equation for the pressure is then obtained,

$$\frac{R^2 p}{8\mu \tilde{R} T}\frac{dp}{dx} + \frac{3\mu_b / 4 + \mu}{p}\frac{dp}{dx} = -\frac{\dot{M}_T}{\pi R^2} = \text{constant} . \quad (5.63)$$

This pressure equation is the same as equation (15) of Jaishankar & McKinley (2014) after adjusting for the self-diffusion coefficient. The pressure distribution is given implicitly by

$$\bar{p}_i^2 - \bar{p}^2 + \prod_\mu \ln \frac{\bar{p}_i^2}{\bar{p}^2} = \left(\bar{p}_i^2 - \bar{p}_o^2 + \prod_\mu \ln \frac{\bar{p}_i^2}{\bar{p}_o^2} \right) \bar{x}, \tag{5.64}$$

where p_i, p_o are the inlet and outlet pressures, respectively; $\bar{x} = x/L$; $\bar{p} = pR \big/ \mu\sqrt{8\tilde{R}T}$, $\prod_\mu = 3\mu_b/(4\mu) + 1$. By integrating equation (5.63) from the tube inlet to the outlet, the mass flow rate is found:

$$\dot{M}_T = \frac{\pi R^4}{16\mu\tilde{R}T} \frac{p_i^2 - p_O^2}{L} + \pi R^2 \frac{3\mu_b/4 + \mu}{L} \ln \frac{p_i}{p_o}, \tag{5.65}$$

where p_i, p_o are the inlet and outlet pressures. The mass flow rate depends on both the pressure drop and the pressure ratio. The second term is due to self-diffusion, and it provides a slip-like mass flow rate as it is proportional to R^2 instead of R^4 for the Hagen-Poiseuille flow (the first term on the rhs). Equation (5.65) shows that for a very narrow tube, the slip-like term dominates, leading to a slip-like mass flow rate for the overall flow.

For channel flow, the overall velocity is

$$\mathbf{v} = \left[-\frac{1}{2\mu} \frac{dp}{dx} \left(h^2 - y^2 \right) + \frac{3}{2} V_D \left(1 - \frac{y^2}{h^2} \right) \right] \mathbf{e_x} + \frac{y}{2} \left(\frac{y^2}{h^2} - 1 \right) \frac{dV_D}{dx} \mathbf{e_y}, \tag{5.66}$$

$$V_D = -\frac{5}{6} \frac{\mu_b + 4\mu/3}{\rho^2} \frac{d\rho}{dx}. \tag{5.67}$$

The pressure is given by equation (5.64) with $\bar{p} = ph \big/ \mu\sqrt{3\tilde{R}T}$, $\prod_\mu = 5\mu_b/(6\mu) + 10/9$. The mass flow rate is

$$\dot{M}_T = \frac{h^3 w}{3\mu L\tilde{R}T} \left(p_i^2 - p_o^2 \right) + \frac{2hw\left(5\mu_b/6 + 10\mu/9\right)}{L} \ln \frac{p_i}{p_o}. \tag{5.68}$$

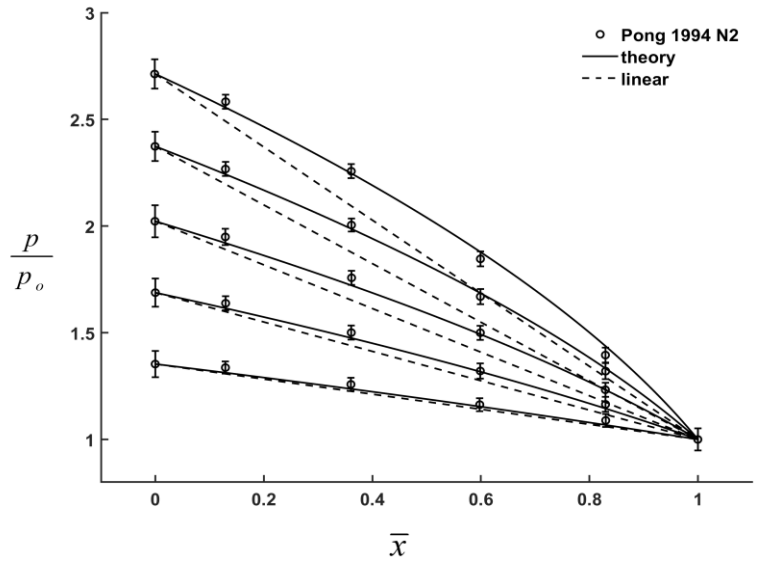

Figure 5.2. Comparison of the predicted pressure profiles with the measurements of Pong et al. (1994), as well as the incompressible flow linear pressure profiles. The five profiles correspond to five different inlet pressures. The outlet pressure is atmospheric.

5.3. Comparison with experiments and other works

The solution in the previous section is compared to experiments as well as other published works in this section.

5.3.1. *Pressure profile*

The theoretical stream wise pressure distribution is compared to the pressure profile measured by Pong et al. (1994) for the flow of nitrogen through a micro-channel (height $1.2\mu m$, width $40\mu m$, length $3000\mu m$) with a fixed outlet pressure p_o of 1atm and different inlet pressures. Figure 5.2 shows the dimensionless pressure profile p / p_o for the five sets of measurements with different inlet pressures. The pressure profiles are nonlinear, and the predicted profiles agree very well with the measurements. The deviation from the linear pressure profile of the incompressible flow $(p - p_{inc}) / p_o$ are shown in figure 5.3a–e.

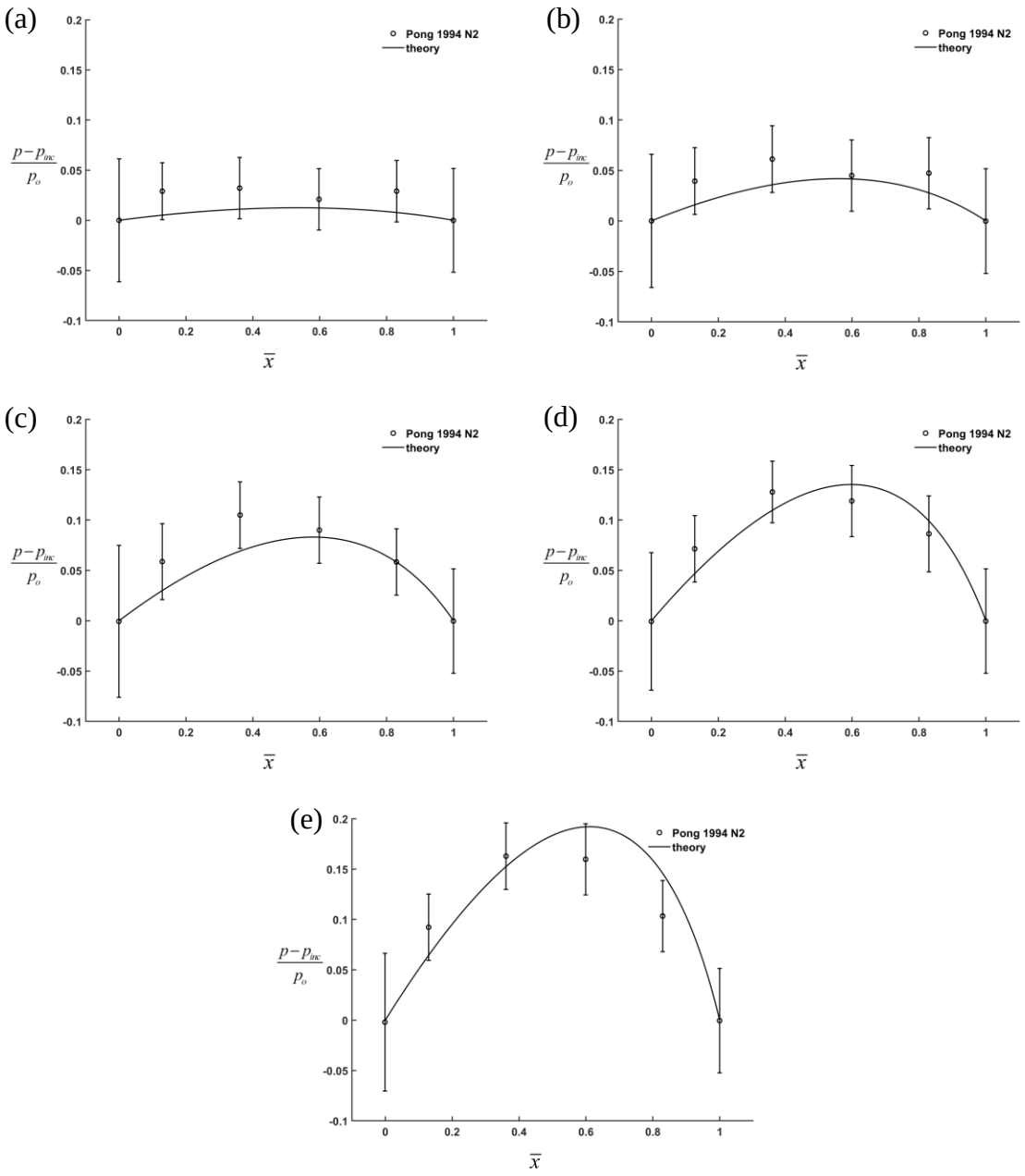

Figure 5.3. (a)−(e) Comparison of the pressure deviations from the incompressible pressure with the measurements of Pong et al. (1994).

Clearly, the theoretical curves all fall within the error bars of the measurements.

5.3.2. *Mass flow rate*

As noted in the previous section, the mass flow rate for the no-slip flow derived in this work is the same as that of the slip-theory of ENSE when the self-diffusion coefficient in ENSE is adjusted for the contribution from the bulk viscosity. Many authors have previously reported good agreements between ENSE theory and experiments (Durst et al. 2006; Chakraborty & Durst 2007; Dongari et al. 2007; Dongari et al. 2009; Dadzie & Brenner 2012; Jaishankar & McKinley 2014). These comparisons, however, were mostly carried out by plotting the dimensional mass flow rate $\dot{M}_T$ against $\Delta p \cdot p_m = (p_i^2 - p_o^2)/2$ on log-log scales. A logarithmic scale plot, however, can artificially distort the magnitudes of errors. It is also noted that in studies using Maxwell-type slip-boundary-conditions, it is customary to plot dimensionless mass flow rate normalized by the Hagen-Poiseuille rate, $S = \dot{M}_T / \dot{M}_{HP}$, against the mean Knudsen number $Kn_m = \lambda_m / d$ (λ_m is the average mean free path and d is the tube diameter or the channel height; see the supplementary section below) on linear scale (the "S" plot). Some authors have also used the Knudsen diffusion mass flow rate, $\dot{M}_K = \pi R^3 (p_i - p_o) / L\sqrt{2\tilde{R}T}$ for tube, $\dot{M}_K = (2h)^2 w(p_i - p_o) / L\sqrt{2\tilde{R}T}$ for channel, to normalize the mass flow rate, $G = \dot{M}_T / \dot{M}_K$ (the "G" plot). In order to provide an unbiased assessment of the mass flow rate prediction, we use all three types of mass flow rate plot in the comparison.

In the ENSE literature, the most frequently used experimental data for mass flow rate comparison are Ewart et al. (2006) for tube; Ewart et al. (2007) and Maurer et al. (2003) for channels. The three types of plots for the mass flow rate comparison between the theory and experiments are shown in figures 5.4a–c, 5.5a–c, 5.6a–c, respectively. A close inspection of these comparisons shows that, while the dimensional mass flow rates on the

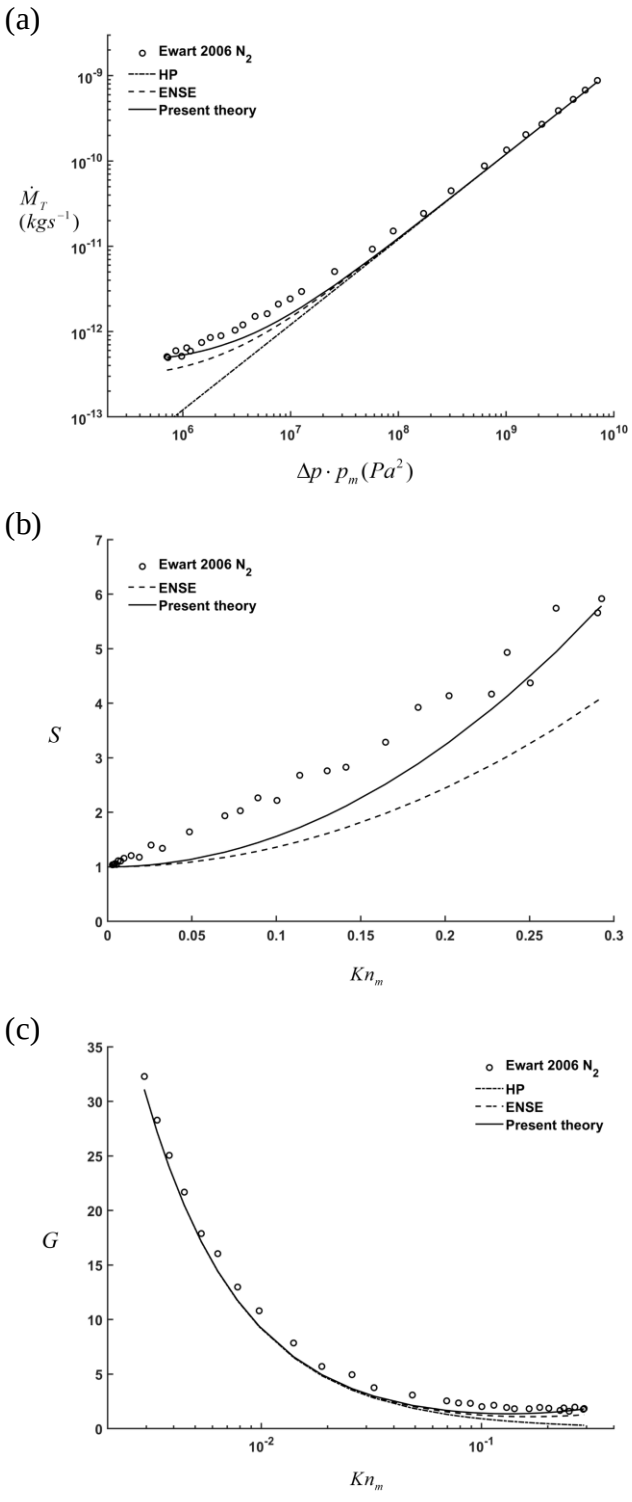

Figure 5.4. (a)−(c) Mass flow rate comparison between theory and the experiment of Ewart et al. (2006) for nitrogen flow through a micro-tube. (a) Dimensional mass flow rates in log-log scale; (b) S plots in linear-linear scale; (c) G plots in linear-log scale.

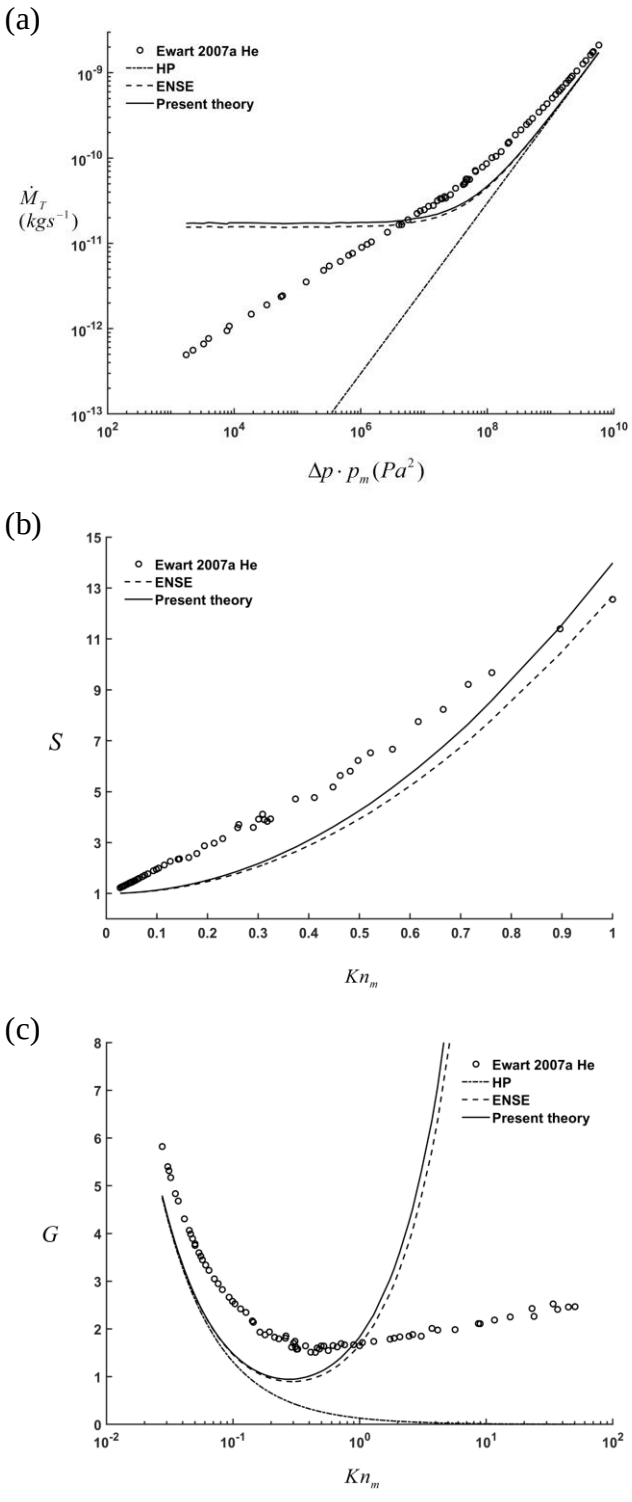

Figure 5.5. (a)−(c) Mass flow rate comparison between theory and the experiment of Ewart et al. (2007) for helium flow through a microchannel. (a) Dimensional mass flow rates in log-log scale; (b) S plots in linear-linear scale; (c) G plots in linear-log scale.

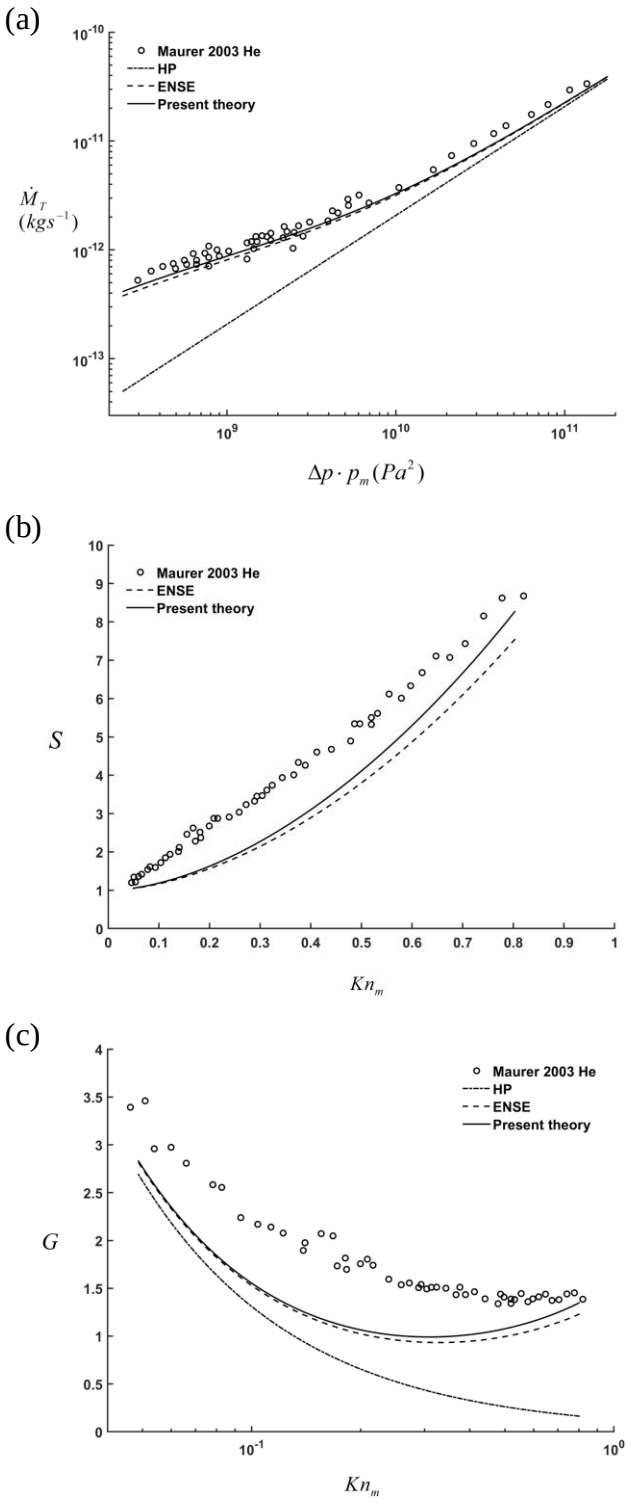

Figure 5.6. (a)−(c) Mass flow rate comparison between theory and the experiment of Maurer et al. (2003) for helium flow through a microchannel. (a) Dimensional mass flow rates in log-log scale; (b) S plots in linear-linear scale; (c) G plots in linear-log scale.

log-log plots demonstrate reasonably good agreements between the theory (the present theory, or ENSE) and experiment, both S-plots and G-plots show significant gaps between theoretical predictions and experimental measurements. These meaningful discrepancy between the predicted mass flow rate and the measured mass flow rate is suppressed by the use of the logarithmic scale in the dimensional mass flow rate plots. It is noted the G-plot in figure 5.4c has much large values of G than the G-plots in figure 5.5c and figure 5.6c. Thus, the difference between the theory and the experiments in figure 5.5c are actually larger when viewed at the same scale as figure 5.5c and figure 5.6c. We have also carried out similar comparisons for 32 additional independent experiments (Ewart et al. 2007; Yamaguchi et al. 2011; Zohar et al. 2002; Anderson 2014; Arkilic et al. 2001; Graur et al. 2009) for both micro-tubes and micro-channels and they are shown in the Supplement. These additional comparisons confirm the above observation that the theory under-predicts the mass flow rate. Thus, we conclude that the self-diffusion effect is not strong enough to account for the experimentally observed mass flow rate enhancement from the Hagen-Poiseuille flow solution. This is in contrast to the claims made in most of the ENSE publications. The only ENSE publication that mentioned this shortfall is (Dadzie & Brenner 2012).

5.3.3. *Supplementary experiment comparison*

This section provides supplementary details about the mean Knudsen number calculation and the rest experimental mass flow rate comparisons which has not been discussed above. As shown in figure 5.4−5.6, the experimental measured mass flow rates are usually plotted

Gas	μ_{ref} $(10^{-5} Pa \cdot s)$	ω	k_λ
N_2	1.656	0.74	0.731
He	1.865	0.66	0.786
Ar	2.117	0.81	0.684

Table 5.1. Properties of Nitrogen, Helium and Argon.

Gas	μ $(10^{-5} Pa \cdot s)$	μ_b $(10^{-5} Pa \cdot s)$	$\Re$ $(J/K \cdot kg)$
N_2	1.7596	1.2845	296.8
He	1.9687	0	2077.1
Ar	2.2624	0	208.13

Table 5.2. Shear, bulk viscosity and specific gas constant for Nitrogen, Helium and Argon at room temperature 296.5K.

against a mean Knudsen number based on the mean free path calculated from the mean pressure between the inlet and the outlet:

$$\lambda_m = k_\lambda \frac{\mu\sqrt{2\tilde{R}T}}{p_m}, \tag{S1}$$

$$p_m = \frac{p_i + p_o}{2}, \tag{S2}$$

where k_λ is a coefficient that depends on the molecular interaction model. The frequently used hard-sphere model (HS) (Chapman 1970) gives $k_\lambda = \sqrt{\pi}/2$. The more general variable-hard-sphere model (VHS) (Bird 1994) gives

$$k_\lambda = \frac{(7-2\omega)(5-2\omega)}{15\sqrt{\pi}}, \tag{S3}$$

where ω is the viscosity index for the gas.

$$\mu = \mu_{ref} \left(\frac{T}{T_{ref}} \right)^{\omega}, \tag{S4}$$

where $T_{ref} = 273.15\ K$. Commonly used gas in the experiments are N_2, Ar, He and their properties are listed in table 5.1, table 5.2 (Nacer 2014). The mean Knudsen number is defined as

$$Kn_m = \frac{\lambda_m}{d}. \tag{S5}$$

Only those experiments that have provided sufficient data that allow for calculations of the inlet and outlet pressures will be used in the comparisons. If tabulated data is not provided, a plot digitizer is used to extract them from the published plots. Experiments were conducted either under the constant pressure ratio condition or fixed exit pressure condition ($p_o = const.$). The experimental values of p_i, p_o are used to compute the corresponding theoretical mass flow rate. Interpolation of these theoretical points creates the theoretical curves shown in the figures.

5.3.3.1. Micro-tube experiments

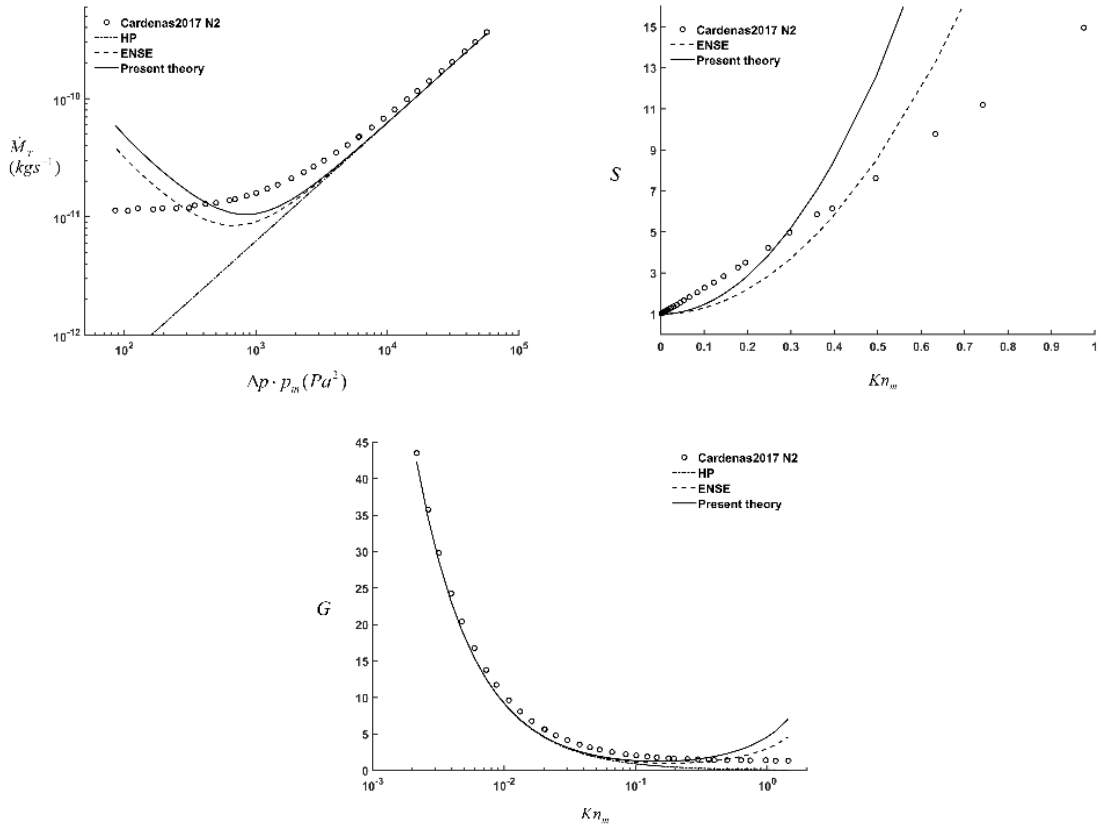

Figure 5.7. Cardenas 2017 N_2 comparison of mass flow rate.

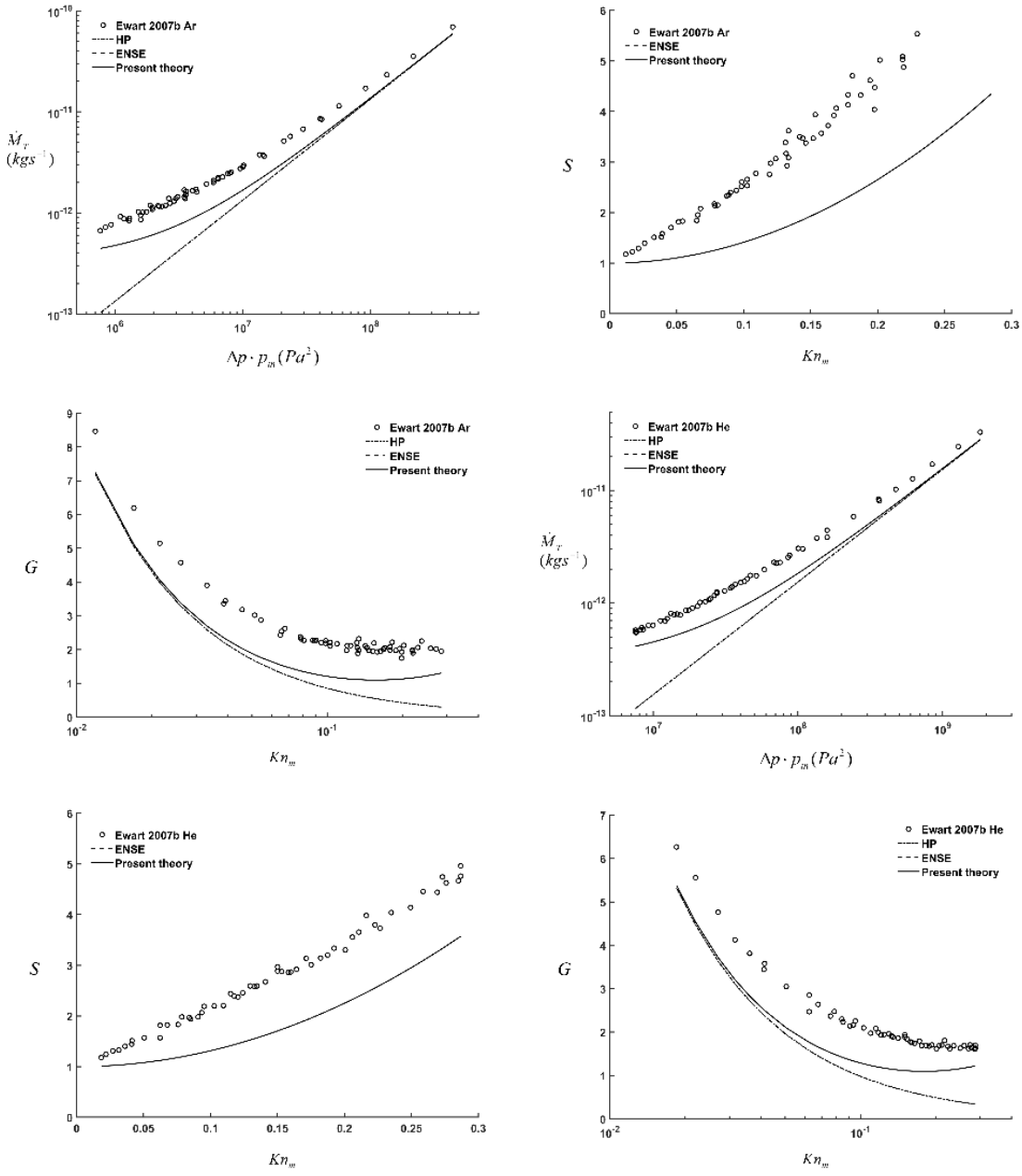

Figure 5.8. Ewart 2007b Ar and He comparison of mass flow rate.

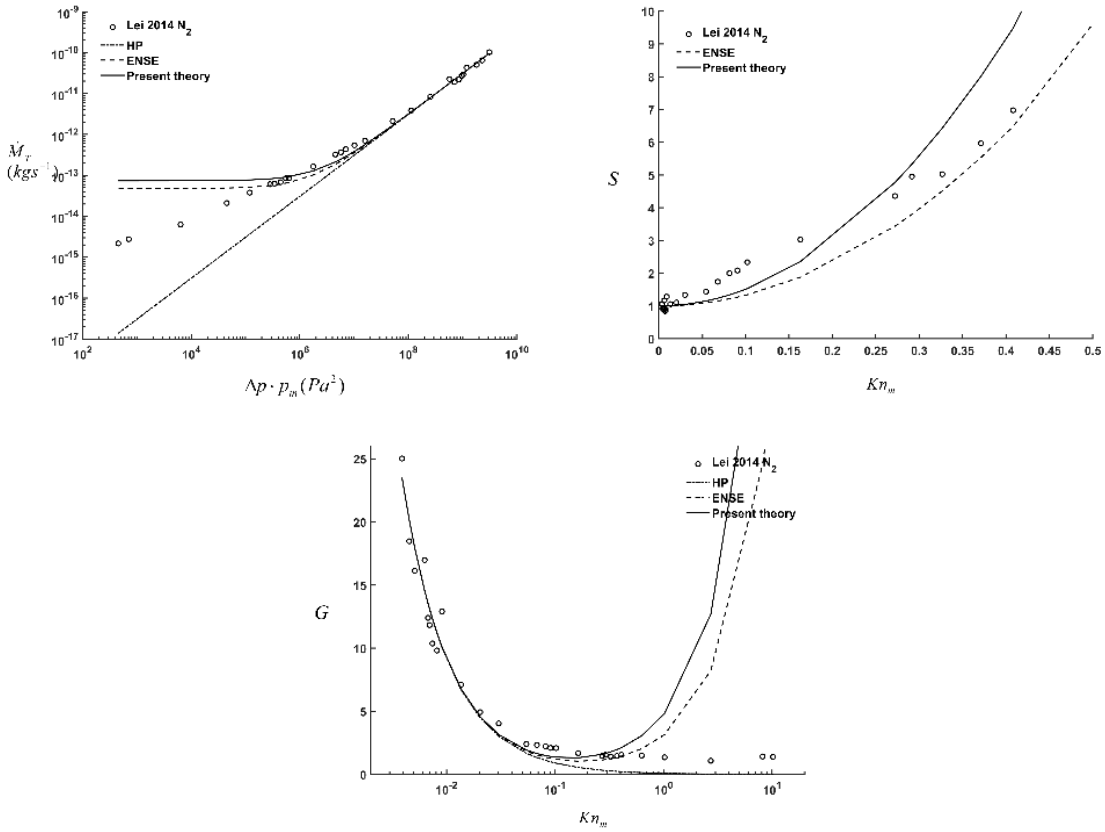

Figure 5.9. Lei 2014 N_2 comparison of mass flow rate.

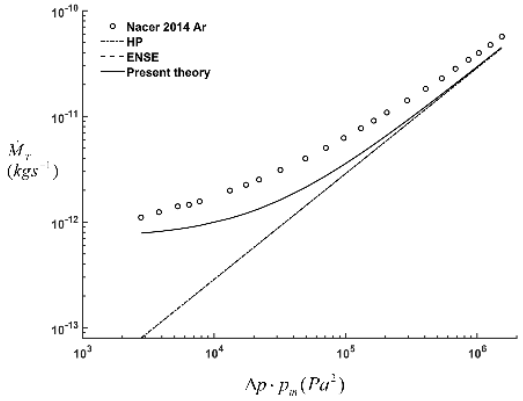
Nacer 2014 Ar
HP
ENSE
Present theory
$\dot{M}_T$ (kgs^{-1})
$\Delta p \cdot p_{in}(Pa^2)$

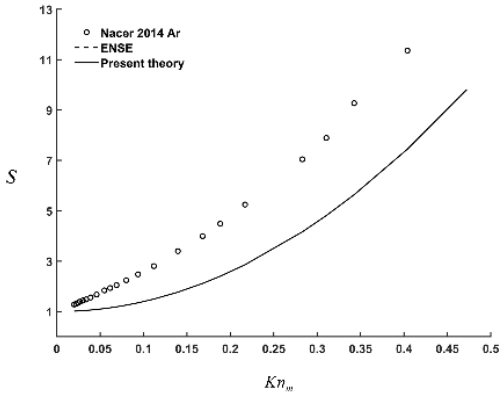
Nacer 2014 Ar
ENSE
Present theory
S
Kn_m

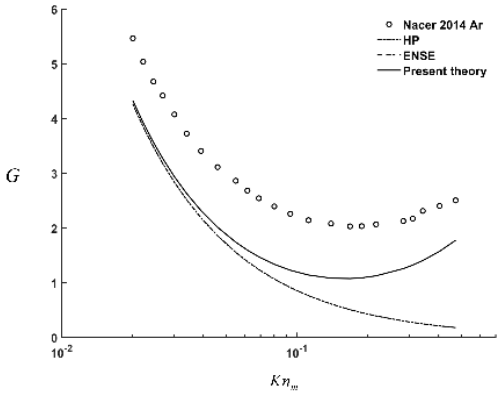
Nacer 2014 Ar
HP
ENSE
Present theory
G
Kn_m

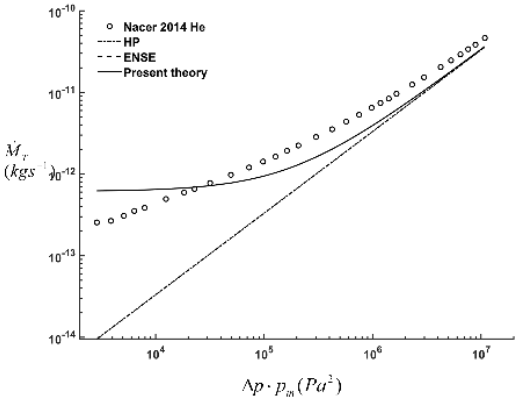
Nacer 2014 He
HP
ENSE
Present theory
$\dot{M}_T$ (kgs^{-1})
$\Delta p \cdot p_{in}(Pa^2)$

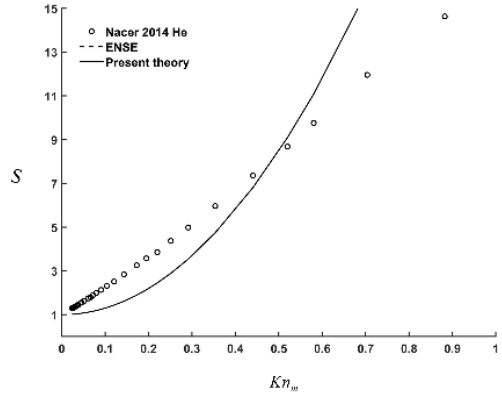
Nacer 2014 He
ENSE
Present theory
S
Kn_m

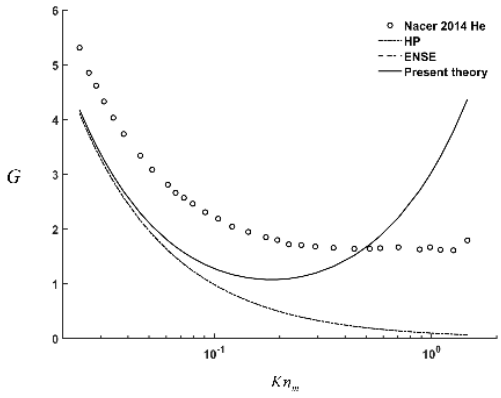
Nacer 2014 He
HP
ENSE
Present theory
G
Kn_m

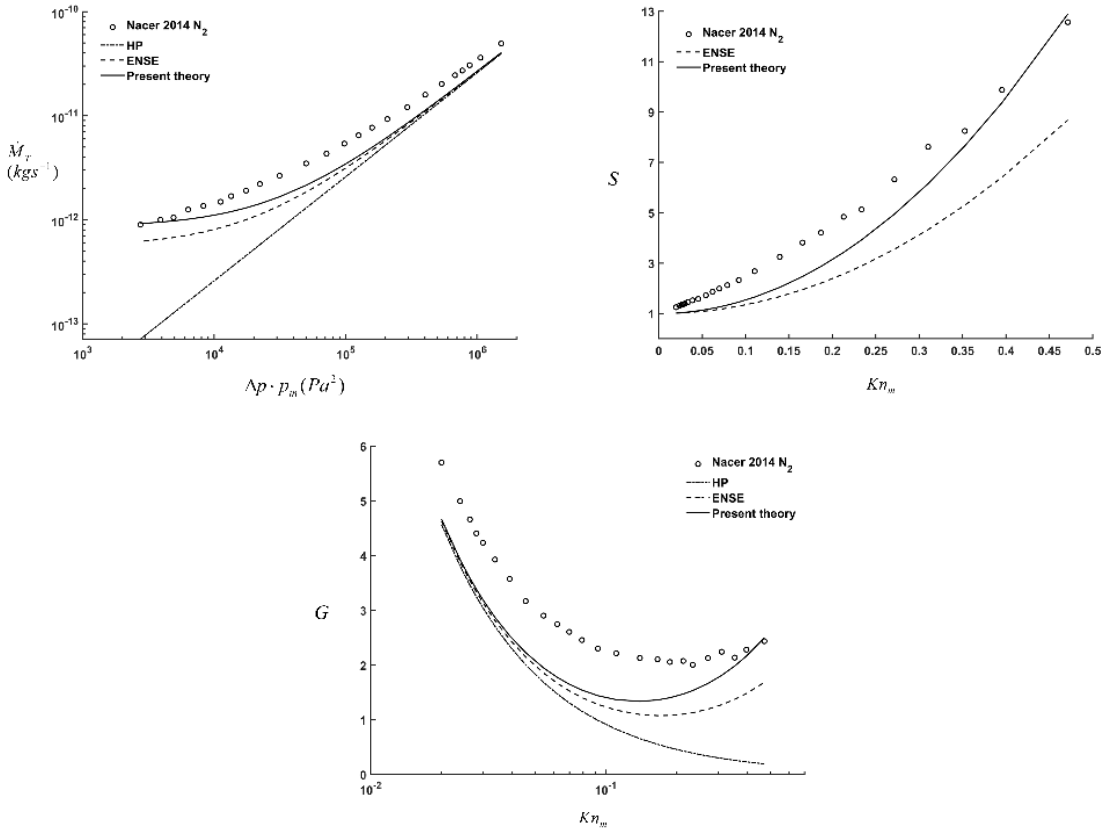

Figure 5.10. Nacer 2014 Ar, He and N_2 comparison of mass flow rate.

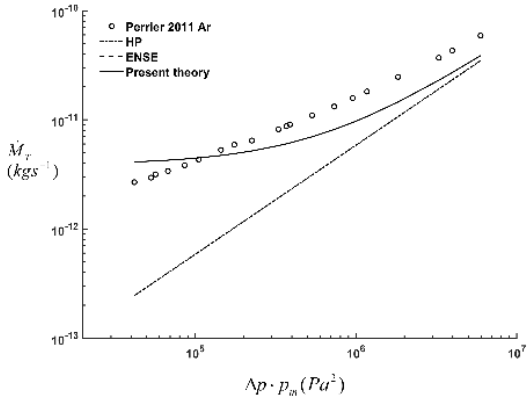
Perrier 2011 Ar
HP
ENSE
Present theory
$\dot{M}_T$ (kgs^{-1})
$\Delta p \cdot p_{in}(Pa^2)$

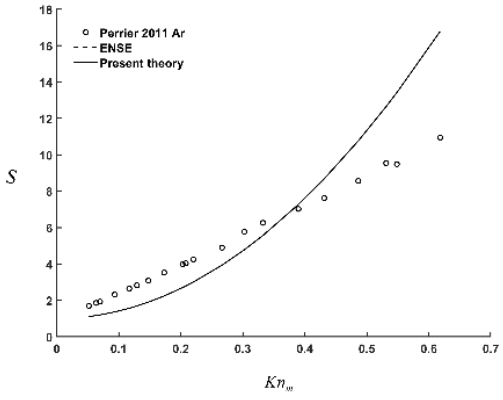
Perrier 2011 Ar
ENSE
Present theory
S
Kn_m

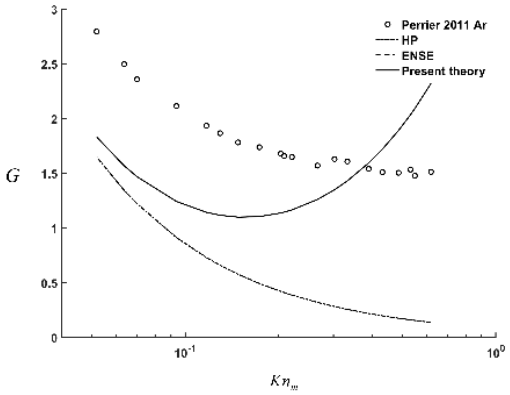
Perrier 2011 Ar
HP
ENSE
Present theory
G
Kn_m

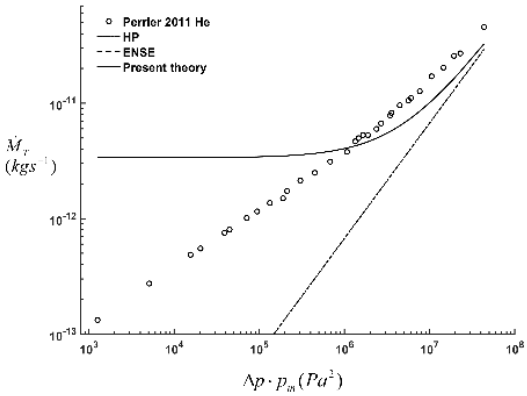
Perrier 2011 He
HP
ENSE
Present theory
$\dot{M}_T$ (kgs^{-1})
$\Delta p \cdot p_{in}(Pa^2)$

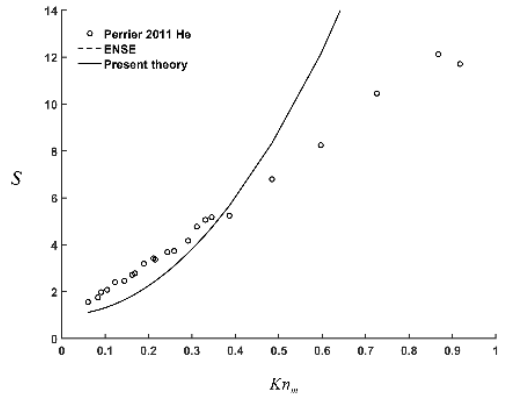
Perrier 2011 He
ENSE
Present theory
S
Kn_m

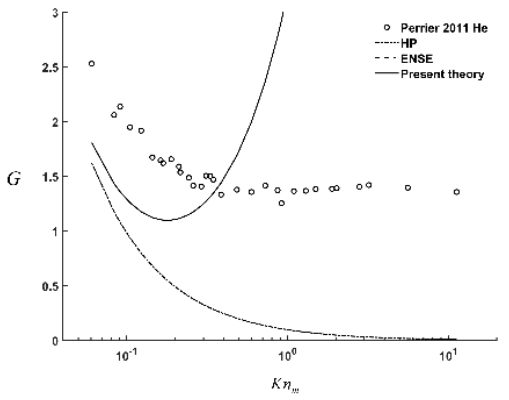
Perrier 2011 He
HP
ENSE
Present theory
G
Kn_m

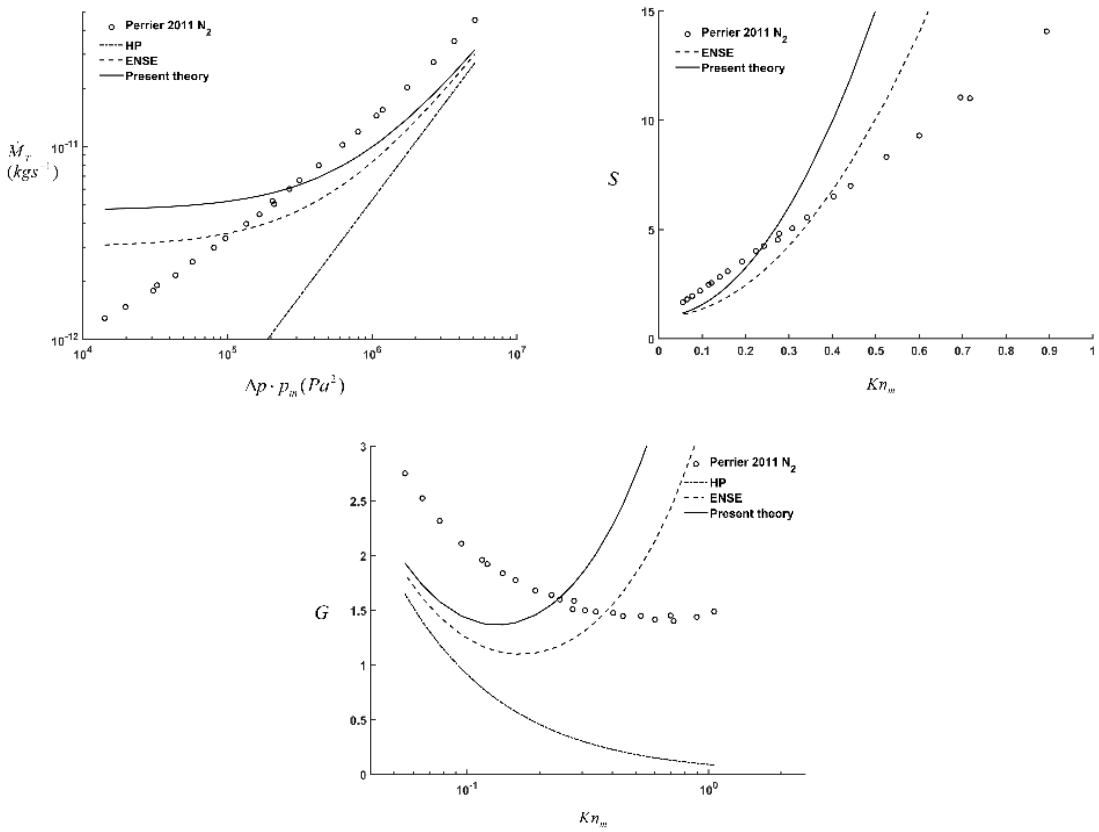

Figure 5.11. Perrier 2011 Ar, He and N_2 comparison of mass flow rate.

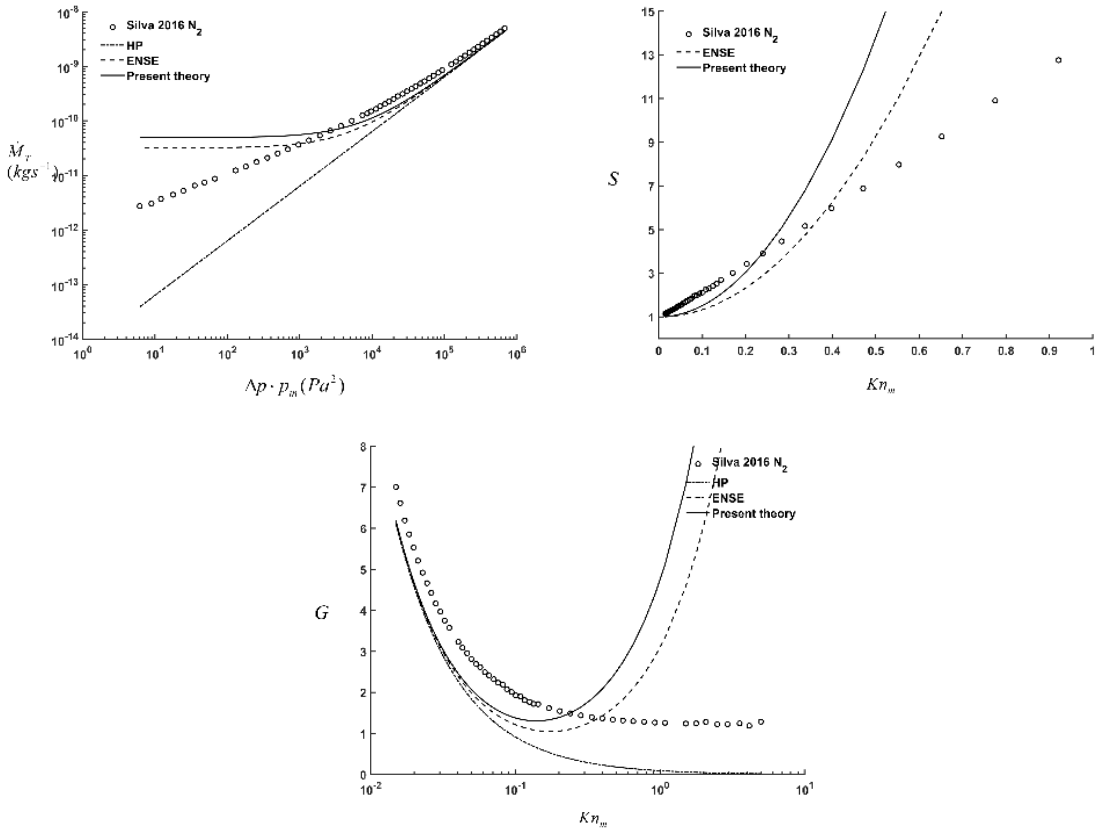

Figure 5.12. Silva 2016 N_2 comparison of mass flow rate.

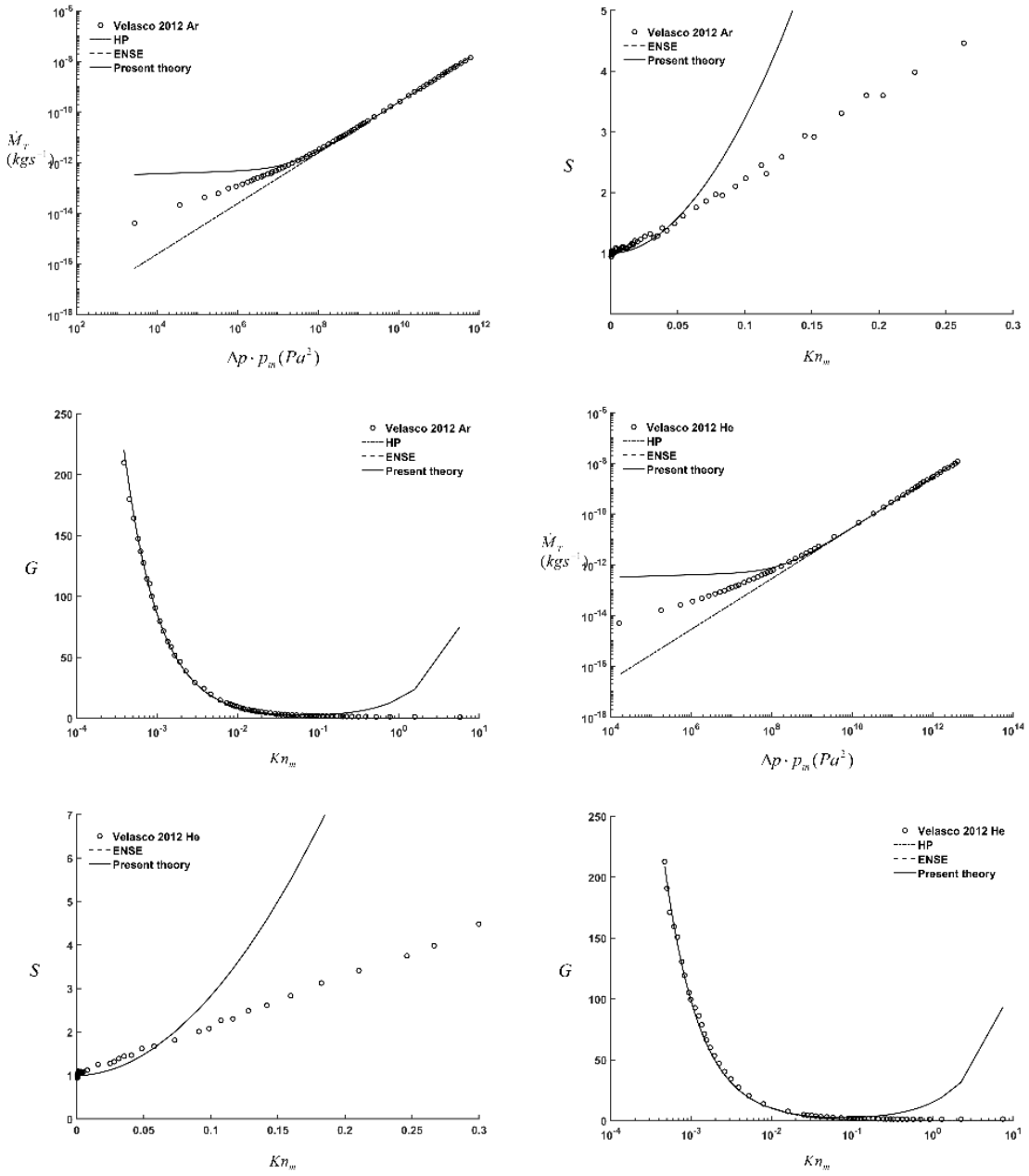

Figure 5.13. Velasco 2012 Ar and He comparison of mass flow rate.

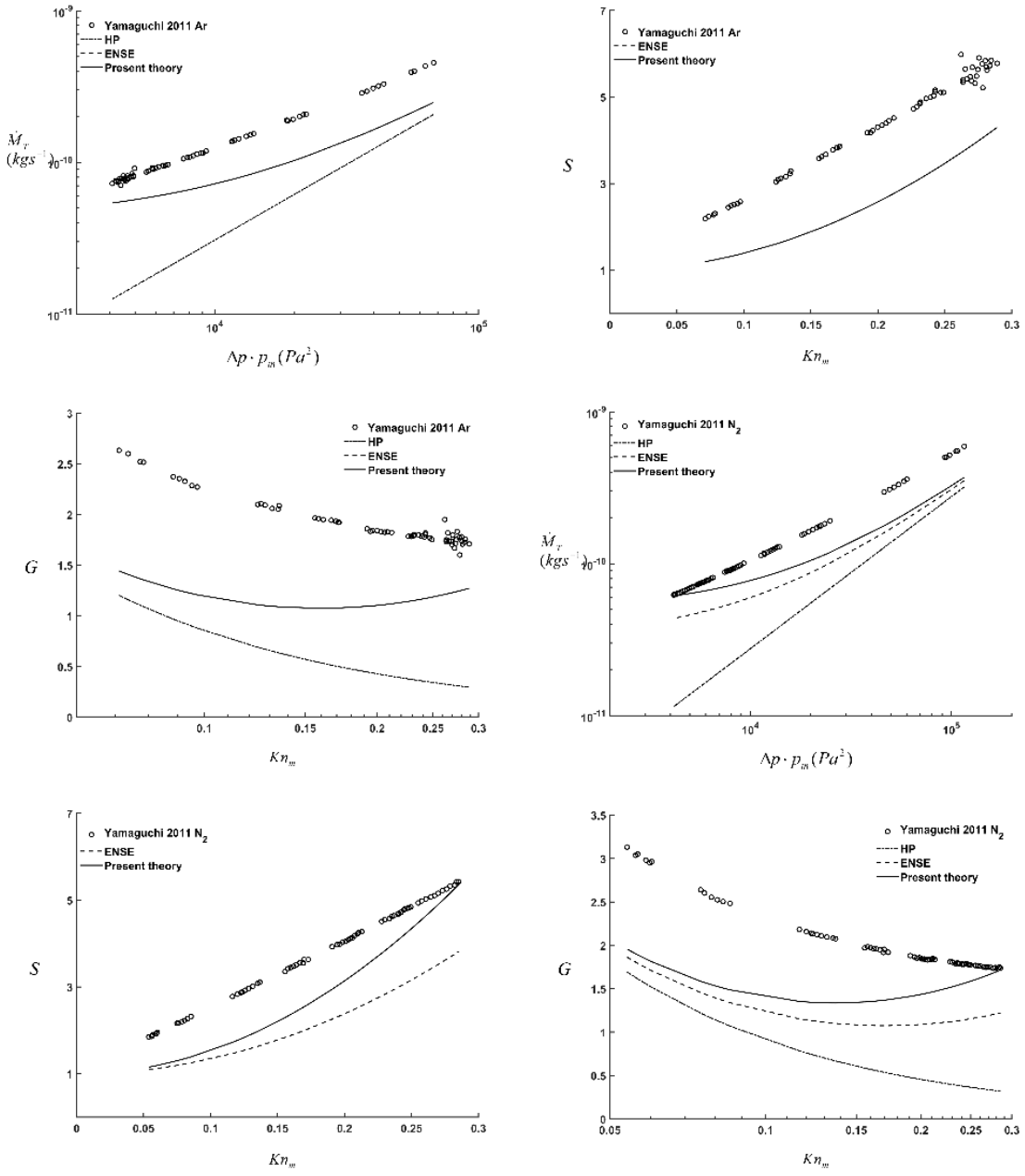

Figure 5.14. Yamaguchi 2011 Ar and N_2 comparison of mass flow rate.

5.3.3.2. Micro-channel experiments with fixed pressure ratio

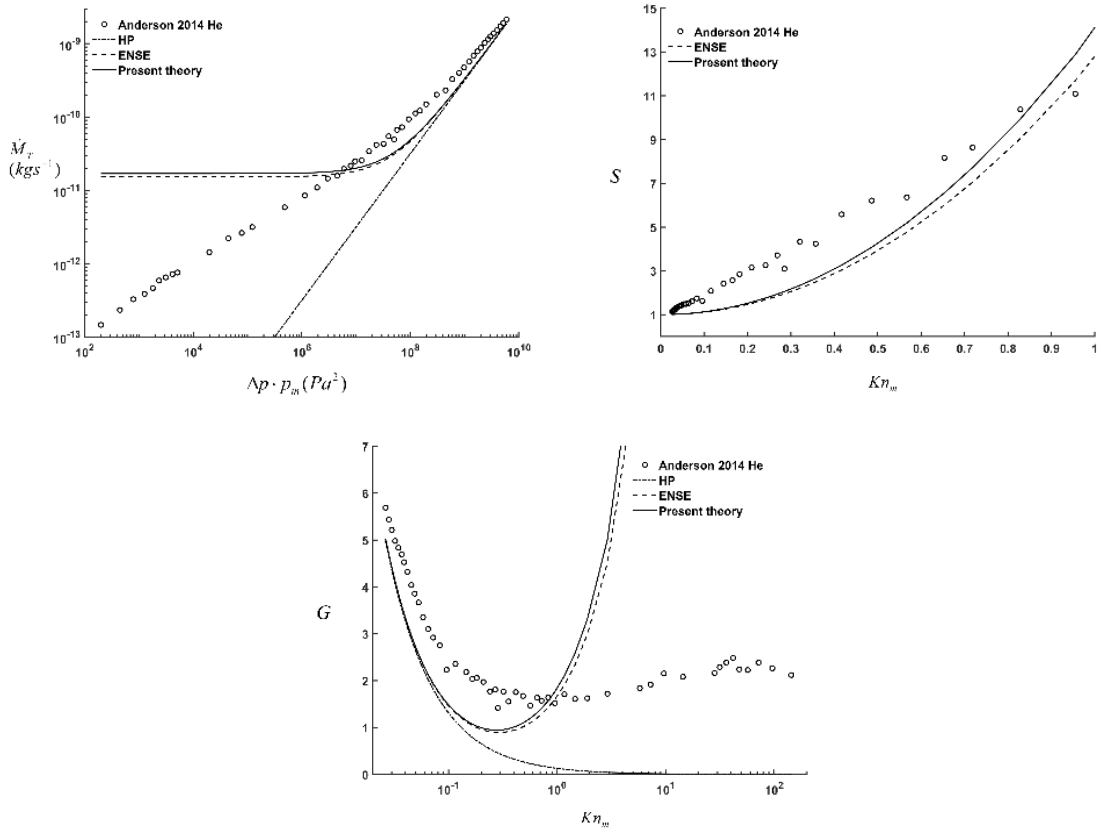

Figure 5.15. Anderson 2014 He comparison of mass flow rate.

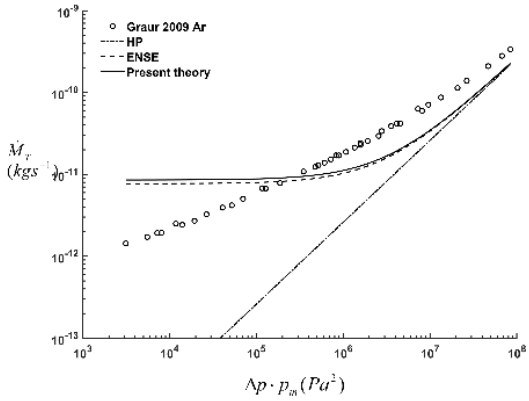
Graur 2009 Ar
HP
ENSE
Present theory
$\dot{M}_T$ (kgs^{-1})
$\Delta p \cdot p_{in}(Pa^2)$

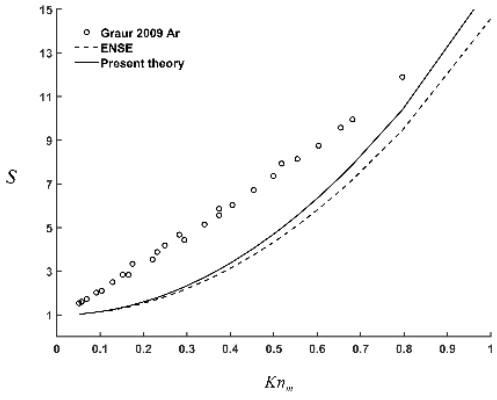
Graur 2009 Ar
ENSE
Present theory
S
Kn_m

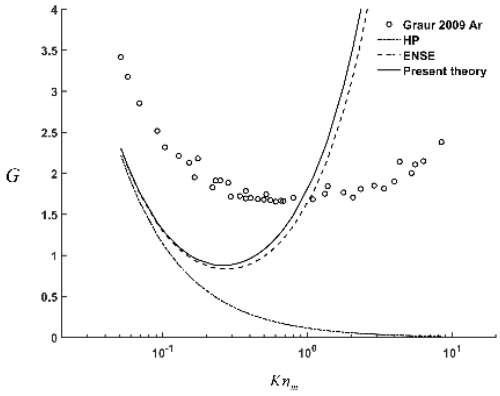
Graur 2009 Ar
HP
ENSE
Present theory
G
Kn_m

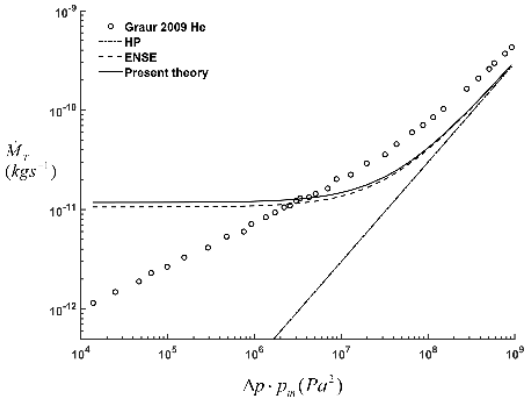
Graur 2009 He
HP
ENSE
Present theory
$\dot{M}_T$ (kgs^{-1})
$\Delta p \cdot p_{in}(Pa^2)$

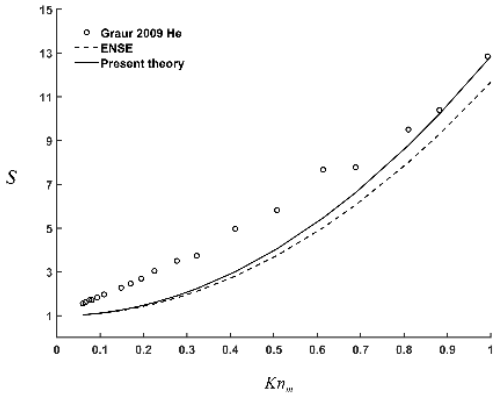
Graur 2009 He
ENSE
Present theory
S
Kn_m

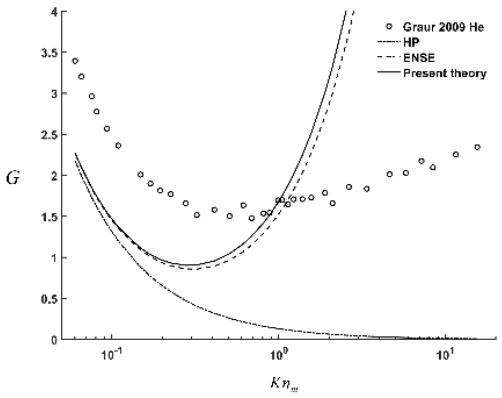
Graur 2009 He
HP
ENSE
Present theory
G
Kn_m

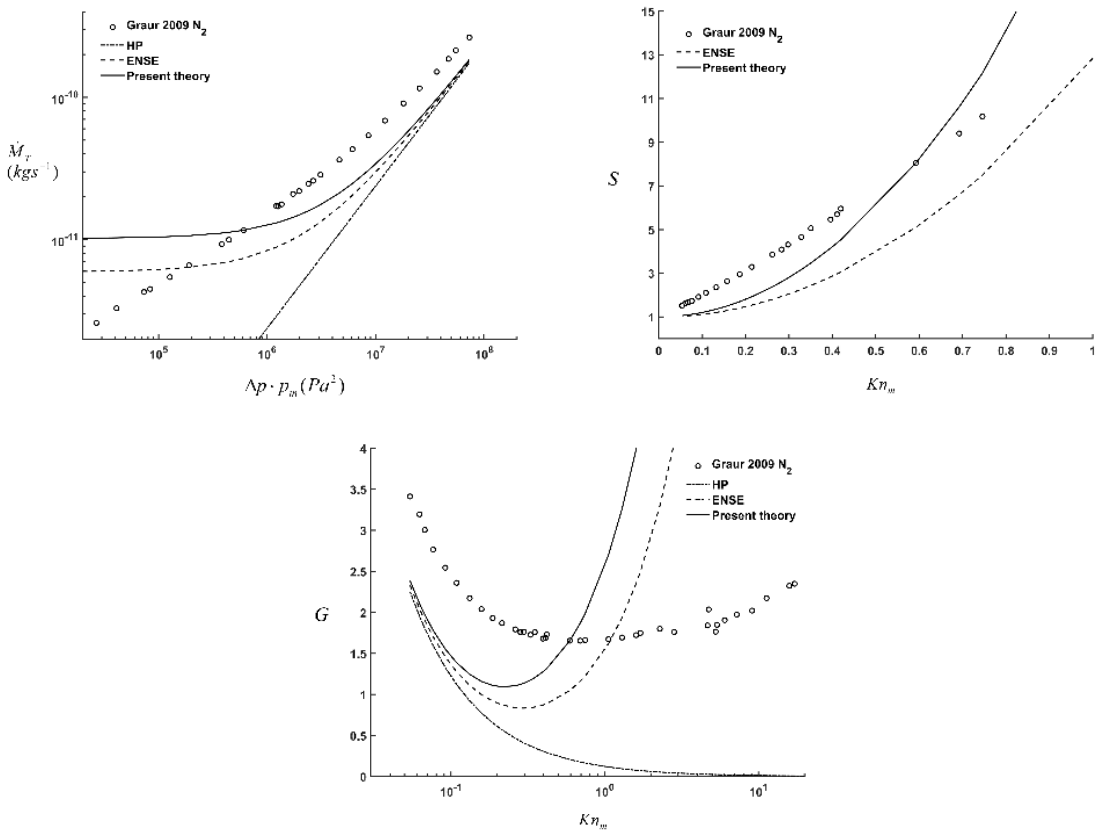

Figure 5.16. Graur 2009 Ar, He and N_2 comparison of mass flow rate.

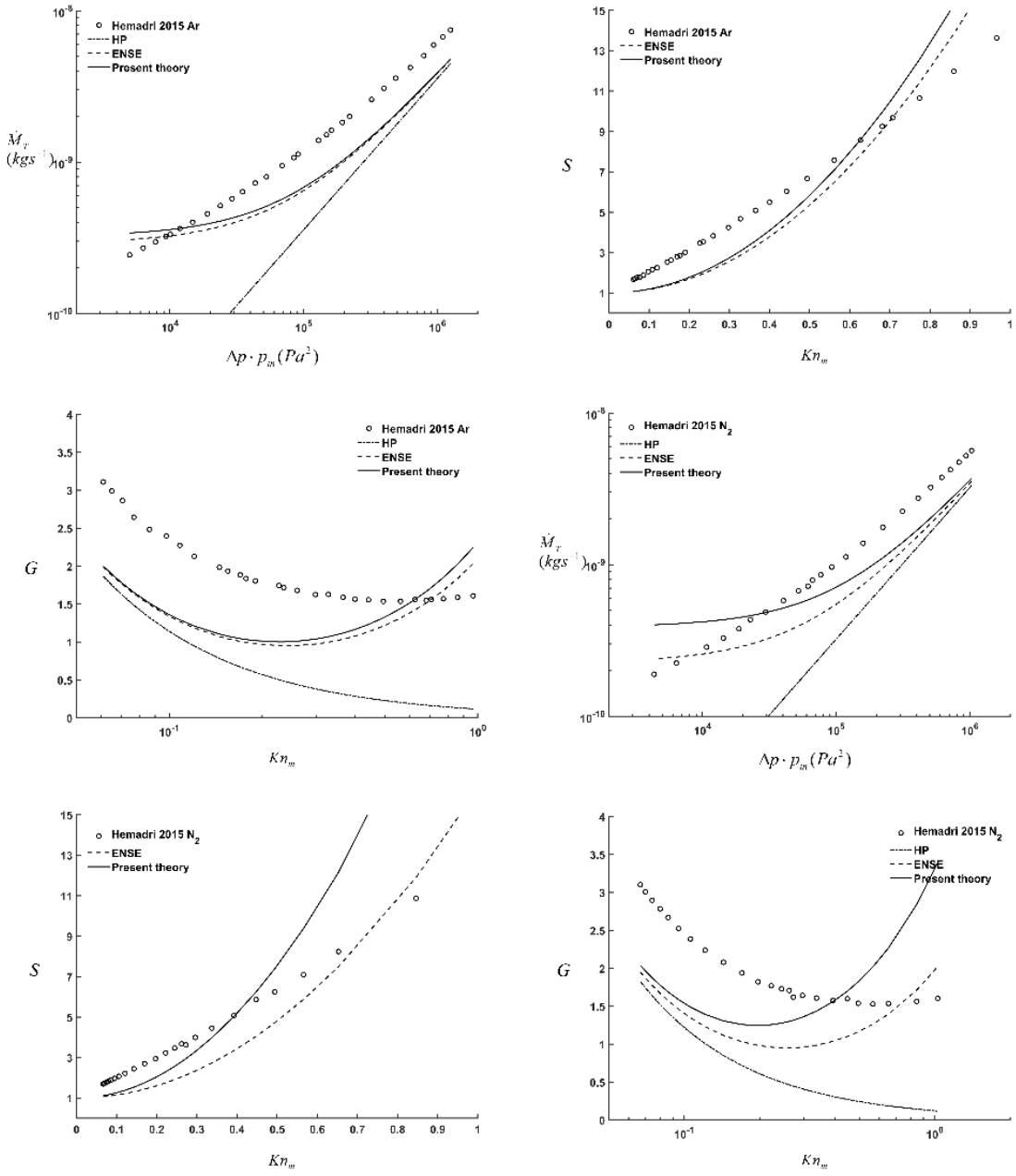

Figure 5.17. Hemadri 2015 Ar and N_2 comparison of mass flow rate.

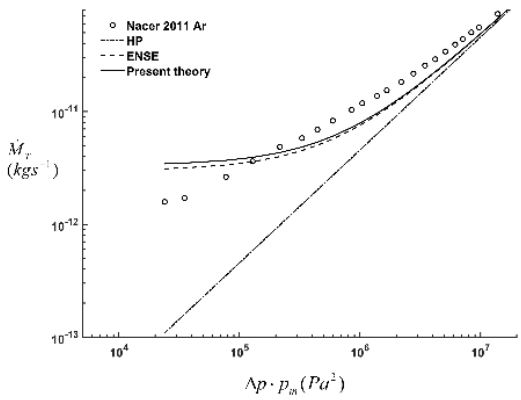
Nacer 2011 Ar
HP
ENSE
Present theory
$\dot{M}_T$ (kgs^{-1})
$\Delta p \cdot p_{in}(Pa^2)$

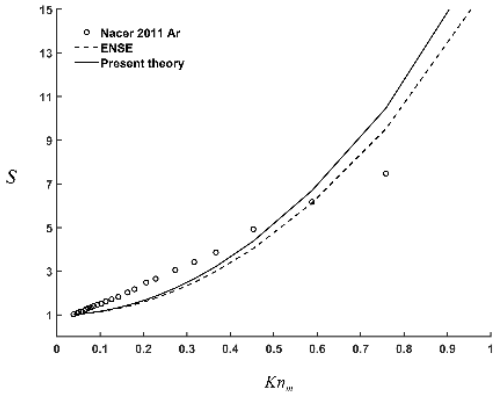
Nacer 2011 Ar
ENSE
Present theory
S
Kn_m

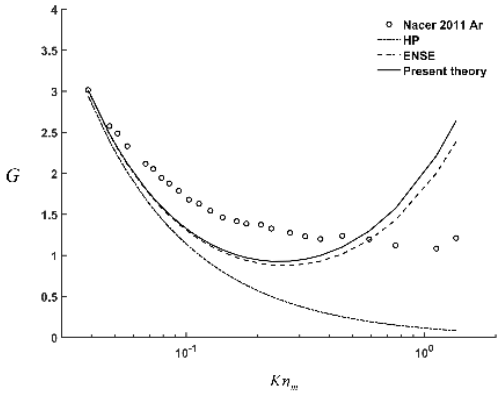
Nacer 2011 Ar
HP
ENSE
Present theory
G
Kn_m

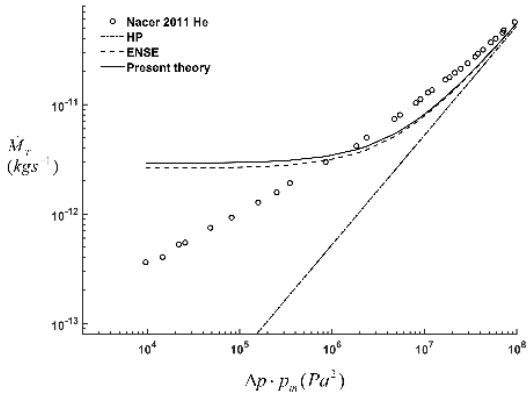
Nacer 2011 He
HP
ENSE
Present theory
$\dot{M}_T$ (kgs^{-1})
$\Delta p \cdot p_{in}(Pa^2)$

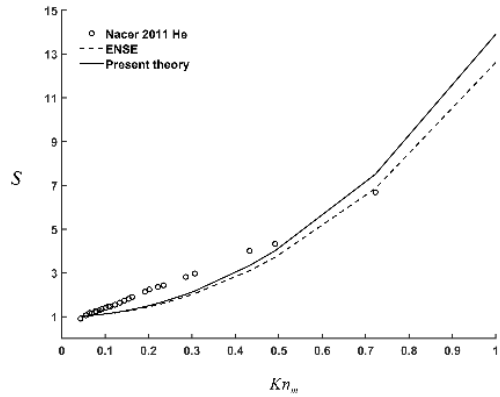
Nacer 2011 He
ENSE
Present theory
S
Kn_m

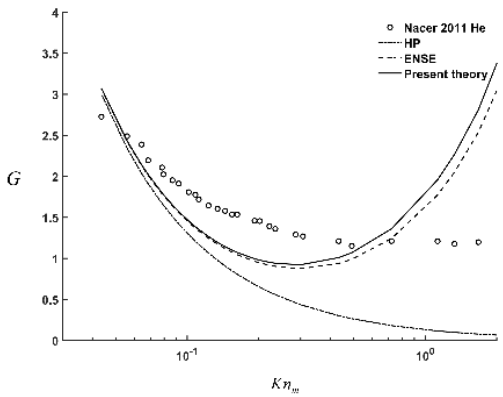
Nacer 2011 He
HP
ENSE
Present theory
G
Kn_m

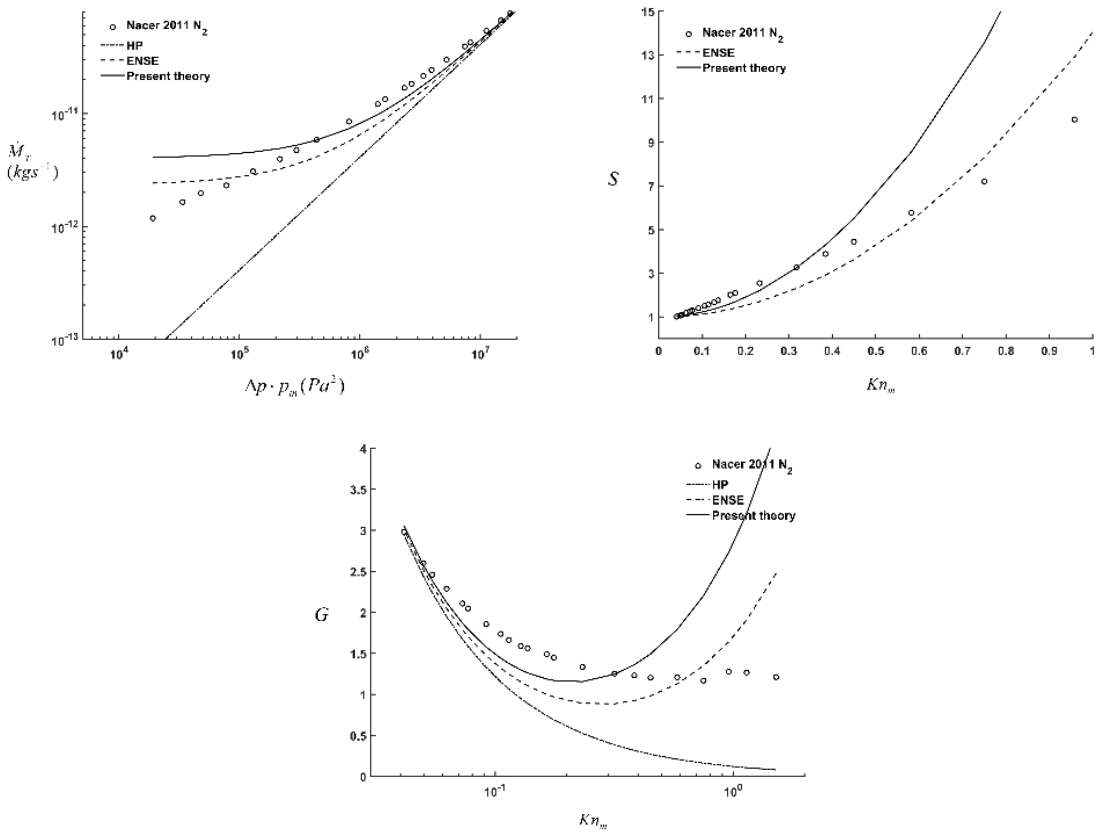

Figure 5.18. Nacer 2011 Ar, He and N_2 comparison of mass flow rate.

5.3.3.3. Micro-channel experiments with fixed outlet pressure ratio

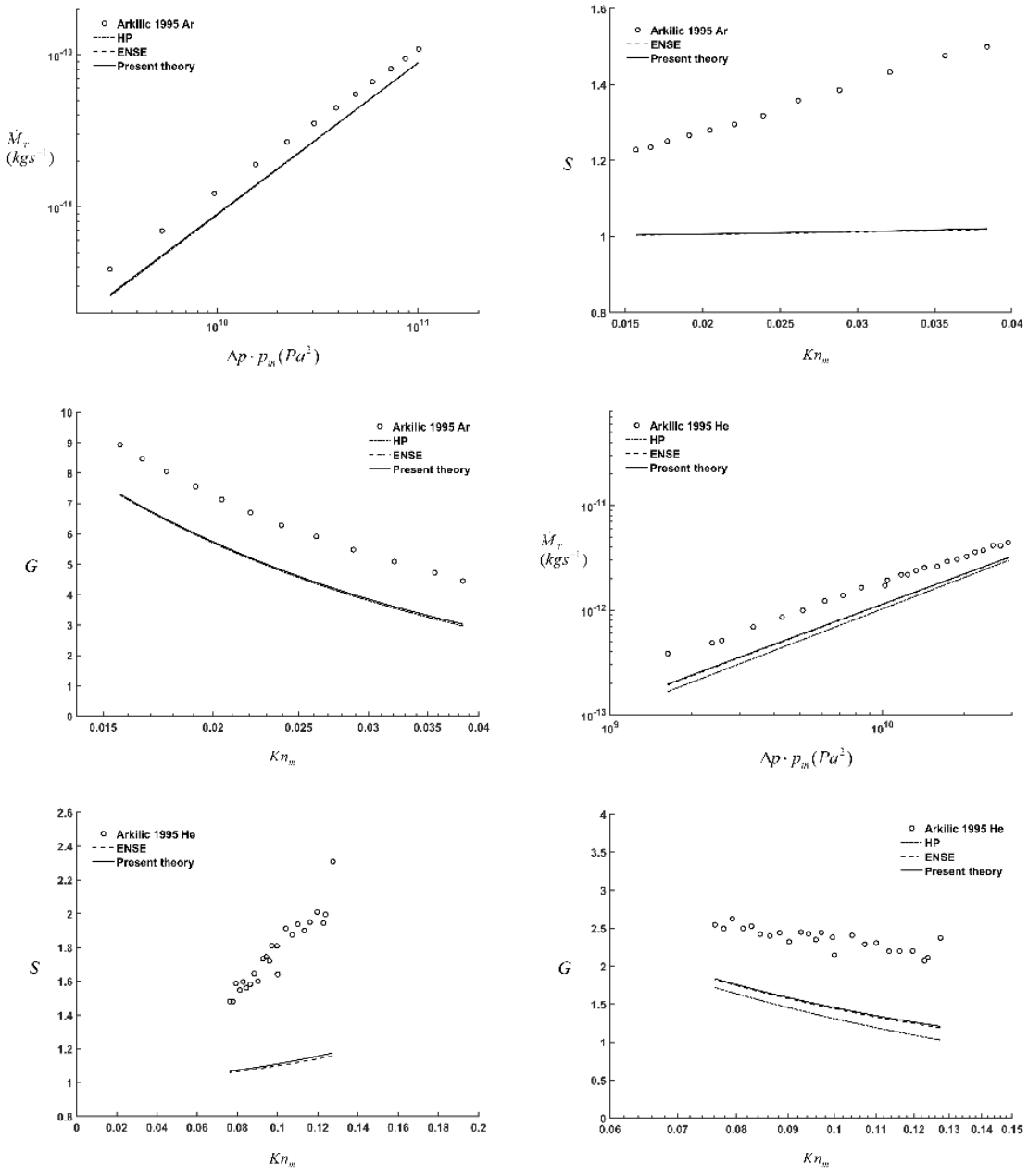

Figure 5.19. Arkilic 1995 Ar and He comparison of mass flow rate.

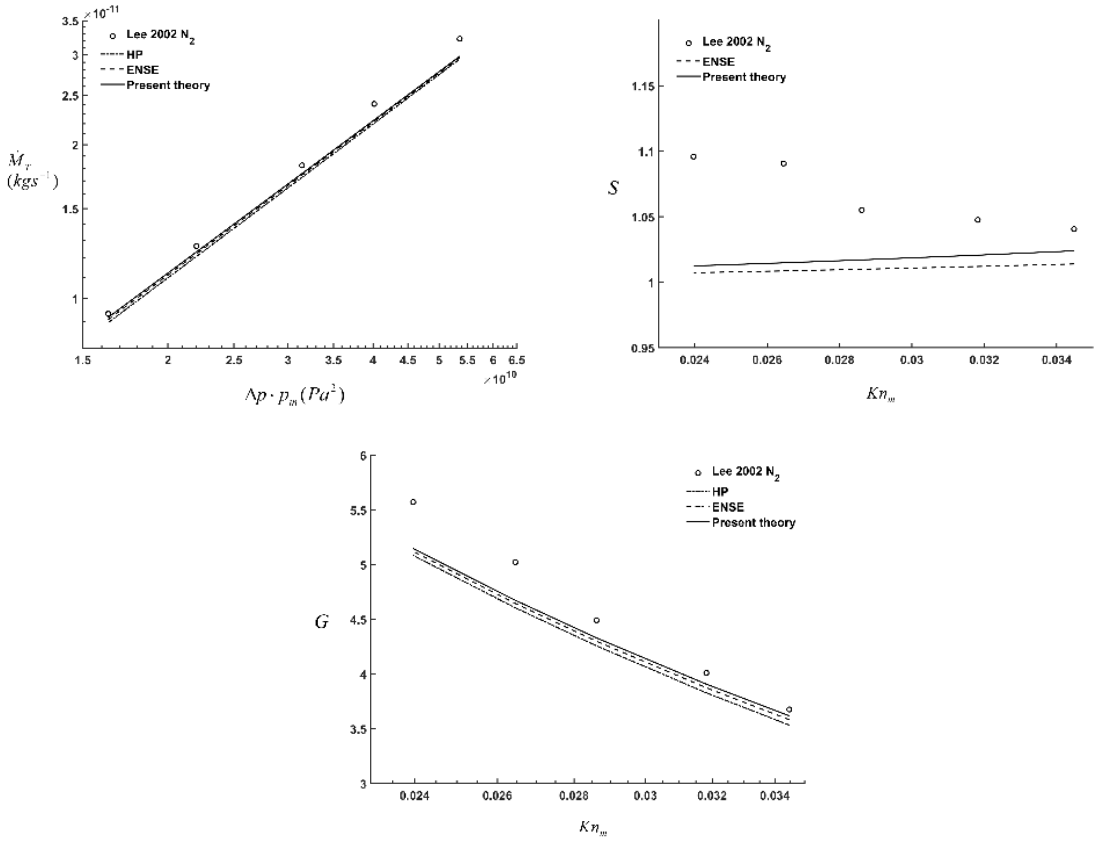

Figure 5.20. Lee 2002 N_2 comparison of mass flow rate.

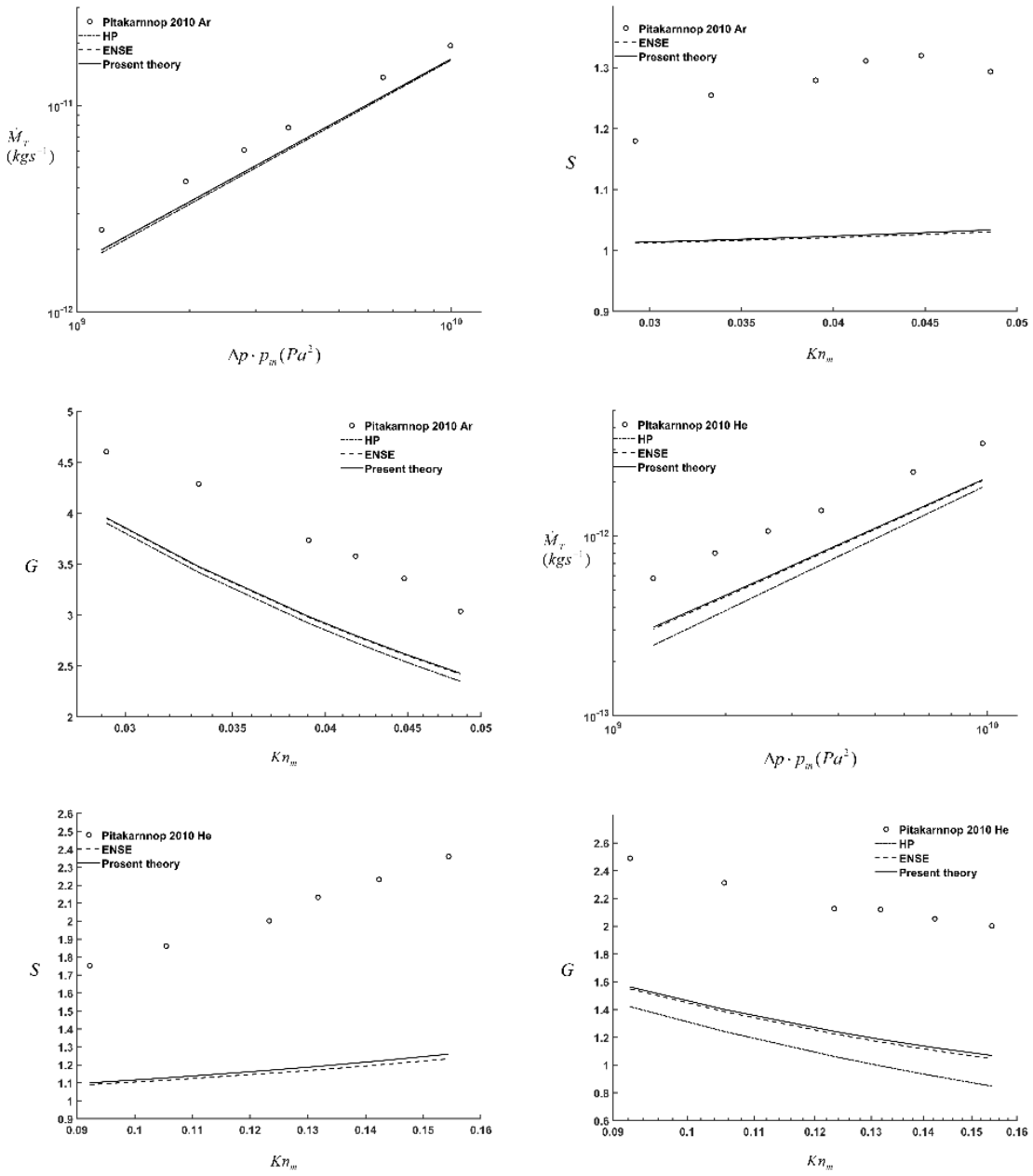

Figure 5.21. Pitakarnnop 2010 Ar and He comparison of mass flow rate.

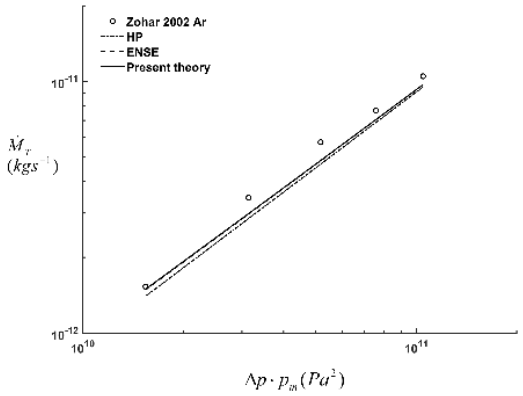
Zohar 2002 Ar
HP
ENSE
Present theory
$\dot{M}_T$ (kgs^{-1})
10^{-11}
10^{-12}
10^{10}
10^{11}
$\Delta p \cdot p_{in}(Pa^2)$

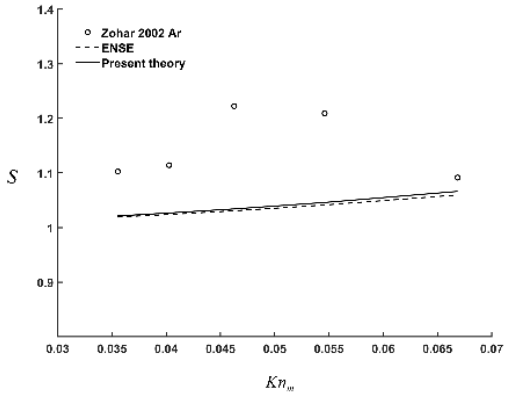
Zohar 2002 Ar
ENSE
Present theory
S
1.4
1.3
1.2
1.1
1
0.9
0.03
0.035
0.04
0.045
0.05
0.055
0.06
0.065
0.07
Kn_m

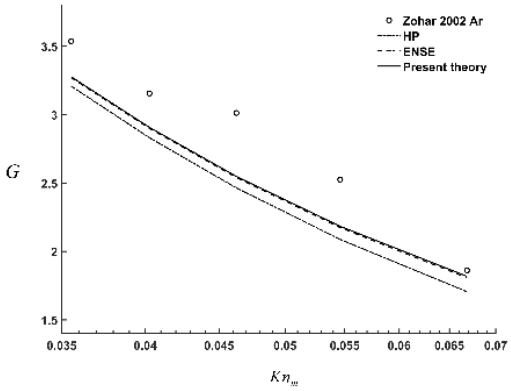
Zohar 2002 Ar
HP
ENSE
Present theory
G
3.5
3
2.5
2
1.5
0.035
0.04
0.045
0.05
0.055
0.06
0.065
0.07
Kn_m

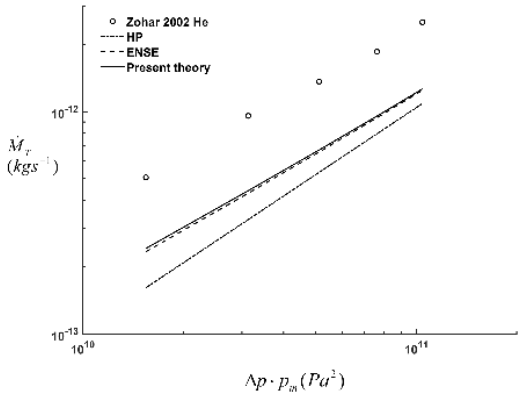
Zohar 2002 He
HP
ENSE
Present theory
$\dot{M}_T$ (kgs^{-1})
10^{-12}
10^{-13}
10^{10}
10^{11}
$\Delta p \cdot p_{in}(Pa^2)$

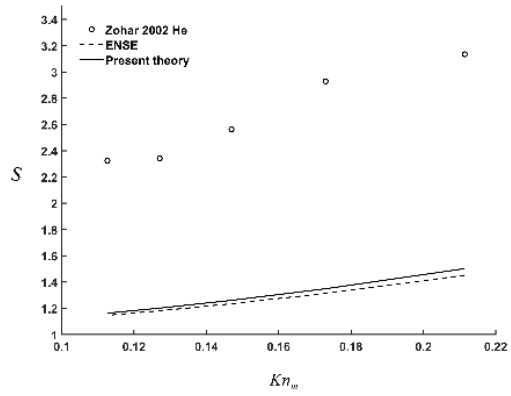
Zohar 2002 He
ENSE
Present theory
S
3.4
3.2
3
2.8
2.6
2.4
2.2
2
1.8
1.6
1.4
1.2
1
0.1
0.12
0.14
0.16
0.18
0.2
0.22
Kn_m

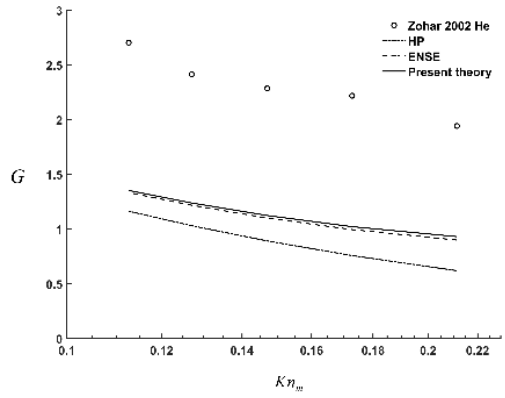
Zohar 2002 He
HP
ENSE
Present theory
G
3
2.5
2
1.5
1
0.5
0
0.1
0.12
0.14
0.16
0.18
0.2
0.22
Kn_m

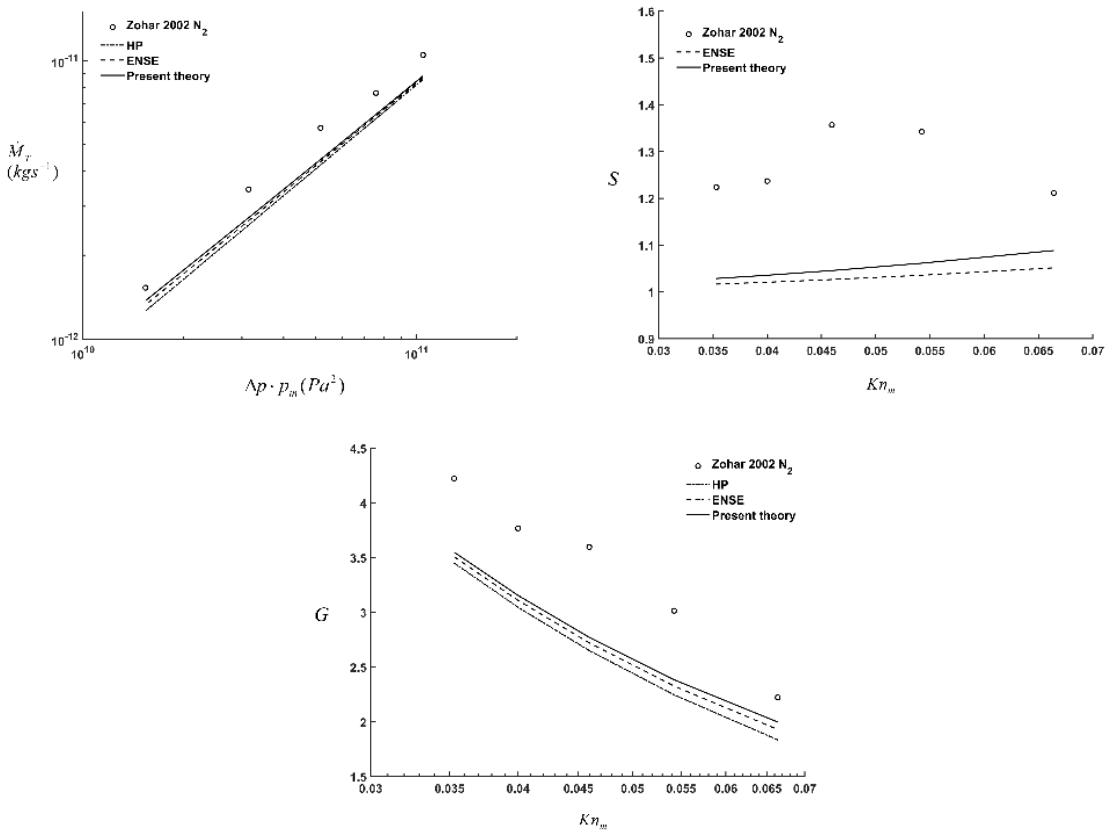

Figure 5.22. Zohar 2002 Ar, He and N_2 comparison of mass flow rate.

5.3.4. *Velocity profile*

Using molecular dynamics (MD) simulation, Barisik & Beskok (2014) computed the velocity profile of the flow of argon through a micro-channel with a 54nm height. The MD simulation converts a pressure-driven flow into a force-driven flow and the stream wise velocity normalized by the mean velocity is shown in their figure 5.4c for a modified Knudsen number 0.1. In figure 5.23, the stream wise velocity from the present theory is compared to figure 5.4c of Barisik & Beskok (2014). The normalized velocity from the MD simulation is much fuller than that from the present theory. The smaller magnitude of

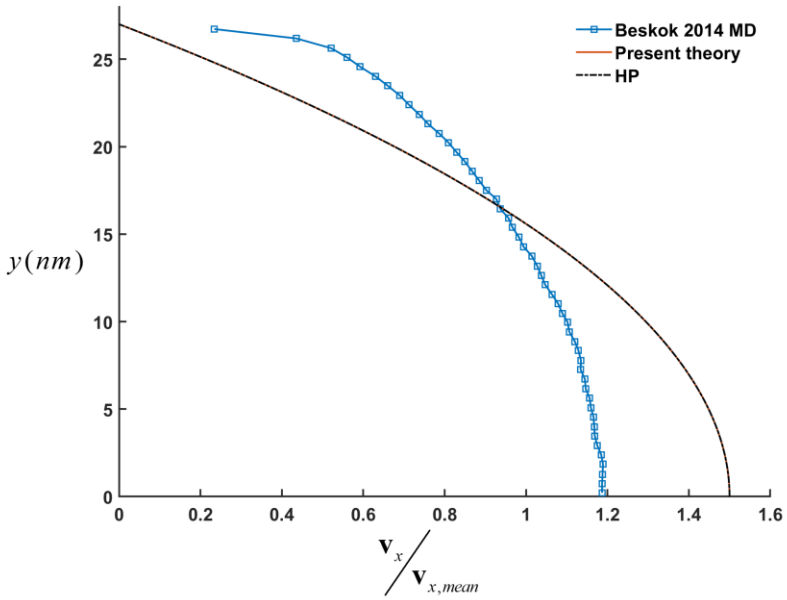

Figure 5.23. Stream wise velocity profile in a micro-channel flow. The stream wise velocity is normalized by the mean velocity. There is no difference between the normalized velocity from the Hagen-Poiseuille flow and the present theory (they differ in dimensionally; see figure 5.24a).

the normalized velocity of MD simulation reflects the fact that its mean velocity is larger than the one from the present theory. Although the Hagen-Poiseuille flow and the present theory have the same normalized velocity, they differ significantly in dimensional terms, as shown in figure 5.24. As shown in figure 5.24a for the cross-section at the channel entry, the middle and the exit, the Hagen-Poiseuille flow velocity and the stream wise velocity of the present theory are both parabolic; but they are different parabolas: the self-diffusion effect makes the velocity much larger than that of Hagen-Poiseuille. As the gas moves down the channel, the stream wise velocity increases. Figure 5.24b shows the corresponding y-component of the velocity at these cross sections.

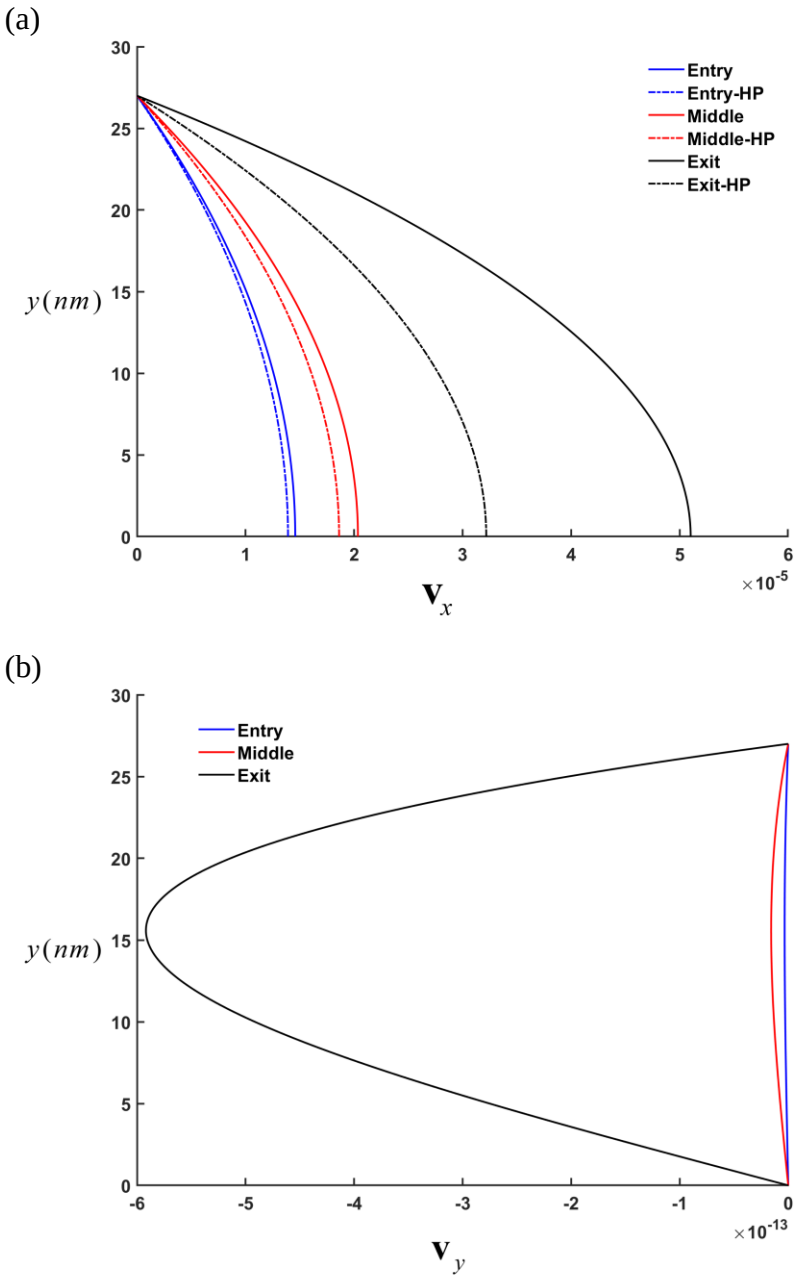

Figure 5.24. Stream wise and cross stream velocity profiles in a micro-channel flow at the entry, the middle and the exit sections of the micro-channel.

Chapter 6

Conclusions

In this dissertation, we derived a new theory for the viscous compressible drainage flow from a micro-conduit and revisited classical theory for steady viscous compressible flow through micro-conduits. The first new theory shows that even with the no-slip condition, the solution of the linearized compressible Navier–Stokes equations for the volume-expansion driven low Mach number viscous compressible flow in a small capillary with a sealed end exhibits a slip-like mass flow rate. Drainage of the fluid is controlled by the slow decay of the standing acoustic wave inside the capillary and the drainage rate is proportional to the fluid's kinematic viscosity via the density diffusion coefficient instead of the reciprocal of the kinematic viscosity as predicted by the lubrication-based theory. The drainage speed is independent of the capillary radius versus the radius square dependence from the Poiseuille flow, allowing fluid to escape from very small capillaries with a finite speed. These counterintuitive findings are valid for arbitrarily small capillaries as long as the continuum assumption holds. These results provide new insights to the nature of slow viscous compressible flow in micro/nano-conduits, as it reveals a unified mechanism for fluid production from the nanopores of shale.

Numerical simulations were conducted for a more realistic drainage flow model with a reservoir or a contraction based on the new linearized theory. The numerical results show that the acoustic wave inside the capillary can leak outside, which eventually alters the drainage performance in large time-scale. The drainage process can be approximated using an analytical derived diffusion model with effective diffusive coefficient, which is computed from an empirical equation.

For the steady compressible gas flow section, we revisited the classical theory for steady viscous compressible flow through micro-conduits. It shows the four distinctive aspects as following:

(a) Contrary to previous claims in the literature, the classical formulation of the compressible Navier-Stokes equations with the no-slip condition includes the self-diffusion (bulk diffusion) effect. Furthermore, the classical formulation also admits a no-slip solution which exhibits a slip-like mass flow rate due to the self-diffusion effect.

(b) The pressure profile and the mass flow rate of the no-slip solution are the same as those of the ENSE theory when the self-diffusion coefficient is adjusted to take into account the contribution from the bulk viscosity. The ENSE theory, however, introduces an additional constitutive hypothesis and assumes slip at the wall. These additional requirements are not necessary as far as micro-conduit flow is concerned.

(c) The predicted pressure profile agrees well with the measured data.

(d) A more careful and comprehensive comparison with 35 experiments from 19 authors clearly shows that, in the slip-flow regime, the predicted mass flow rate is significantly below the measured flow rate. The self-diffusion effect is too small to account for the observed mass flow-rate enhancement from the Hagen-Poiseuille solution in the slip-flow regime, contrary to reports in many ENSE publications.

REFERENCES

Amann-Hildenbrand, A., Ghanizadeh, A. and Krooss, B. M. 2012 Transport properties of unconventional gas systems. *Mar. Petrol. Geol.* **31**, 90–99.

Anderson, J. D. Jr. 1995 *Computational Fluid Dynamics*, McGraw-Hill, New York.

Anderson, J. M., Moorman, M. W., Brown, J. R., et al. 2014 Isothermal Mass Flow Measurements in Microfabricated Rectangular Channels over a Very Wide Knudsen Range. *J. Micromech. Microeng.* **24**(5): 1–12.

Aris, R. 1989 *Vectors, Tensors, and the Basic Equations of Fluid Mechanics.* Dover Publications, New York.

Arkilic, E. B. 1994 *Gaseous Flow in Micron-sized Channels*. Master's thesis, Massachusetts Institute of Technology, Cambridge, MA.

Arkilic, E. B., Schmidt, M. A. & Breuer, K. S. 1997a Gaseous slip flow in long microchannels. *J. Microelectromech Syst.* **6**(2), 167–178.

Arkilic, E. B., Schmidt, M. A. & Breuer, K. S. 1997b TMAC measurement in silicon micromachined channels. In *Proceedings of 20th Symposium on Rarefied Gas Dynamics*, Beijing. Peking University Press, Beijing, China.

Arkilic, E., Breuer, K., & Schmidt, M. 2001 Mass flow and tangential momentum accommodation in silicon micromachined channels. *J. Fluid Mech.* **437**, 29-43.

Barisik, M., Beskok, A. 2014 Scale effects in gas nano flows. *Phys Fluids* 26:052003.

Bear, J. 1988 *Dynamics of Fluids in Porous Media* (Dover Publications, New York)

Bender, C. M. and Orszag, S. A. 1978 *Advanced Mathematical Methods for Scientists and Engineer.* McGraw-Hill, New York.

Beskok, A. and Karniadakis, G. E. 1999 Report: a model for flows in channels, pipes, and ducts at micro and nano scales. *Microscale Thermophys. Eng.* **3**, 43-77.

Bird, R. B., Stewart, W. E. and Lightfoot, E. N. 2007 *Transport Phenomena* (Revised Second Ed.), Wiley, New York.

Bird, G. A. 1994 *Molecular Gas Dynamics and the Direct Simulation of Gas Flows.* Clarendon, Oxford.

Bousige, C., Ghimbeu, C.M., Vix-Guterl, C., Pomerantz, A. E., Suleimenova, A., Vaughan, G., Garbarino, G., Feygenson, M., Wildgruber, C., Ulm1, F., Pellenq, R. J.-M.,

Coasne, B. 2016 Realistic molecular model of kerogen's nanostructure, *Nature Materials* **15**, 576.

Brenner, H. 2005 Navier-Stokes revisited. *Physica A*: *Statistical Mechanics and its Applications* **349**, 60-132.

Buckingham, M. J. 2005 Causality, Stokes' wave equation, and acoustic pulse propagation in a viscous fluid. *Phys. Rev. E* **72**, 026610.

Cai, C., Sun, Q. and Boyd, I. D. 2007 Gas flows in microchannels and microtubes. *J. Fluid. Mech.* **589**, 305–314.

Clarkson, C. 2013 Production data analysis of unconventional gas wells: Review of theory and best practices. *Intl. J. Coal Geol.* **109**, 101.

Carslaw, H. S. & Jaeger, J. C. 1959 *Conduction of Heat in Solids*, 2nd Ed. Oxford Science Publications, New York.

Chakraborty, S. & Durst, F. 2007 Derivations of extended Navier-Stokes equations from upscaled molecular transport considerations for compressible ideal gas flows: Towards extended constitutive forms. *Physics of Fluids* **19**(8), 088104.

Chapman, S., Cowling, T. G. 1970 *The Mathematical Theory of Non-Uniform Gases. 2nd edition*. Cambridge University Press, Cambridge, UK

Chen, K. P., Shen, D. 2018a Drainage flow of a viscous compressible fluid from a small capillary with a sealed end. *J. Fluid Mech.* **839**, 621-643.

Chen, K. P., Shen, D. 2018b Mechanism of fluid production from the nanopores of shale. *Mech. Res. Comm.* **88**, 34-39.

Chorin, A. J. & Marsden, J. E. 1992 *A Mathematical Introduction to Fluid Mechanics.* Springer-Verlag, New York.

Cipolla, C. L., Lolon, E. P., Erdle, J. C., Rubin, B. 2010 Reservoir modeling in shale-Gas reservoirs, *SPE Reservoir Eval. & Eng*. **13**(4), 638.

Civan, F. 2010 Effective correlation of apparent gas permeability in tight porous media, *Transp. Porous Media* **82**, 375.

Civan, F., Rai, C. S., Sondergeld, C. H. 2011 Shale-gas permeability and diffusivity inferred by improved formulation of relevant retention and transport mechanisms, *Transp. Porous Media* **86**, 925.

Colin, S. 2005 Rarefaction and compressibility effects on steady and transient gas flows in microchannels. *Microfluid Nanofluid* **1**, 268–279.

COMSOL Multiphysics® Modeling Software, Burlington, MA, USA.

Cramer, M. S. 2012 Numerical estimates for the bulk viscosity of ideal gases, *Phys. Fluids* **24**, 066102.

Curtis, M. E., Sondergeld, C. H., Ambrose, R. J., & Rai, C. S. 2012 Microstructural investigation of gas shales in two and three dimensions using nanometer-scale resolution imaging. *Am. Assoc. Pet. Geol. Bull.* **96**, 665–677.

Dadzie, S. K. & Brenner, H. 2012 Predicting enhanced mass flow rates in gas microchannels using nonkinetic models. *Phys. Rev. E*. **86**, 036318.

Darabi, H., Ettehad, A., Javadpour, F., Sepehrnoori, K. 2012 Gas flow in ultra-tight shale strata, *J. Fluid Mech.* **710**, 641.

Dongari, N. & Agrawal, A. 2007 Analytical solution of gaseous slip flow in long microchannels. *Intl. J Heat Mass Transf*. **50**, 3411–3421.

Dongari, N., Sharma, A., & Durst, F. 2009 Pressure-driven diffusive gas flows in micro-channels: from the Knudsen to the continuum regimes. *Microfluid Nanofluid* **6**, 679–692.

Draper, N. R., Smith, H. 1998 *Applied Regression Analysis (3rd ed.)*, John Wiley, ISBN 0-471-17082-8.

Durst, F., J. Gomes & Sambasivam, R. 2006 Thermofluiddynamics: Do we solve the right kind of equations. In *Proceeding of the International Symposium on Turbulence, Heat and Mass Transfer*, Dubrovnik, 25-29.

Ertekin, T., King, G. A., Schwerer, F. C. 1986 Dynamic gas slippage: a unique dual-mechanism approach to the flow of gas in tight formations, *SPE Form. Eval.* **1**, 43.

Ewart, T. P., Perrier, P., Graur, I. A. & Meolans, J. G., "Mass flow rate measurements in gas micro flows," *Exp. Fluids* **41**, 487–498 (2006).

Ewart, T. P., Perrier, P., Graur, I. A. & Meolans, J. G. 2007a Mass flow rate measurements in a microchannel, from hydrodynamic to near free molecular regimes. *J. Fluid Mech.* **584**, 337–356.

Ewart, T. P., Perrier, P., Graur, I. A. & Meolans, J. G. 2007b Tangential momentum accommodation in microtube. *Microfluid Nanofluid* **3**, 689–695.

Felderhof, B. U. 2010 Transient flow of a viscous compressible fluid in a circular tube after a sudden point impulse. *J. Fluid Mech*. **644**, 97-106.

Friend, J., & Yeo, L. Y. 2011 Microscale acoustofluidics: Microfluidics driven via acoustics and ultrasonics. *Rev. Modern Phys.* **83**(4), 647-704.

Frydel, D. & Diamant, H. 2012 Sound-mediated dynamic correlations between colloidal particles in a quasi-one-dimensional Channel. *Microparticles in Stokes Flows 2011, J. Phys.: Conf. Ser.* **392** 012007.

Gad-el-Hak, M. 1999 The fluid mechanics of microdevices -The Freeman scholar lecture. *ASME Trans. J. Fluids Eng.* **121**, 5-33.

Gottlieb, M. & Bird, R. B. 1979 Exit effects in non-Newtonian liquids: an experimental study. *Ind. Eng. Chem. Fundam.* **18**(4), 357-368.

Graur, I. A., Perrier, P., Ghozlani, W., et al. 2009. Measurements of Tangential Momentum Accommodation Coefficient for Various Gases in Plane Microchannel. *Phys. Fluids.* **21**, 10.

Graves, R.E. and Argrow, B.A. 1999 Bulk viscosity: past to present, *J. Thermophys. Heat Transfer* **13**, 337.

Gresho, P.M. 1991 Incompressible fluid dynamics: some fundamental formulation issues. *Annu. Rev. Fluid Mech.* **23**, 413–453.

Guo, Z.Y. & Wu, X. B. 1997 Compressibility effect on the gas flow and heat transfer in a microtube. *Intl. J. Heat Mass Transfer* **40**(13), 3251-3254.

Haberman, R. 2013 *Applied Partial Differential Equations, 5th Ed.*, Pearson Education, Upper Saddle River, New Jersey.

Hadjiconstantinou, N. G. 2003 Comment on Cercignani's second-order slip coefficient. *Phys Fluids* **15**(8):2352-2354.

Hadjiconstantinou, N. G. 2006 The limits of Navier-Stokes theory and kinetic extensions for describing small-scale gaseous hydrodynamics. *Phys. Fluids*. **18**, 111301.

Hagen, M. H. J., Pagonabarraga, I., Lowe, C. P., & Frenkel, D. 1997 Algebraic decay of velocity fluctuations in a confined fluid. *Phys. Rev. Ltr.* **78** (19), 3785-3788.

Harley, C., Huang, Y. H., Bau, H. & Zemel, J. N. 1995 Gas flow in microchannels. *J. Fluid Mech.* **284**, 257-274.

Hemadri, V., Varade, V.V., Agrawal, A., Bhandarkar, U.V. 2016 Investigation of rarefied gas flow in microchannels of non-uniform cross section. *Phys. Fluids.* **28** 022007.

Herzfeld, K. F. & Litovitz, T. A. 1959 *Absorption and Dispersion of Ultrasonic Waves.* Academic Press, New York.

Hill, D. G., Nelson, C. 2000 Gas productive fractured shales: an overview and update. *Gas Tips* **6**, 4.

Hirschfelder, J. O., Curtiss, C. F. and Bird, R. B. 1954 *Molecular Theory of Gases and Liquids.* John Wiley & Sons, New York.

Ho, C. M. & Tai, Y. C. 1998 Micro-electro-mechanical-systems (MEMS) and fluid flows. *Annu. Rev Fluid Mech.* **30**, 579-612.

Hong, C., Asako, Y. & Lee, J. 2008 Poiseuille number correlation for high speed micro-flows. *J. Phys. D: Appl. Phys.* **41**, 105111.

Hughes, D. 2013 *Drill, Baby, Drill: Can Unconventional Fuels Usher in a New Era of Energy Abundance?* (Post Carbon Institute, Santa Rosa, California).

Hultmark, M., Aristoff, J. M. & Stone, H. A. 2011 The influence of the gas phase on liquid imbibition in capillary tubes. *J. Fluid Mech.* **678**, pp. 600–606.

Huang, R., Chavez, I., Taute, K.M., Branimir, L., Jeney, S., Raizen, M.G., Florin, E.L. 2011 Direct observation of the full transition from ballistic to diffusive Brownian motion in a liquid. *Nature Physics* **7**, DOI:10.1038/NPHYS1953.

Islam, A., Patzek, T. 2014 Slip in natural gas flow through nanoporous shale reservoirs, *J. Uncon. Oil and Gas Resour.* **7**, 49.

Jain, V. & Lin, C. X. 2006 Numerical modeling of three-dimensional compressible gas flow in microchannels. *J. Micromech. Microeng.* **16**, 292-302.

Jaishankar, A. & McKinley, G. H. 2014 An analytical solution to the extended Navier Stokes equations using the Lambert W function. *AIChE J.* **60**(4), 1413-1423.

Jang, J., Zhao, Y., Wereley, S. T. & Gui, L. 2002 Mass flow measurement of gases in deep-RIE microchannels. In *Proceedings of IMECE2002 ASME International Mechanical Engineering Congress & Exposition*, New Orleans, Louisiana, 17–22. ASME.

Javadpour, Fisher, F., D., Unsworth, M. 2007 Nanoscale gas flow in shale gas sediments, *J. Can. Pet. Technol.* **46**, 55.

Javadpour, F. 2009 Nanopores and apparent permeability of gas flow in mudrocks (shales and siltstone), *J. Can. Pet. Technol.* **48**, 16.

Johnson, S. G. 2008 *Notes on perfectly matched layers (PMLs)*. LECTURE NOTES, Massachusetts Institute of Technology, Massachusetts, 29.

Karniadakis, G., Beskok, A. & Aluru, N. 2005 Microflows and Nanoflows: Fundamentals and Simulation. Springer, New York.

Kennard, E. H. 1938 *Kinetic Theory of Gases*. McGraw Hill, New York.

Klainerman, S. and Majda, A. 1981 Singular limits of quasilinear hyperbolic systems with large parameters and the incompressible limit of compressible fluids. *Comm. Pure Appl. Math.* **34** (4), 481–524.

Klainerman, S. and Majda, A. 1982 Compressible and incompressible fluids. *Comm. Pure Appl. Math.* **35**(5), 629–651.

Klein, R. 1995 Semi-implicit extension of a Godunov-type scheme based on low Mach number asymptotics. I. One-dimensional flow. *J. Comput. Phys.* **121,** No. 2, 213–237.

Knudsen, M. 1909 Die Gesetze der Molekularstroemung und der inneren Reibungsstroemung der Gase durch Roehren. *Ann. Phys.* **333**, 75–130.

Leal, L. G. 2010 *Advanced Transport Phenomena*. Cambridge University Press, New York.

Lee, W., Wong, M., & Zohar, Y. 2002 Microchannels in series connected via a contraction/expansion section. *J. Fluid Mech.* **459**, 187-206.

Lei, W., McKenzie, D. R. 2014 Revisiting Maxwell's accommodation coefficient: A study of nitrogen flow in a silica microtube across all flow regimes. *Ann. Phys.* **351**, 828-836.

Li, X. D., Hu, Z. M., Jiang, Z. L. 2017 Continuum perspective of bulk viscosity in compressible fluids, *J. Fluid Mech.* **812**, 966.

Lighthill, J. 1978 *Waves in Fluids*. Cambridge University Press, New York.

Lunati, I., Lee, S. H. 2014 A dual-tube model for gas dynamics in fractured nanoporous shale formations, *J. Fluid Mech.* **757**, 943.

Lund, L. M. & Berman A. S. 1966 Flow and self-diffusion of gases in capillaries. Part II. *J. Appl. Phys.* **37**, 2489-2496.

Malek, K. & Coppens, M. O. 2003 Knudsen self- and Fickian diffusion in rough nanoporous media. *J. Chem. Phys*. 119(5), 2801-2811.

Maurer, J., Tabeling, P., Joseph, P. & Willaime, H. 2003 Second-order slip laws in microchannels for helium and nitrogen. *Phys. Fluids* **15**, 2613–2621.

Maxwell, J. C. 1879 On stresses in rarified gases arising from inequalities of temperature. *Phil. Trans. Roy. Soc.* **170**, 231–256.

Mehmani, A., Prodanović, M., Javadpour, F. 2013 Multiscale, multiphysics network modeling of shale matrix gas flows, *Transp. Porous Media* **99**, 377.

Monkewitz, P. A. 1979 The linearized treatment of forced gas oscillations in tubes. *J. Fluid Mech.* **91,** 357-397.

Morse, P. M. & Ingard, K. Uno 1968 *Theoretical Acoustics*. McGraw-Hill, New York.

Munz, C.D., Roller, S., Klein, R. and Geratz, K.J. 2003 The extension of incompressible flow solvers to the weakly compressible regime. *Comput. Fluids* **32**, 173–196.

Munz, C.D., Dumbser, M. and Roller, S. 2007 Linearized acoustic perturbation equations for low Mach number flow with variable density and temperature. *J. Comput. Phys.* **224**, 352–364.

Muskat, M. 1949 *Physical principles of oil production*, McGraw-Hill, New York.

Nacer, H. M., Graur, I., Perrier, P. 2011 Mass flow measurement through rectangular microchannel from hydrodynamic to near free molecular regimes. *La Houille Blanche* **4**, 49-54.

Nacer, H. M., Graur, I., Perrier, P., & Meolans, J. G. 2014 Gas flow through microtubes with different internal surface coatings. *Journal of Vacuum Science & Technology* A **32**, 021601.

Nasrifar, K., Bolland, O. 2006 Prediction of thermodynamic properties of natural gas mixtures using 10 equations of state including a new cubic two-constant equation of state, *J. Pet. Sci. Eng.* **51**, 253.

Nelson, P. H. 2009 Pore-throat sizes in sandstones, tight sandstones, and shales, *AAPG Bulletin* **93**, 329.

Ohwada, T., Sone, Y. & Aoki, K. 1989 Numerical analysis of the shear and thermal creep flows of a rarefied gas over a plane wall on the basis of the linearized Boltzmann equation for hard-sphere molecules. *Phys. Fluids* A **1**, 1588–1599.

Panton, R. L. 2013 *Incompressible Flow 4th Ed.* Wiley, New York.

Perrier, P., Graur, I. A., Ewart, T. and Méolans, J.G. 2011 Mass flow rate measurements in microtubes: From hydrodynamic to near free molecular regime. *Phys Fluids* **23**, 042004.

Pierce, A. D. 1981 *Acoustics: An Introduction to Its Physical Principles and Applications.* McGraw-Hill, New York.

Pitakarnnop, J., Varoutis, S., Valougeorgis, D., Geoffroy, S., Baldas, L., and Colin, S. 2010 A Novel Experimental Setup for Gas Microflows. *Microfluid Nanofluid* **8**(1), pp. 57–72.

Poinsot, T. J. & Lele, S. K. 1992 Boundary conditions for direct simulations of compressible viscous flows. *J. Compt. Phys.* **101**,104-129.

Pong, K. C., Ho, C. M., Liu, J. Q. and Tai, Y. C. 1994 Non-linear pressure distribution in uniform micro-channels. *Application of Microfabrication to Fluid Mechanics*, ASME-FED **197**, 51.

Prud'homme, R. K., Chapman, T. W., & Bowen, J. R. 1986 Laminar compressible flow in a tube. *Appl. Sci. Res.* **43**, 67-74.

Rajagopal, K. R. 2013 A new development and interpretation of the Navier–Stokes fluid which reveals why the "Stokes assumption" is inapt, *Intl. J. of Non-Linear Mech.* **50**, 141.

Rayleigh, J. W. S. 1945 *The Theory of Sound*. Vol. 2. Dover, New York.

Rassenfoss, S. 2015 Unconventional rock defies old rules, but new rules are far from being ready. *JPT* **67** (9), 64-66.

Rojas-Cárdenas, M., Silva, E., Ho, MT. et al. 2017 Time-dependent methodology for non-stationary mass flow rate measurements in a long micro-tube. *Microfluid Nanofluid* 21: 86.

Sani, R.L. & Gresho, P.M. 1994 Resume and remarks on the open boundary condition minisymposium. *Int. J. Numer. Methods Fluids* **18,** 983-1008.

Scarton**,** H. A. & Rouleau, W. T. 1973 Axisymmetric waves in compressible Newtonian liquids contained in rigid tubes: steady-periodic mode shapes and dispersion by the method of Eigenvalleys. *J. Fluid Mech.* **58**, 595-621.

Schwartz, L. W. 1987 A perturbation solution for compressible viscous channel flow. *J. Eng. Math.* **21**, 69-86.

Schwartz, M. D. 2016 *The physics of Waves,* Physics 15c, LECTURE NOTE 9, Harvard University.

Shapiro, A. H. 1953 The Dynamics and Thermodynamics of Compressible Fluid Flow, Vol. 1 & 2. Wiley & Sons, New York.

Shih, J., Ho, C., Liu, J. & Tai, Y. 1996 Monoatomic and polyatomic gas flow through uniform microchannels. In *Application of Microfabrication to Fluid Mechanics*, ASME Winter Annual meeting, Atlanta, GA, ASME, 197–203.

Silva, E., Rojas-Cardenas, M., Deschamps, C. J. 2016 Experimental analysis of velocity slip at the wall for gas flows of nitrogen, R134a, and R600a through a metallic microtube. *Intl. J. Refrigeration* **66**, 121–132.

Sod, G. A. 1978 A Survey of Several Finite Difference Methods for Systems of Nonlinear Hyperbolic Conservation Laws. *J. Comput. Phys* **27**, 1–31.

Squires, T. M. 2005 Microfluidics: Fluid physics at the nanoliter scale. *Rev. Modern Phys.* **77**(7), 977–1026.

Stone, H. A., & Kim, S. 2001 Microfluidics: Basic issues, applications, and challenges. *AIChE J.* **47**, 1250–1254.

Stone, H. A., Stroock, A. D. and Ajdari, A. 2004 Engineering flows in small devices: Microfluidics toward a lab-on-a-chip. *Annu. Rev. Fluid Mech*. **36**, 381–411.

Taliadorou, E. G., Neophytou, M. & Georgiou, G. C. 2009 Perturbation solutions of Poiseuille flows of weakly compressible Newtonian liquids. *J. Non-Newt. Fluid Mech.* **163**, 25-34.

Temkin, S. 1981 *Elements of Acoustics*. John Wiley & Sons, New York.

Tsien, H.-S. 1946 Superaerodynamics, mechanics of rarefied gases. *J. Aeronautical Sciences* **13**, 653-664.

Van den Berg, H. R., Seldam, C. A., & van der Gulik, P. S. 1993 Compressible laminar flow in a capillary. *J. Fluid Mech*. **246**, 1–20.

Venerus, D. C. & Bugajsky, D. J. 2010 Compressible laminar flow in a channel. *Phys Fluids.* **22**, 046101.

Venerus, D. C. 2006Laminar capillary flow of compressible viscous fluids.*J. Fluid Mech.* **555**, 59-80.

Velasco, A. E., Friedman, S. G., Pevarnik, M., Siwy, Z. S. & Taborek, P. 2012 Pressure-driven flow through a single nanopore. *Phys. Rev.* E **86**, 025302(R).

Veltzke, T. & Thaming, J. 2012 An analytically predictive model for moderately rarefied gas flow. *J. Fluid Mech*. **698**, 406-422.

Wang, L., Torres, A., Xiang, L., Fei, X., Naido, A., Wu, W. 2015 A technical review on shale gas production and unconventional reservoirs modeling, *Nat. Resour.* **6**, 141.

Whitesides, G.M. 2006 The origins and the future of microfluidics. *Nature* **442**(7101), 368–73.

Wu, L. 2008 A slip model for rarefied gas flows at arbitrary Knudsen number. *Appl. Phys. Lett.* **93**(25), 253103.

Yamaguchi, H., Hanawa, T., Yamamoto, O., Matsuda, Y., Egami, Y. & Niimi, T. 2011 Experimental measurement on tangential momentum accommodation coefficient in a single microtube. *Microfluid Nanofluid* **11**, 57–64.

Yuan, J. & Chen, K. P. 2016 Choked gas flow at pore-scale and its implications to production from high-pressure gas wells. *J. Fluids Eng.* **138**, 014501.

Zhang, W. M., Meng, G., & Wei, X. 2012 A review on slip models for gas microflows. *Microfluid Nanofluid* **13**(6), 845–882.

Zohar, Y., Lee, S. Y. K., Lee, W. Y., Jiang, L. & Tong, P. 2002 Subsonic gas flow in a straight and uniform microchannel. *J. Fluid Mech.* **427**, 125-151.

APPENDIX A

TYPICAL SHALE GAS AND OIL PROPERTY VALUES AT 80°C, 25MPa

The typical shale gas and oil property values are generated from the website calculator http://www.peacesoftware.de/einigewerte/methan_e.html, which is used to calculate the thermodynamic state variables of methane.

1. Gas (methane) properties: $\mu = 1.99\times10^{-5}\,\text{Pa}\cdot\text{s}$, $\mu_b = 6.368\times10^{-3}\,\text{Pa}\cdot\text{s}$, $\rho_i = 136.78\text{kg/m}^3$, $c = 584\text{m/s}$, $D_\rho = 4.82\times10^{-5}\,\text{m}^2/\text{s}$ (based on $\rho_e = 132.68\text{kg/m}^3$).
2. 40^0 API crude oil properties: $\mu_b = \mu = 2.89\times10^{-3}\,\text{Pa}\cdot\text{s}$, $\rho_i = 825\text{kg/m}^3$, $c = 1300\text{m/s}$, $D_\rho = 8.43\times10^{-6}\,\text{m}^2/\text{s}$ (based on $\rho_e = 800.25\text{kg/m}^3$).

APPENDIX B

EFFECTIVE DIFFUSION COEFFICIENT MULTIPLIERS OF MICRO-CHANNEL WITH INFINITY LARGE RESERVOIR AND THE CORRESPONDING EMPIRICAL EQUATIONS

$H\,(\mu\text{m})$	L/H	Re_a	k_{optimal}
0.25	25	1.125	0.463529
0.5	25	2.25	0.475257
1	25	4.5	0.499904
0.25	50	1.125	0.480638
0.5	50	2.25	0.487071
1	50	4.5	0.500349
0.25	75	1.125	0.486889
0.5	75	2.25	0.491338
1	75	4.5	0.500420
0.25	100	1.125	0.490033
0.5	100	2.25	0.493412
1	100	4.5	0.500296

Table B1. Effective diffusion coefficient multipliers for 3D micro-channel drainage flow with channel half-width w as H.

$$k_{emp} = \left[-1.092\left(\frac{h}{L}\right)^2 + 0.3157\left(\frac{h}{L}\right) + 6.665\times10^{-7} \right]\frac{c\sqrt{4hw}}{D_\rho} + \left[3.965\left(\frac{h}{L}\right)^2 - 1.384\left(\frac{h}{L}\right) + 0.5 \right] \quad \text{(B1)}$$

$H\,(\mu\text{m})$	L/H	Re_a	k_{optimal}
0.25	25	1.591	0.458361
0.5	25	3.182	0.481186
1	25	6.364	0.527866
0.25	50	1.591	0.477697
0.5	50	3.182	0.490393
1	50	6.364	0.516198
0.25	75	1.591	0.484861
0.5	75	3.182	0.493704
1	75	6.364	0.511529
0.25	100	1.591	0.488433
0.5	100	3.182	0.495162
1	100	6.364	0.508753

Table B2. Effective diffusion coefficient multipliers for 3D micro-channel drainage flow with channel half-width w as $2H$.

$$k_{emp} = \left[-1.873\left(\frac{h}{L}\right)^2 + 0.4374\left(\frac{h}{L}\right) + 7.967\times10^{-5} \right]\frac{c\sqrt{4hw}}{D_\rho} + \left[6.507\left(\frac{h}{L}\right)^2 - 1.88\left(\frac{h}{L}\right) + 0.4998 \right] \quad \text{(B2)}$$

$H\,(\mu\text{m})$	L/H	Re_a	k_{optimal}
0.25	25	2.25	0.462152
0.5	25	4.5	0.505606
1	25	9	0.593476
0.25	50	2.25	0.479832
0.5	50	4.5	0.504546
1	50	9	0.554607
0.25	100	2.25	0.486390
0.5	100	4.5	0.503786
1	100	9	0.538714
0.25	200	2.25	0.489556
0.5	200	4.5	0.502850
1	200	9	0.529620

Table B3. Effective diffusion coefficient multipliers for 3D micro-channel drainage flow with channel half-width w as $4H$.

$$k = \left[-3.194\left(\frac{h}{L}\right)^2 + 0.6103\left(\frac{h}{L}\right) + 1.653\times10^{-4} \right]\frac{c\sqrt{4hw}}{D_\rho} + \left[10.24\left(\frac{h}{L}\right)^2 - 2.445\left(\frac{h}{L}\right) + 0.4996 \right] \quad \text{(B3)}$$

$H\,(\mu\text{m})$	L/H	Re_a	k_{optimal}
0.25	25	3.182	0.483557
0.5	25	6.364	0.564452
1	25	12.7279	0.727699
0.25	50	3.182	0.492584
0.5	50	6.364	0.540572
1	50	12.7279	0.637145
0.25	75	3.182	0.495730
0.5	75	6.364	0.529757
1	75	12.7279	0.597988
0.25	100	3.182	0.496680
0.5	100	6.364	0.522894
1	100	12.7279	0.575509

Table B4. Effective diffusion coefficient multipliers for 3D micro-channel drainage flow with channel half-width w as $8H$.

$$k = \left[-5.573\left(\frac{h}{L}\right)^2 + 0.8558\left(\frac{h}{L}\right) + 2.721\times10^{-4} \right]\frac{c\sqrt{4hw}}{D_\rho} + \left[16.25\left(\frac{h}{L}\right)^2 - 3.098\left(\frac{h}{L}\right) + 0.4998 \right] \quad \text{(B4)}$$

$H\,(\mu\mathrm{m})$	L/H	Re_a	k_{optimal}
0.25	10	0.5625	0.534939
0.5	10	1.125	0.747541
1	10	2.25	1.180021
0.25	20	0.5625	0.627010
0.5	20	1.125	0.884111
1	20	2.25	1.400605
0.25	50	0.5625	0.724931
0.5	50	1.125	1.024987
1	50	2.25	1.625338
0.25	100	0.5625	0.775261
0.5	100	1.125	1.096438
1	100	2.25	1.737995
0.25	200	0.5625	0.807958
0.5	200	1.125	1.142543
1	200	2.25	1.810784
0.25	300	0.5625	0.820925
0.5	300	1.125	1.160726
1	300	2.25	1.839331
0.25	400	0.5625	0.827941
0.5	400	1.125	1.170559
1	400	2.25	1.854750

Table B5. Effective diffusion coefficient multipliers for 2D micro-channel drainage flow.

$$k = \left[124.5\left(\frac{h}{L}\right)^2 - 6.614\left(\frac{h}{L}\right) + 0.6242\right]\frac{ch}{D_\rho} + \left[124.4\left(\frac{h}{L}\right)^2 - 5.735\left(\frac{h}{L}\right) + 0.4994\right] \qquad \text{(B5)}$$

APPENDIX C

EFFECTIVE DIFFUSION COEFFICIENT MULTIPLIERS FOR MICRO-CAPILLARY WITH SIZE EFFECT

$R(\mu m)$	R/H	Re_a	A/A_{out}	$k_{optimal}$
0.25	25	3.988	1	17.717357
0.5	25	7.976	1	35.726406
1	25	15.9521	1	71.747513
0.25	50	3.988	1	35.726253
0.5	50	7.976	1	71.747209
1	50	15.9521	1	143.790624
0.25	100	3.988	1	71.752880
0.5	100	7.976	1	143.796012
1	100	15.9521	1	287.883209
0.25	200	3.988	1	144.142356
0.5	200	7.976	1	288.231188
1	200	15.9521	1	576.4066
0.25	25	3.988	1/4	5.873799
0.5	25	7.976	1/4	11.057422
1	25	15.9521	1/4	21.243037
0.25	50	3.988	1/4	11.199452
0.5	50	7.976	1/4	21.502351
1	50	15.9521	1/4	41.788417
0.25	100	3.988	1/4	21.630377
0.5	100	7.976	1/4	42.063428
1	100	15.9521	1/4	82.484488
0.25	200	3.988	1/4	42.328773
0.5	200	7.976	1/4	82.871880
1	200	15.9521	1/4	163.336316
0.25	25	3.988	1/16	1.791954
0.5	25	7.976	1/16	3.065450
1	25	15.9521	1/16	5.541602
0.25	50	3.988	1/16	3.142416
0.5	50	7.976	1/16	5.672448
1	50	15.9521	1/16	10.600037
0.25	100	3.988	1/16	5.744422
0.5	100	7.976	1/16	10.726515
1	100	15.9521	1/16	20.493781
0.25	200	3.988	1/16	10.806047
0.5	200	7.976	1/16	20.622904
1	200	15.9521	1/16	39.951502
0.25	25	3.988	1/36	1.053958
0.5	25	7.976	1/36	1.630003
1	25	15.9521	1/36	2.755082
0.25	50	3.988	1/36	1.679924

0.5	50	7.976	1/36	2.833228
1	50	15.9521	1/36	5.075166
0.25	100	3.988	1/36	2.876477
0.5	100	7.976	1/36	5.147388
1	100	15.9521	1/36	9.568211
0.25	200	3.988	1/36	5.190298
0.5	200	7.976	1/36	9.638860
1	200	15.9521	1/36	18.350153
0.25	25	3.988	1/64	0.793869
0.5	25	7.976	1/64	1.121131
1	25	15.9521	1/64	1.764513
0.25	50	3.988	1/64	1.159202
0.5	50	7.976	1/64	1.819718
1	50	15.9521	1/64	3.107828
0.25	100	3.988	1/64	1.850519
0.5	100	7.976	1/64	3.155973
1	100	15.9521	1/64	5.693632
0.25	200	3.988	1/64	3.184621
0.5	200	7.976	1/64	5.738963
1	200	15.9521	1/64	10.717947
0.25	25	3.988	1/100	0.672924
0.5	25	7.976	1/100	0.883430
1	25	15.9521	1/100	1.299557
0.25	50	3.988	1/100	0.915544
0.5	50	7.976	1/100	1.342989
1	50	15.9521	1/100	2.180469
0.25	100	3.988	1/100	1.367240
0.5	100	7.976	1/100	2.216515
1	100	15.9521	1/100	3.869408
0.25	200	3.988	1/100	2.237583
0.5	200	7.976	1/100	3.901910
1	200	15.9521	1/100	7.138914

Table C1. Effective diffusion coefficient multipliers for micro-capillary drainage flow with different size reservoirs.

$R(\mu m)$	R/H	Re_a	A/A_{out}	$k_{optimal}$
0.25	25	3.988	1	17.717357
0.5	25	7.976	1	35.726406
1	25	15.9521	1	71.747513
0.25	50	3.988	1	35.726253
0.5	50	7.976	1	71.747209
1	50	15.9521	1	143.790624
0.25	100	3.988	1	71.752880
0.5	100	7.976	1	143.796012
1	100	15.9521	1	287.883209
0.25	200	3.988	1	144.142356
0.5	200	7.976	1	288.231188
1	200	15.9521	1	576.4066
0.25	25	3.988	4	4.6269178
0.5	25	7.976	4	9.2741709
1	25	15.9521	4	18.56862
0.25	50	3.988	4	9.2871787
0.5	50	7.976	4	18.58324
1	50	15.9521	4	37.17694
0.25	100	3.988	4	18.673002
0.5	100	7.976	4	37.262582
1	100	15.9521	4	74.439948
0.25	200	3.988	4	37.446022
0.5	200	7.976	4	74.629649
1	200	15.9521	4	148.99551
0.25	25	3.988	25	0.7483184
0.5	25	7.976	25	1.4918168
1	25	15.9521	25	2.9789917
0.25	50	3.988	25	1.4987391
0.5	50	7.976	25	2.985831
1	50	15.9521	25	5.9599758
0.25	100	3.988	25	2.9988268
0.5	100	7.976	25	5.9729671
1	100	15.9521	25	11.9214
0.25	200	3.988	25	5.9986446
0.5	200	7.976	25	11.947076
1	200	15.9521	25	23.84389
0.25	25	3.988	100	0.1874255
0.5	25	7.976	100	0.3733146
1	25	15.9521	100	0.7450847
0.25	50	3.988	100	0.3749146

0.5	50	7.976	100	0.746689
1	50	15.9521	100	1.4902256
0.25	100	3.988	100	0.7498777
0.5	100	7.976	100	1.493448
1	100	15.9521	100	2.9805377
0.25	200	3.988	100	1.4997843
0.5	200	7.976	100	2.9869318
1	200	15.9521	100	5.961137

Table C2. Effective diffusion coefficient multipliers for micro-capillary drainage flow with different size contractions.

APPENDIX D

THE ACOUSTIC LIMIT OF THE SHOCK-TUBE PROBLEM IN NARROW CONDUIT

The shock-tube problem is a classical problem in gas dynamics: a diaphragm separates a gas with high pressure from the same gas with a lower pressure in a long tube; when the diaphragm is burst instantaneously, the high pressure gas expands towards the low pressure gas as a compression wave which leads to the formation of a shock wave. The shock-tube problem is a standard problem for studying shock waves experimentally and it is also used as a benchmark problem to test numerical schemes for high speed compressible flows and nonlinear hyperbolic equations (Shapiro 1953; Sod 1978).

As discussed in Chapter 4 section 4.4.1.1, an analytical transient solution of the damped wave equation in infinitely long conduit can be derived using the Green's function for pressure found by Buckingham (2005).

Assuming the channel/tube is infinitely long. Initially there is a density plug in the section $-L < x < L$ with density ρ_i; while the rest of the channel/tube with a density $\rho_e (< \rho_i)$ is separated from the plug with diaphragms. At t = 0, the diaphragms are broken instantaneously, resulting two waves moving in opposite directions. Assuming the density difference is infinitesimal, $(\rho_i - \rho_e)/\rho_i << 1$, so that nonlinear effect is negligible (no shock waves). See Figure below.

The transient density can be obtained from the solution of the damped wave eqn. for the density increment $\rho' = \rho - \rho_e$:

$$\frac{\partial^2 \rho'}{\partial t^2} = \left(c^2 + D_\rho \frac{\partial}{\partial t} \right) \nabla^2 \rho' \qquad \text{(D1)}$$

subject to the initial condition. Buckingham (2005) has found the Green's function for the pressure corresponding to concentrated impulse at the origin at t = 0, which is in an integral form and it is explicitly given as his equation (24). An approximate expression for

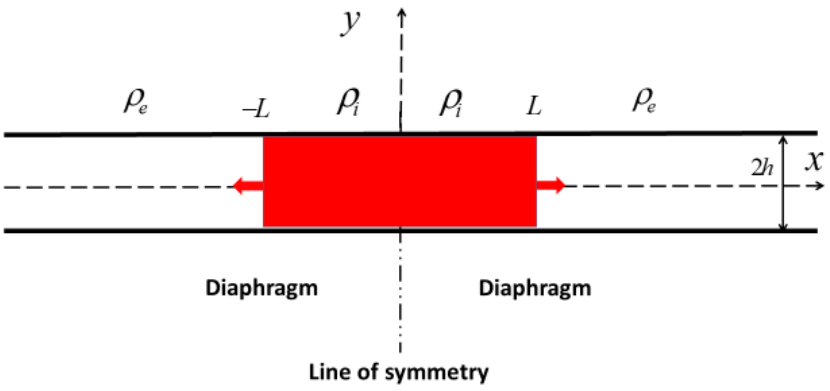

Figure D1. Initial condition for the shock-tube problem.

the solution is given by equation (29a, b) in Buckingham (2005),

$$G = Sign(t)\frac{\rho_0 c^2 Q_p}{4\sqrt{2\pi\gamma t}}\left[F(x,t)+F(-x,t)\right]$$
$$F(x,t)=\left(1+\frac{x}{ct}\right)\exp\left[-\frac{(ct-x)^2}{2\gamma c^2 t}\right] \quad , \tag{D2}$$
$$\gamma=\frac{4\mu}{3\rho_0 c^2}=\frac{D_\rho}{c^2}$$

where $Sign(t)$ is the unit step function.

Let $x \to x - x_0$, then we have obtained the Green's function for an impulse located at $x = x_0$ at t = 0:

$$G(x,x_0;t) = Sign(t)\frac{\rho_0 c Q_p}{4\sqrt{2\pi\gamma t}}\left[F(x,x_0;t)+F(-x,x_0;t)\right]$$
$$F(x,x_0;t)=\left(1+\frac{x-x_0}{ct}\right)\exp\left[-\frac{(ct-x+x_0)^2}{2\gamma c^2 t}\right] \quad . \tag{D3}$$

The initial condition we have is

$$t=0: p = f(x) = rect[x,L] = \frac{1}{2}Sign[L-x]+\frac{1}{2}Sign[L+x], \tag{D4}$$

where $rect[x,L]$ is the rectangular function. Thus, from the theory of Green's function, we have the pressure solution as

$$\begin{aligned} p(x,t) &= \int_{-\infty}^{\infty} f(x_0)G(x,x_0;t)dx_0 = \int_{-L}^{L} f(x_0)G(x,x_0;t)dx_0 = \int_{-L}^{L} G(x,x_0;t)dx_0 \\ &= \frac{\rho_0 c^2 Q_p}{4\sqrt{2\pi\gamma t}} \int_{-L}^{L} \left[F(x,x_0;t) + F(-x,x_0;t)\right]dx_0 \end{aligned} \quad . \qquad \text{(D5)}$$

This integral can be carried out analytically in MATHEMATICA, and the solution is then

$$p(x,t) = \frac{\rho_0 c^2 Q_p}{8} \left\{ \begin{aligned} &\sqrt{\frac{2\gamma}{\pi t}} \left[e^{-\frac{(L+x+ct)^2}{2c^2\gamma t}} - e^{-\frac{(L+x-ct)^2}{2c^2\gamma t}} + e^{-\frac{(L-x+ct)^2}{2c^2\gamma t}} - e^{-\frac{(L-x-ct)^2}{2c^2\gamma t}} \right] \\ &+ \left[erf\left(\frac{L+x-ct}{c\sqrt{2\gamma t}}\right) - erf\left(-\frac{L+x-ct}{c\sqrt{2\gamma t}}\right) + erf\left(\frac{L-x+ct}{c\sqrt{2\gamma t}}\right) - erf\left(-\frac{L-x+ct}{c\sqrt{2\gamma t}}\right) \right] \\ &+ 2erf\left(\frac{L+x+ct}{c\sqrt{2\gamma t}}\right) - 2erf\left(\frac{-L+x+ct}{c\sqrt{2\gamma t}}\right) \end{aligned} \right\} \qquad \text{(D6)}$$

Thus, the excess density is then

$$\begin{aligned} \rho' &= \frac{p(x,t)}{c^2} \\ &= \frac{\rho_0 Q_p}{8} \left\{ \begin{aligned} &\sqrt{\frac{2\gamma}{\pi t}} \left[e^{-\frac{(L+x+ct)^2}{2c^2\gamma t}} - e^{-\frac{(L+x-ct)^2}{2c^2\gamma t}} + e^{-\frac{(L-x+ct)^2}{2c^2\gamma t}} - e^{-\frac{(L-x-ct)^2}{2c^2\gamma t}} \right] \\ &+ erf\left(\frac{L+x-ct}{c\sqrt{2\gamma t}}\right) - erf\left(-\frac{L+x-ct}{c\sqrt{2\gamma t}}\right) + erf\left(\frac{L-x+ct}{c\sqrt{2\gamma t}}\right) - erf\left(-\frac{L-x+ct}{c\sqrt{2\gamma t}}\right) \\ &+ 2erf\left(\frac{L+x+ct}{c\sqrt{2\gamma t}}\right) - 2erf\left(\frac{-L+x+ct}{c\sqrt{2\gamma t}}\right) \end{aligned} \right\} \end{aligned} \qquad \text{(D7)}$$

We know that,

$$\lim_{t\to 0, x\to 0} \rho' = \rho_i - \rho_e \,. \tag{D8}$$

From the above solution, the two terms in the bracket takes the value of "0" and "8" in such limit. Thus,

$$\rho_0 Q_p = \rho_i - \rho_e \,. \tag{D9}$$

The complete solution for the excessive density is then

$$\rho' = \frac{\rho_i - \rho_e}{8}\left\{\begin{array}{l}\sqrt{\frac{2\gamma}{\pi t}}\left[e^{-\frac{(L+x+ct)^2}{2c^2\gamma t}} - e^{-\frac{(L+x-ct)^2}{2c^2\gamma t}} + e^{-\frac{(L-x+ct)^2}{2c^2\gamma t}} - e^{-\frac{(L-x-ct)^2}{2c^2\gamma t}}\right] \\ +\left[erf\left(\frac{L+x-ct}{c\sqrt{2\gamma t}}\right) - erf\left(-\frac{L+x-ct}{c\sqrt{2\gamma t}}\right) + erf\left(\frac{L-x+ct}{c\sqrt{2\gamma t}}\right) - erf\left(-\frac{L-x+ct}{c\sqrt{2\gamma t}}\right)\right] \\ +2erf\left(\frac{L+x+ct}{c\sqrt{2\gamma t}}\right) - 2erf\left(\frac{-L+x+ct}{c\sqrt{2\gamma t}}\right)\end{array}\right\} \tag{D10}$$

Let

$$h(x,t) = \frac{1}{8}\left\{\begin{array}{l}\sqrt{\frac{2\gamma}{\pi t}}\left[e^{-\frac{(L+x+ct)^2}{2c^2\gamma t}} - e^{-\frac{(L+x-ct)^2}{2c^2\gamma t}} + e^{-\frac{(L-x+ct)^2}{2c^2\gamma t}} - e^{-\frac{(L-x-ct)^2}{2c^2\gamma t}}\right] \\ +erf\left(\frac{L+x-ct}{c\sqrt{2\gamma t}}\right) - erf\left(-\frac{L+x-ct}{c\sqrt{2\gamma t}}\right) + erf\left(\frac{L-x+ct}{c\sqrt{2\gamma t}}\right) - erf\left(-\frac{L-x+ct}{c\sqrt{2\gamma t}}\right) \\ +2erf\left(\frac{L+x+ct}{c\sqrt{2\gamma t}}\right) - 2erf\left(\frac{-L+x+ct}{c\sqrt{2\gamma t}}\right)\end{array}\right\} \tag{D11}$$

Then, the density solution can be expressed as,

$$\rho' = \left(\rho_i - \rho_e\right) h(x,t) \,. \tag{d12}$$

(a)

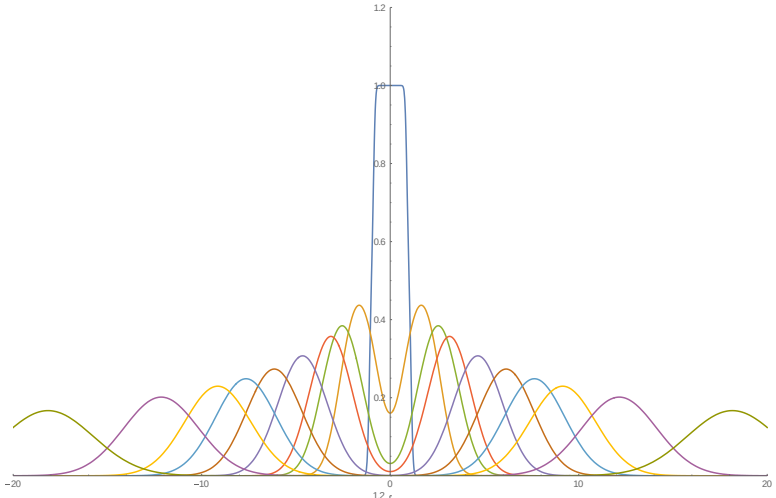

(b)

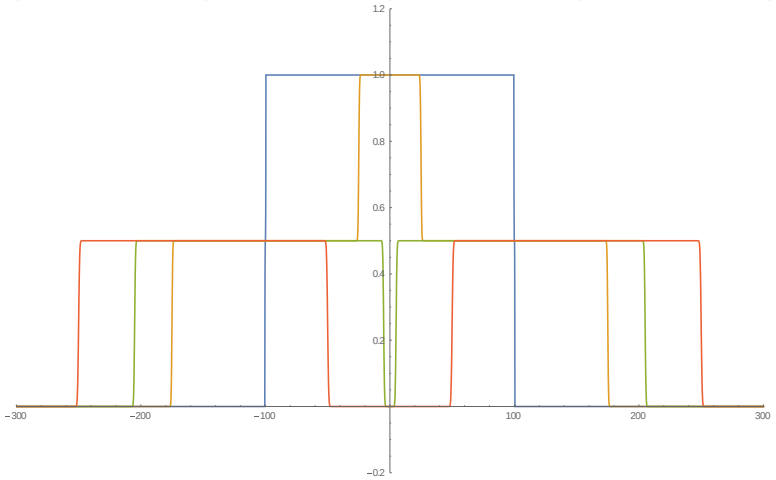

Figure D2. Density solution $h(x,t)$ with (a) $L=1,\ c=3,\ \gamma=0.1$, and (b) $L=100,\ c=300,\ \gamma=10^{-7}$.

Figure D2a shows the solution for $h(x,t)$ with $L=1,\ c=3,\ \gamma=0.1$. This clearly shows how the "cell/plug" is emptied in time. A more realistic case with $L=100,\ c=300,\ \gamma=10^{-7}$ (with $\gamma=D_\rho/c^2$) is shown in figure D2b, which shows no damping/smoothing of the square waves. Noticed, the excessive density ρ' inside the cell stays above 0 at all times and there is no "oscillation" in the excess density inside the cell. This indicates gas is just like an inviscid fluid, being pushed away by their volumetric expansion.

The analytical square wave solution is consistent with the numerical density perturbation solution shown in figure 4.4a.

APPENDIX E

DETAILED DOCUMENTATION OF NUMERICAL SIMULATIONS

E1. Governing equation, boundary conditions and initial conditions

In order to properly simulate the drainage flow in a system with a micro-conduit connected to a reservoir/contraction, COMSOL 5.3 is employed. COMSOL Multiphysics is a general-purpose simulation software for modeling designs, devices, and processes in all fields of engineering manufacturing and scientific research. It is a finite element analysis based simulation software, which allows a user to easily manipulate and expand its pre-constructed modules depending on specific requirements. The damped wave equation can be simulated using COMSOL's 2D/3D Pressure Acoustic, Transient Module.

The viscous fluid model is selected under the Transient Pressure Acoustic Module. The model adds a scalar wave equation into the system,

$$\frac{1}{\rho c^2}\frac{\partial^2 p_t}{\partial t^2}+\nabla\cdot\left(-\frac{1}{\rho}\left(\nabla p_t-q_d\right)-\frac{1}{\rho c^2}\left(\frac{4\mu}{3}+\mu_b\right)\frac{\partial\nabla p_t}{\partial t}\right)=Q_m, \tag{E1}$$

where p_t is the total acoustic pressure, ρ is the fluid density and c is the speed of sound, q_d and Q_m are two domain sources, which can be used in a more complex model. Since our drainage system is governed by the damped wave equation (2.3), which governs the density perturbation, we can transform the scalar wave equation (E1) by taking the total acoustic pressure variable p_t as the density perturbation ρ' and setting the fluid density term ρ to one. The dynamic viscosity μ and the bulk viscosity μ_b is set to $3D_\rho/4$ and zero respectively in the damping term. The two domain sources are set to zero. Thus, the scalar wave equation (E1) is reduced to the damped wave equation,

$$\frac{\partial^2\rho'}{\partial t^2}=\left(c^2+D_\rho\frac{\partial}{\partial t}\right)\nabla^2\rho'. \tag{E2}$$

Sound hard Boundary (Wall) is chosen for the boundaries with the default setting. The initial values are set as $\rho_i - \rho_e$ and zero in the micro-conduit and the reservoir/contraction, respectively.

E2. Meshing and time stepping for the wave simulation

Meshing and time-stepping are critical for obtaining accurate results especially for acoustic wave simulations, which usually requires fine mesh and small-time steps to resolve the wave evolution. By default, second order (quadratic) Free Triangular element is used in the capillary and 2D channel models. Free Tetrahedral element is used in 3D channel models. In order to satisfy the Nyquist criterion, at least two elements per local wavelength is required, and 5 elements per local wavelength can provide a higher accuracy (COMSOL). Unlike traditional periodic waves, the oscillating density perturbation wave within the micro-conduit is always initiated from a density discontinuity at the conduit exit (wavelength $\lambda \approx 0$). As it oscillates within the conduit, the wave front will be continuously smoothed out due to the diffusive damping or wave leaking. In other words, the wavelength increases from zero to $2L$ gradually during the drainage process (figure 2.1). Thus, density wave propagation in the early time stage requires the finest meshing. However, it would be impossible to fully resolve the wave in its initial time stage ($t \ll T/8$) using finite size meshing as the wavelength is close to zero (very steep wave front). Fortunately, this initial time stage is of very short duration, about $t \sim O(10^{-8})$ seconds, with usual parameters (section 4.7.1), and it's influences to the drainage result at large time $t \sim O(10^{-3})$ seconds can be neglected.

For practical purposes, the maximum mesh size within the conduit is set to $\Delta x_{\max} = R/2$, which is calculated based on the wavelength at $t = T$ (first oscillating period), and it satisfies $N > 5$ condition (more than 5 elements per local wavelength) for micron size conduit and $N = 2$ condition for millimeter size conduit. Finer mesh ($\Delta x = R/10$) is used at the conduit exit in order to increase the accuracy of the wave propagating from the conduit to the reservoir/contraction. For simulations for an infinitely large reservoir ($R_{out}/R = 250$), a coarser mesh is used in the reservoir, $\Delta x_{\max} = 10R$, because only a small amount of density wave will leak into the reservoir and they will eventually be absorbed by the PML. As for the simulations for a finite size reservoir or contraction, we set $\Delta x_{\max} = R_{out}/2$. From the region with small elements to the region with large elements, the element growth rate is set to 1.02 (2% size grow per adjacent element), ensuring a smooth element size transition. For the PML region, a mapped quadrilateral mesh is used with element size same as the largest element in the reservoir $\Delta x = 10R$.

For time stepping, a CFL condition is defined as $\mathrm{CFL} = c\Delta t N/\lambda$ based on the wave speed c, time step Δt, wavelength λ and the maximum number of elements per local wavelength N (COMSOL). Thus, with maximum mesh size set as $\Delta x_{\max} = R/2$ inside the conduit, the time step can be calculated as $\Delta t = \mathrm{CFL}\cdot\Delta x_{\max}/c = \mathrm{CFL}\cdot R/2c$, or $\Delta t = (\mathrm{CFL}\cdot T)/(8L/R)$, where $T = 4L/c$ is the oscillating period. In order to find out an optimal CFL number, a convergence test is performed in terms of the excess mass solution shown in section 4.7.1.

As shown in figure E1a, the results for the excess mass converges when the CFL number is reduced. When $\mathrm{CFL} \le 10$, the difference between the excess mass calculated using two

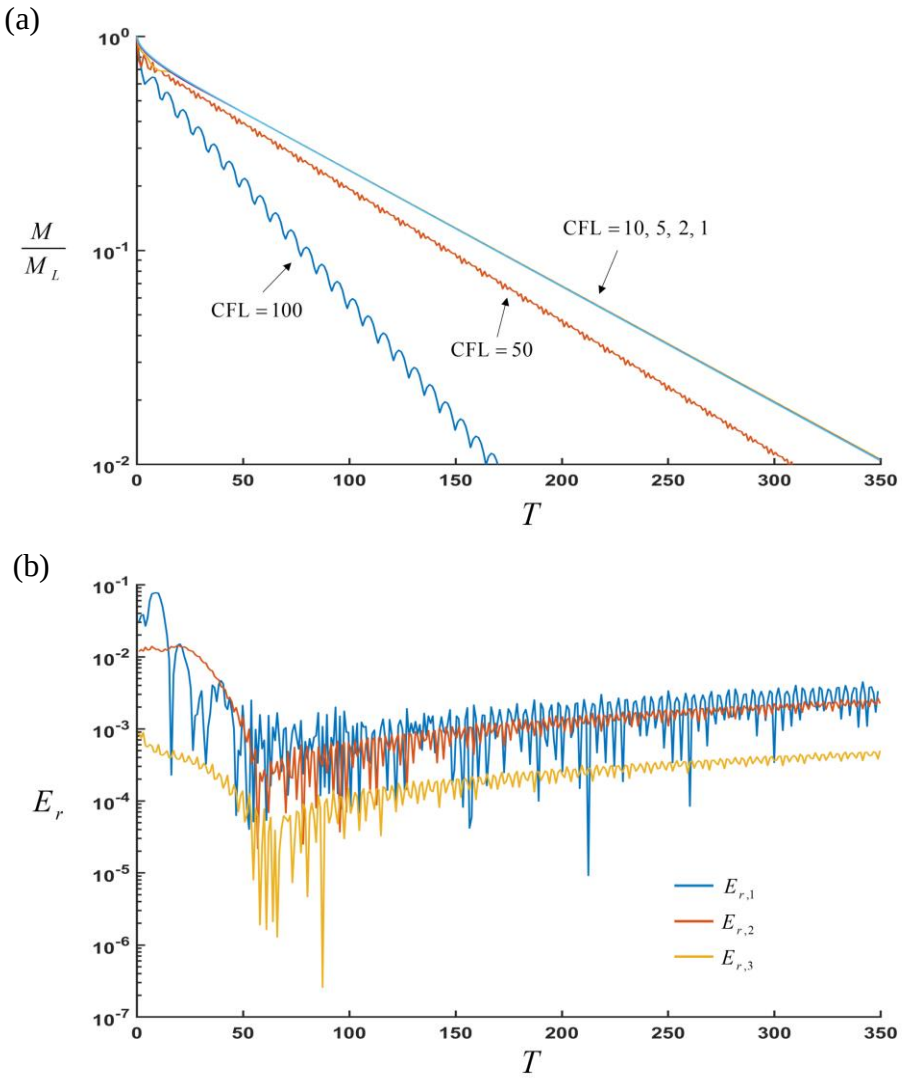

Figure E1. (a) Normalized excess mass envelope vs. oscillating period $T = 4L/c$ simulated by using different CFL number. M_L is the total amount of producible fluid from the capillary. (b) Relative error between each CFL result.

CFL numbers are indistinguishable. The relative error in the excess mass for two CFL numbers are calculated as,

$$E_{r,1} = \left| \frac{M_{\text{CFL=10}} - M_{\text{CFL=5}}}{M_{\text{CFL=10}}} \right|, \quad E_{r,2} = \left| \frac{M_{\text{CFL=5}} - M_{\text{CFL=2}}}{M_{\text{CFL=5}}} \right|, \quad E_{r,3} = \left| \frac{M_{\text{CFL=2}} - M_{\text{CFL=1}}}{M_{\text{CFL=2}}} \right| \qquad \text{(E3)}$$

and they are plotted in figure E1b.

As shown in figure E1b, by decreasing the CFL from 2 to 1, the maximum excess mass envelope result only changes 0.1% (figure E3b yellow curve) which indicates the excess mass result is fully resolved. Thus, we set our optimal CFL number to be 1, which gives a time step $\Delta t = T/400$ for a capillary with 50 length to radius ratio. CFL = 2 is also acceptable for some cases that requires simulations to large times.

E3. Numerical schemes

The "Time Dependent" solver is used for the transient simulation. In COMSOL, the Time-Dependent solver provides three optional numerical schemes: the implicit time-stepping methods BDF (Backward Differentiation Formula), the implicit generalized-alpha method and the explicit method from a family of Runge-Kutta methods. BDF methods have been used for long time wave simulations and are known for their stability, but they can also bring severe damping effects. On the other hand, the generalized-alpha scheme is similar to the second order BDF method but it contains a parameter called alpha ($0 < \alpha < 1$) in the formula. The value of alpha controls the degree of damping for high frequencies, with $\alpha = 1$ representing no numerical damping and $\alpha = 0$ representing maximum numerical damping. Thus, for small time scale simulations, both BDF (second order) and the generalized-alpha perform well. For simulations to large time, however, the generalized-alpha scheme causes much less numerical damping, thus it is more accurate. Explicit Runge-Kutta methods are suitable for non-stiff problems. However, for the damped wave equation, large stiffness is detected by the Runge-Kutta solver, which demands an extremely small time-step. Also, with the PML installed within the domain, a singular explicit time-stepping matrix error is preventing the program from completing the

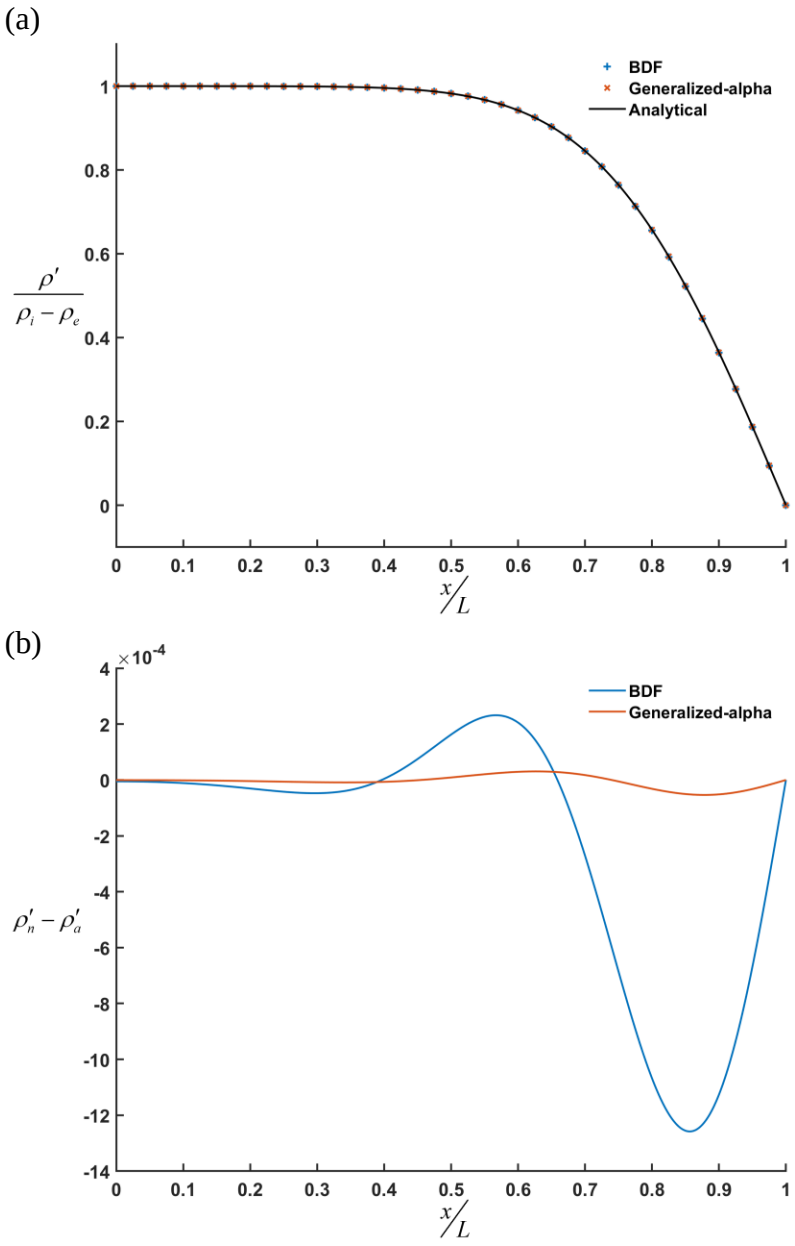

Figure E2. (a) Density perturbation wave curve at $t = 5T$ solved by two different implicit methods and the analytical result. (b) Density perturbation difference between the numerical result and the analytical result for the two implicit methods.

task. Thus, Runge-Kutta method is not suitable for the present simulations. Based on the above discussions, the generalized-alpha scheme is used here for the wave model with $\alpha = 0.75$ by default.

A benchmarking test is performed by simulating the capillary drainage flow with fixed outlet density (chapter 2) using two different implicit methods with the same time-step and meshing. The test model is created using Pressure Acoustic Transient Module with the same input parameters as the damped wave equation discussed above: the capillary dimension is $R = 1\mu\text{m}$, $L = 50\mu\text{m}$. Gas property inputs, $\rho_i = 1.01\text{kg/m}^3$, $\rho_e = 1\text{kg/m}^3$, $D_\rho = 5\times10^{-5}\text{m}^2/\text{s}$, $c = 450\text{m/s}$. Free triangular element is used with identical element size, $\Delta x = R/4$, CFL is set to 1 for the time step ($\Delta t = T/800$). For the generalized-alpha method, $\alpha = 0.75$ is used by default. For BDF method, second order is selected. Both methods are solved with absolute tolerance factor set as 1×10^{-4}.

As shown in figure E2a, with the fine mesh and small-time step, after 5 oscillation period, both the BDF method and the generalized-alpha method show good agreements with the analytical solution (2.19). However, by taking the differences $\rho'_{\text{numerical}} - \rho'_{\text{analytical}}$ (figure E2b), the numerical result solved by the BDF method shows a larger error than generalized-alpha method, which is caused by a higher numerical damping effect. Since most of the wave models require long time simulations ($t > 500T$), even such small error can accumulate in time, leading to meaningful errors at larger times. For this reason, using the generalized-alpha method can provide more accurate results for larger times.

E4. Perfectly matched layer setting

As discussed in section 4.2, a Perfectly Matched Layer (PML) is set at the outer edge of the reservoir/contraction in order to fully absorb the acoustic wave. In COMSOL, the PML can be implemented under the Definitions node. The geometry type of the PML is selected as “Cylindrical” for the tube system, “Cartesian” for the 2D channel system and

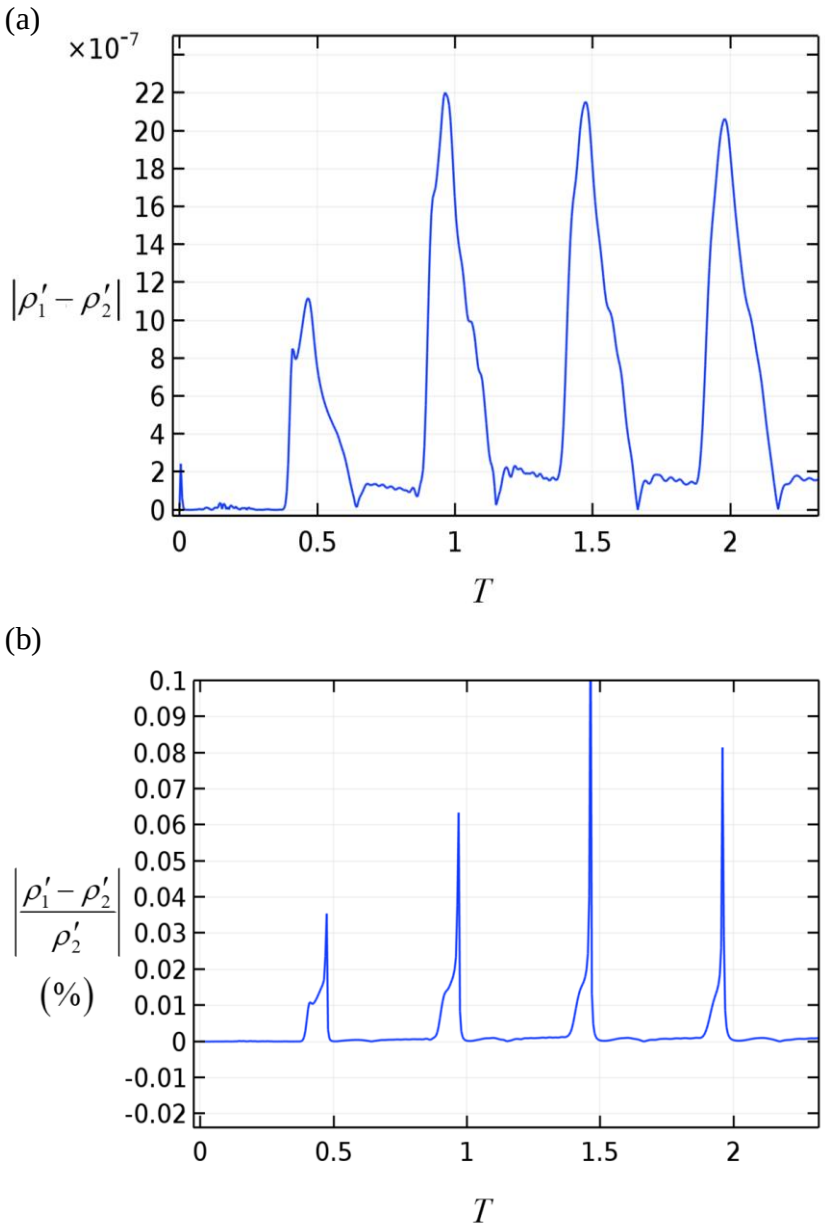

Figure E3. (a) Absolute error and (b) relative error of the density perturbation at conduit exit within 2.5 oscillating period.

"Spherical" for the 3D channel system with the origin of the coordinate set at the channel exit. The Rational stretching function type is used with PML, with scaling factor and scaling curvature parameters set as 6 and 3, respectively.

In order to validate that such a PML results in a high quality of wave absorption, a simulation test is performed. Two different size quarter-sector-shape reservoirs are modeled in the test. One with a small radius, the same as the conduit length, $R_{out} = L$, where a ring shape PML is placed at $0.8R_{out} \sim R_{out}$. The second model, as a benchmark, has a large reservoir radius $R_{out} = 10L$ without any PML installed. Since $L = 100R$, these two models can be considered as drainage flow into an infinite large reservoir (section 4.5). As the drainage starts, a periodic density perturbation wave pulse is propagating into the reservoir from the conduit exit. Each outgoing wave will be absorbed by the PML within the smaller reservoir model $R_{out} = L$, and only a very small fraction will be reflected back to the conduit exit due to the PML numerical error. For the larger reservoir model $R_{out} = 10L$, waves will continuously propagate until it hits the outer edge. By comparing the time-dependent density perturbation value at the conduit exit, we can observe how much the numerical-error-induced reflected wave is altering the drainage process.

As shown in figure E3, the absolute error of the density perturbation spikes every half period as the numerical-error-induced reflected wave reaches the conduit exit. The maximum density error is below 2.2×10^{-6} or 0.1%. Thus, the PML provides a very good wave absorption.